

# Study of the Galactic Diffuse X-Ray Emission with the Suzaku Satellite

Hideki Uchiyama

Department of Physics, Graduate School of Science, Kyoto University  
*Kitashirakawa Oiwake-cho, Sakyo-ku, Kyoto, 606-8502, Japan*

## Abstract

The Milky Way galaxy emits diffuse X-rays (the Galactic Diffuse X-ray Emission, GDXE) from the center, ridge and bulge. The GDXE accompanies the strong Fe XXV  $K\alpha$  (6.7 keV), Fe XXVI  $K\alpha$  (6.97 keV) and Fe I  $K\alpha$  (6.4 keV) lines. The origin of the GDXE and the three Fe  $K\alpha$  lines has been an open question though supernova remnants (SNRs) or cataclysmic variables (CVs) are suggested as the probable candidates of the origin. The spatial distributions and properties of the Fe  $K\alpha$  lines in the GDXE are the key to revealing the origin.

In this thesis, we show the results of the Suzaku observation of the region from the Galactic center (GC) to the ridge and the bulge ( $-3^\circ < l < 2^\circ$ ,  $-2^\circ < b < 1^\circ$ ). We also report the analysis results of a SNR located in the GC region, Sgr A East, and a newly found X-ray point source, Suzaku J1740.5–3014, in the data set.

The intensity profiles of the highly ionized Fe  $K\alpha$  lines and the continuum in the GDXE are described with a phenomenological two-exponential component model. The e-folding scale of the intensity profile along the Galactic longitude changes around  $|l| = 1^\circ$ – $2^\circ$ . The transition of the line intensity ratio of Fe XXVI  $K\alpha$  to Fe XXV  $K\alpha$  also occurs in  $|l| = 1^\circ$ – $2^\circ$ , which corresponds to the border between the nuclear bulge (NB) and the Galactic disk (GD). These facts suggest that the GDXE contains two components which accompany the NB and the GD, respectively. The scale height of the intensity profile along the Galactic latitude changes around  $|b| = 0^\circ$ .5– $1^\circ$ . The line intensity ratio of Fe XXVI  $K\alpha$  to Fe XXV  $K\alpha$  is not different in  $-2^\circ < b < 1^\circ$ , significantly.

The equivalent widths of the Fe I  $K\alpha$  and Fe XXV  $K\alpha$  lines are anti-correlated in the GD regions ( $|l| = 1^\circ$ – $3^\circ$ ,  $|b| < 0^\circ$ .1). From this relation, we obtained the equivalent widths of the Fe I  $K\alpha$  and Fe XXV  $K\alpha$  lines to their associated continua,  $EW'_{6.4}$  and  $EW'_{6.7}$ , respectively. The  $EW'_{6.4}$  is significantly smaller than those reported previously in the inner NB regions (Sgr A and C) though the  $EW'_{6.7}$  is almost same among the every region. It suggests that the origin of the Fe I  $K\alpha$  line might be different between the NB and the GD.

To reveal whether the GDXE is the superposition of point sources or truly diffuse plasma, we compared the intensity profile of the GDXE with those of near-infrared observations and X-ray point sources. However, conclusive results are not obtained.

In the analysis of Sgr A East, we detected the non-thermal component for the first time and determined the temperature accurately. Sgr A East has two-temperature plasma of  $kT \sim 6$  and  $\sim 1.2$  keV. The temperature of  $kT \sim 6$  keV is peculiarly hot as a SNR and close to that of the GDXE. However, the total line intensity ratio of Fe XXVI  $K\alpha$  to Fe XXV  $K\alpha$  is 0.05, and too low to explain that (0.2–0.4) of the GDXE.

From Suzaku J1740.5–3014, we detected three Fe  $K\alpha$  lines and the coherent and clear pulsation of 432.1 s. These features are typical for an intermediate polar (IP), one of the categories of cataclysmic variables. The interstellar absorption indicates that Suzaku J1740.5–3014 is located not in the GC region but in the distance of  $\sim 2$  kpc from the Sun. The luminosity of  $\sim 10^{33}$  erg  $\text{s}^{-1}$  is also typical for an IP.

We compared the GDXE spectra with those of Sgr A East, Suzaku J1740.5–3014, other CVs, other SNRs and point sources in the GC region. The spectra of these sources are different from that of the GDXE.

# Contents

<b>1</b>	<b>Introduction</b>	<b>1</b>
<b>2</b>	<b>Review</b>	<b>3</b>
2.1	Structure of the Milky Way Galaxy and the Galactic Center Region . . . . .	3
2.2	Discovery of the Galactic Diffuse X-ray Emission and its Fe K $\alpha$ Lines . . . . .	5
2.3	Candidates for the Origin of the Fe XXV K $\alpha$ and Fe XXVI K $\alpha$ Line Emissions .	6
2.3.1	Truly Diffuse Plasma Origin . . . . .	6
2.3.2	Faint Point Sources Origin . . . . .	7
2.3.3	Charge Exchange Origin . . . . .	10
2.4	Candidates for the Origin of the Fe I K $\alpha$ Line Emission . . . . .	10
2.4.1	Truly Diffuse Interstellar Gas Origin . . . . .	10
2.4.2	Faint Point Sources Origin . . . . .	10
2.5	Recent Observation of the GDXE . . . . .	11
2.5.1	GDXE in the Sgr A Region ( $ l  < 0.3^\circ$ ) . . . . .	11
2.5.2	GDXE in the Inner Region of the NB ( $0^\circ.3 <  l  < 2^\circ$ ) . . . . .	12
2.5.3	GDXE in the Galactic Ridge ( $ l  > 8^\circ$ ) . . . . .	13
2.5.4	GDXE in the Galactic Bulge ( $ b  > 1^\circ$ ) . . . . .	14
2.6	Review of Sgr A East . . . . .	16
2.7	Summary of the Recent Study and Subjects Tackled in This thesis . . . . .	16
<b>3</b>	<b>Instrument</b>	<b>19</b>
3.1	Overview of the Suzaku Satellite . . . . .	19
3.2	X-Ray Telescope (XRT) . . . . .	20
3.3	X-Ray Imaging Spectrometer (XIS) . . . . .	23
3.3.1	Introduction of X-ray Charge Coupled Device Cameras . . . . .	23
3.3.2	Overview of the XIS . . . . .	24
3.3.3	Charge Injection Capability . . . . .	26
3.3.4	Performance of the XIS . . . . .	29
<b>4</b>	<b>Galactic Diffuse X-ray Emission</b>	<b>35</b>
4.1	Observation & Data Reduction . . . . .	35
4.1.1	Observation . . . . .	35
4.1.2	Data Reduction . . . . .	35
4.1.3	Response Function of the XIS . . . . .	37
4.1.4	Background . . . . .	37
4.1.5	Exclusion of Bright Sources . . . . .	37

4.2	Spatial Distribution of the GDXE . . . . .	40
4.2.1	Intensity Profiles along the Galactic Longitude . . . . .	40
4.2.2	Intensity Profiles along the Galactic Latitude . . . . .	43
4.2.3	Two-Dimensional Model for the Intensity Profile . . . . .	53
4.3	Detailed Spectral Analysis . . . . .	56
<b>5</b>	<b>Sgr A East</b>	<b>69</b>
5.1	Observation & Data Reduction . . . . .	69
5.2	Spectral Analysis . . . . .	70
5.2.1	Emission Lines . . . . .	70
5.2.2	Sulfur Line Diagnostics . . . . .	71
5.2.3	Iron and Nickel Line Diagnostics . . . . .	72
5.2.4	Thin Thermal Plasmas and Power-Law Component . . . . .	76
5.3	Short Discussion for Sgr A East . . . . .	76
5.3.1	Thermal Plasma . . . . .	76
5.3.2	Hard Tail . . . . .	76
5.3.3	Chemical Compositions . . . . .	79
<b>6</b>	<b>Suzaku J1740.5–3014</b>	<b>81</b>
6.1	Observation & Data Reduction . . . . .	81
6.2	Analysis . . . . .	82
6.2.1	Imaging . . . . .	82
6.2.2	Spectrum . . . . .	83
6.2.3	Timing . . . . .	86
6.3	Short Discussion for Suzaku J1740.5-3014 . . . . .	87
6.3.1	Identify of Suzaku J1740.5-3014 by Comparison with Previous X-ray Observations . . . . .	87
6.3.2	Suzaku J1740.5-3014 as a New Intermediate Polar Candidate . . . . .	88
<b>7</b>	<b>Discussion</b>	<b>91</b>
7.1	Spatial Distributions of the Fe $K\alpha$ Line Emissions of the GDXE . . . . .	91
7.1.1	Uncertainty of the Intensity Measurement . . . . .	91
7.1.2	Comparisons with Stellar Mass Distribution Observed in the Infrared . . . . .	91
7.1.3	Comparisons with Distribution of X-ray Point Sources Observed with Chandra . . . . .	95
7.2	Spectra of the GDXE . . . . .	95
7.2.1	Line Intensity Ratios of Fe XXVI $K\alpha$ to Fe XXV $K\alpha$ . . . . .	95
7.2.2	Relation between the Equivalent Widths of the Fe I $K\alpha$ and Fe XXV $K\alpha$ Line Emissions . . . . .	100
7.2.3	Center Energy of the Fe XXV $K\alpha$ Line Emission . . . . .	102
7.3	Comparison between the Intensities of the GDXE and X-ray Point Sources Detected with Chandra . . . . .	103
7.4	Properties of Sgr A East and Other GC SNR and Their Contribution to the GDXE103	
7.5	Properties of Suzaku J1740.5-3014 and Other Point Sources and Their Contribution to the GDXE . . . . .	105

<b>8 Conclusion</b>	<b>107</b>
<b>A X-ray Emission from Thin-Thermal Plasma</b>	<b>109</b>
<b>B CTI Correction and In-Orbit Calibration for SCI</b>	<b>113</b>
B.1 Property of the CTI in the SCI Mode and the “Sawtooth” CTI model . . . . .	113
B.2 CTI Measurement in Orbit . . . . .	115
B.2.1 Calibration Data . . . . .	115
B.2.2 Determination of the CTI Parameters . . . . .	118
B.3 Energy Scale Uniformity and Resolution in the SCI Mode . . . . .	121



# Chapter 1

## Introduction

Since the beginning of the astronomy, people had observed the sky in the visible light mainly. Visible light is emitted from objects at a temperature of a few thousands K like the Sun. The temperature of the X-ray emitting object is about  $10^7$  K. Before 1960s, most of scientists did not imagine that such a hot object commonly exists in the universe. Ricardo Giacconi and Bruno Benedetto Rossi, however, launched an Aerobee rocket carrying Geiger counters and discovered the first extrasolar X-ray source, Sco X-1 [23]. It was the beginning of the X-ray astronomy. Bruno Benedetto Rossi said;

”I must admit that my main motivation for pressing forward was a deep seated faith in the boundless resourcefulness of nature, which so often leaves the most daring imagination of man far behind.”

As he said, ”unimaginable” X-ray emissions have been discovered from a lot of celestial objects, for example, X-ray binaries like Sco X-1, of course, young stellar objects [116], late type stars [67], clusters of the galaxies [13], and comets [57] etc. Our Galaxy (the Milky Way galaxy) is one of the most unimaginable X-ray sources.

The Galactic Diffuse X-ray Emission (GDXE) extends over more than  $100^\circ$  along the Galactic plane but only  $\sim 2^\circ$  across it (e.g. [137, 142]) and thus it has been called as the Galactic “ridge” X-ray emission. One of the most interesting features of the GDXE is its strong Fe  $K\alpha$  line emissions discovered with the Tenma satellite [44]. With the Ginga satellite, it was revealed that the Fe  $K\alpha$  emission concentrates sharply at the Galactic center (GC) region [47]. With the ASCA satellite, the Fe  $K\alpha$  line feature is resolved to three lines at the energy of 6.4, 6.7 and 6.97 keV [48].

The 6.7 and 6.97 keV lines correspond to the Fe XXV  $K\alpha$  and XXVI  $K\alpha$  line emissions. These Fe ions imply the existence of the optically thin high-temperature plasma ( $kT = 5\text{--}10$  keV or  $T = \text{several } 10^7$  K). If there is truly diffuse hot plasma gas which fills the Galactic plane, the huge energy input is required to sustain it. The most probable energy suppliers are supernovae but the required supernova rate is about one per 10 years [45], which is one order larger than the recently estimated rate [17, 65]. In addition, the temperature of the GDXE is higher than those of known young supernova remnants (SNRs). Unknown energy suppliers and plasma heating process might exist in our Galaxy. An alternatively explanation of the GDXE, proposed soon after its discovery (e.g. [44]), is the superposition of unresolved faint point sources. The most probable candidates of such faint point sources are now thought to be cataclysmic variables (CVs), which are binaries of a white dwarf and a main-sequence star. CVs have three Fe  $K\alpha$  lines and thus resemble the spectrum of the GDXE. However, the detail spectral analysis shows

the difficulty of this scenario. The equivalent widths of Fe  $K\alpha$  lines of CVs in the vicinity of the Sun are typically 100–200 eV [20]. The equivalent width of Fe XXV  $K\alpha$  of the GDXE, however, is more than 400 eV [55, 143]. It means that the integration of the spectra of known CVs cannot explain the spectrum of the GDXE. The GDXE might be composed of unknown type of faint point sources with larger equivalent widths of Fe  $K\alpha$  lines than those of well-known CVs.

The origin of the GDXE has been still an open question, which might link to unknown activities of our Galaxy or new X-ray sources. The recent studies, especially spectral analysis using the Suzaku data, have shown that the properties of the GDXE in the GC region ( $|l| < 1^\circ$ )<sup>1</sup> [51, 55, 83] and the ridge ( $|l| > 8^\circ$ ) [143] are clearly different. The intermediate region between them, however, has not been studied well. This region is important to know the transition of the property of the GDXE from the GC to the ridge. To know the entire structure of the GDXE, this region is one of the last lacked pieces. In addition, the edge of the nuclear bulge (NB) is located around  $|l| = 1^\circ\text{--}3^\circ$  [68]. The NB is a stellar complex in which recent star formations or young ionizing stars are present differently from the old Galactic bulge. If the GDXE is related to the NB, the property of the GDXE might change around  $|l| = 1^\circ\text{--}3^\circ$ . In this region, however, neither of the spatial profile and spectra of the GDXE has been known well. The X-ray point sources around this region also have not been studied well.

In this thesis, we analyzed the data of the Suzaku observation of the regions from the GC to the ridge and the bulge ( $-3^\circ < l < 2^\circ$ ,  $-2^\circ < b < 1^\circ$ ). The main aim of this thesis is to reveal the properties of the GDXE from the GC to the ridge and the bulge and to make clear the difference of the GDXE of each region, especially the Fe  $K\alpha$  line emissions. Based on these results, we will tackle the origin of the GDXE. This thesis is organized as below. In chapter 2, we reviewed the past and recent study of the GDXE, especially its Fe  $K\alpha$  lines. In chapter 4, the Suzaku data of GDXE of the GC to ridge region ( $-3^\circ < l < 2^\circ$ ,  $|b| < 1^\circ$ ) and the bulge region ( $b = -2^\circ$ ) were analyzed. The intensity profile of the Fe  $K\alpha$  line emissions and the results of detail analysis of the GDXE spectra are shown in this chapter. In the following two sections, we analyzed peculiar sources as samples of the possible origin of the GDXE. In chapter 5, a peculiar hot SNR in the GC, Sgr A East was studied. In chapter 6, a newly found CV candidate, Suzaku J1740.5–3014 was studied as a sample of X-ray point sources in the region between the GC and ridge. In chapter 7, we made discussions. Chapter 8 is the conclusion of this thesis.

---

<sup>1</sup>The notations  $l$  and  $b$  denote the coordinates of the Galactic longitude and latitude.

# Chapter 2

## Review

The instruction for the structure of the Milky Way galaxy is in section 2.1. The candidate origins of the Fe K $\alpha$  lines in the GDXE are reviewed in section 2.3 and 2.4. Recent studies of the GDXE with Suzaku, Chandra and RXTE are reviewed in section 2.5. Review of Sgr A East is in section 2.6. The summary of the recent studies is tabled in section 2.7.

### 2.1 Structure of the Milky Way Galaxy and the Galactic Center Region

Here we review the structure of the Milky Way galaxy and the Galactic center (GC) region briefly according to mainly Mezger et al. [67]. The Milky Way galaxy is composed of the Galactic disk (GD), the Galactic bulge (GB), the nuclear bulge (NB) and the Galactic halo as shown in figure 2.1.

The GD ( $3 \text{ kpc} < R < 14 \text{ kpc}$  where  $R$  is the radius from the dynamical center.) is the main component of the Milky Way galaxy. The GB ( $0.3 \text{ kpc} < R < 3 \text{ kpc}$ ) is the ellipsoidal region in the inner region. The GB consists of mainly old evolved stars.

The GC is thought to be at a distance of 7.5–8.5 kpc from the Sun. In this thesis, we adopt 8 kpc as the distance to the GC (see [66] and references therein). The typical interstellar absorption toward the GC region is  $N_{\text{H}} = 6 \times 10^{22} \text{ cm}^{-2}$  [96] and thus the visible light from the GC region is absorbed. We can observe the GC region only in the limited band; below  $\lambda \geq 2 \mu\text{m}$  (radio and near-infrared) and above  $E \geq 2 \text{ keV}$  (X- and  $\gamma$ -ray).

The large and dense stellar complex of the innermost region ( $R \leq 300 \text{ pc}$  or  $|l| \leq 2^\circ$ ) is called the nuclear bulge (NB). The NB shows ample evidence of recent and ongoing star formation (e.g. populous clusters of massive stars, very young IR clusters, molecular clouds that are able to form new massive clusters, and massive main-sequence stars etc. See van Loon et al. [136] and references therein.) and thus this region is distinct from the old GB. An unusually dense molecular cloud complex exists in the central few hundred pc ( $|l| \leq 1^\circ$ ) of the Milky Way galaxy and it is often referred to as the Central Molecular Zone (CMZ). The CMZ contains roughly 10% of our Galaxy's molecular gas. The Sgr A–D clouds are well-known massive molecular clouds in the CMZ. The CMZ is thought to be associated with the NB.

The central region ( $R \leq 5 \text{ pc}$ ) is known as the Sgr A complex which was found as a very strong radio source in the dawn of the radio astronomy [37]. Now the Sgr A complex is decomposed to two components, Sgr A West and Sgr A East (figure 2.2). Sgr A West is a thermal radio source

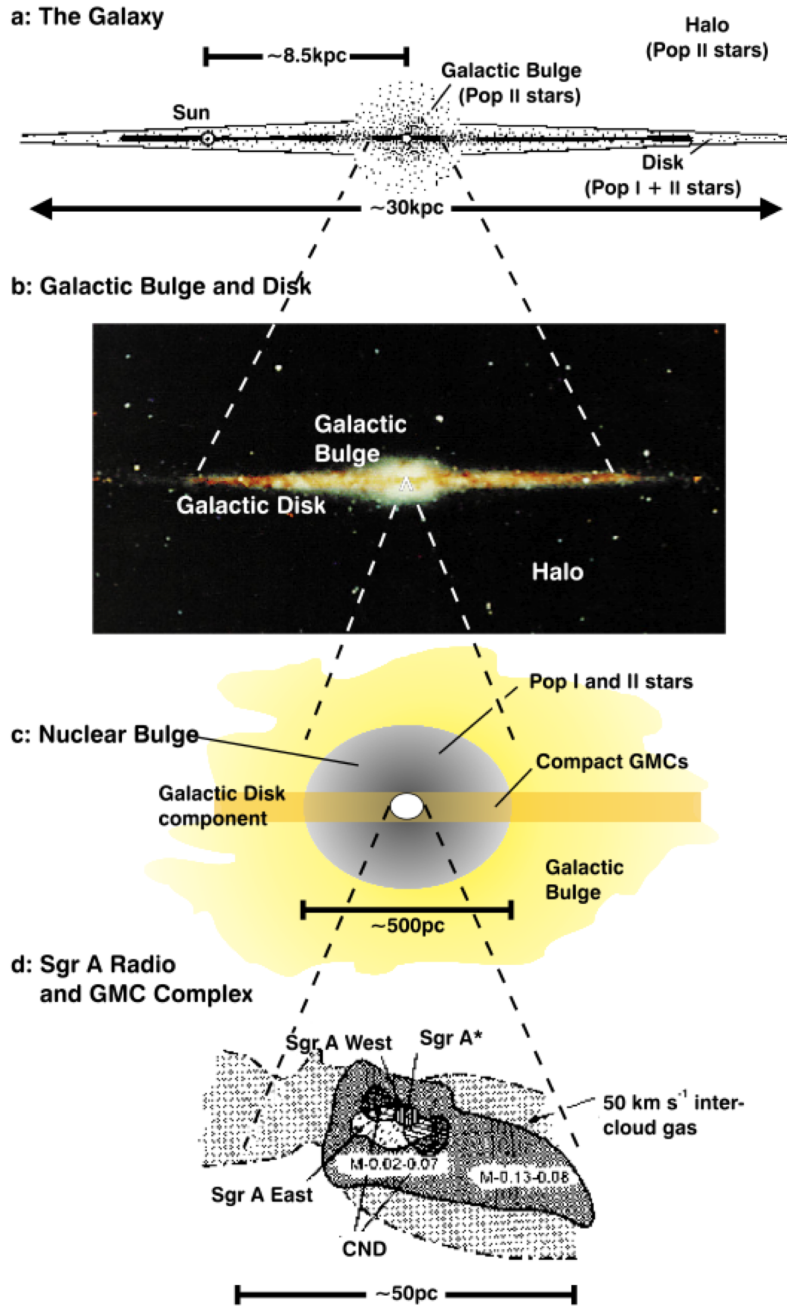


Figure 2.1: Zoom picture of the Galaxy: a: Schematic cross section of the Galaxy. b: False color COBE/DIRBE image of the Galactic Bulge c: Schematic representation of Galactic and Nuclear Bulge. d: Schematic representation of the Sgr A Radio and Giant Molecular Cloud Complex. [68]

which has a characteristic spiral structure. A compact radio source, Sgr A\*, is located in the center of Sgr A West. Observations of the orbital motions of the stars near Sgr A\* reveal that the mass of Sgr A\* is  $\sim 4 \times 10^6 M_\odot$  (e.g. [25]) and thus Sgr A\* is thought to be the nuclear massive black hole and the dynamical center of the Milky Way galaxy. The X-ray from Sgr A\* is detected with Chandra and the flux is  $1.3 \times 10^{-13} \text{ erg cm}^{-2} \text{ s}^{-1}$  in the 2–10 keV band (figure 2.3) [3]. The X-ray luminosity of Sgr A\* is  $2 \times 10^{33} \text{ erg s}^{-1}$ , which is much lower than those of other active galactic nuclei ( $\sim 10^{42-49} \text{ erg s}^{-1}$ ). The spirals of Sgr A West are thought to be the flows of gas falling into Sgr A\* [67]. Sgr A East is a non-thermal radio shell embedding Sgr A West. Now it is thought to be a supernovae remnant. More detail review of Sgr A East is shown in section 2.6.

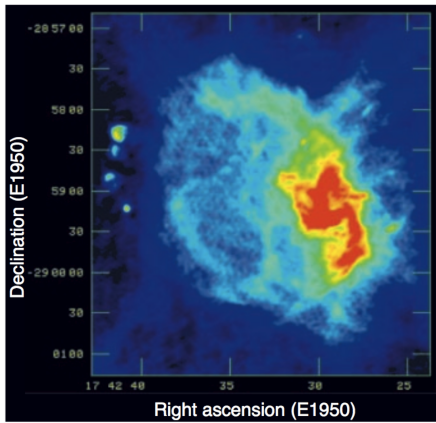


Figure 2.2: VLA radio continuum image of the GC showing the shell-like structure of non-thermal Sgr A East (light blue and green) and the spiral-shaped structure of thermal Sgr A West (red) at  $\lambda = 6 \text{ cm}$  [144].

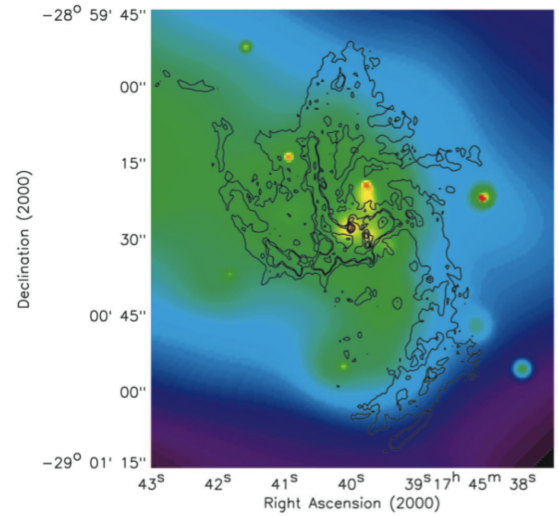


Figure 2.3: Chandra image of Sgr A West in the 0.5–7 keV band with contours of VLA 6 cm [3]. The central radio and X-ray point source is Sgr A\*.

## 2.2 Discovery of the Galactic Diffuse X-ray Emission and its Fe $K\alpha$ Lines

The large extended X-ray emission from our Galaxy – the Galactic Diffuse X-ray Emission, hereafter GDXE — has been known since the dawn of the X-ray astronomy. For example, in 1970, just 8 years later after the first X-ray observation of Giacconi et al., Cooke et al. [14] observed with the Skylark rocket and reported a clear excess of X-ray flux on the Galactic plane where no strong X-ray point sources present. With early X-ray astronomy satellites such as UHURU, ARIEL-V, HEAO-1 and EXOSAT, it was revealed that the GDXE extends over more than  $100^\circ$  along the Galactic plane but only  $\sim 2^\circ$  across it (see [137] and references therein). Thus it has been called as the Galactic “ridge” X-ray emission.

One of the most interesting features of the GDXE is its strong Fe  $K\alpha$  line emissions. Japanese X-ray satellites have contributed the discovery and the study of these lines. With the Gas Scintillation Proportional Counter (GSPC) on the Tenma satellite, the Fe  $K\alpha$  line feature was

discovered [44] (figure 2.4). With the Ginga satellite, it was revealed that the Fe  $K\alpha$  emission extends over  $100^\circ$  along the plane and concentrates sharply at the center region [47] (figure 2.5). Due to the high energy resolution of the CCD camera (Solid state Imaging Spectrometer; SIS) on the ASCA satellite, the Fe  $K\alpha$  line feature in the GC region is resolved to three lines at the energy of 6.4, 6.7 and 6.97 keV [48] (figure 2.6). The 6.7 and 6.97 keV lines correspond to the Fe XXV  $K\alpha$  and XXVI  $K\alpha$  line emissions. These Fe ions imply the existence of hot plasma whose temperature is  $kT = 5\text{--}10$  keV or  $T = \text{several } 10^7$  K. The 6.7 and 6.97 keV lines correspond to the Fe XXV  $K\alpha$  and XXVI  $K\alpha$  line emissions. These Fe ions imply the existence of extremely hot plasma whose temperature is  $kT = 5\text{--}10$  keV or  $T = \text{several } 10^7$  K. The 6.4 keV line, on the other hand, corresponds to the Fe I (or low-ionized Fe)  $K\alpha$  line emission. It indicates that cold matter should be excited by some high-energy process to radiate X-rays.

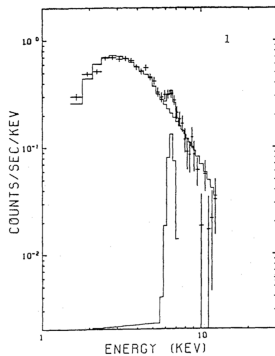


Figure 2.4: X-ray spectrum of the Galactic ridge obtained with the Tenma satellite [44].

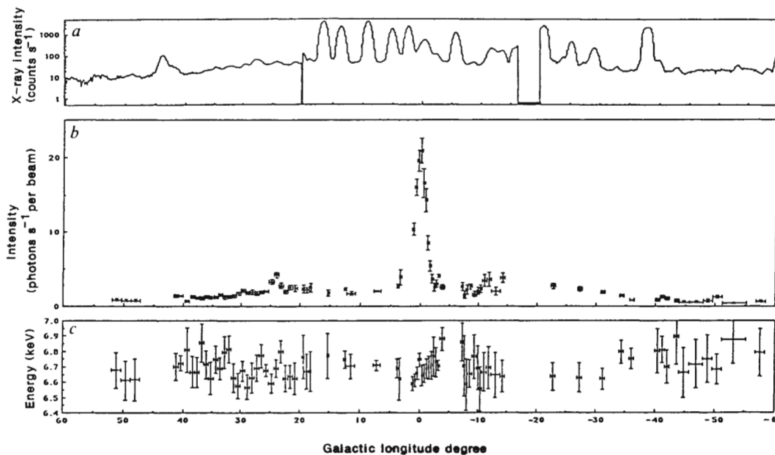


Figure 2.5: The profile of the X-ray emission in the 2–18 keV energy range (a) and that of the iron-line emission (b) on the Galactic plane scanned with the Ginga satellite. The line center energy is plotted in (c). [47]

## 2.3 Candidates for the Origin of the Fe XXV $K\alpha$ and Fe XXVI $K\alpha$ Line Emissions

Thin thermal plasma is the most probable origin of the Fe XXV  $K\alpha$  and Fe XXVI  $K\alpha$  line emissions. We show the outline of X-ray emission from optically thin thermal plasma, especially collisional ionization equilibrium (CIE) plasma in appendix A. In the following sections, we show candidate emitters of the highly ionized Fe  $K\alpha$  lines in the case of the truly diffuse plasma origin (section 2.3.1) or the unresolved point sources origin (section 2.3.2). Charge exchange origin is reviewed in section 2.3.3.

### 2.3.1 Truly Diffuse Plasma Origin

One possible origin of the highly ionized Fe  $K\alpha$  lines in the GDXE is truly diffuse hot plasma filling the Milky Way galaxy. The most probable candidate to supply such diffuse hot plasma are supernova explosions. The ejected material from a supernova explosion expands supersonically and generate shock waves, which heat interstellar matter and the ejected material. As a result,

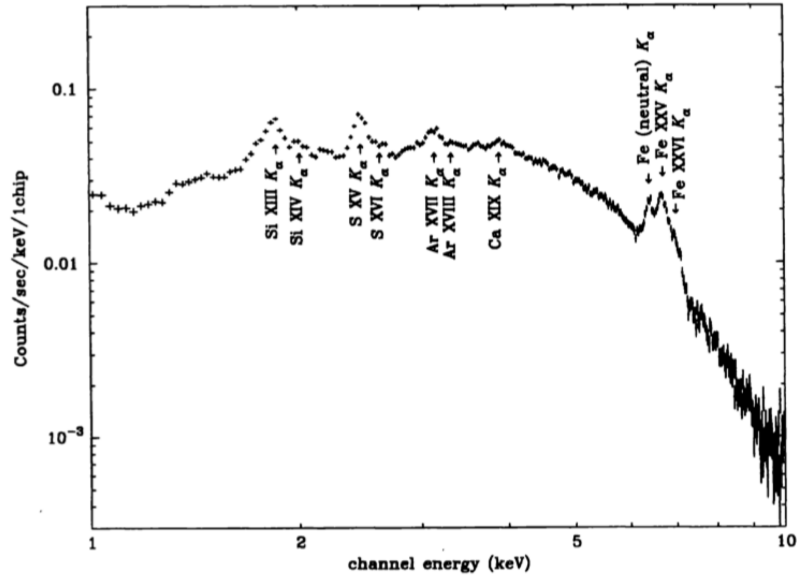


Figure 2.6: X-ray spectrum of the Galactic center obtained with the ASCA satellite [48].

the plasma of a supernovae remnant (SNR) are made. The integration of the SNR plasma might be the origin of the GDXE [45].

SNRs have, however, two defects as the origin of the GDXE. First, the typical temperature of the SNRs is lower than that of the GDXE ( $kT = 5\text{--}10$  keV). Even in the case of young SNRs whose age  $t$  is less than 1000 yr, the temperature  $kT$  is lower than 4 keV. The observed temperatures of famous young SNRs are summarized in table 2.1. The second problem is the energy budget. If truly diffuse hot plasma gas fills the Galactic plane ( $V \sim 10^{66}$  cm<sup>3</sup>), its total luminosity and energy are about  $2 \times 10^{38}$  erg s<sup>-1</sup> and  $10^{56} \eta^{1/2}$  erg ( $\eta$  is a filling factor) [41]. The total energy is extremely large. The sound speed of such high temperature plasma ( $v_s \sim 1400$  km s<sup>-1</sup> for  $kT = 6$  keV) is higher than the escape velocity from the Galactic plane (according to [11],  $v_{\text{escape}} \sim 700$  km s<sup>-1</sup> at the region on the Galactic plane of 3 kpc from the center). The hot plasma will escape from the Galactic plane (thickness  $\sim 1$  kpc) within  $\sim 10^6$  years. The energy input of  $10^{50}$  erg yr<sup>-1</sup> is required to sustain this plasma. The most probable energy suppliers are supernovae whose energy is  $\sim 10^{51}$  erg. The required supernova rate is about one per 10 years [45], which is one order larger than the recently estimated rate [17, 65]. The luminosity of the GDXE cannot be explained, either. The X-ray luminosity ( $L_X$ ) of the SNRs is  $L_X = 10^{35\text{--}36}$  erg s<sup>-1</sup> (see table 2.1 and [45, 131]). To explain the luminosity  $\sim 10^{38}$  erg s<sup>-1</sup> of the GDXE by young SNRs ( $t \sim 1000$  yr), one supernova must occur every 10 years in the Galaxy [45] again. If the origin of the GDXE is the truly diffuse hot plasma, unknown plasma heating process might exist in the Milky Way galaxy.

### 2.3.2 Faint Point Sources Origin

Some kinds of X-ray point sources emit the highly ionized Fe  $K\alpha$  lines. The superposition of such point sources might be origin of the GDXE. For example, binaries of Wolf-Rayet and OB star have the spectra of thin-thermal plasma at  $kT = 0.1\text{--}6$  keV and emit the Fe XXV  $K\alpha$  line (e.g. [29]). Wolf-Rayet binaries are, however, so luminous ( $L_X > 10^{33}$  erg s<sup>-1</sup>) that they are

Table 2.1: Examples of young supernova remnants.

	$kT$ (keV)	$L_X$ (erg s $^{-1}$ )	Thermal energy (erg)	Age $t$ (yr)	Ref.
Cas A	3.8	$1 \times 10^{36}$	$5 \times 10^{49}$	$\sim 300$	[132]
Kepler	4.5	$3 \times 10^{35}$	$4 \times 10^{49}$	$\sim 300$	[9, 27]
Tycho	2.9	$2 \times 10^{35}$	$1 \times 10^{49}$	$\sim 400$	[132]
SN1006	1.9	$1 \times 10^{35}$	$2 \times 10^{49}$	$\sim 1000$	[38, 46]

resolved easily. In addition, they are not numerous and thus cannot be the origin of the GDXE. The candidate source should be faint, numerous and hot.

Cataclysmic variables (CVs) are the possible origin of the GDXE. They are binaries of a white dwarf and an ordinary star and the most numerous accretion-powered X-ray sources. Their local space density is  $3 \times 10^{-5}$  pc $^{-3}$  [114] or  $1.2 \times 10^{-5}$  M $_{\odot}^{-1}$  [115].

Systems with non-magnetized white dwarfs, which comprise 80% of CVs, have luminosities between  $10^{29.5}$ – $10^{32}$  erg s $^{-1}$  and spectra that can be described with  $kT = 1$ – $25$  keV plasma from an accretion shock (figure 2.7).

Magnetized cataclysmic variables (mCVs), which are referred to as polars and intermediate polars (IPs) depending on whether or not the rotational period of the white dwarf is synchronized to its orbital period. The magnetic field of the polars is so strong ( $10^{7-7.8}$  G) that the rotational and orbital periods are synchronized and accretion disks are not formed. IPs are thought to form accretion disks (figure 2.8). In mCVs, the matter spilled over Roche Lobe of the star accretes onto the magnetic pole and becomes hot by the free-fall shock. Thus, they have spectra that can be described with  $kT = 1$ – $25$  keV plasma and often have X-ray pulses synchronizing to their rotational periods. IPs have hard continuum components ( $\Gamma \sim 0$ ) due to the self-absorption. The typical luminosities of the polars and the IPs are  $L_X = 10^{30-33}$  and  $10^{31-33}$  erg s $^{-1}$ .

The line intensity ratio of Fe XXVI K $\alpha$  to Fe XXV K $\alpha$  of the CVs is typically  $\sim 0.5$  and higher than that of the GDXE (0.3–0.4). The equivalent widths of the Fe XXV K $\alpha$  and XXVI K $\alpha$  lines are, however, typically  $\sim 200$  and  $\sim 100$  eV and too small to explain those of the GDXE,  $\sim 400$  and  $\sim 150$  eV (figure 2.9).

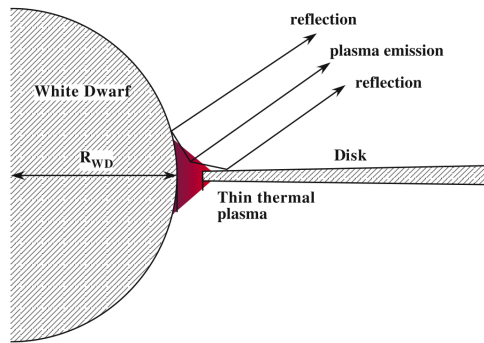


Figure 2.7: Schematic view of a non-magnetic CV [33]. Matter transferred through the accretion disk onto a white dwarf releases its Keplerian motion energy and become plasma by the shock.

### 2.3. CANDIDATES FOR THE ORIGIN OF THE FE XXV $K\alpha$ AND FE XXVI $K\alpha$ LINE EMISSIONS<sup>9</sup>

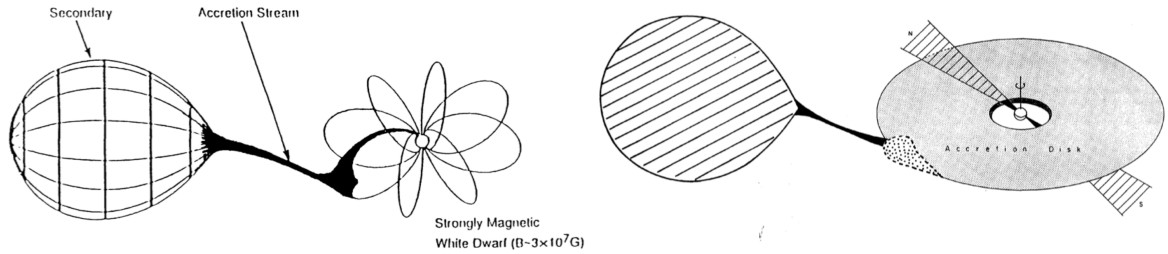


Figure 2.8: Schematic view of magnetic cataclysmic variables. Left: Polar [15]. Right: Intermediate Polar (IP) [93].

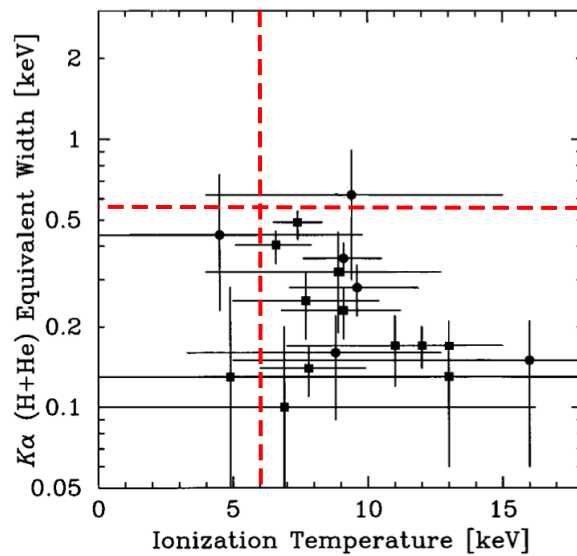


Figure 2.9: Relation between the ionization temperature (horizontal axis) and the summed equivalent width of the Fe XXV  $K\alpha$  and Fe XXVI  $K\alpha$  lines of mCVs [20]. The circle and rectangle marks show polars and IPs respectively. The ionization temperature is determined from the line intensity ratio of Fe XXVI  $K\alpha$  to Fe XXV  $K\alpha$ . The typical values of the GDXE, the ionization temperature  $\sim 6$  keV and the summed equivalent width  $\sim 550$  eV, are shown by the red dashed lines.

### 2.3.3 Charge Exchange Origin

The charge exchange scenario is that bare or hydrogen-like Fe ions in cosmic-ray capture an electron in the interstellar matter and emit the Fe XXVI  $K\alpha$  and Fe XXV  $K\alpha$  lines. The scenario was proposed mainly to explain the line broadening observed with ASCA [122]. The spectrum of the GDXE in the Sgr A region revealed with Suzaku, however, prefers the thermal plasma origin to the charge exchange origin (see section 2.5.1).

## 2.4 Candidates for the Origin of the Fe I $K\alpha$ Line Emission

The Fe I  $K\alpha$  line is emitted from the cold matter when a K-shell electron in a neutral Fe atom is given the energy higher than the K-edge energy (7.1 keV) and ionized.

The origin of the Fe I  $K\alpha$  line in the GDXE can be truly diffuse source or integrated point sources. In the case of the diffuse scenario, the cold interstellar diffuse gas is ionized by hard X-ray photons (photoionization) or electrons in the cosmic-ray (collisional ionization). In section 2.4.1, we show the difference between the photoionization and the electron-collisional ionization. In the case of the point sources scenario, the most probable candidates are CVs. We review the Fe I  $K\alpha$  emission of CVs in section 2.4.2.

### 2.4.1 Truly Diffuse Interstellar Gas Origin

The continuum component is emitted by the Thomson scattering of the incident X-ray photon in the photoionization case, and by the bremsstrahlung of the incident electrons in the collisional ionization case. The equivalent width is different between the photoionization and the collisional ionization. In the case of the photoionization, the calculated equivalent width of the Fe I  $K\alpha$  line is  $\sim 700$  eV assuming  $\Gamma \sim 2$  for the incident photons [87]. In the case of the electron-collisional ionization, the calculated equivalent width of the Fe I  $K\alpha$  line is  $\sim 300$  eV assuming that the energy distribution of the incident electrons  $dN/dE$  is proportional to  $E^{-2}$  [124].

Tatischeff [124] pointed out that, in the electron-collisional ionization scenario, the incident electrons cannot penetrate the interstellar gas thicker than  $N_{\text{H}} = 4 \times 10^{21} \text{ cm}^{-2}$  and thus the intrinsic absorption of the bremsstrahlung should be less than this value.

In the Galactic center region, clumpy Fe I  $K\alpha$  line emissions (hereafter "6.4 keV-clumps"), which are correlated to the distribution of the molecular clouds in the CMZ, have been found [48, 50, 85]. The spectral parameters of the 6.4 keV-clumps are summarized in table 2.2. Because of the large equivalent widths of 1–2 keV and large absorptions of  $N_{\text{H}} = 10^{23-24} \text{ cm}^{-2}$ , the Fe I  $K\alpha$  line emissions of the 6.4-keV clumps are thought to be the photoionization origin and called as X-ray reflection nebulae (XRNe). The past flare of Sgr A\* is suggested as the external X-ray radiation source [35, 53, 54, 77, 108] for the 6.4-keV clumps in the CMZ. The origin of the Fe I  $K\alpha$  in the GDXE might be thinly extended XRNe but it is still an open question.

### 2.4.2 Faint Point Sources Origin

CVs emit the Fe I  $K\alpha$  lines. The origin is thought to be the photoionization of the cold matter in the accretion disk or the surface of the white dwarf irradiated by the hot plasma emission (see figure 2.7 and 2.8). The typical equivalent width of the Fe I  $K\alpha$  line of CVs is  $\sim 100$  eV. It is small because the continuum includes not only the Thomson scatter component but also

Table 2.2: Properties of the 6.4-keV Clumps in the GC Region.

	$EW_{6.4}^*$ (keV)	$\Gamma$	$N_{\text{H}}$ ( $10^{22}$ cm $^{-2}$ )	Ref.
Sgr A source 1	$1.2 \pm 0.1$	$1.83 \pm 0.03$	$23_{-3}^{+4}$	[55]
Sgr A source 2	$1.1 \pm 0.1$	$1.86_{-0.02}^{+0.03}$	$23_{-4}^{+2}$	[55]
Sgr B2 cloud	$1.13_{-0.02}^{+0.05}$	$3.2_{-0.6}^{+0.9}$	$96_{-8}^{+25}$	[53]
M 0.74–0.9	$1.6_{-0.3}^{+0.4}$	$1.4_{-0.7}^{+0.4}$	$40_{-11}^{+14}$	[53]
M 0.51–0.10	$1.4 \pm 0.3$	$1.8_{-0.3}^{+0.4}$	$15_{-1}^{+2}$	[85]
M 359.43–0.07	$2.2_{-0.4}^{+0.3}$	$1.7_{-0.2}^{+0.1}$	$9_{-4}^{+5}$	[84]
M 359.47–0.15	$2.0_{-0.1}^{+0.2}$	$1.6_{-0.1}^{+0.3}$	$8_{-1}^{+4}$	[84]

\* The equivalent width of the Fe I K $\alpha$  line.

direct component. Note that the equivalent width strongly depends on the geometry of the CV structure.

## 2.5 Recent Observation of the GDXE

Recently, the study of the GDXE has been improved very much, especially with Suzaku and Chandra. Due to the good energy resolution of the Suzaku satellite, it has been revealed that the GDXE spectra are different between the Galactic center (GC) and the ridge [51, 143]. With the good spatial resolution of the Chandra satellite, some fraction of the GDXE has been resolved into point sources. Here we review the results of the recent GDXE observations.

### 2.5.1 GDXE in the Sgr A Region ( $|l| < 0.3^\circ$ )

The spectrum of the GDXE in  $|l| < 0.3^\circ$ , the Sgr A region, is studied well by Koyama et al. [50] with the Suzaku XIS (figure 2.10). The center energy of the Fe XXV K $\alpha$  line is determined to be  $6680_{-6}^{+3}$  eV with the careful calibration. This observed value supports not the charge exchange scenario (6666 eV) but the CIE plasma scenario (6680 eV) as the origin of the Fe XXV K $\alpha$  line emission. The line intensity ratio of Fe XXVI K $\alpha$  to Fe XXV K $\alpha$  is determined to be  $0.33 \pm 0.02$ . Using the intensity ratios among highly ionized Fe and Ni K $\alpha$  and K $\beta$  lines, the temperature of the plasma is determined to be  $kT = 6.5 \pm 0.1$  keV. The line ratios severely constraint the shape of the bremsstrahlung continuum of the thermal component. The non-thermal hard tail with  $\Gamma = 1.4_{-0.7}^{+0.5}$  was successfully detected for the first time by subtracting the thermal continuum from the observed one. The line intensity ratio or the temperature along the longitude is almost constant (0.3–0.4,  $kT=6$ –7 keV) in the region of  $-0.4 < l < 0.2$ . The intensity profile of the Fe XXV K $\alpha$  line disagrees with that of X-ray point sources detected with Chandra (figure 2.11). This result indicates that the major fraction of the Fe XXV K $\alpha$  line emission is not due to the integration of the unresolved point sources but truly diffuse.

Koyama et al. [55] analyzed the GDXE spectra in the Sgr A region ( $|l| < 0.3^\circ$ ) and found the anti-correlation between the equivalent widths of the Fe I K $\alpha$  and Fe XXV K $\alpha$  lines (figure 2.12). The relation between the equivalent widths of the Fe I K $\alpha$  ( $EW_{6.4}$ ) and Fe XXV K $\alpha$  ( $EW_{6.7}$ ) lines can be fitted with the equation  $EW_{6.7} + 0.50 (\pm 0.06) \times EW_{6.4} = 0.62 (\pm 0.07)$  keV. Using this relation, they phenomenologically decomposed the GDXE in the Sgr A into two

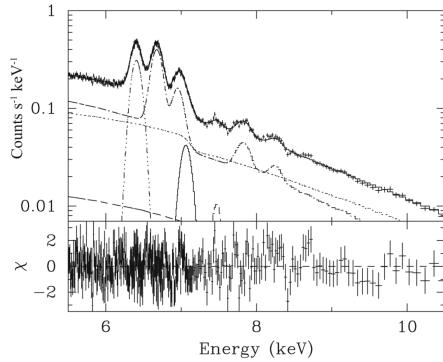


Figure 2.10: The GDXE spectrum in the Sgr A region with the Suzaku XIS. The models of the thermal plasma of  $kT = 6.5$  keV and the non-thermal hard tail are also shown [50].

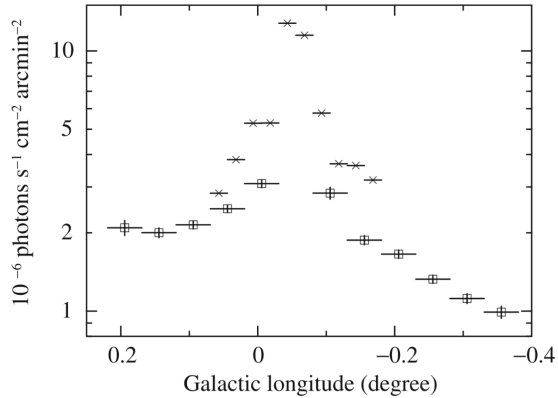


Figure 2.11: The intensity profile in the Sgr A region of Fe XXV  $K\alpha$  are given by the squares, while the integrated point sources in the 4.7–8 keV band are plotted by the crosses [50].

components; the Fe I  $K\alpha$  line emission with its associated continuum (6.4-component) and Fe XXV  $K\alpha$  line emission with its associated continuum (6.7-component). From the line intensity ratio of Fe I  $K\alpha$  to Fe XXV  $K\alpha$  in the Sgr A region ( $\sim 1 : 1$ ), Koyama et al. determined that the flux ratio of the 6.4-component to the 6.7-component is 1:2. Combined with the result [50] that the flux ratio of the non-thermal component to the thermal component is 1:1, Koyama et al. determined that the lower limit of the contribution of the point sources is 1/6 [55].

Using the Chandra data, Munro et al. [78] found that the integrated spectrum of the point sources in the Sgr A region ( $R < 9'$ ) has three Fe  $K\alpha$  lines like the GDXE (figure 2.13). The line intensity ratio of Fe XXVI  $K\alpha$  to Fe XXV  $K\alpha$  is  $\sim 0.6$ , similar to those of CVs near the Sun. The point sources in the Sgr A region also have hard continuum emissions ( $\Gamma \sim 0.9$ ) and the typical luminosities of  $10^{31-33}$  erg  $s^{-1}$ . Munro et al. [78] suggest that most of the point sources in the Sgr A region are IPs. The equivalent width of the Fe XXV  $K\alpha$  line of the point sources in the Sgr A region is  $\sim 400$  eV and larger than that of a typical CV, but close to that of the GDXE.

Revnivtsev et al. [103] observed the region of about 10 arcmin<sup>2</sup> at  $(l, b) = (-0^\circ.09, -0^\circ.03)$  for 918 ks with Chandra and resolved 40% of the GDXE into X-ray point sources at the sensitivity limit of  $1.4 \times 10^{-15}$  erg  $cm^{-2}$   $s^{-1}$  (2–10 keV).

### 2.5.2 GDXE in the Inner Region of the NB ( $0^\circ.3 < |l| < 2^\circ$ )

The GDXEs in the Sgr B ( $0^\circ.3 < l < 0^\circ.8$ ) and C ( $-0^\circ.8 < l < -0^\circ.6$ ) regions have been studied in detail by Nobukawa et al. [85] and Nakajima et al. [84] with the Suzaku data. Nobukawa et al. [85] reported that the line intensity ratio of Fe XXVI  $K\alpha$  to Fe XXV  $K\alpha$  of the Sgr B region is 0.3–0.4, same as that of the Sgr A region. The line intensity profile along the longitude also connects to that of the Sgr A region smoothly. Nakajima et al. [84] analyzed the Suzaku data of the Sgr C region in the same way as Koyama et al. [55] and found the anti-correlation of the equivalent widths between the Fe I  $K\alpha$  and Fe XXV  $K\alpha$  lines. The obtained relation is different from that of the Sgr A region and given by the equation  $EW_{6.7} + 0.22 (\pm 0.12) \times EW_{6.4} = 0.53 (\pm 0.06)$  keV (figure 2.14).



systematically. They found that the line intensity ratio of Fe XXVI  $K\alpha$  to Fe XXV  $K\alpha$  in the ridge is  $0.22 \pm 0.06$ , significantly smaller than that in the GC region ( $|l| < 1^\circ$ ),  $0.38 \pm 0.02$  (figure 2.15). These line ratios correspond to the plasma temperatures of  $kT \sim 7$  keV (0.38) and  $\sim 5.5$  keV (0.22). Yamauchi et al. [143] suggested that the difference in the line intensity ratios might come from the spatial difference of the plasma in the diffuse scenario or the candidate sources in the GC region have a higher temperature plasma emission than those in the ridge systematically in the point sources scenario.

Using the data of the RXTE satellite [10], Revnivtsev et al. studied the intensity profile of the GDXE in the 3–20 keV band in  $|l| = 1\text{--}100^\circ$  and compared it with the near-infrared (NIR) observation [101]. The intensities of the GDXE and the NIR are correlated. Revnivtsev et al. calculated the X-ray luminosity to the stellar mass ratio of the GDXE in the ridge,  $L_X/M = (3.5 \pm 0.5) \times 10^{27} \text{ erg s}^{-1} M_\odot^{-1}$ , which is close to that of the point source in the vicinity of the Sun,  $L_{X,\text{local}}/M = (5.3 \pm 1.5) \times 10^{27} \text{ erg s}^{-1} M_\odot^{-1}$  and suggested that the origin of the GDXE is the integration of X-ray point sources of the known class like the solar neighborhood. Revnivtsev et al. also studied the line intensity profile of the Fe  $K\alpha$  complex of the GDXE in  $|l| = 1\text{--}100^\circ$  and showed that it agrees with that of the NIR (the left panel of figure 2.16). Revnivtsev et al. did not resolve the three Fe  $K\alpha$  lines because they used a proportional counter (PCA) on RXTE, whose energy resolution is  $\sim 18\%$  at 6 keV [102].

Using the Chandra data of the 200 ks exposure, Ebisawa et al. [18] and Revnivtsev et al. [103] resolved 10 or 19% of the GDXE at  $l = 28^\circ.5$  into point sources at the sensitivity limit of  $3 \times 10^{-15} \text{ erg cm}^{-2} \text{ s}^{-1}$  (2–10 keV) or  $1.2 \times 10^{-15} \text{ erg cm}^{-2} \text{ s}^{-1}$  (1–7 keV).

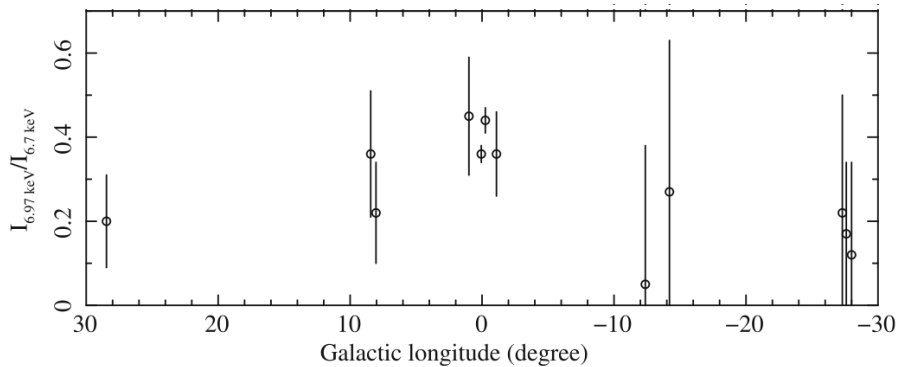


Figure 2.15: Profile of the line intensity ratio of Fe XXVI  $K\alpha$  to Fe XXV  $K\alpha$  along the longitude [143].

#### 2.5.4 GDXE in the Galactic Bulge ( $|b| > 1^\circ$ )

Using the RXTE data, Revnivtsev et al. revealed that the intensity profiles of the Fe  $K\alpha$  complex (the right panel of figure 2.16) [102] and the continuum [101] (3–20 keV) in the bulge match that of the NIR similarly to the ridge.

Using the Chandra data with 1 Ms exposure, Revnivtsev et al. resolved 85% of the GDXE in the 2.6 arcmin-radius region at  $(l, b) = (0^\circ.113, -1^\circ.424)$  into point sources at the sensitivity limit of  $10^{-16} \text{ erg cm}^{-2} \text{ s}^{-1}$  in the 0.5–7 keV band (figure 2.17) [105].

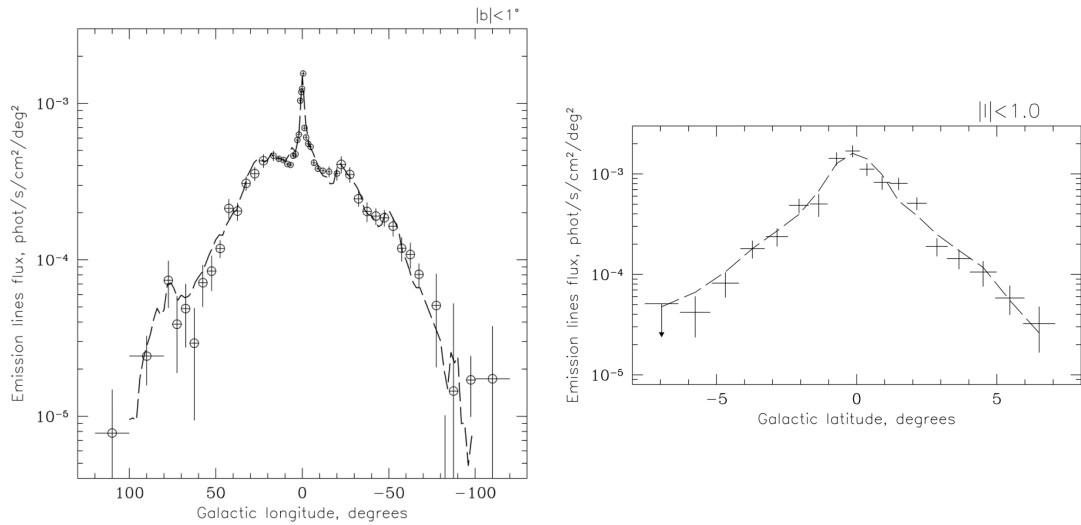


Figure 2.16: The intensity profile of the Fe K $\alpha$  complex along the longitude (left) and the latitude (right) observed with the RXTE. The dashed line shows the intensity profile of the NIR (COBE/DIRBE, 4.9  $\mu\text{m}$ ) [102].

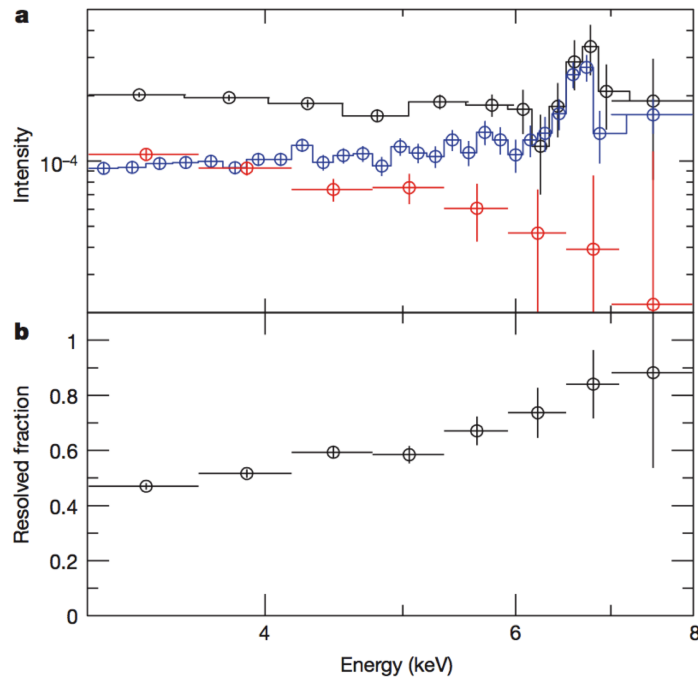


Figure 2.17: GDXE spectrum and its resolved fraction. (a) Spectra collected by Chandra. Black data points show the spectrum of the total emission from the 2.6 arcmin-radius region; the collective spectrum of all detected point sources is presented in blue and the spectrum of the remaining unresolved emission in the current observations is in red. (b) Fraction of the X-ray emission resolved by Chandra into point sources as a function of X-ray photon energy [105].

## 2.6 Review of Sgr A East

Sgr A East is a non-thermal radio-shell structure filled with thermal X-ray emission in the GC region. In X-rays, Chandra (Maeda et al. [63]) found a center filled morphology, and the spectrum consisted of strong  $K\alpha$  lines from highly ionized S, Ar, Ca, and Fe. The spectrum was fitted with a simple isothermal plasma model of temperature  $\sim 2$  keV, an absorption column of  $N_{\text{H}} \sim 10^{23} \text{ cm}^{-2}$  and a luminosity of  $\sim 8 \times 10^{34} \text{ ergs s}^{-1}$  in the 2–10 keV band. From the radio and X-ray morphologies, Sgr A East is classified to be a “mixed morphology” SNR [63].

XMM-Newton (Sakano et al. [112]) found a two-temperature structure of  $0.94^{+0.06}_{-0.09}$  keV and  $4.2^{+0.5}_{-0.4}$  keV. The age of Sgr A East is estimated to be 4000–10000 yr [63, 112] so the temperature of  $kT \sim 4$  keV is hot as SNRs. With follow-up deep Chandra observation, Park et al. [92] analyzed the spectra spatially divided in the Center, Plume and North regions of Sgr A East. The Center and North spectra require two-temperature structures composed of  $kT \sim 1$  keV and  $kT = 5.3^{+0.7}_{-0.6}$  keV (Center) or  $kT = 11^{+19}_{-4}$  keV (North). Such hot temperatures are close to that of the GDXE. Sgr A East is located in the GC region, where extreme physical conditions are manifested. These are a high stellar density, dense stellar gas, a strong magnetic field and the presence of a massive black hole. Hot SNRs like Sgr A East might be made in such an extreme environment and contribute to the strong GDXE in the GC region. Chandra found many clumpy and filamentary structures in Sgr A East. Some of them must be non-thermal X-ray filaments, which would be related to the extreme conditions. The existence of the non-thermal component, however, brings the uncertainty to the previous temperature determinations, which were mainly based on the shape of the thermal bremsstrahlung continuum.

## 2.7 Summary of the Recent Study and Subjects Tackled in This thesis

The recent results we have reviewed above are summarized in table 2.3. This table shows the intermediate region between the GC and ridge regions has not been studied well. In this thesis, we study the subjects shown in green.

Table 2.3: Summary of the recent studies of the GDXE. The results written in red (blue) support whether diffuse (point sources) origin. The issues studied in this thesis are shown in green.

	<b>Sgr A region</b> $ l  < 0.3$	<b>Between GC &amp; Ridge</b> $ l  = 0.3 - 3^\circ$	<b>Ridge</b> $ l  > 8^\circ$	<b>Bulge</b> $ b  > 1^\circ$
<b>Comparison between the profiles of the GDXE and point sources</b>	<ul style="list-style-type: none"> <li>The profile of Fe XXV <math>K\alpha</math> is different from that of X-ray point source detected with Chandra.</li> </ul>	<ul style="list-style-type: none"> <li>Not studied.</li> </ul>	<ul style="list-style-type: none"> <li>The profile of the GDXE of <math> l  &gt; 1^\circ</math> matches that of the NIR observation.</li> </ul>	
<b>Equivalent widths (EW) of Fe <math>K\alpha</math></b>	<ul style="list-style-type: none"> <li>The EWs of the GDXE are too large as known CVs.</li> <li>The EWs of the point sources in the GC are as large as those of the GDXE.</li> </ul>	<ul style="list-style-type: none"> <li>The EWs of the GDXE has not been not studied well.</li> <li>The spectra of point sources in this region have not been studied well.</li> </ul>	<ul style="list-style-type: none"> <li>The EWs of the GDXE are too large as known CVs.</li> <li>The EWs of known CVs near the Sun are too small as the GDXE.</li> </ul>	
<b>EW of Fe XXV <math>K\alpha</math> v.s. EW of Fe I <math>K\alpha</math></b>	<ul style="list-style-type: none"> <li>They are anti-correlated.</li> </ul>	<ul style="list-style-type: none"> <li>Except for the Sgr C region, other regions are not studied.</li> </ul>	<ul style="list-style-type: none"> <li>Not studied.</li> </ul>	
<b>Intensity ratio of Fe XXVI <math>K\alpha</math> to Fe XXV <math>K\alpha</math></b>	<ul style="list-style-type: none"> <li>0.33</li> <li>It is too large as well-known SNRs. Sgr A East might be hot?</li> </ul>	<ul style="list-style-type: none"> <li>Not studied.</li> </ul>	<ul style="list-style-type: none"> <li>0.22</li> </ul>	<ul style="list-style-type: none"> <li>Not studied.</li> </ul>
<b>Fraction of the GDXE resolved into point sources.</b>	<ul style="list-style-type: none"> <li>40%</li> </ul>	<ul style="list-style-type: none"> <li>The flux of the GDXE itself has not been studied.</li> </ul>	<ul style="list-style-type: none"> <li>19%</li> </ul>	<ul style="list-style-type: none"> <li>85%</li> </ul>



## Chapter 3

# Instrument

### 3.1 Overview of the Suzaku Satellite

Suzaku (ASTRO-E2) [69] is the fifth Japanese X-ray astronomy satellite following Hakucho, Tenma, Ginga and ASCA (figure 3.1). It was launched by Japan Aerospace Exploration Agency (JAXA) with the M-V launch vehicle from Uchinoura Space Center (USC) on 2005 July 10. The length is 6.5 m after an extensible optical bench (EOB) deployment. The total mass is 1700 kg. The attitude is controlled by momentum wheels and magnetic torquers to make the angle between the Sun and the solar panel less than  $30^\circ$ . The area of the sky accessible at a time is a belt within which the Sun angle is between  $65^\circ$  and  $115^\circ$  because the pointing direction is limited by the power constraint of the solar paddle, which is perpendicular to the optical axes of the instruments.

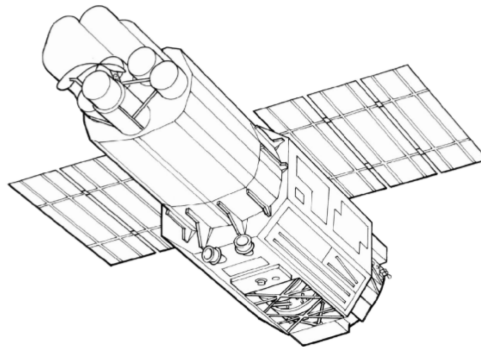


Figure 3.1: Schematic view of the Suzaku satellite in orbit [69].

The orbit of Suzaku is a near circular orbit at 570 km altitude with an inclination angle of  $31^\circ$ . Compared with the high-altitude ellipsoidal orbits of Chandra [138] and XMM-Newton [36], this low-altitude orbit has a low and timely stable non-X-ray background (NXB). Thus Suzaku is good at detecting faint and diffuse X-ray emissions. On the other hand, the observing efficiency is lower than those of Chandra and XMM-Newton. Most targets are occulted by the Earth for about one third of each orbit. Observation is also interrupted by passages of the South Atlantic Anomaly, where the inner Van Allen radiation belt makes its closest approach to the Earth's surface and thus the intensity of cosmic-rays is extremely high. The observing efficiency is about 40%.

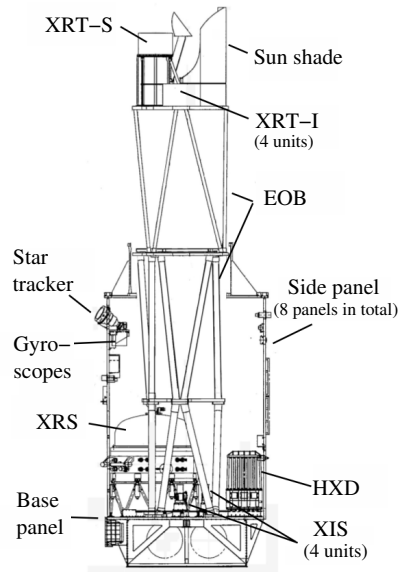


Figure 3.2: Side view of Suzaku with the internal structures [69].

Suzaku is equipped with five sets of X-Ray Telescopes (XRT [117]). At the focal plane, there are four X-ray sensitive CCD cameras (the X-ray Imaging Spectrometer; XIS [50]) and an X-ray micro-calorimeter (the X-Ray Spectrometer; XRS [43]). The Hard X-ray Detector (HXD [126]), a non-imaging collimated hard X-ray scintillating instrument, is also installed. The optical axes of these instruments are co-aligned. Thus Suzaku can observe a celestial object with these instruments at the same time and obtain a broadband spectrum which extends from 0.2 to a few hundred keV. The arrangement of these instruments is shown in figure 3.2.

Before the start of astronomical observations, XRS was out of function because a thermal short between liquid helium and solid neon tanks resulted in the liquid evaporation. The data of the HXD are not used in this thesis. The details of the XRT and the XIS are show in the following sections.

### 3.2 X-Ray Telescope (XRT)

The XRT [117] is a X-ray telescope with grazing-incidence reflective optics consisting of tightly nested, thin-foil conical mirror shells (figure 3.3). There are five sets of the XRT onboard the Suzaku. One is for the XRS (XRT-S) and the others are for the XIS (XRT-I).

Refractive indices of matter to X-rays is less than 1 and thus X-rays cannot be focused by a refracting telescope. X-rays are full-reflected if the incident grazing angle is shallow enough ( $\leq 1^\circ$ ), and thus X-rays are focused using this full-reflection. An approximate Wolter-I optics is used in the XRT. The shapes of the primary and secondary reflectors, which are a paraboloid and hyperboloid respectively in the original Wolter type I optics, are both approximated by cones (figure 3.4). This approximation ultimately limits the imaging capability of the mirror shell but contributes to make the weight of XRT reduced. The focal length of the XRT is 4.75 m.

The mirror shell is made of aluminum and a gold layer adhered to it. About 170 mirror shells mounted concentrically in one XRT module. Due to the tightly nested thin-foil structure,



Figure 3.3: Picture of the XRT [117].

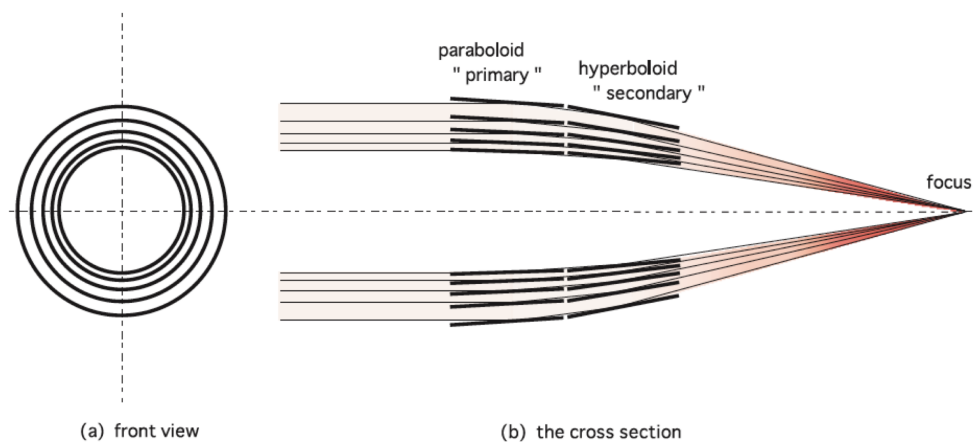


Figure 3.4: Schematic view of an X-ray telescope composed of nested mirror shells with a Wolter-I optics [72].

the XRT provides a large aperture efficiency with a moderate imaging capability in the energy range of 0.2–12 keV despite a total weight of only 20 kg. For example, the effective area of one XRT is as large as that of the HRMA, which is the X-ray telescope onboard Chandra. The weight of the HRMA is, however,  $\sim 1500$  kg. The total on-axis effective area of the four XRTs is shown in figure 3.5 compared with the other X-ray missions.

The effective area for off-axis incident X-rays is smaller than that for on-axis X-rays because off-axis X-rays are partially obscured by neighbor mirror shells. This "vignetting" effect is prominent at high energy. A maximum incident angle for full-reflection is smaller for higher energy X-rays than for lower ones. High energy X-rays are reflected only at inner mirror shells, where the cone angles is small and the mirror shells are tightly packed (see figure 3.4), and highly subject to shadowing. The off-axis angle dependences of the effective area for the soft (3–6 keV) and the hard (8–10 keV) bands are shown in figure 3.6.

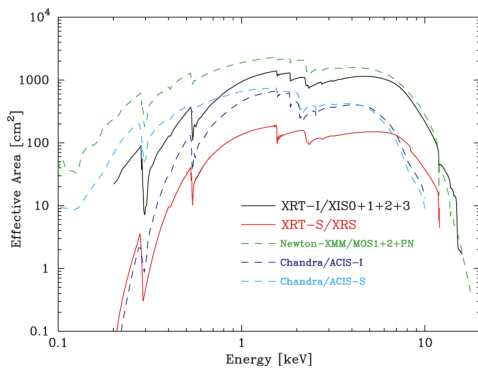


Figure 3.5: Total effective area of the four XRT-Is compared with these of XMM-Newton and Chandra. Transmissions of the thermal shield and the optical blocking filter, and the quantum efficiency of the CCD are all taken into account [117].

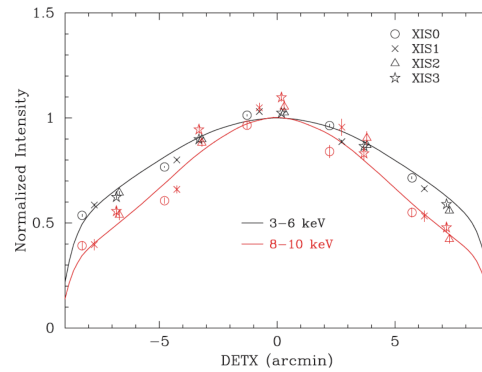


Figure 3.6: Off-axis angle dependence of the effective area normalized at the optical axes in the soft and hard bands shown with black and red points respectively (vignetting). Data are obtained with the Crab nebula observations. The solid lines show the simulated models [117].

Half power diameter (HPD) is the diameter of a circle which contains 50% of flux of a point source. HPD is a standard value to evaluate the imaging capability. The HPDs of the XRTs are  $1'.8$ – $2'.3$ . Point spread function (PSF) is an intensity profile of a point source as a function of radius from the point source. Enclosed energy function (EEF) is an integration of PSF and shows the ratio of the flux of the enclosed circle to the total flux of a point source. PSF and EEF of one of the XRTs are shown in figure 3.7 and 3.8.

Each XRT is made of four sections ("quadrants", see figure 3.3). Since the spaces between the quadrants are dead areas, point source images appear to be a cross.

Tightly-nested structures increases the possibility of reflection other than the normal double reflection within the telescope structure. Because of these unexpected incidences, X-ray of bright sources outside the field of view reaches the focal plane. This is called stray light and it has been a large problem for nested X-ray telescopes (e.g. ASCA/XRT). In the case of Suzaku XRT,

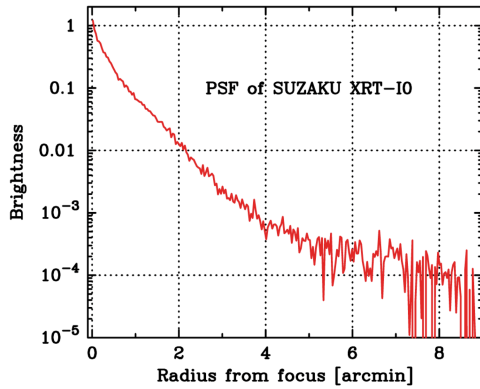


Figure 3.7: Point spread function of the XRT of XIS 0. This is obtained with the observation of SS Cyg, which is a bright point-like source [117].

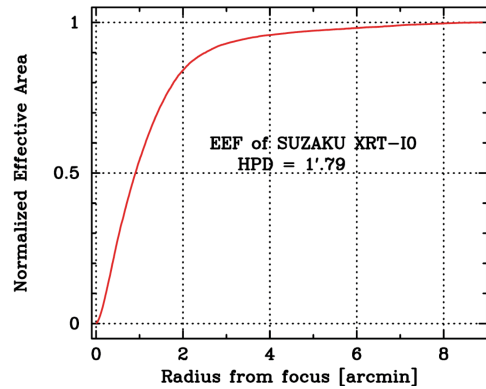


Figure 3.8: Enclosed energy function of XRT of XIS 0. This is obtained with the integration of the PSF in figure 3.7 [117].

front-mounted pre-collimators are installed and decrease the stray light by one order compared with that of ASCA [72].

### 3.3 X-Ray Imaging Spectrometer (XIS)

#### 3.3.1 Introduction of X-ray Charge Coupled Device Cameras

The XIS consists of MOS-type charge coupled devices (CCDs). An X-ray CCD is a silicon semiconductor detector with two-dimensional imaging capability. Each pixel consists of Metal (polysilicon), Oxide ( $\text{SiO}_2$ ) as an insulator and p-type Semiconductor (silicon). This is called a MOS structure (figure 3.9).

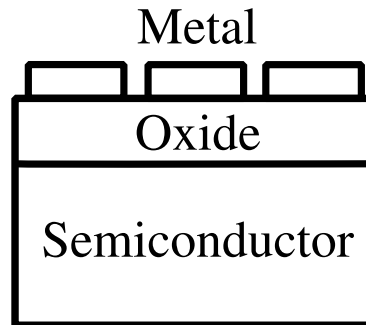


Figure 3.9: Schematic view of a MOS structure.

A brief explanation of the principle of an X-ray CCD is the following. In a p-type semiconductor, holes are the major carriers. A positive voltage applied to the metal electrodes repels holes in the semiconductor and leaves behind a depleted layer where an electric field exists. When an X-ray photon enters into a pixel, photoelectrons are created and then electron-hole

pairs are generated. The number of the generated electrons is proportional to the energy of the incident photon. The average energy required to form an electron-hole pair is 3.65 eV in  $-90^{\circ}\text{C}$ . The holes and electrons are separated by the electronic field in the depletion layer before they recombine. The electrons are collected into the potential wells beneath the electrodes as signal charges. After the exposure period, the signal charges are transferred to the readout node by clocking the voltages of the electrodes.

The CCDs of the XIS employ the three-phase transfer type electrode structure. As shown in figure 3.10, in this type, three electrodes are deposited on each pixel. By applying the three-phase clock voltage to the electrodes, the potentials beneath the electrodes change periodically and the signal charges are transferred.

The CCD of the XIS is classified as a frame transfer (FT) CCD in the scheme of the charge transfer and readout. A FT CCD consists of an imaging area and a frame-store region shown in figure 3.11. The imaging area is exposed but the frame-stored region is shielded from light. After the exposure period, the signal charges are transferred in a short time from the imaging area to the frame-store region. The signal charges in the frame-store region are transferred vertically to the horizontal shift register by each row. The charges in the horizontal shift register are transferred to the readout node by each pixel. This process is repeated until the charges in all the pixels of the frame-store are read out. During this readout of the charges, new exposure starts in the imaging area. The signal charges for the next exposure time can be read out continuously.

In this way, amounts of charges in each pixel are measured and an image and a spectrum are taken with an X-ray CCD camera. An X-ray CCD camera has also time resolution depending on the exposure time.

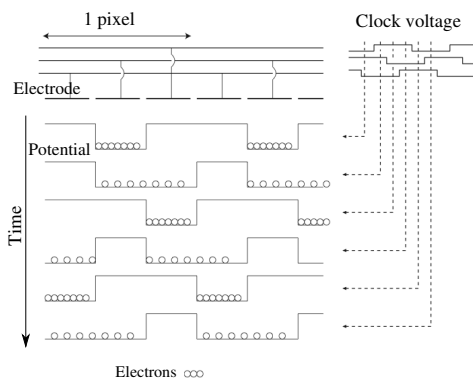


Figure 3.10: Three phase transfer [121].

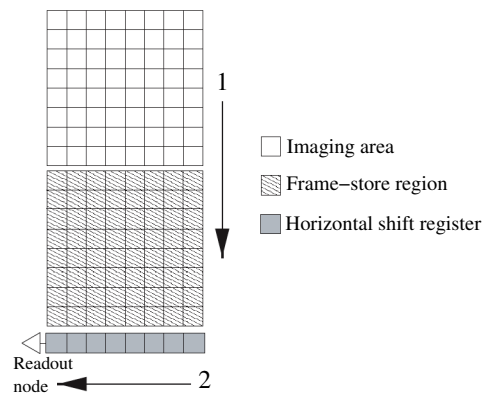


Figure 3.11: Frame transfer CCD [121].

### 3.3.2 Overview of the XIS

The XIS is an X-ray CCD camera system which can take image, spectral and photometrical data in the 0.2–12 keV band. The XIS has four sensors (XIS 0, 1, 2, and 3). Each sensor consists of one CCD chip and a camera body. A photograph and the cross section of one of the XIS sensors (CCD + camera body) are shown in figure 3.12 and 3.13.

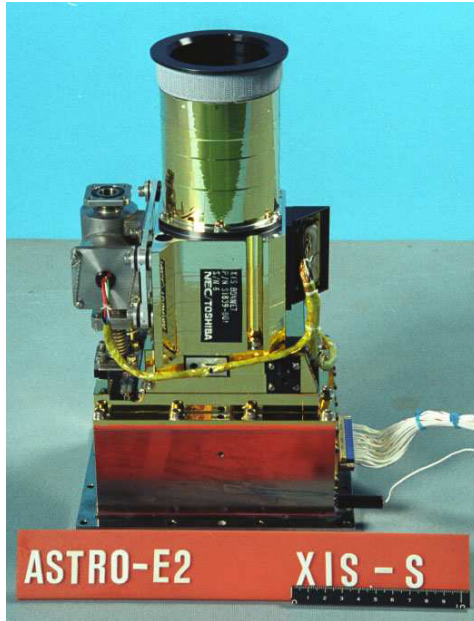


Figure 3.12: Picture of one of the XIS sensors [50].

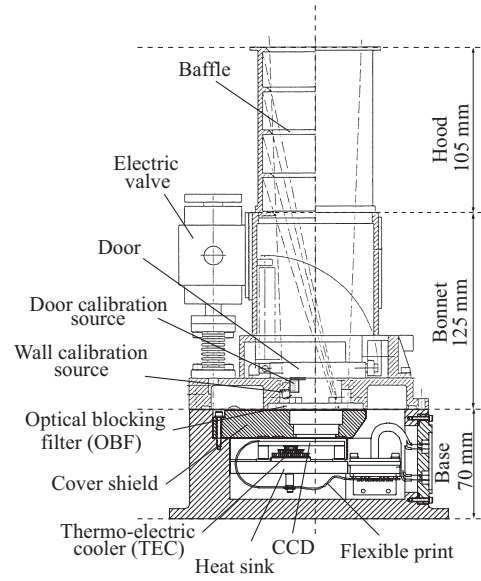


Figure 3.13: Cross section of the XIS sensor [50].

The CCD chip of the XIS is a MOS-type three-phase FT CCD. A photograph and the schematic view of the CCD is shown in figure 3.14 and 3.15. The CCD chips of the XIS are fabricated by the Lincoln Laboratory of MIT and basically same as those of ACIS/Chandra [12] except for a charge injection structure. The details of the charge injection structure are found in the following section 3.3.3.

The upper half of the CCD shown in figure 3.15 is an imaging area, and the lower half is a frame-store region. Both regions have  $1024 \times 1024$  pixels. The signal charges are transferred down in figure 3.15. The pixel sizes of the imaging area and the frame-store region are  $24 \mu\text{m} \times 24 \mu\text{m}$  and  $21 \mu\text{m} \times 13.5 \mu\text{m}$  respectively. In the imaging area, one pixel and the entire field of view correspond to  $1''.04 \times 1''.04$  and  $17'.8 \times 17'.8$ , respectively, combined with the XRT whose focal length is 4.75 m. Note that the spatial resolution of the XIS for celestial objects is determined by not the pixel size of the XIS but the imaging capability of the XRT.

Each CCD chip are divided into four segments (from A to D) and each segment has one readout node. One of the CCD chips (XIS 1) is a back-illuminated type (BI) and the others are a front-illuminated type (FI). The front side of a CCD has a structure of electrode and insulator (“gate” structure) made of poly-Si and  $\text{SiO}_2$  layers. The thicknesses of the poly-Si and  $\text{SiO}_2$  layers are  $\sim 0.28 \mu\text{m}$  and  $\sim 0.44 \mu\text{m}$  in the case of the XIS. The FI CCD is less sensitive than the BI CCD to soft X-rays since the gate structure absorbs soft incident X-rays. On the other hand, the depletion layer of the FI CCD is thicker ( $\sim 65 \mu\text{m}$ ) than that of the BI CCD ( $\sim 42 \mu\text{m}$ ) and thus the FI CCD is more sensitive to hard X-rays than the BI CCD.

For the in-orbit calibration, calibration sources of  $^{55}\text{Fe}$  are equipped (“Wall calibration source” in figure 3.13). They emit the Mn I  $K\alpha$  (5.895 keV) and  $K\beta$  (6.492 keV) [8, 56] lines to the upper edge of the segment A and D constantly (see figure 3.15).

The CCDs of the XIS are operated at a temperature of  $-90^\circ\text{C}$  cooled by radiators and

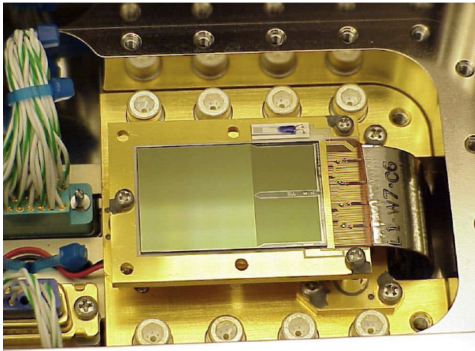


Figure 3.14: Picture of the CCD installed in the base [50].

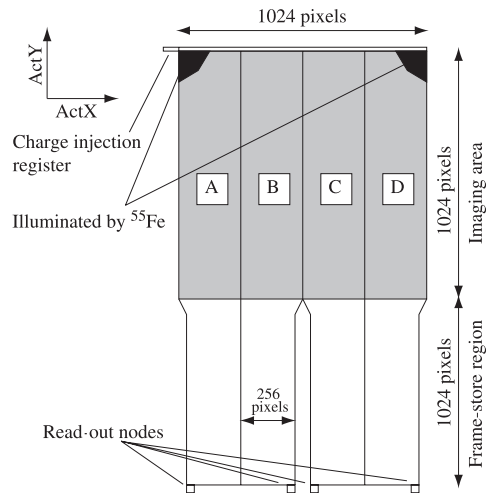


Figure 3.15: Schematic view of the CCD [50].

Pertier coolers. Each XIS has an optical blocking filter (OBF) to block optical and UV photons. The OBF is made of 100 nm polyimide coated with Al of a 120 nm thickness.

XIS 2 suddenly showed an anomaly on November 9, 2006, and it has not been operated since then. Although there is no direct evidence, the micro-meteoroid impact might have caused the anomaly <sup>1</sup>.

### 3.3.3 Charge Injection Capability

A charge injection (CI) structure is installed adjacent to the topmost row of the imaging area. The CI structure allows us to inject a commandable amount of charge in a nearly arbitrary spatial pattern. The XIS is equipped with the CI structure for the first time among the satellite-onboard CCD cameras. In the case of the XIS, the CI has been used in two ways to mitigate the effect of the radiation damage in orbit; checker-flag CI (CFCI) and spaced-row CI (SCI) techniques. The CI of the XIS is important to analyze the data used in this thesis because the difference of the observation dates are up to three and half years. Generally, systematic errors from a time degradation of a CCD become serious problems for such data sets. In the case of the XIS data used in this thesis, however, such systematic errors are small due to these CI techniques.

The essential function of the CI is described in figure 3.16 and 3.17. A serial CI register of 1024 pixels long is attached next to the upper edge of the imaging area. An input gate is equipped left of the CI register (figure 3.16). Pulling down the potential for electrons at the input gate and the next electrode (S3 in figure 3.17), the potential well is filled with charges with an amount of  $Q$ . Then, pulling up the potential, the charges are spilled. The amount of charges is controlled by the offset voltage between the input gate and the next electrode (S3). It can inject charges from  $\sim 50 e^-$  to  $\sim 4000 e^-$  per pixel; the equivalent X-ray energies range from  $\sim 300$  eV to  $\sim 15$  keV. The deposited charges are transferred horizontally through the serial

<sup>1</sup>See <http://www.astro.isas.jaxa.jp/suzaku/proposal/ao3/suzaku.td/> and similar micro-meteoroid impact events of XMM-Newton are reported by Strüder et al. [120].

CI resister, vertically through transferred into the imaging area, and to an arbitrary position of the CCD chip. Prigozhin et al. [97] have reported details concerning the CI structure.

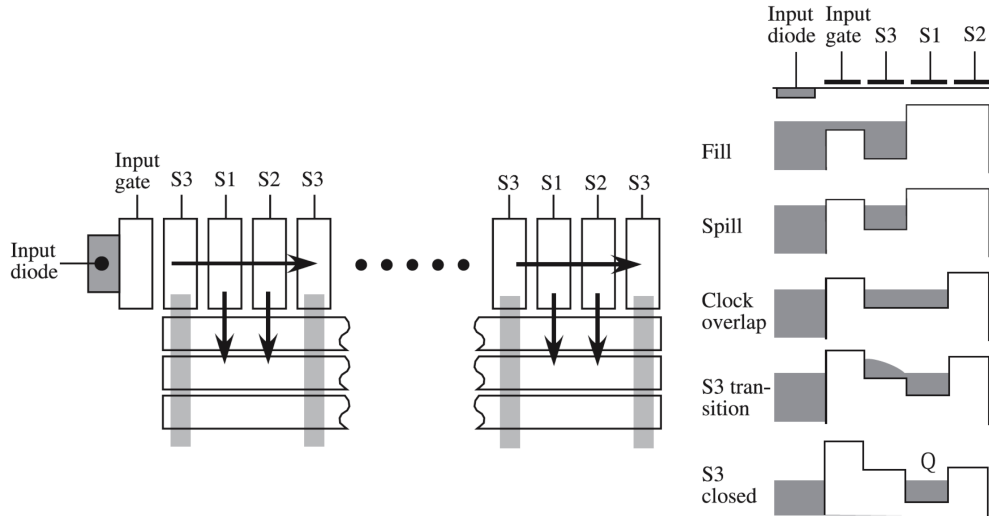


Figure 3.16: Schematic view of the CI structure [83].

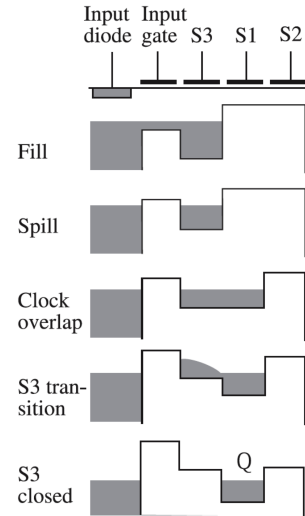


Figure 3.17: Schematic view for the CI at the input gate [83].

X-ray CCDs in orbit suffer from radiation damage. The damage causes the increase of the charge transfer inefficiency (CTI) which is defined as the ratio of lost charges to transferred charges in one pixel by one transfer. The main origin of the CTI thought to be the increase of defects in the crystal lattice generated by cosmic-rays in orbit. These defects form charge traps that can capture signal electrons. The CTI results in the degradation of the determination accuracy of the energy and the energy resolution for two reasons: (1) the pulse height strongly depends on the position of an X-ray event, since the X-ray event loses more electric charges as the number of transfer increases, and (2) the loss of charge is a stochastic process, and thus there is a fluctuation in the amount of lost charge.

### Checker-Flag Charge Injection

One strategy to mitigate the effect of the CTI is to measure the CTI of each column precisely and correct the lost charges. Here the "column" is defined as the vertical column of the pixels along the ACTY in figure 3.15. The checker-flag CI (CFCI) technique makes the column-to-column CTI measurement possible. Here the outline of the CFCI technique is described referring figure 3.18. First, a "test" charge packet is injected into the top CCD row. Then, after a gap of a few rows, five continuous packets are injected with the same amount of charge of the test packet. The former four packets are called "sacrificial" charge packets, while the last one is called a "reference" charge packet. The test packet loses its charge by charge traps. On the other hand, the reference packet does not suffer from any charge loss, because the traps are already filled by the preceding sacrificial charges. Thus, we can measure the CTI of each column by comparing the pulse heights of the reference charge and the test charge.

Using the obtained CTI values, the column-to-column CTI correction is applied for the data

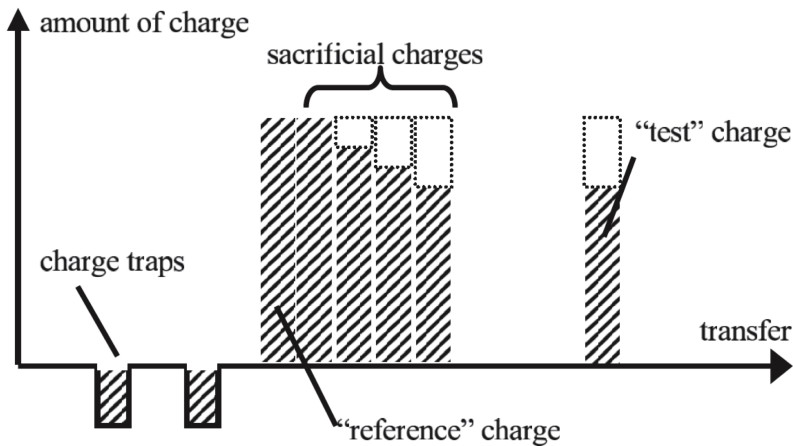


Figure 3.18: Schematic view of how to measure CTI with the CFCI technique [83].

observed between the launch and September 2006. The energy resolution of the FI CCD at 5.9 keV was  $\sim 140$  eV (FWHM) at August 2005, and had degraded to  $\sim 200$  eV at August 2006 without the column-to-column CTI correction. The column-to-column CTI correction improves the energy resolution to  $\sim 170$  eV (FWHM) at August 2006. Nakajima et al. [83] and Ozawa et al. [89] reported the details of the CFCI in orbit and the column-to-column correction.

However, we cannot correct the fluctuation by the readout-to-readout in a specific column, which still degrades energy resolution even after the column-to-column CTI correction in principle.

### Spaced-row Charge Injection

Spaced-row charge injection (SCI) technique can reduce the CTI actively and improve the energy resolution. In the SCI mode, a charge packet is injected into CCD rows periodically during the observation. The injected charge fills the radiation-induced traps as a sacrificial charge packet, and thus prevents some of the traps from capturing signal charges produced by X-rays. Results based on ground experiments using the SCI technique with radiation-damaged CCDs have been reported by Tomida et al. [128] and Bautz et al. [5], but no in-orbit experiment had been done. The Suzaku XIS operated with the SCI technique in orbit for the first time from August 2006. In the SCI mode of the XIS, a charge is injected into every 54th row. The amounts of the injected charge into each pixel are equivalent to the X-ray energy of  $\sim 6$  keV and of  $\sim 2$  keV, for the FI and BI, respectively. The energy resolution was improved from  $\sim 200$  eV to  $\sim 140$  eV at 5.9 keV [6]. The SCI has been applied in a normal observation since October 2006 (the SCI mode). In the SCI mode, since the CTI depends on the distance from a charge injected row, the pulse heights show a sawtooth distribution depending on the transfer number shown in figure 3.19. This non-uniformity of the pulse heights degrades the determination accuracy of the energy and the energy resolution. Thus we developed a new CTI correction method for the SCI mode, which is called a “sawtooth” CTI correction. This method corrects the non-uniformity like shown in figure 3.19. All the XIS data of the SCI mode are processed with the sawtooth correction. The details of the sawtooth correction and CTI measurement method for the SCI mode are described in appendix B and [134].

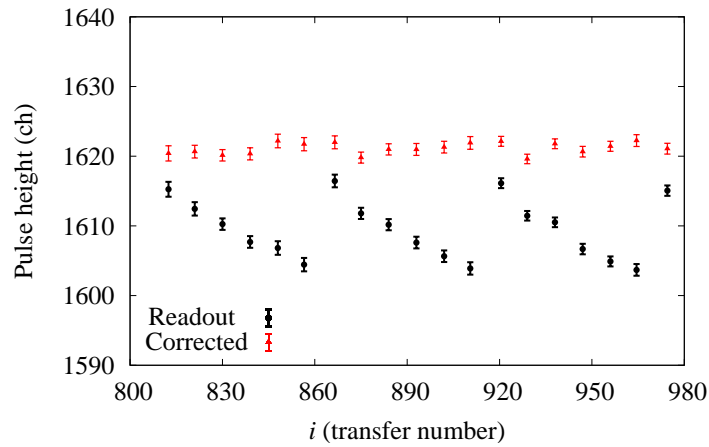


Figure 3.19: Relation between pulse height of the Mn I  $K\alpha$  line from the onboard calibration source and transfer number  $i$ : This is the data of February 2008. Black and red marks are data before and after our new CTI correction, respectively [134].

### 3.3.4 Performance of the XIS

#### Determination Accuracy of the Energy Scale

Figure 3.20 shows the time histories of the center energy of the Mn I  $K\alpha$  line obtained with the onboard calibration sources. These data are processed with the column-to-column CTI correction for the SCI-off data or the saw-tooth CTI correction for the SCI-on data. The center energy of the Mn I  $K\alpha$  line had been constantly 5.895 keV until January 2009 but that of the BI decreased systematically by 20 eV. The reason is not clear now. The uncertainty of the energy-scale determination is less than  $\sim 20$  eV (0.3%) at 5.9 keV except for these BI data.

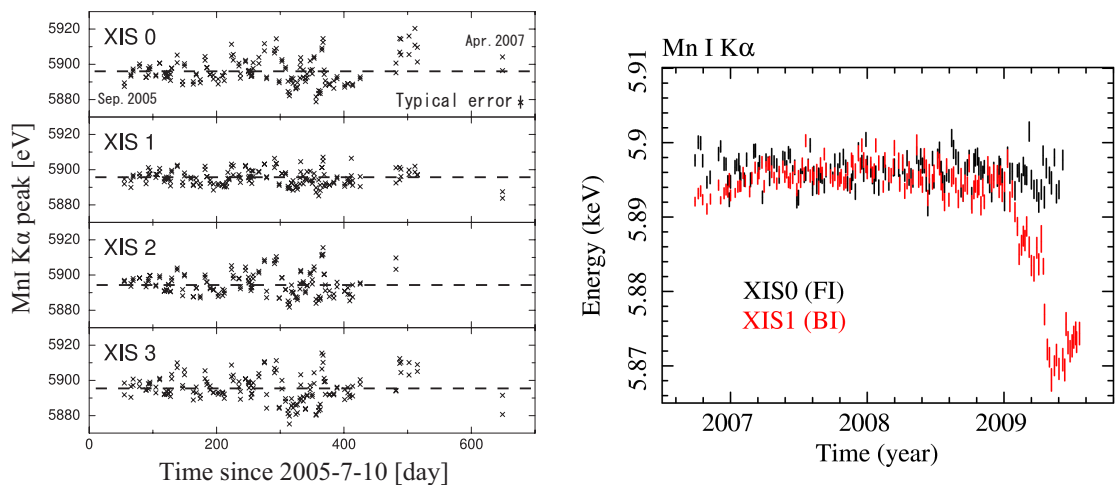


Figure 3.20: Time histories of the center energy of the Mn I  $K\alpha$  line obtained with the onboard calibration sources. Left: SCI-off mode [89]. Right: SCI-on mode [145].

Figure 3.21 shows the time histories of the center energy of the O VII  $K\alpha$  line (0.570 keV)

obtained from 1E 0102-7219, which is a well-studied supernovae remnant (SNR) and used as a celestial calibration source for X-ray astronomical satellites recently [94]. The uncertainty of energy-scale determination of the XIS is less than  $\sim 10$  eV (1 – 2%) at 0.5 – 1 keV.

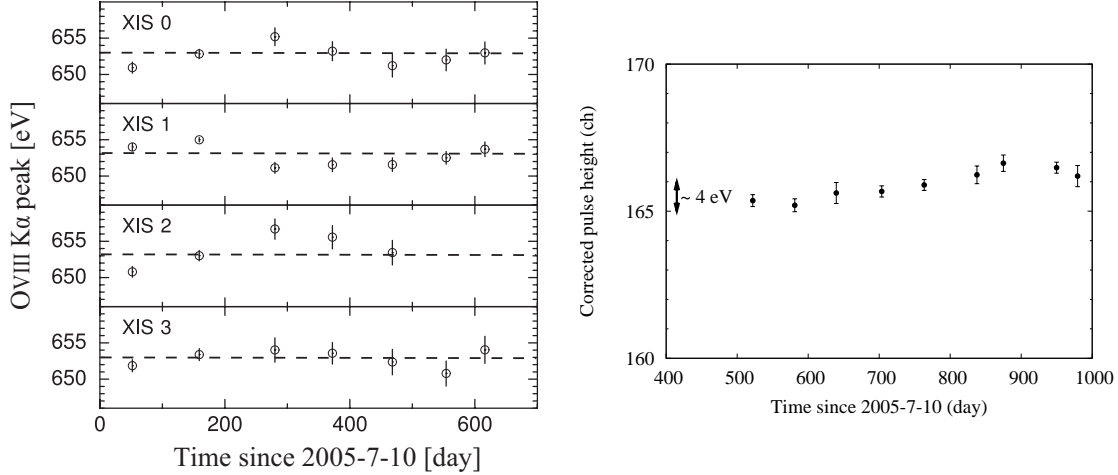


Figure 3.21: Time histories of the center energy of the O VII  $K\alpha$  of 1E 0102.2-7219. Left: SCI-off mode [89]. Right: SCI-on mode, where the center energy is described in the unit of pulse height channel and the result of XIS 1 is shown [134].

There is no good celestial calibration source for the 1.5 – 3 keV band, the uncertainty is largest in this band. Recent studies of SNRs using the XIS show the energy-scale determination in the 1.5 – 3 keV can have the systematic error of 20–30 eV (1 – 2%).

### Response and Energy Resolution

The pulse height distribution of the signals for a monochromatic incident X-ray energy is called a response function of the detector. The schematic response function of the XIS is shown in figure 3.22. The main-peak component is made by completely-gathered signal charges. The sub-peak, triangle and constant components come from events in which some of signal charges are lost. The Si escape and Si  $K\alpha$  lines happen in the cases that a fluorescent Si X-ray photon generated by a photoelectric absorption escapes or is absorbed in other pixels. The detail of physical interpretations of the response function are reported by Matsumoto et al. [64].

The energy resolution of the XIS is defined as the width of the main peak. The time history of the widths of Mn I  $K\alpha$  from the onboard calibration sources is shown in figure 3.23. The width of the Mn I  $K\alpha$  is almost  $0$  eV<sup>2</sup>, and thus figure 3.23 shows the time histories of the energy resolution at 5.9 keV. The energy resolution of the BI has degraded more rapidly than that of the FI in the SCI mode.

The time history of the energy resolution at 0.57 keV (O VII  $K\alpha$ ) is shown in figure 3.24. This figure is obtained with the observations of 1E 0102.2-7219, whose emitting narrow lines were resolved with the grating spectrometer of XMM-Newton (see [98] and [94] in detail).

The calibration data base for the XIS includes these time history of the energy resolution properly.

<sup>2</sup>Strictly speaking, since this line is a blend of Mn K I  $\alpha_1$  5.888 keV and  $\alpha_2$  5.899 keV, the width of the merged Mn I  $K\alpha$  is a few eV. See figure 42 of [43] for examples

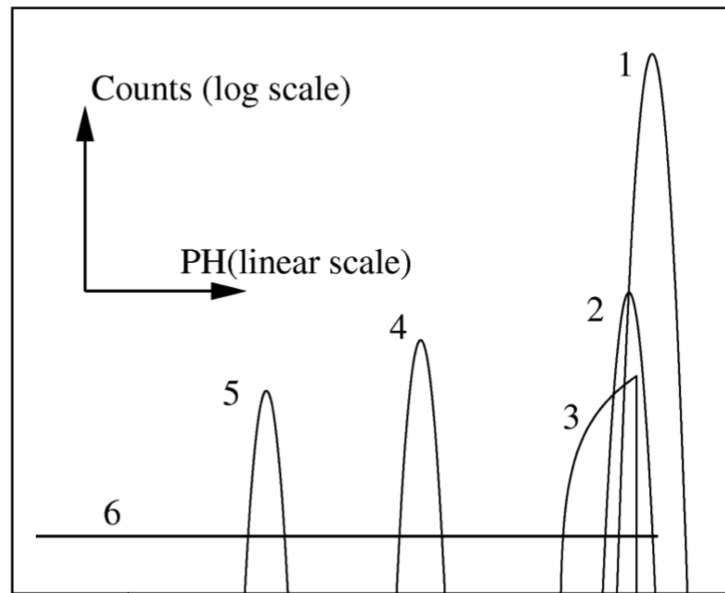


Figure 3.22: Schematic response function of the XIS. 1. main peak, 2. sub peak, 3. triangle component, 4. Si escape, 5. Si  $K\alpha$  line, and 6. constant component. The physical interpretation of the each component is shown in [64].

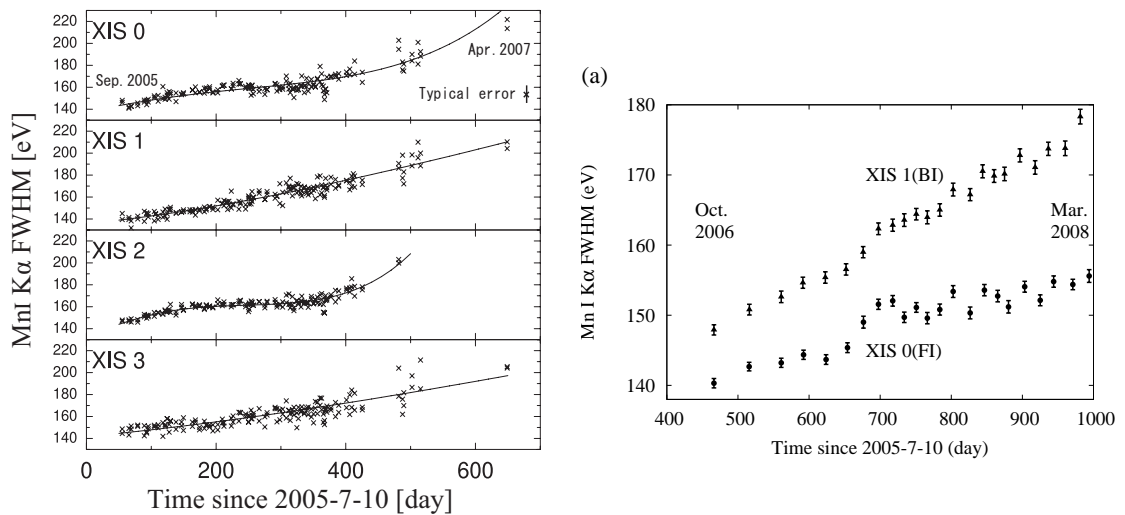


Figure 3.23: Time histories of the width of the Mn I  $K\alpha$  line obtained with the onboard calibration sources. Left: SCI-off mode [89]. Right: SCI-on [134].

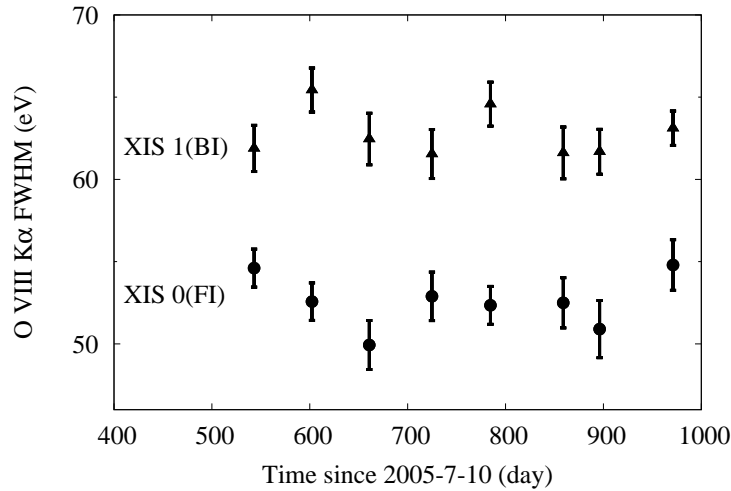


Figure 3.24: Time history of the line widths of the O VII  $K\alpha$  obtained with the onboard calibration sources in the SCI-on mode [134].

### Quantum Efficiency and Effective Area

Conversion efficiency of an incident X-ray photon to an detected X-ray event is called quantum efficiency (QE). QE of the XIS is shown in figure 3.25. The difference of the QE between the FI and the BI comes from the illumination type and the thickness of the depletion layers.

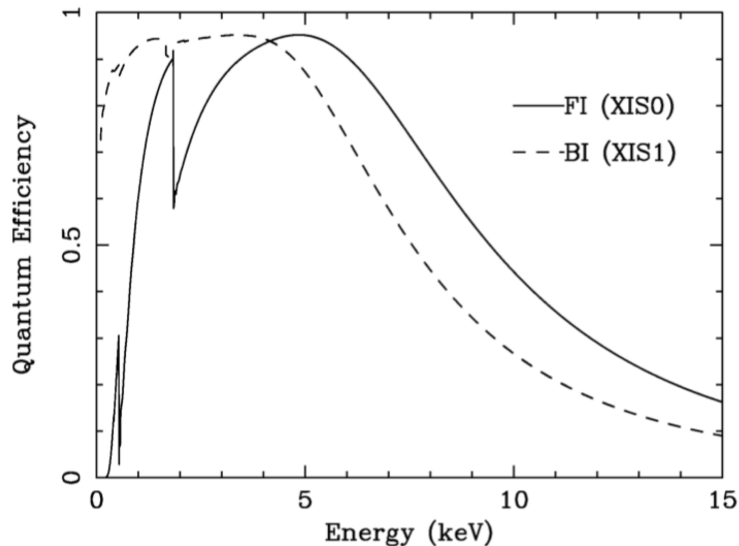


Figure 3.25: Quantum efficiency of the XIS as a function of incident energy [50].

The QE in the low energy band has degraded by unexpected contamination (due to out-gassing from the satellite) accumulating on the OBF [50, 73]. The contaminant is mainly composed of carbon and oxygen. Although the chemical composition of the contaminant is still uncertain, it is assumed to be C/O=6 in number. The time evolution of the contamination has been measured using regular observations of 1E 0102-072. The effect of contamination is

included in the effective area of the XRT properly. Note that, in this thesis, Fe  $K\alpha$  lines ( $\sim 7$  keV) are main targets and the contamination effects almost nothing to the  $\sim 7$ -keV band.

When the XIS data are analyzed, the observed pulse height distribution is fitted with models convolved with this response function including the quantum efficiency of the XIS and the effective area of the XRT.

### Non-X-ray Background

Cosmic-rays in orbit causes non-X-ray background (NXB). Figure 3.26 shows the spectra of NXB accumulated during night-earth observations in which no celestial X-ray is incident.

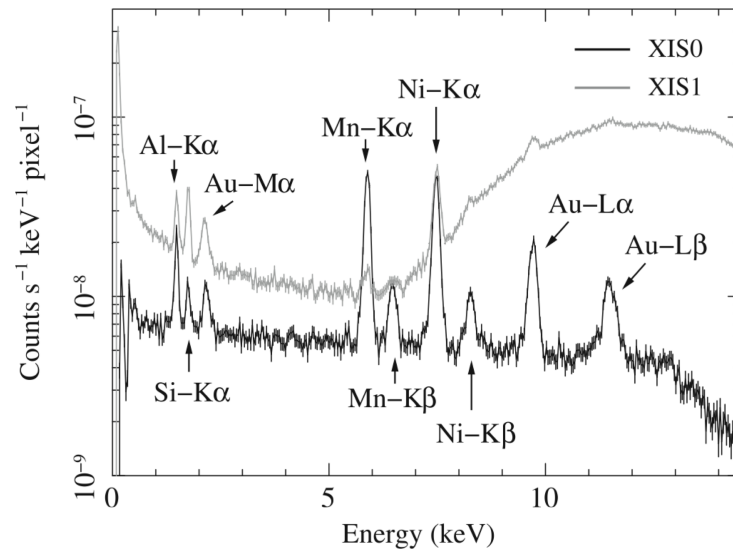


Figure 3.26: Spectra of the NXB of the FI (XIS 0) and the BI (XIS 1) [125].

The flux of the NXB depends on the geomagnetic cut of rigidity (COR). A COR is the minimum energy of the cosmic-ray which can penetrate the magnetic field of the Earth and a standard value to evaluate the strength of the cosmic-ray of orbits. The flux of the NXB also depends on the position on the CCD chip. It increases along ActY (figure 3.27) because pixels of the larger ActY take the longer time before the readout in the frame-store region and suffer the more cosmic-ray radiation [140]. Tawa et al. [125] modeled the NXB spectra as a function of the COR and the position on the CCD. The model reconstruct the NXB spectra with the accuracy of 5% for any observation. In this thesis, the reconstructed spectra are used.

Due to the near-earth orbit, the NXB of the XIS is lower than X-ray CCD cameras on other satellites, especially in the 7–10 keV band (figure 3.28). The XIS is the best instrument to detect diffuse faint X-ray emissions like the Galactic diffuse X-ray emission studied in this thesis.

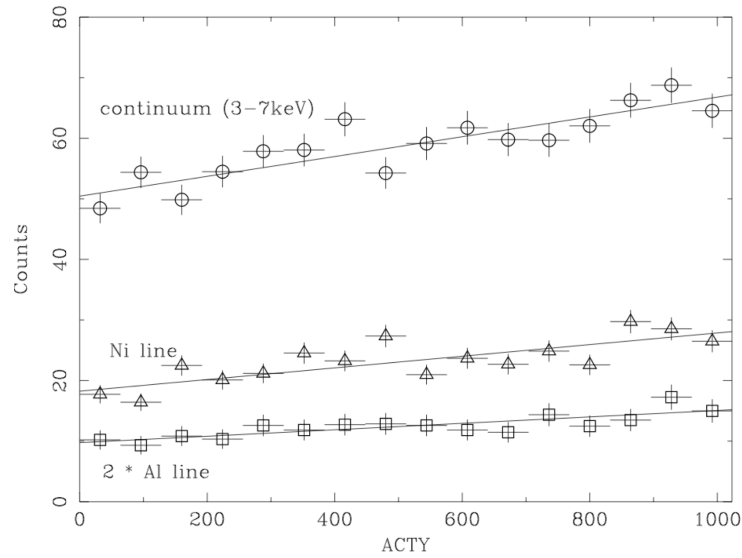


Figure 3.27: Dependence of the NXB on ACTY in the case of XIS 2 [140].

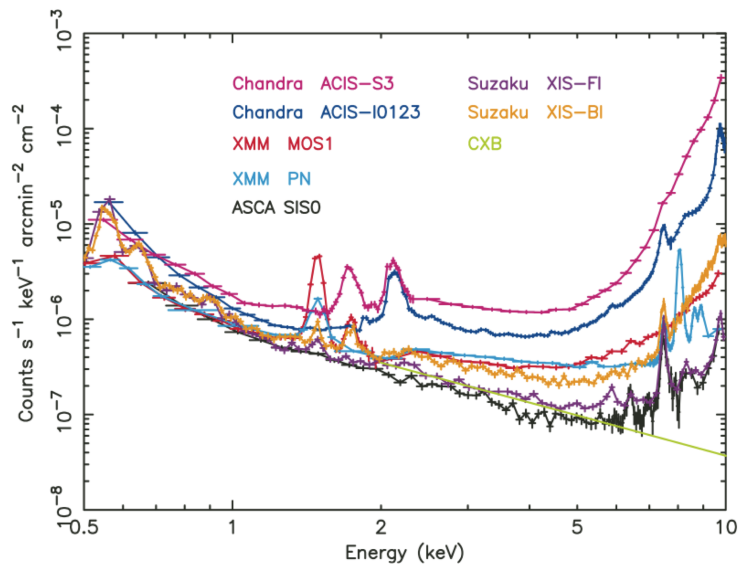


Figure 3.28: XIS background counting rate as a function of energy. The background rate was normalized with the effective area and the field of view, which is a good measure of the sensitivity determined by the background for spatially extended sources. The background spectra of ASCA, Chandra, and XMM-Newton are shown for comparisons [69].

## Chapter 4

# Galactic Diffuse X-ray Emission

In this chapter, we show the result of the Suzaku observation of the region from the GC to the ridge and the bulge ( $-3^\circ < l < 2^\circ$ ,  $-2^\circ < b < 1^\circ$ ). In section 4.1, we describe about the observations and the data reduction. In section 4.2, we give the spatial distribution of the GDXE in the 5–10 keV band, especially the Fe K $\alpha$  line emissions. In section 4.3, we show the detailed spectral analysis of the GDXE. Discussions based on the results given here will be made in chapter 7.

### 4.1 Observation & Data Reduction

#### 4.1.1 Observation

The Suzaku data of the GC region used in this thesis were obtained from October 2005 to March 2009. The data in  $b = -2^\circ$  were also analyzed. The total effective exposure is about 3.2 Ms. The logs of the observations are summarized in table 4.1.

In these observation, the XIS operated in the normal clocking full window mode<sup>1</sup>. In this mode, the time resolution of the XIS is 8.0 s. 71 % of the total exposure was observed without XIS2. The SCI technique was used in 75 % of the total exposure. We did not use the BI data after January 2009 because the energy-scale uncertainty is large as described in section 3.3.4.

#### 4.1.2 Data Reduction

The observation data were downloaded from DARTS/ISAS<sup>2</sup>. In order to apply the latest CTI correction, we reprocessed the data using the calibration data base (CALDB) released at 2008-10-20<sup>3</sup> and `xispi` in the HEADAS software package version 6.6.1<sup>4</sup>. This CALDB includes the time history of the CTI. Hereafter, `Typewriter` means the name of the software in the HEADAS package.

After the reprocessing, we cut the epoch of Earth elevation angles less than  $5^\circ$  (to avoid targets hiding the edge of the Earth), the day Earth elevation angle less than  $20^\circ$  (to avoid

---

<sup>1</sup>In the normal clocking full window mode, the FT CCDs are operated in the way described in section 3.3.1. The details of the clocking and window modes are shown in Koyama et al. [50].

<sup>2</sup><<http://www.darts.isas.jaxa.jp/astro/suzaku/>>.

<sup>3</sup><<http://www.astro.isas.jaxa.jp/suzaku/caldb/history/>>.

<sup>4</sup>See <[http://heasarc.gsfc.nasa.gov/FTP/software/ftools/release/archive/Release\\_Notes\\_6.6.1](http://heasarc.gsfc.nasa.gov/FTP/software/ftools/release/archive/Release_Notes_6.6.1)>. The HEADAS package is released by Goddard Space Flight Center/NASA and generally used for the data analysis of high energy astronomy. Tools released by the Suzaku team are also included in this package.

Table 4.1: Observation data list

OBSID	Pointing Direction				Observation	Observation	Exp. (ks)	XIS2	SCI	Object Name
	$\alpha_{2000}(\circ)$	$\delta_{2000}(\circ)$	$l(\circ)$	$b(\circ)$	Start (UT)	End (UT)				
Galactic center $5^\circ \times 2^\circ$ region										
100027010	266.51	-28.92	0.05	-0.07	2005-09-23T07:18:25	2005-09-24T11:05:19	44.7	ok	off	Sgr A East
100027020	266.30	-29.17	-0.25	-0.05	2005-09-24T14:17:17	2005-09-25T17:27:19	37.4	ok	off	Sgr A west
100037010	266.30	-29.17	-0.25	-0.05	2005-09-29T04:35:41	2005-09-30T04:29:19	43.5	ok	off	Sgr A west
100037030	266.20	-29.35	-0.45	-0.07	2005-09-30T06:06:32	2005-09-30T07:41:20	3.0	ok	off	KS1741-293(GCBGD2)
100037040	266.51	-28.93	0.06	-0.07	2005-09-30T07:43:01	2005-10-01T06:21:24	42.9	ok	off	Sgr A East
100037060	266.88	-28.44	0.64	-0.10	2005-10-10T12:28:01	2005-10-12T07:05:23	76.4	ok	off	Sgr B2
500018010	266.16	-29.47	-0.57	-0.09	2006-02-20T12:45:25	2006-02-23T10:50:14	106.9	ok	off	SGR C
500005010	266.77	-28.63	0.43	-0.12	2006-03-27T23:00:22	2006-03-29T18:12:15	88.4	ok	off	GC CENTER #2
100048010	266.51	-28.93	0.06	-0.07	2006-09-08T02:23:24	2006-09-09T09:06:15	63.0	ok	off	GALACTIC CENTER
501040010	266.69	-28.38	0.61	0.07	2006-09-21T17:29:01	2006-09-23T06:52:20	61.4	ok	on	GC SGR B NORTH
501040020	266.69	-28.38	0.61	0.07	2006-09-24T05:03:12	2006-09-25T07:00:24	44.8	ok	on	GC SGR B NORTH
501008010	266.50	-29.17	-0.15	-0.19	2006-09-26T14:18:16	2006-09-29T21:25:14	129.6	ok	on	GC SOUTH
501009010	266.19	-28.93	-0.07	0.18	2006-09-29T21:26:07	2006-10-01T06:55:19	51.2	ok	on	GC SOUTH BGD
501010010	266.26	-30.37	-1.29	-0.64	2006-10-07T02:16:52	2006-10-08T10:19:19	50.7	ok	off	HESS J1745-303
501049010	265.38	-29.75	-1.17	0.33	2006-10-08T10:22:40	2006-10-09T02:19:24	19.6	ok	on	GALACTIC CENTER
501050010	265.91	-29.65	-0.83	0.00	2006-10-09T02:20:25	2006-10-09T13:39:24	22.0	ok	on	GALACTIC CENTER
501051010	265.70	-29.93	-1.17	-0.00	2006-10-09T13:40:09	2006-10-10T06:44:24	21.9	ok	on	GALACTIC CENTER
501052010	265.50	-30.21	-1.50	0.00	2006-10-10T06:45:09	2006-10-10T21:18:14	19.3	ok	on	GALACTIC CENTER
501053010	265.30	-30.50	-1.83	-0.00	2006-10-10T21:18:59	2006-10-11T10:06:14	21.9	ok	on	GALACTIC CENTER
501057010	266.03	-30.11	-1.17	-0.33	2006-10-11T10:07:27	2006-10-12T03:28:14	20.5	ok	on	GALACTIC CENTER
501039010	267.02	-28.35	0.78	-0.16	2007-03-03T12:20:20	2007-03-05T12:39:25	96.4	ok	on	GC SGR B EAST
501046010	265.98	-28.90	-0.17	0.33	2007-03-10T15:03:10	2007-03-11T03:55:14	25.2	ok	on	GALACTIC CENTER
501047010	265.78	-29.19	-0.50	0.33	2007-03-11T03:55:59	2007-03-11T19:04:14	25.6	ok	on	GALACTIC CENTER GC2
501048010	265.58	-29.47	-0.83	0.33	2007-03-11T19:04:59	2007-03-12T08:09:14	27.5	ok	on	GALACTIC CENTER GC3
501054010	266.63	-29.25	-0.17	-0.33	2007-03-12T08:11:07	2007-03-12T23:58:24	26.1	ok	on	GALACTIC CENTER GC9
501055010	266.43	-29.54	-0.50	-0.33	2007-03-12T23:59:09	2007-03-13T15:40:19	27.2	ok	on	GALACTIC CENTER GC10
501056010	266.23	-29.82	-0.83	-0.33	2007-03-13T15:41:12	2007-03-14T05:00:24	26.5	ok	on	GALACTIC CENTER GC11
501058010	266.98	-27.72	1.30	0.20	2007-03-14T05:02:29	2007-03-15T18:55:14	63.3	ok	on	GC SGR D NORTH
501059010	267.09	-27.94	1.17	0.00	2007-03-15T18:55:51	2007-03-17T05:06:19	62.2	ok	on	GC SGR D
501060010	267.29	-27.65	1.50	0.00	2007-03-17T05:07:04	2007-03-18T20:58:14	64.8	ok	on	GC SGR D EAST
502022010	266.81	-28.88	0.23	-0.27	2007-08-31T12:33:33	2007-09-03T19:00:25	134.8	ok	on	(L,B)=(0.25,-0.27)
102013010	266.51	-28.93	0.06	-0.07	2007-09-03T19:01:10	2007-09-05T05:20:20	51.4	ok	on	GALACTIC CENTER
502020010	267.19	-28.13	1.05	-0.17	2007-09-06T00:26:47	2007-09-09T16:10:19	139.1	ok	on	SGR D SNR
502002010	267.16	-29.14	0.17	-0.67	2007-10-09T16:40:54	2007-10-10T03:40:24	23.2	ok	on	GC14
502003010	266.96	-29.42	-0.17	-0.67	2007-10-10T03:41:13	2007-10-10T15:20:24	21.5	ok	on	GC15
502004010	267.48	-29.31	0.17	-1.00	2007-10-10T15:21:17	2007-10-11T01:00:24	19.9	ok	on	GC16
502005010	267.29	-29.60	-0.17	-1.00	2007-10-11T01:01:17	2007-10-11T11:32:20	20.6	ok	on	GC17
502006010	266.18	-28.62	0.17	0.33	2007-10-11T11:34:01	2007-10-11T23:07:14	22.6	ok	on	GC18
502007010	265.86	-28.45	0.17	0.67	2007-10-11T23:09:15	2007-10-12T09:52:14	22.0	ok	on	GC19
502008010	265.66	-28.73	-0.17	0.67	2007-10-12T09:52:59	2007-10-12T21:50:19	23.8	ok	on	GC20
502009010	267.48	-27.37	1.83	-0.00	2007-10-12T21:52:24	2007-10-13T07:30:19	20.9	ok	on	GC21
502010010	266.38	-28.34	0.50	0.33	2007-10-13T07:32:00	2007-10-13T18:50:24	21.6	ok	on	GC22
502011010	266.57	-28.05	0.83	0.33	2007-10-13T18:51:09	2007-10-14T05:30:24	23.0	ok	on	GC23
502016010	266.23	-30.11	-1.08	-0.48	2008-03-02T18:08:00	2008-03-04T17:40:19	70.5	ok	on	HESS J1745-303 1
502017010	266.47	-30.09	-0.95	-0.65	2008-03-06T13:26:36	2008-03-08T16:00:24	72.6	ok	on	HESS J1745-303 2
502018010	266.06	-30.24	-1.27	-0.43	2008-03-08T16:02:17	2008-03-10T21:00:19	79.0	ok	on	HESS J1745-303 3
502051010	266.94	-28.15	0.91	0.01	2008-03-11T06:19:45	2008-03-15T05:30:18	138.8	ok	on	GC G0.9+0.1
503007010	266.44	-28.57	0.33	0.17	2008-09-02T10:15:27	2008-09-03T22:52:24	52.2	ok	on	GC LARGEPROJECT1
503008010	266.78	-29.13	0.00	-0.38	2008-09-03T22:53:29	2008-09-05T06:56:19	53.7	ok	on	GC LARGEPROJECT2
503009010	266.45	-29.34	-0.33	-0.24	2008-09-05T06:57:08	2008-09-06T15:55:24	52.4	ok	on	GC LARGEPROJECT3
503010010	266.04	-29.55	-0.70	-0.05	2008-09-06T15:56:13	2008-09-08T01:39:24	53.1	ok	on	GC LARGEPROJECT4
503011010	265.95	-29.83	-0.97	-0.13	2008-09-08T09:08:09	2008-09-09T21:33:19	57.6	ok	on	GC LARGEPROJECT5
503012010	266.30	-29.94	-0.91	-0.44	2008-09-14T19:35:07	2008-09-16T00:50:14	57.7	ok	on	GC LARGEPROJECT6
503013010	265.67	-30.07	-1.30	-0.05	2008-09-16T00:51:19	2008-09-18T04:44:24	104.8	ok	on	GC LARGEPROJECT7
503014010	265.18	-30.75	-2.10	-0.05	2008-09-18T04:46:49	2008-09-19T07:32:20	55.4	ok	on	GC LARGEPROJECT8
503015010	265.03	-30.96	-2.35	-0.05	2008-09-19T07:33:05	2008-09-20T09:56:13	56.8	ok	on	GC LARGEPROJECT9
503016010	264.87	-31.17	-2.60	-0.05	2008-09-22T06:47:49	2008-09-23T08:07:17	52.2	ok	on	GC LARGEPROJECT10
503017010	264.72	-31.38	-2.85	-0.05	2008-09-23T08:08:10	2008-09-24T09:21:13	51.3	ok	on	GC LARGEPROJECT11
503018010	264.56	-31.60	-3.10	-0.05	2008-09-24T09:27:54	2008-09-24T22:30:24	29.4	ok	on	GC LARGEPROJECT12
503072010	265.99	-29.21	-0.42	0.17	2009-03-06T02:39:11	2009-03-09T02:55:24	140.6	ok	on	EXTENDED CHIMNEY
403009010	266.48	-28.78	0.17	0.02	2009-03-21T02:03:27	2009-03-23T18:26:09	110.8	ok	on	ARCHES CLUSTER
$b = -2^\circ$										
502059010	268.38	-29.96	-0.00	-2.00	2007-09-29T01:40:51	2007-10-02T14:10:16	136.8	ok	on	GALACTIC BULGE

reflected X-rays from the Earth) and the South Atlantic Anomaly (to minimum the NXB). The effective exposures after this screening of each data were shown in table 4.1.

We confirmed that the center energy of the Mn I  $K\alpha$  line of the onboard calibration sources ( $^{55}\text{Fe}$ ) is 5.895 eV within the calibration uncertainty of 20 eV during the observation period.

### 4.1.3 Response Function of the XIS

Using `xissimarfgen` [34] and `xisrmfgen`, the effective area of the XRT and the response of the XIS for spectra were calculated, and ancillary response files (ARFs) and redistribution matrix files (RMFs) were made. ARFs and RMFs are telescope and detector response files used in a spectral analysis tool, `xspec11`. The ARFs and RMFs depend on the observation date, the target positions on the CCD and in the sky, and the attitudes of the Suzaku satellite during the observation.

Since the responses of the FIs are almost same, we merged the FI spectra into one for the following spectral analysis. The RMFs and ARFs were merged for the FIs with `addrmf` and `addarf`.

### 4.1.4 Background

The background of the GDXE observation composes of mainly the NXB and the cosmic X-ray background (CXB). The detail of NXB was summarized in section 3.3.4. The NXB spectra sorted by the COR were made from the same source region in the detector coordinate using `xisnxbgen` [125]. The NXB spectra were averaged for the FIs. These NXB spectra were subtracted from the observed GDXE spectra in the following spectral fittings. The CXB is celestial X-rays coming from all over the sky almost uniformly. The CXB is due to unresolved extra-galactic X-ray sources, the bulk of which are active galactic nuclei (AGN) [24, 70]. According to Kushino et al. [58], the averaged CXB is described with a power-law model with a photon index  $\Gamma = 1.4$  and the intensity is  $5.4 \times 10^{-15} \text{ erg s}^{-1} \text{ cm}^{-2} \text{ arcmin}^{-2}$  in the 2–10 keV band. This CXB model was used in the following spectral fittings.

In figure 4.1, we compare the observed spectra of the GDXE without the background subtraction, with the spectra of the reconstructed NXB and the GDXE spectra subtracted the NXB and the modeled CXB spectra. Here, the interstellar absorption of the CXB is assumed to be  $N_{\text{H}} = 3 \times 10^{22} \text{ cm}^{-2}$ . The spectra of region 5 and  $b = -2^\circ$  (section 4.3) are chosen as examples of dark GDXE regions. We did not use the BI data above  $\sim 8 \text{ keV}$  in the following analyses because the signal to noise ratio is low as shown in figure 4.1. Note that even in the dark GDXE regions, the intensity ratios of the CXB to the GDXE are 10 % and 20 % at most for the GC and  $b = -2^\circ$  regions, respectively.

### 4.1.5 Exclusion of Bright Sources

Bright sources listed in table 4.2 were excluded to make the GDXE spectra. In the case of the data at  $b = -2^\circ$ , seven point sources were found in the FOV and summarized in table 4.3. The circles with a radius of  $1'.5$  centered at the point sources were excluded.

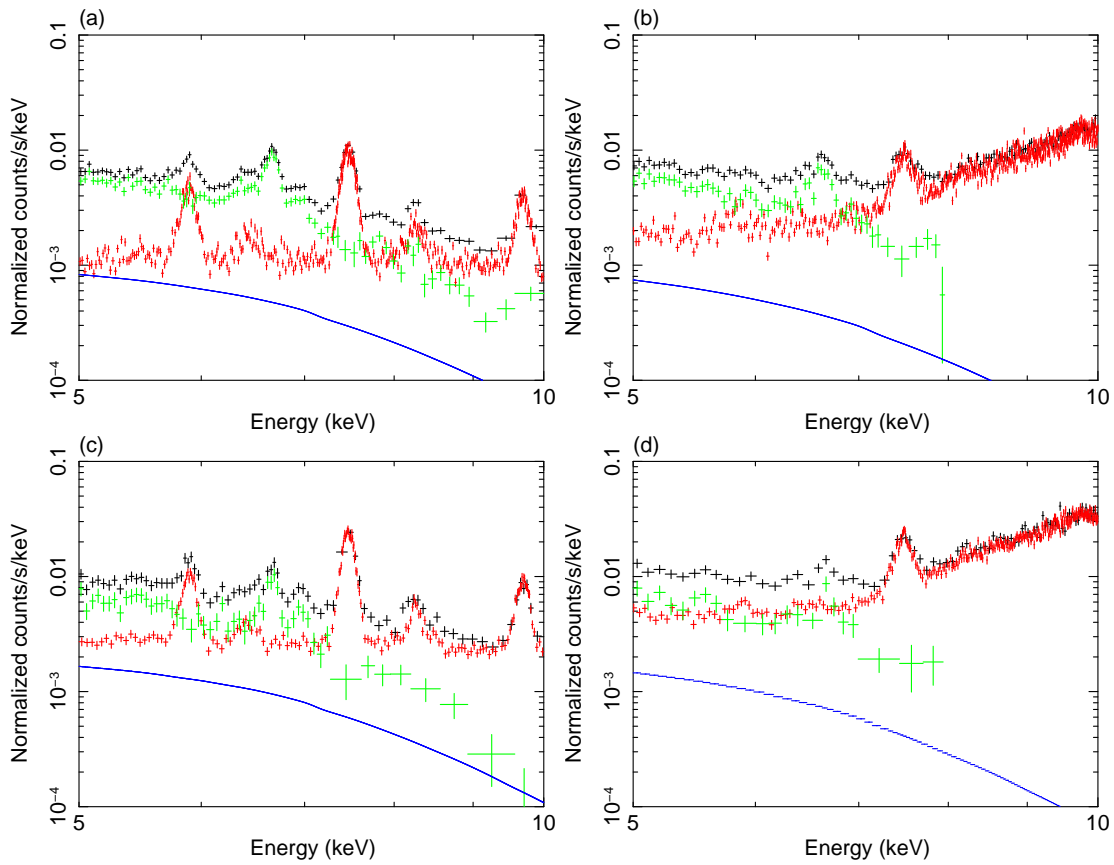


Figure 4.1: Comparison of the spectra of the GDXE, NXB and CXB. Black: observed spectra of the GDXE without the background subtraction. Red: the reconstructed NXB. Green: GDXE spectra subtracted the NXB. Blue: modeled CXB spectra. (a) (b) Spectra at region 5 of the FIs and the BI. (c) (d) Spectra at  $b = -2^\circ$  of the FIs and the BI, respectively.

Table 4.2: List of the bright sources excluded to make the GDXE spectra.

Name	Position*		Radius* (arcmin)
	$l$	$b$	
Great Annihilator	$-0^{\circ}.887$	$-0^{\circ}.097$	4
CXOGCS J174445.5–295042	$-0^{\circ}.774$	$-0^{\circ}.062$	2
2E 1742.9–2929	$-0^{\circ}.439$	$-0^{\circ}.383$	5
KS 1741–293	$-0^{\circ}.432$	$-0^{\circ}.074$	3
Sgr A East	$-0^{\circ}.047$	$-0^{\circ}.053$	3
Arches cluster	$0^{\circ}.123$	$0^{\circ}.024$	2
1E 1743.1–2843	$0^{\circ}.256$	$-0^{\circ}.029$	3
G0.61+0.01	$0^{\circ}.620$	$0^{\circ}.016$	4
CXOGC J174645.3–281546	$0^{\circ}.712$	$0^{\circ}.141$	2
HD 161507	$0^{\circ}.837$	$0^{\circ}.085$	2
G0.9+0.1	$0^{\circ}.866$	$0^{\circ}.077$	2
SAX J1748.2-2808	$0^{\circ}.994$	$-0^{\circ}.086$	2
AX J1749.1–2733	$1^{\circ}.592$	$-0^{\circ}.062$	2

\*The position and the radius show those of the excluded circles.

Table 4.3: List of the seven point sources excluded from the  $b = -2^{\circ}$  data.

Position		Identification*
$l$	$b$	
$-0^{\circ}.079$	$-1^{\circ}.945$	None
$-0^{\circ}.067$	$-2^{\circ}.073$	2XMM J175339.3–300334
$-0^{\circ}.020$	$-2^{\circ}.125$	2XMM J175358.1–300234
$0^{\circ}.002$	$-2^{\circ}.053$	2XMM J175344.7–295905
$0^{\circ}.004$	$-1^{\circ}.985$	2XMM J175327.8–295719
$0^{\circ}.046$	$-2^{\circ}.007$	2XMM J175341.2–295521
$0^{\circ}.089$	$-2^{\circ}.077$	2XMM J175402.7–295524

\* We searched corresponding objects in the 2XMM catalog [139].

## 4.2 Spatial Distribution of the GDXE

### 4.2.1 Intensity Profiles along the Galactic Longitude

To study the intensity profile of the Fe  $K\alpha$  line along the galactic longitude, X-ray spectra were made from the rectangles shown in figure 4.2. The Galactic latitude coordinate of each rectangle is the same as that of Sgr A\* ( $b = -0^\circ.046$ ) [100]. The size of each rectangle is  $6' \times 12'$ .

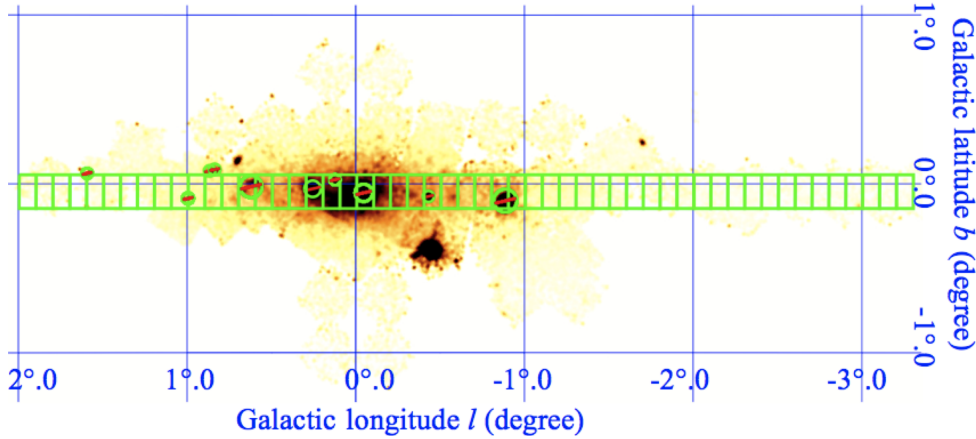


Figure 4.2: Regions from which spectra were extracted along the galactic longitude. They are overlaid on the X-ray image in the 6.55-6.8 keV band.

The spectra of the NXB, the ARFs and the RMFs were generated in the way described in section 4.1.3. We fitted a phenomenological model below to the spectra subtracted the NXB spectra in the 5–10 keV band:

$$4 \text{ Gaussians} + PL \times Abs1 + CXB \times Abs2. \quad (4.1)$$

$PL$  is a power-law model.  $Abs$  is the interstellar absorption model. The line centers of the gaussians were fixed to 6.40 (Fe I  $K\alpha$ ), 6.68 (Fe XXV  $K\alpha$ ), 6.97 (Fe XXVI  $K\alpha$ ) and 7.06 (Fe I  $K\beta$ ) keV according to APEC model [119] for the ionized lines and Kaastra & Mewe [40] for the neutral lines. Width of the each line was fixed to 0 eV. The intensities of the Fe I  $K\alpha$ , Fe XXV  $K\alpha$ , and Fe XXVI  $K\alpha$  lines in the models were free in the fittings. The intensity of the Fe I  $K\beta$  line was fixed to 0.125 times that of the Fe I  $K\alpha$  line according to [40]. The normalization and photon index  $\Gamma$  of the power-law model were free.  $CXB$  is a power-law model as the CXB and the normalization and  $\Gamma$  were fixed as described in section 4.1.4.  $Abs = \exp(-\sigma(E) \times N_H)$  where  $E$  is the energy of the incident photon and  $\sigma(E)$  is the cross section of the interstellar absorption. We calculated  $\sigma(E)$  referring to [1] and [4].  $N_H$  is the column density of hydrogen in the interstellar matter. The column density of  $Abs1$  was free. The column density of  $Abs2$  was the interstellar absorption of the CXB and fixed to be  $N_H = 1.2 \times 10^{23} \text{ cm}^{-2}$ , which is twice the typical interstellar absorption toward the GC region,  $N_H = 6 \times 10^{22} \text{ cm}^{-2}$  [96, 110].

The FIs and BI spectra of each region were fitted simultaneously. The spectra of the same region but of different observations were fitted simultaneously using different ARFs and RMFs. Some examples of the spectra and the best-fit models are shown in figure 4.3.

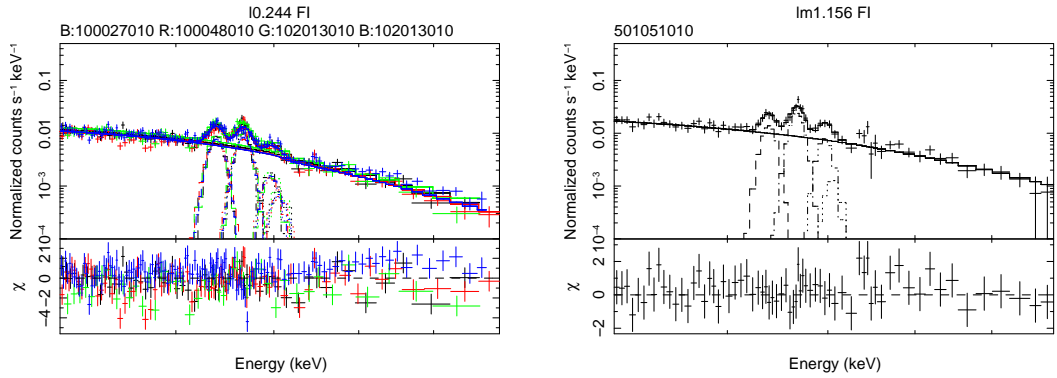


Figure 4.3: Examples of the spectra and the best-fit models. The data of the different observations are shown in the different colors. Only the FIs spectra are shown for the simplicity although we simultaneously fitted the FIs and BI spectra. The vertical error bars show the  $1\sigma$  errors. Left :  $l = 0^\circ.244$ . Right:  $l = -1^\circ.156$ .

### Fe XXV $K\alpha$ and Fe XXVI $K\alpha$

The intensity profiles of the Fe XXV  $K\alpha$  and Fe XXVI  $K\alpha$  lines were shown in figure 4.4 in which the results of  $|l| > 8^\circ$  by Yamauchi et al. [143] are also added. Note that the galactic latitudes of the data of [143] were  $-0^\circ.05 < b < 0^\circ.7$  and different from those of ours ( $b = -0^\circ.046$ ). The data of [143] were corrected assuming that the scale height of the intensity profile along the galactic latitude is  $0^\circ.5$  according to Kaneda et al. [41].

We fitted phenomenological models to the profiles to obtain a typical e-folding scale along the galactic longitude  $h_l$  (degree). We firstly made a fitting with a one-component model;  $A_l \times \exp(-l_*/h_l)$ . The symbol  $l_*$  denotes the distance from Sgr A\* ( $l = -0^\circ.056$ ) along the Galactic plane measured in the unit of degree, i.e.  $l_* = |l + 0^\circ.056|$ .  $A_l$  (photons  $s^{-1} \text{ cm}^{-1} \text{ arcmin}^{-2}$ ) is the line intensity at  $l_* = 0^\circ$ . The data points of  $l_* > 2^\circ$ , however, excess the best-fit one-component models. Thus we tried a two-component model;  $A_{l1} \times \exp(-l_*/h_{l1}) + A_{l2} \times \exp(-l_*/h_{l2})$ . The fittings are significantly improved.  $\chi^2/d.o.f.$  are 2805.6/59 (Fe XXV  $K\alpha$ ) and 255.1/59 (Fe XXVI  $K\alpha$ ) with the one-component models, and 1946.9/57 (Fe XXV  $K\alpha$ ) and 217.0/57 (Fe XXVI  $K\alpha$ ) with the two-component models. The best-fit model and parameters are shown in figure 4.4 and table 4.4.

### Fe I $K\alpha$

The intensity profile of Fe I  $K\alpha$  line along the galactic longitude is shown in figure 4.5. The results of  $|l| > 8^\circ$  by Yamauchi et al. [143] are also added after the correction assuming that the scale height of the intensity profile along the galactic latitude is  $0^\circ.5$ . The intensity profile of the Fe I  $K\alpha$  line is clumpy compared with the smooth profile of the Fe XXV  $K\alpha$  line. The bright clumps corresponds to radio-observed giant molecular clouds in the CMZ. It is difficult to model the effect of the molecular clouds so the intensity profile of the Fe I  $K\alpha$  line was not fitted with phenomenological models.

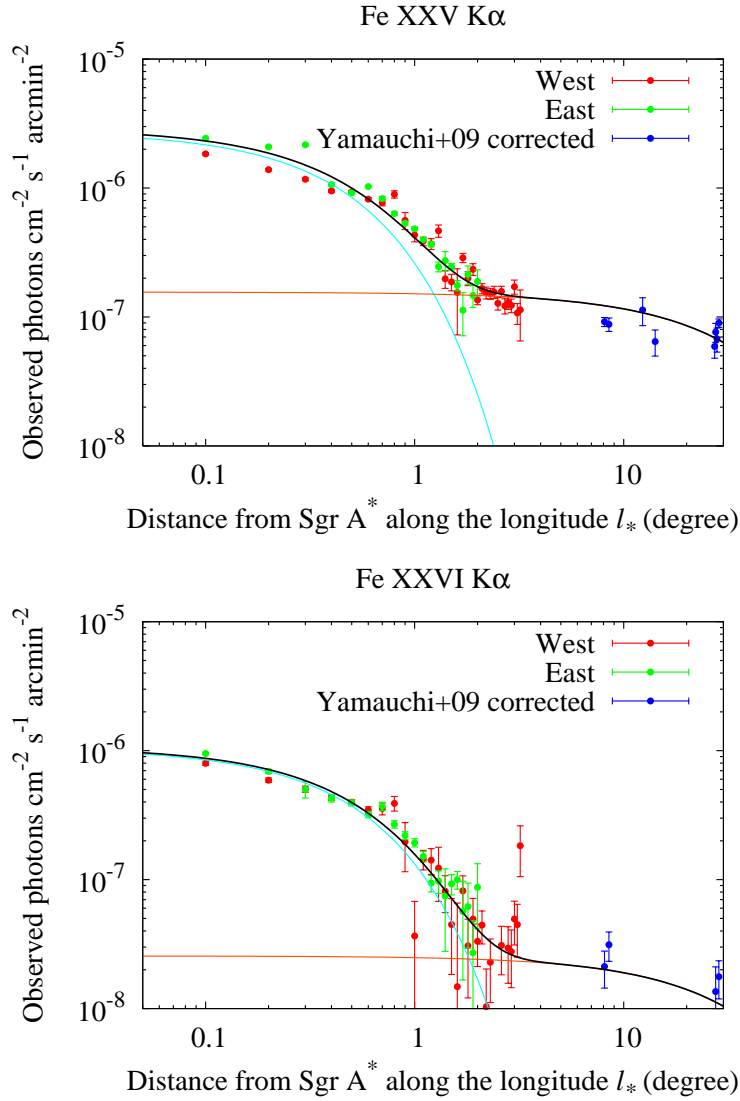


Figure 4.4: Intensity profiles of the Fe XXV  $K\alpha$  (top) and Fe XXVI  $K\alpha$  line (bottom) along the galactic latitude. The error bars show the  $1\sigma$  errors. The black lines show the best-fit two-component models. The cyan and orange lines show the components with e-folding scales  $h_{l1}$  and  $h_{l2}$ , respectively.

Table 4.4: Best-fit parameters of the two-component model to the intensity profiles of the highly ionized Fe  $K\alpha$  lines along the galactic longitude.\*

	$A_{l1}(10^{-7})^\dagger$	$A_{l2}(10^{-7})^\dagger$	$h_{l1}$ (degree)	$h_{l2}$ (degree)
Fe XXV $K\alpha$	$27.3 \pm 1.4$	$1.6 \pm 0.3$	$0.43 \pm 0.03$	$33 \pm 20$
Fe XXVI $K\alpha$	$10.4 \pm 0.4$	$0.26 \pm 0.08$	$0.48 \pm 0.02$	$33 \pm 37$

<sup>†</sup> The uncertainties show the  $1\sigma$  errors. \*The unit is photons  $s^{-1} \text{ cm}^{-2} \text{ arcmin}^{-2}$ .

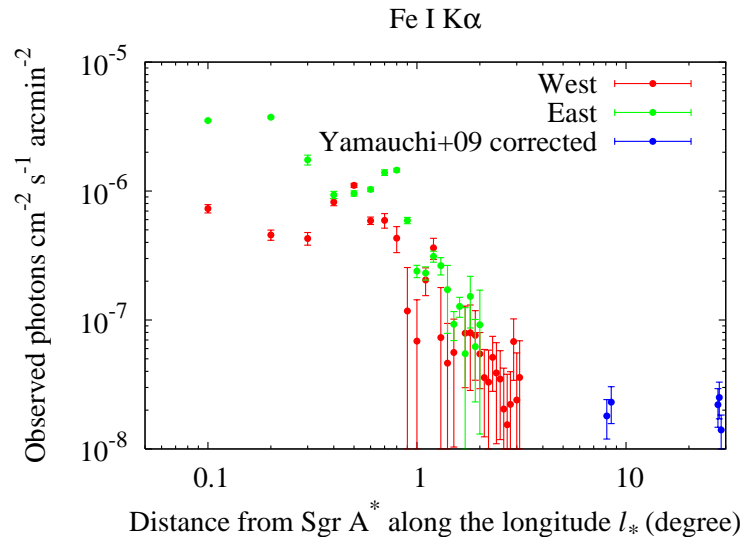


Figure 4.5: Intensity profile of the Fe I  $K\alpha$  line. The error bars show the  $1\sigma$  errors.

### Intensity in the 5–10 keV Band

The intensity profile of the GDXE in the 5–10 keV band is shown in figure 4.6. The results of  $|l| > 8^\circ$  by Yamauchi et al. [143] are also added after the correction assuming that the scale height of the intensity profile along the galactic latitude is  $0^\circ.5$ . This intensity includes both of the line and continuum emissions. The CXB and the NXB were already subtracted. The interstellar absorption is not corrected. We tried two-component model fittings. We did not use the data points of  $l = -0^\circ.96 \sim -0^\circ.75$  for the fittings because they were clearly contaminated by the Great Annihilator at  $(l, b) = (-0^\circ.89, -0^\circ.10)$ . The best-fit model and parameters are shown in figure 4.6 and table 4.5.

#### 4.2.2 Intensity Profiles along the Galactic Latitude

To study the intensity profile of the Fe K  $\alpha$  lines along the Galactic latitude, X-ray spectra were made from the rectangle regions show in figure 4.7. The regions were selected along the Galactic latitude at  $l = -1^\circ.16, -0^\circ.84, -0^\circ.56, -0^\circ.17, 0^\circ.17, 0^\circ.50, 0^\circ.82, 1^\circ.17$ . The size of each rectangle region is  $12' \times 6'$ .

In the case of the data of  $b = -2^\circ$ , the spectrum was obtained from a circle with a radius of  $7'.4$  at the center of the FOV. This radius was chosen to avoid the area illuminated by the calibration source on the CCD chip.

The NXBs, ARFs and RMFs were generated in the way described in section 4.1.3. We fitted a phenomenological model shown in equation 4.1 to the spectra subtracted the NXB in the 5–10 keV band. Some examples of the spectra and the fitting results are shown in figure 4.8. Thus the intensity profiles of the three Fe K  $\alpha$  lines and the 5–10 keV band for each longitude were obtained. The result of  $b = -2^\circ$  was added to the profile of  $l = -0^\circ.17$ .

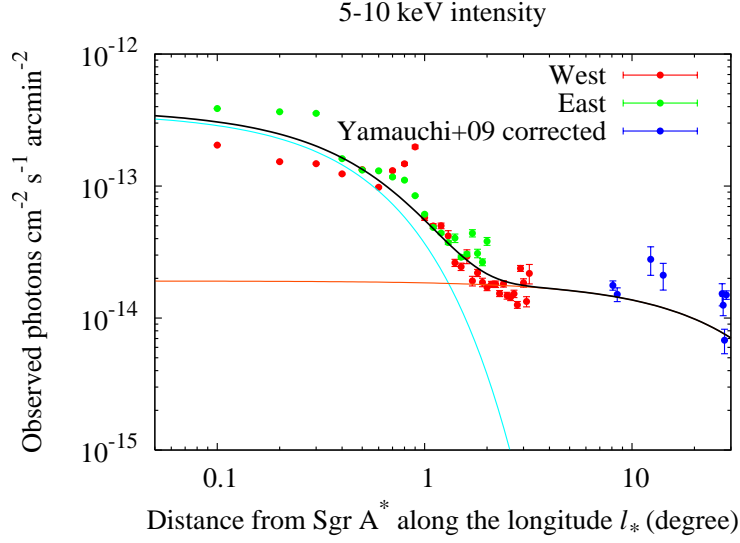


Figure 4.6: Intensity profile in the 5–10 keV band along the galactic longitude. The error bars show the  $1\sigma$  errors. The black lines show the best-fit two-component models. The cyan and orange lines show the components with e-folding scales  $h_{l1}$  and  $h_{l2}$ , respectively.

Table 4.5: Best-fit parameters of the two-component model to the intensity profile in the 5–10 keV band along the galactic longitude.\*

$A_{l1}(10^{-13})^\dagger$	$A_{l2}(10^{-13})^\dagger$	$h_{l1}$ (degree)	$h_{l2}$ (degree)
$3.6 \pm 0.2$	$0.19 \pm 0.07$	$0.43 \pm 0.04$	$30 \pm 62$

$^\dagger$  The uncertainties show the  $1\sigma$  errors. \*The unit is  $\text{erg s}^{-1} \text{cm}^{-2} \text{arcmin}^{-2}$ .

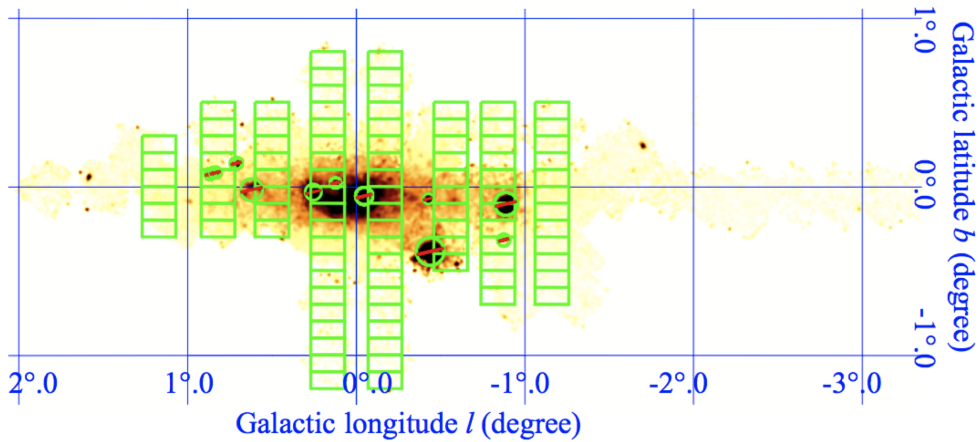


Figure 4.7: Regions from which spectra were made along the galactic latitude. They are overlaid on the XIS image in the 6.55–6.8 keV band.

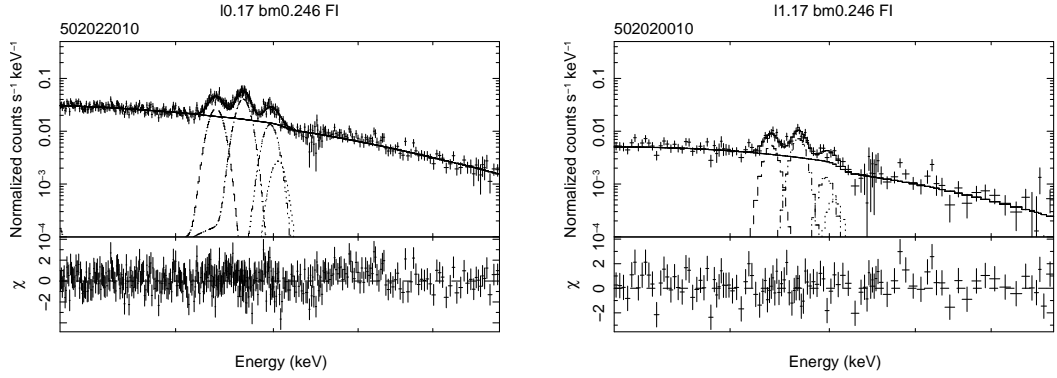


Figure 4.8: Examples of the spectra and the best-fit models. Only the FIs spectra are shown for the simplicity although we simultaneously fitted the FIs and BI spectra. The vertical error bars show the  $1\sigma$  errors. Left :  $(l, b) = (0^\circ.17, -0^\circ.246)$ . Right:  $(l, b) = (1^\circ.17, -0^\circ.246)$ .

### Fe XXV $K\alpha$

The intensity profiles of the Fe XXV  $K\alpha$  line for the each longitude are shown in figure 4.9. We fitted phenomenological models of  $A_b \times \exp(-b_*/h_b)$  to the profiles to obtain typical scale height along the galactic latitude  $h_b$ .  $A_b$  is the line intensity at  $b_* = 0^\circ$ . The symbol  $b_*$  denotes the distance from the Galactic plane ( $b = -0^\circ.046$ ) measured in the unit of degree, i.e.  $b_* = |b + 0^\circ.046|$ . Note that the data point of  $b = -2^\circ$  is added to the profile in  $l = -0^\circ.17$ . The best-fit results are shown in figure 4.9.

For the intensity profiles in  $l = \pm 0^\circ.17$ , the data points in  $b_* > 0.7^\circ$  excess the best-fit models systematically. Thus a two-component models was tried for the profiles in  $l = \pm 0^\circ.17$ ;  $A_{b1} \times \exp(-b_*/h_{b1}) + A_{b2} \times \exp(-b_*/h_{b2})$ . The fittings are significantly improved with this model; the  $\chi^2/d.o.f.$  are 273.1/19 ( $l = -0^\circ.17$ ) and 308.8/18 ( $l = 0^\circ.17$ ) with the one-component model and 174.3/17 ( $l = -0^\circ.17$ ;  $h_{b1} = 0^\circ.16 \pm 0^\circ.03$ ,  $h_{b2} = 1^\circ.1 \pm 0^\circ.2$ ) and 255.8/16 ( $l = 0^\circ.17$ ;  $h_{b1} = 0^\circ.18 \pm 0^\circ.02$ ,  $h_{b2} = 1^\circ.0 \pm 0^\circ.5$ ) with the two-component model ( $1\sigma$  errors).

Figure 4.10 shows the relation between the scale height  $h_b$  of the one-component model and  $l_*$ . The scale height  $h_b$  increase with  $l_*$ . It implied that not only the profiles in  $l = \pm 0^\circ.17$  but also the other profiles would have two scale-height components and the larger scale-height components dominate at large  $l_*$ . Although the second component is not statically required, we fitted the two-component model to all the profiles in figure 4.9. The profiles in  $l_* > 0^\circ.2$ , however, did not require two scale-height components. Thus we fitted the every profiles simultaneously, and  $h_{b1}$  and  $h_{b2}$  were common for the every longitudes but  $A_{b1}$  and  $A_{b2}$  were free for the each longitude. Figure 4.11 shows the fitting results. The best-fit parameters of  $h_{b1}$  and  $h_{b2}$  are  $0^\circ.21 \pm 0^\circ.02$  and  $1^\circ.1 \pm 0^\circ.7$  ( $1\sigma$  errors). The  $\chi^2/d.o.f.$  is 681.4/76. This is better than the total  $\chi^2/d.o.f.$  of 812.9/78 of the one-component model fitting. The best-fit parameters are shown in table 4.6. The relations of  $A_{b1}$ ,  $A_{b2}$  and the galactic longitude are shown in figure 4.12. Figure 4.12 suggests that the  $A_{b1}$  decreases along with the galactic longitude but the  $A_{b2}$  is almost constant.

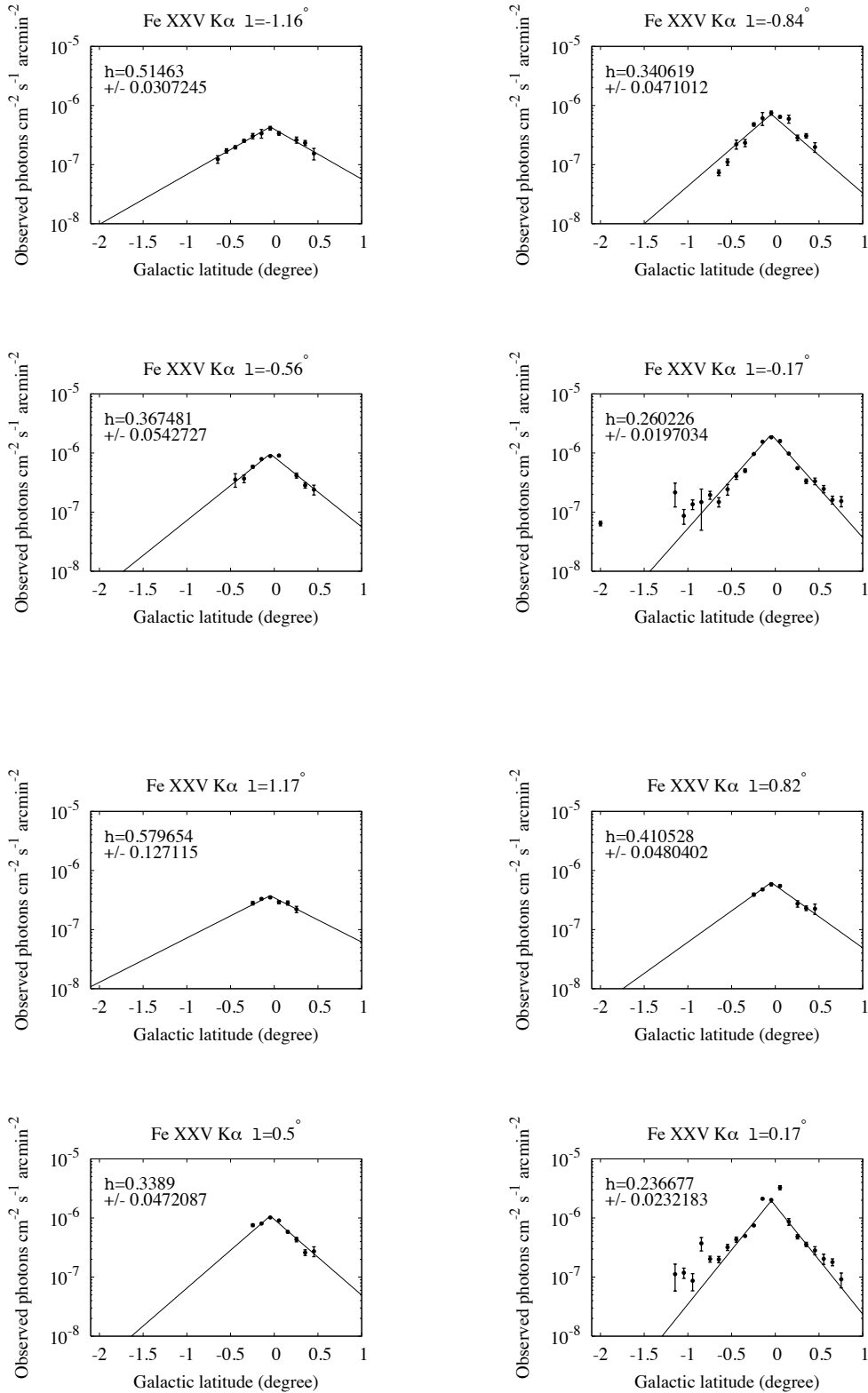


Figure 4.9: Intensity profiles of the Fe XXV K $\alpha$  line along the galactic latitude. The error bars show the  $1\sigma$  errors. The solid lines show the best-fit one-component models. The best-fit scale heights  $h_b$  are shown with the  $1\sigma$  errors.

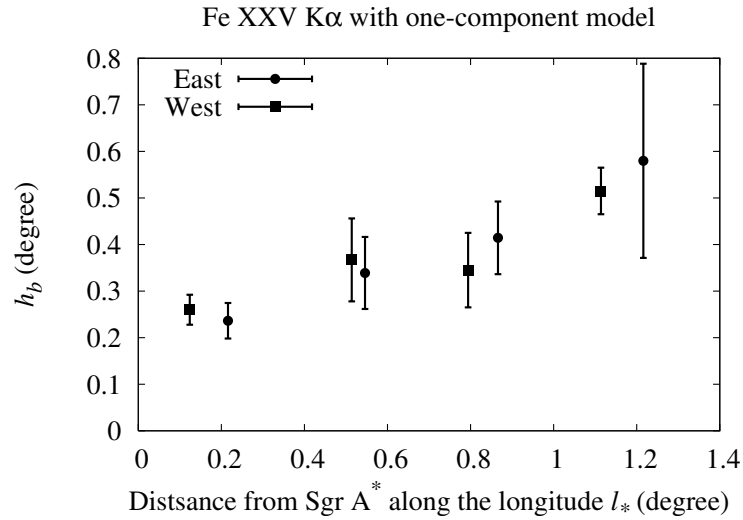


Figure 4.10: Relation between  $l_*$  and  $h_b$  of the Fe XXV  $K\alpha$  line intensity profiles along the galactic latitude with the one-component model. The error bars show the  $1\sigma$  errors.

### Fe XXVI $K\alpha$

The intensity profiles of the Fe XXVI  $K\alpha$  line along the galactic latitude are shown in figure 4.13. We fitted phenomenological models to the profiles to obtain typical scale heights. The intensity profiles were fitted with a one-component model first but those in  $l = \pm 0.17^\circ$  required a two-component model. Thus the every profiles were fitted simultaneously with the two-component models in the same way as the Fe XXV  $K\alpha$  line. The best-fit model is shown in figure 4.13. The  $\chi^2/d.o.f$  of 219.4/76 with the two-component models is better than 296.5/78 with the one-component models. The best fit parameters are shown in table 4.7 and summarized in figure 4.14.

### Fe I $K\alpha$

The intensity profiles of the Fe I  $K\alpha$  line along the galactic latitude are shown in figure 4.15. Note that the Fe I  $K\alpha$  line is not detected from the  $b = -2^\circ$  data significantly. The upper limits of the line intensity and the equivalent width in the 90 % confidence level are  $1.2 \times 10^{-8}$  photons  $s^{-1} \text{ arcmin}^{-2}$  and 97 eV. The intensity profiles of the Fe I  $K\alpha$  line seem asymmetric between the north and the south. We applied a one-component model with different scale heights for north and south. ( $h_N$  for  $b > -0^\circ.046$  and  $h_S$  for  $b \leq -0^\circ.046$ ). The best-fit results are shown in figure 4.15 and table 4.8. The  $\chi^2/d.o.f$ . is smaller than that of the previous symmetry one-component model. The intensity profiles of the Fe XXV  $K\alpha$  line were also fitted with this model for comparison. The comparison of  $\chi^2/d.o.f$ . is shown in table 4.9. In the case of the Fe XXV  $K\alpha$  line emission, the  $\chi^2/d.o.f$ . does not change so much between the symmetry and asymmetry models.

### Intensity in the 5–10 keV Band

The intensity profile of the GDXE in the 5–10 keV band is shown in figure 4.16. This intensity includes both of the line and continuum emissions. The CXB and the NXB were subtracted. The

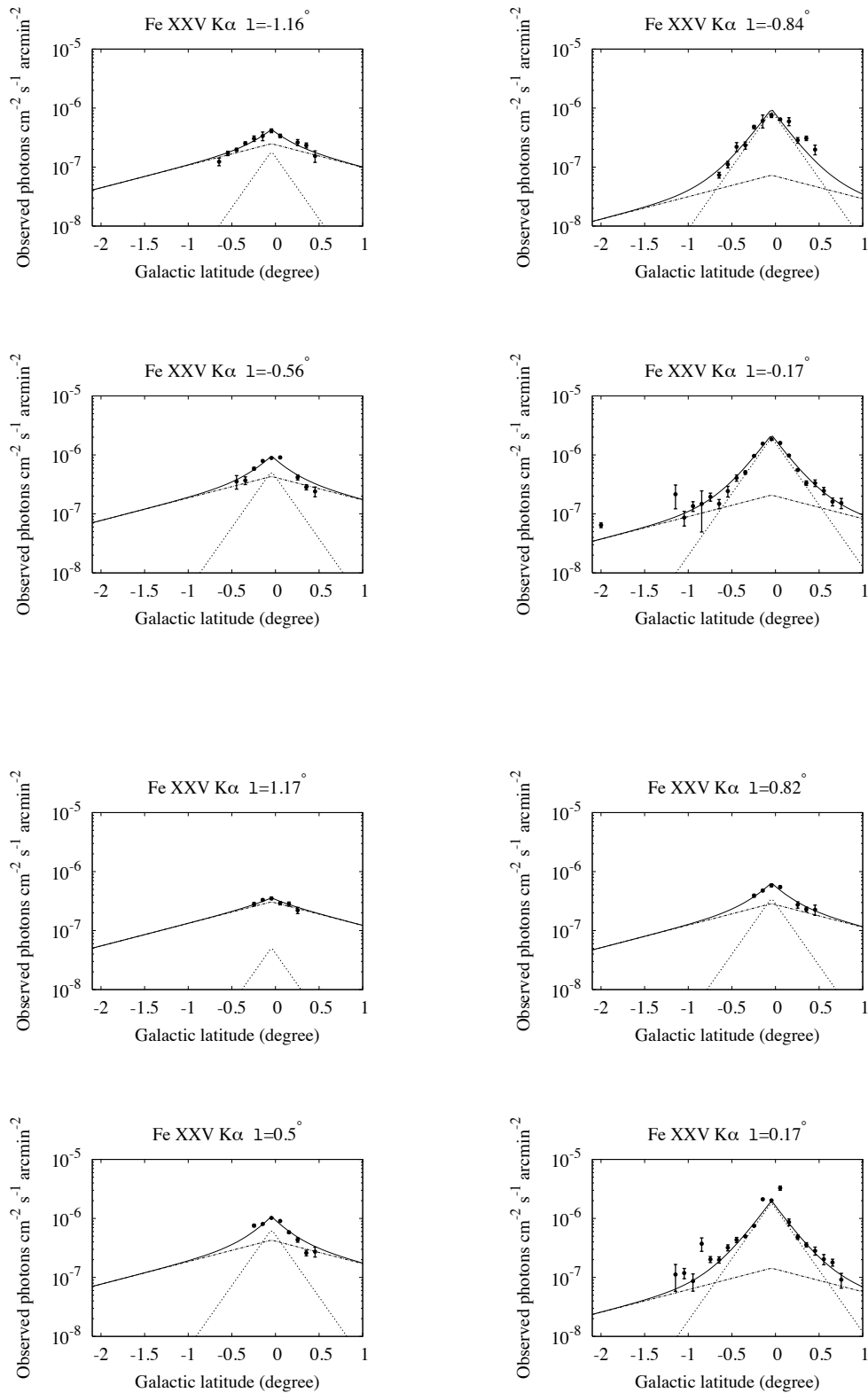


Figure 4.11: Same as figure 4.9 but with the best-fit two-component models. The error bars show the  $1\sigma$  errors. The solid lines show the best-fit two-component models. The dashed and alternate-long-and-short-dash lines show the components with scale heights  $h_{b1}$  and  $h_{b2}$ , respectively.

Table 4.6: Best-fit parameters of the two-component model to the intensity profiles of the Fe XXV K $\alpha$  line along the galactic latitude.\*

$l$ (degree)	$A_{b1}(10^{-6})^\dagger$	$A_{b2}(10^{-6})^\dagger$	$l$ (degree)	$A_{b1}(10^{-6})^\dagger$	$A_{b2}(10^{-6})^\dagger$
-0.17	$1.99 \pm 0.18$	$0.21 \pm 0.16$	0.17	$1.86 \pm 0.17$	$0.14 \pm 0.12$
-0.56	$0.53 \pm 0.18$	$0.43 \pm 0.16$	0.50	$0.65 \pm 0.18$	$0.43 \pm 0.16$
-0.84	$0.90 \pm 0.13$	$0.07(< 0.14)$	0.82	$0.36 \pm 0.17$	$0.29 \pm 0.13$
-1.16	$0.19 \pm 0.13$	$0.25 \pm 0.09$	1.17	$0.05(< 0.19)$	$0.31 \pm 0.11$
$h_{b1}$ (degree)			$h_{b2}$ (degree)		
$0.21 \pm 0.03$			$1.1 \pm 0.7$		

$^\dagger$  The uncertainties show the  $1\sigma$  errors. \*The unit is photons  $s^{-1} \text{ cm}^{-2} \text{ arcmin}^{-2}$ .

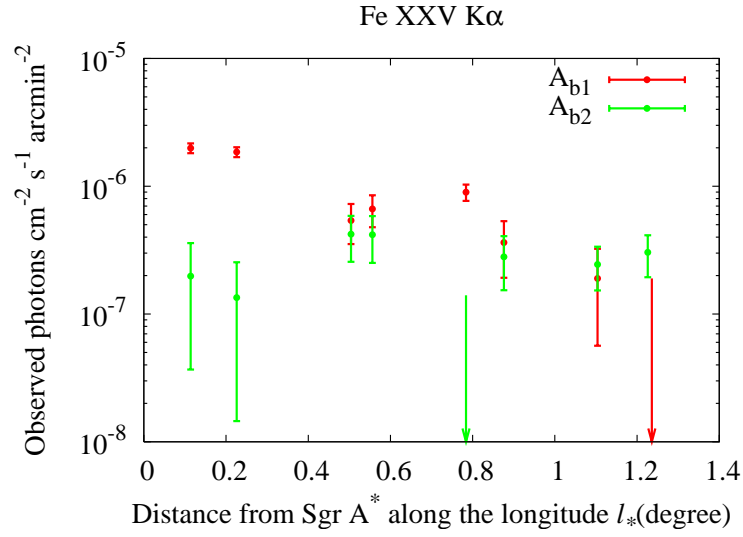


Figure 4.12: Relations among  $l_*$ ,  $A_{b1}$  and  $A_{b2}$  of the Fe XXV K $\alpha$  line intensity. The error bars show the  $1\sigma$  errors.

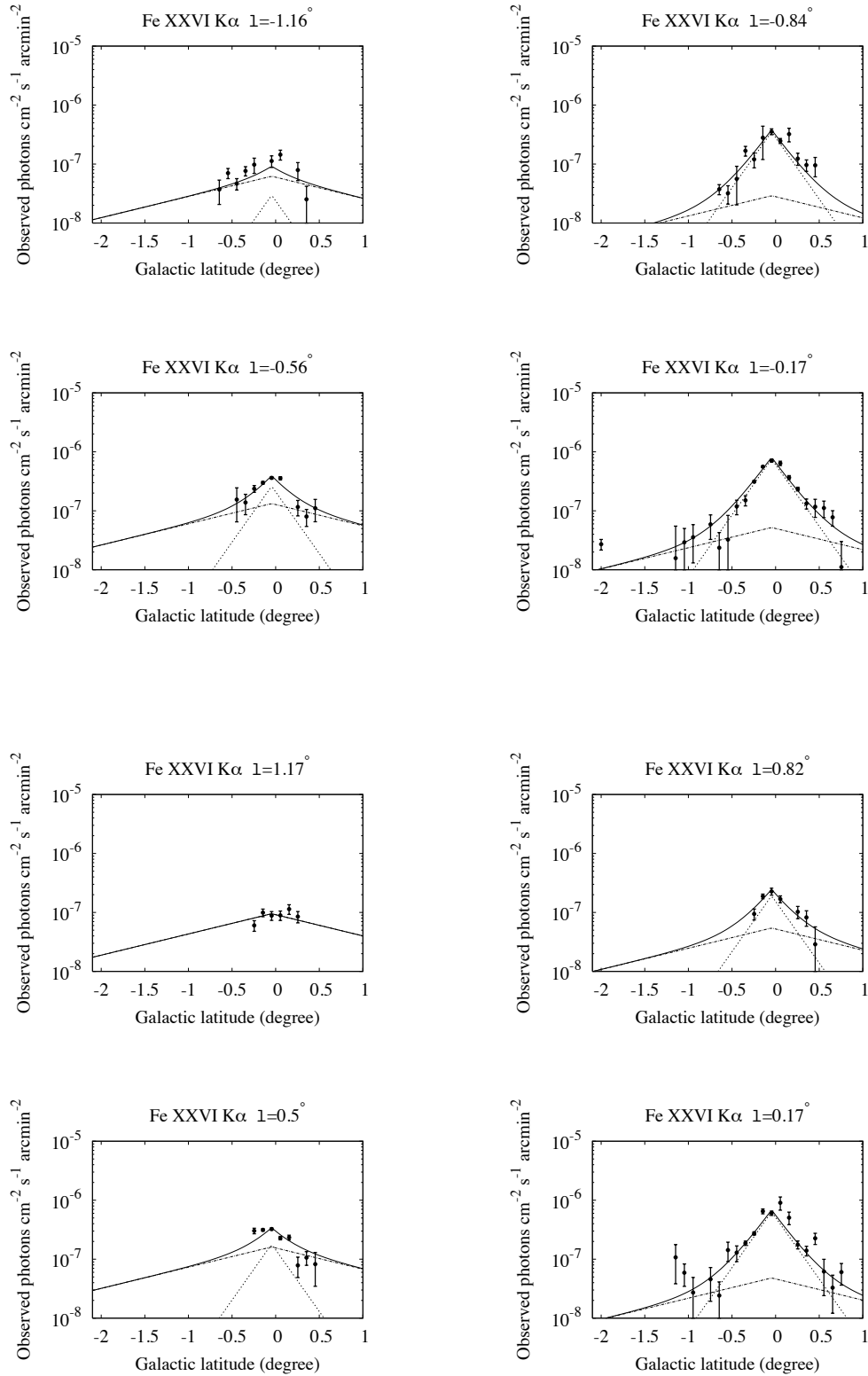


Figure 4.13: Intensity profiles of the Fe XXVI  $K\alpha$  line along the galactic latitude. The error bars show the  $1\sigma$  errors. The solid lines show the best-fit two-component models. The dashed and alternate-long-and-short-dash lines show the components with scale heights  $h_{b1}$  and  $h_{b2}$ , respectively.

Table 4.7: Best-fit parameters of the two-component model to the intensity profiles of the Fe XXVI K $\alpha$  line along the galactic latitude.\*

$l$ (degree)	$A_{b1}(10^{-6})^\dagger$	$A_{b2}(10^{-6})^\dagger$	$l$ (degree)	$A_{b1}(10^{-6})^\dagger$	$A_{b2}(10^{-6})^\dagger$
-0.17	$0.76 \pm 0.07$	$0.05(< 0.11)$	0.17	$0.64 \pm 0.08$	$0.05(< 0.10)$
-0.56	$0.26 \pm 0.09$	$0.13 \pm 0.08$	0.50	$0.18 \pm 0.09$	$0.16 \pm 0.08$
-0.84	$0.35 \pm 0.06$	$0.03(< 0.06)$	0.82	$0.19 \pm 0.08$	$0.05(< 0.10)$
-1.16	$0.03(< 0.09)$	$0.06 \pm 0.03$	1.17	$< 0.05$	$0.09(< 0.25)$
$h_{b1}$ (degree)			$h_{b2}$ (degree)		
$0.21 \pm 0.03$			$1.2(< 2.4)$		

$\dagger$  The uncertainties show the  $1\sigma$  errors. \*The unit is photons  $s^{-1} cm^{-2} arcmin^{-2}$ .

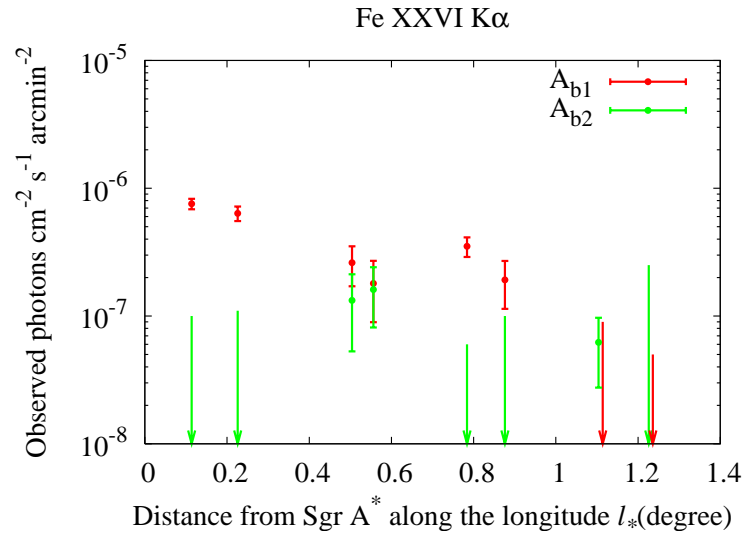


Figure 4.14: Relations among  $l_*$ ,  $A_{b1}$  and  $A_{b2}$  of the Fe XXVI K $\alpha$  line intensity. The error bars show the  $1\sigma$  errors.

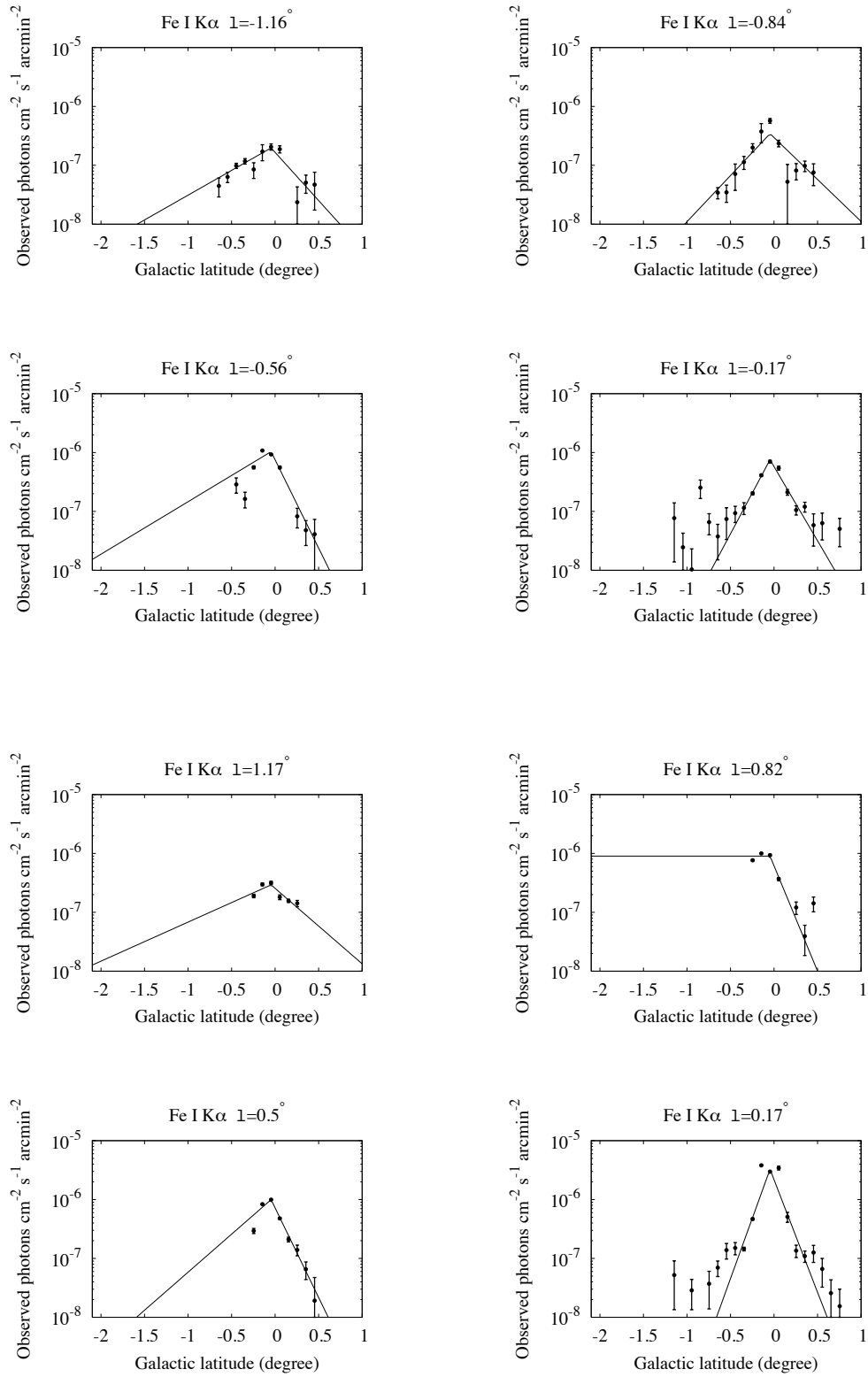


Figure 4.15: Intensity profiles of the Fe I  $K\alpha$  lines along the galactic latitude. The error bars show the  $1\sigma$  errors. The solid lines show the best-fit asymmetry one-component models.

Table 4.8: Best-fit parameters of the asymmetric one-component model to the intensity profiles of the Fe I K $\alpha$  line along the galactic latitude.\*

$l$ (degree)	$h_N$ (degree)	$h_S$ (degree)	$A^\dagger(10^{-6})$
-1.16	$0.27 \pm 0.07$	$0.52 \pm 0.11$	$0.20 \pm 0.03$
-0.84	$0.30 \pm 0.09$	$0.28 \pm 0.05$	$0.34 \pm 0.07$
-0.56	$0.14 \pm 0.05$	$0.49 \pm 0.27$	$1.03 \pm 0.12$
-0.17	$0.17 \pm 0.02$	$0.16 \pm 0.01$	$0.75 \pm 0.05$
0.17	$0.11 \pm 0.03$	$0.11 \pm 0.01$	$3.26 \pm 0.44$
0.5	$0.14 \pm 0.02$	$0.34 \pm 0.12$	$1.00 \pm 0.08$
0.82	$0.11 \pm 0.02$	$> 0.78$	$0.96 \pm 0.09$
1.17	$0.34 \pm 0.12$	$0.66 \pm 0.49$	$0.29 \pm 0.04$

\* The uncertainties show the  $1\sigma$  errors.  $^\dagger$ The unit is photons  $\text{s}^{-1} \text{cm}^{-2} \text{arcmin}^{-2}$ .

Table 4.9: Comparison between the symmetric and asymmetric one-component models.\*

	Fe I K $\alpha$		Fe XXV K $\alpha$	
	Symmetric	Asymmetric	Symmetric	Asymmetric
$\chi^2/\text{d.o.f.}$	2409/77	1315/69	657/77	611/69

\*The data of  $b = -2^\circ$  is omitted for the fittings.

interstellar absorption is not corrected. The profile resembles to those of the highly ionized Fe K $\alpha$  lines. Thus we tried two-component model fittings in the same way as the highly ionized Fe K $\alpha$  lines. The profiles of  $l = -0^\circ.56$  and  $-0^\circ.84$  are, however, clearly contaminated by 2E 1742.9–2929 at  $(l, b) = (-0^\circ.44, -0^\circ.38)$  and the Great Annihilator at  $(l, b) = (-0^\circ.89, -0^\circ.10)$  even though the bright regions around them were excluded from the spectra. Thus we did not use the profiles of  $l = -0^\circ.56$  and  $-0^\circ.84$  for the fittings. We point out that the spectra of these bright sources show no Fe K $\alpha$  lines [62, 109], so the profiles of the Fe K $\alpha$  lines are not affected by them. For the fittings, three data points of  $b_* < 0^\circ.2$  in the profile at  $l = 0^\circ.17$  and those of  $b = 0^\circ.054 - 0^\circ.154$  in the profile of  $l = 0^\circ.82$  were also excluded because they were contaminated by the local structures around the Sgr A region. The best-fit model is shown in figure 4.16. The best fit parameters are shown in table 4.10 and summarized in figure 4.17.

### 4.2.3 Two-Dimensional Model for the Intensity Profile

The relations between  $l_*$  and  $A_{b1}$  or  $A_{b2}$  (the red and green data points in figure 4.12, 4.14 and 4.17) match the profiles of the  $A_{l1}$ - and  $A_{l2}$ -components (the cyan and orange lines in figure 4.4 and 4.6) though we fitted the two-component models to the intensity profiles along the galactic longitude and latitude, independently. It indicates that the two-dimensional intensity distribution can be modeled well with the next function;

$$I(l, b) = A_1 \times \exp\left(-\frac{l_*}{h_{l1}}\right) \times \exp\left(-\frac{b_*}{h_{b1}}\right) + A_2 \times \exp\left(-\frac{l_*}{h_{l2}}\right) \times \exp\left(-\frac{b_*}{h_{b2}}\right) \quad (4.2)$$

We fitted the two-dimensional model to the intensity profiles of the highly ionized Fe K $\alpha$  line and the 5–10 keV band, respectively. The profiles along the galactic longitude and latitude

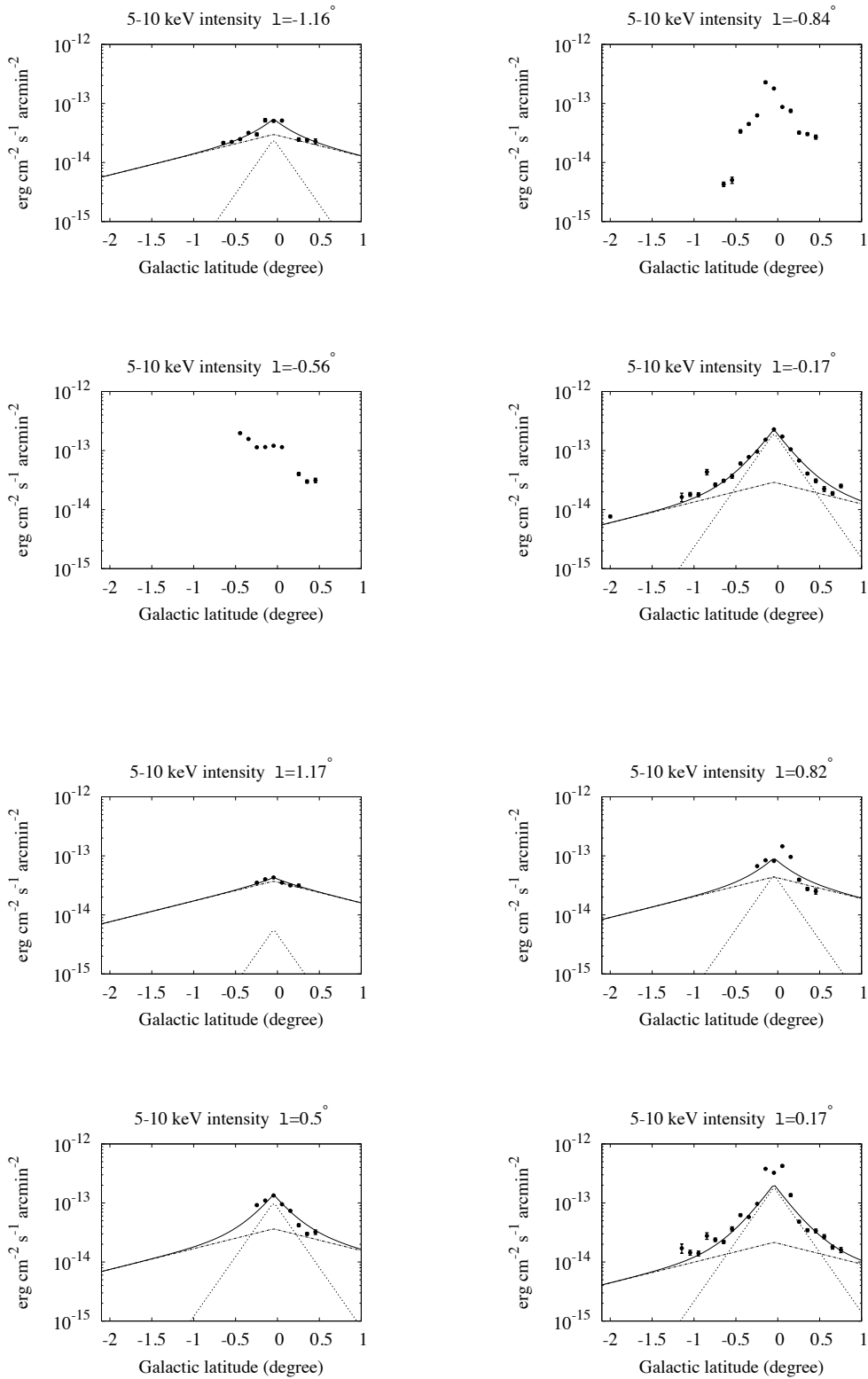


Figure 4.16: Intensity profiles in the 5–10 keV band along the galactic latitude. The error bars show the  $1\sigma$  errors. The solid lines show the best-fit two-component models. The dashed and alternate-long-and-short-dash lines show the components with scale heights,  $h_{b1}$  and  $h_{b2}$  respectively.

Table 4.10: Best-fit parameters of the two-component model to the intensity profiles in the 5–10 keV band along the galactic latitude.\*

$l$ (degree)	$A_{b1}(10^{-13})^\dagger$	$A_{b2}(10^{-13})^\dagger$	$l$ (degree)	$A_{b1}(10^{-13})^\dagger$	$A_{b2}(10^{-13})^\dagger$
-0.17	$1.99 \pm 0.15$	$0.29 \pm 0.16$	0.17	$1.85 \pm 0.21$	$0.22 \pm 0.11$
-0.56	–	–	0.50	$1.03 \pm 0.17$	$0.36 \pm 0.15$
-0.84	–	–	0.82	$0.48 \pm 0.16$	$0.44 \pm 0.13$
-1.16	$0.25 \pm 0.12$	$0.30 \pm 0.08$	1.17	$0.06(< 0.19)$	$0.37 \pm 0.10$
$h_{b1}$ (degree)			$h_{b2}$ (degree)		
$0.21 \pm 0.03$			$1.2 \pm 0.5$		

<sup>†</sup> The uncertainties show the  $1\sigma$  errors. \*The unit is  $\text{ergs s}^{-1} \text{cm}^{-2} \text{arcmin}^{-2}$ .

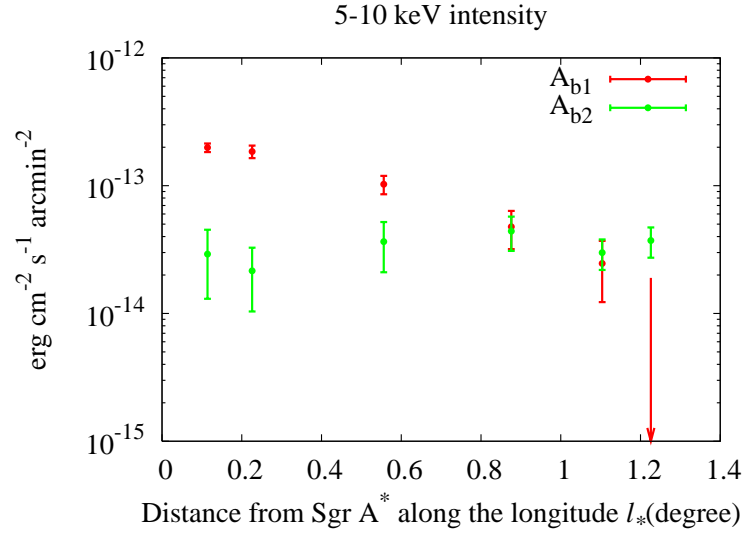


Figure 4.17: Relations among  $l_*$ ,  $A_{b1}$  and  $A_{b2}$  of the 5–10 keV intensity profiles. The error bars show the  $1\sigma$  errors.

Table 4.11: Best-fit parameters of the two-dimensional model shown in equation 4.2.\*

	$A_1^\dagger$	$A_2^\dagger$	$h_{l1}$ (degree)	$h_{b1}$ (degree)	$h_{l2}$ (degree)	$h_{b2}$ (degree)
Fe XXV $K\alpha$	$26.3 \pm 0.9$	$1.6 \pm 0.2$	$0.47 \pm 0.02$	$0.22 \pm 0.01$	$30 \pm 10$	$1.7 \pm 0.7$
Fe XXVI $K\alpha$	$10.0 \pm 0.3$	$0.25 \pm 0.07$	$0.51 \pm 0.02$	$0.22 \pm 0.01$	$47(< 102)$	$17(< 95)$
5–10 keV intensity	$3.4 \pm 0.2$	$0.20 \pm 0.04$	$0.48 \pm 0.04$	$0.19 \pm 0.02$	$55(< 133)$	$2.5 \pm 1.7$

\* The uncertainties show the  $1\sigma$  errors.  $\dagger$  The units are  $10^{-7}$  photons  $s^{-1}$   $cm^{-2}$   $arcmin^{-2}$  for the Fe XXV  $K\alpha$  and Fe XXVI  $K\alpha$  lines, and  $10^{-13}$  erg  $s^{-1}$   $cm^{-2}$   $arcmin^{-2}$  for the 5–10 keV intensity.

were fitted simultaneously. We did not use the data points in the 5–10 keV intensity profile at  $l = -0^\circ.56$  and  $-0^\circ.84$ , and  $l = -0^\circ.96 \sim -0^\circ.75$  because they are contaminated by bright sources. The fitting results show in figure 4.18 – 4.21. The best-fit parameters are summarized in table 4.11.

### 4.3 Detailed Spectral Analysis

We merged the spectra of the regions shown in figure 4.22 to increase statistics. New spectra 1–5 and A–G were shown in figure 4.23 and 4.24. We called the regions 1–5 and A–G as "on-plane" and "off-plane" data, respectively. The weighted averages of the RMFs were made using the counts of the spectra as weights. The ARFs were summed. The central region of  $l_* < 0^\circ.3$  has been studied well with the Suzaku data by Koyama et al. [51, 55] and thus we did not analyze this region. In the discussion (chapter 7), their results will be referred. We fitted the following phenomenological model to the merged spectra according to Koyama et al. [51];

$$Abs1 \times (PL1 + 10 \text{ Gaussians}) + Abs2 \times CXB. \quad (4.3)$$

Compared with the previous model (equation 4.1), weak lines were added, and the center energies and widths of the Fe  $K\alpha$  lines were free. The center energies and intensities of the weak lines were constrained according to APEC model [119].  $CXB$  is a power-law model as the  $CXB$  and the normalization and  $\Gamma$  were fixed as described in section 4.1.4.  $Abs2$  was fixed to be  $N_H = 1.2 \times 10^{23}$   $cm^{-2}$ . The emission lines in this model are summarized in table 4.12.

The best-fit models are shown in figure 4.23 and 4.24. The best-fit parameters are described in table 4.13 and 4.14. The profiles of the line intensity ratio of Fe XXVI  $K\alpha$  to Fe XXV  $K\alpha$  along the galactic longitude and latitude are shown in figure 4.25. The result of  $b = -2^\circ$  is also added. As described in section A, the line intensity profile ratio corresponds to the temperature of the plasma. Corresponding temperatures were calculated according to APEC code. The results are shown in figure 4.25. The ratio decrease along with  $l_*$  significantly. On the other hand, the ratio does not change along the galactic latitude over  $b_* = 0^\circ \sim -2^\circ$  significantly. The profiles of the center energies of the three Fe  $K\alpha$  lines are shown in figure 4.26. The center energy of Fe XXV  $K\alpha$  seems to get smaller along with  $l_*$ . The profiles of the equivalent widths (EWs) of the three Fe  $K\alpha$  lines are shown in figure 4.27. The EW of the Fe XXV  $K\alpha$  line seem to increase along with  $l_*$ . On the other hand, the EW of the Fe I  $K\alpha$  line decrease along with  $l_*$ . Further discussion using these parameters are made in chapter 7.

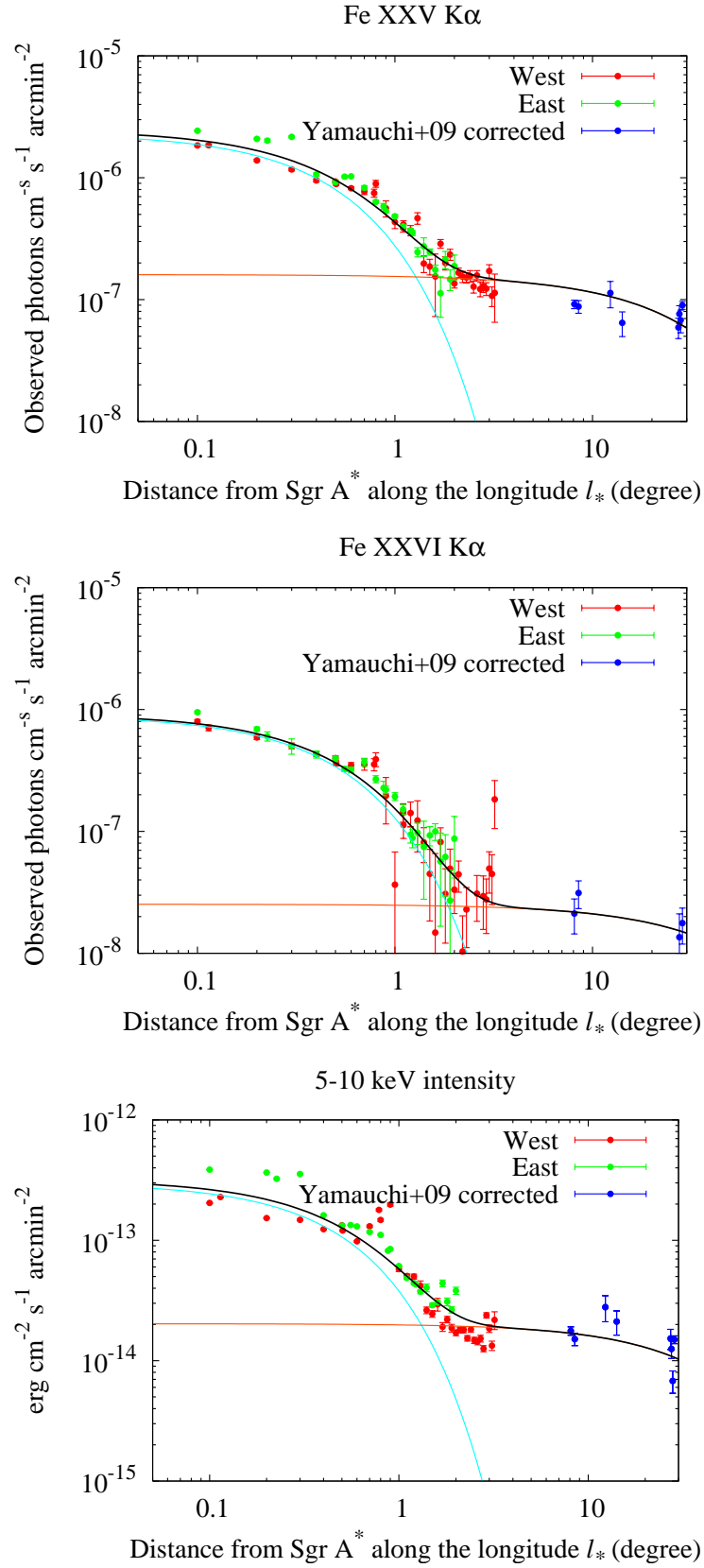


Figure 4.18: Same as figure 4.4 and 4.6 but with the best-fit two-dimensional model shown in equation 4.2. Top: Fe XXV K $\alpha$  line. Middle: Fe XXVI K $\alpha$  line. Bottom: 5–10 keV intensity. The error bars show the  $1\sigma$  errors. The black lines show the best-fit two dimensional models. The cyan and orange lines show the components with  $A_1$  and  $A_2$  respectively.

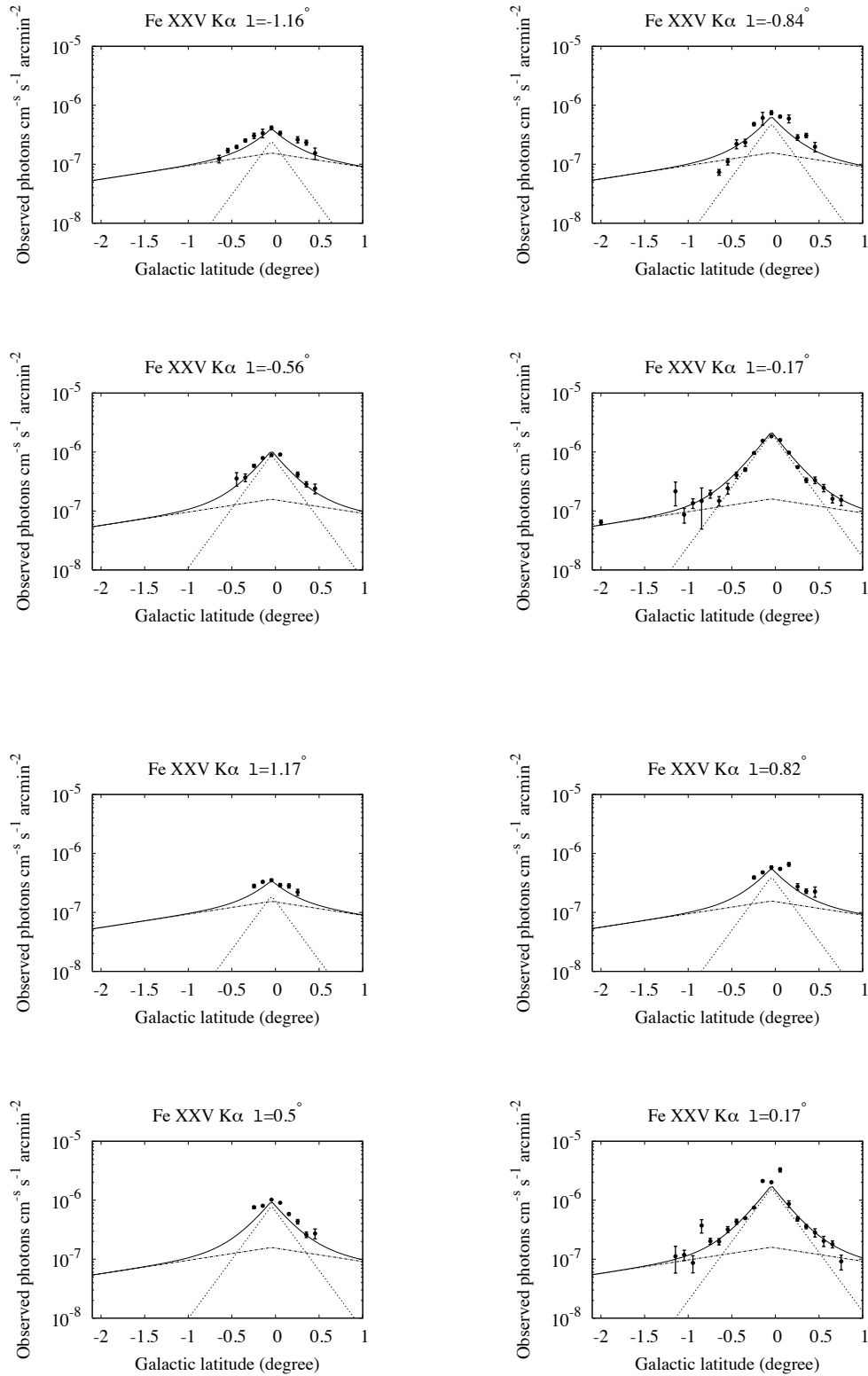


Figure 4.19: Same as figure 4.9 but with the best-fit two-dimensional model shown in equation 4.2. The error bars show the  $1\sigma$  errors. The solid lines show the best-fit two-component models. The dashed and alternate-long-and-short-dash lines show the components with  $A_1$  and  $A_2$  respectively.

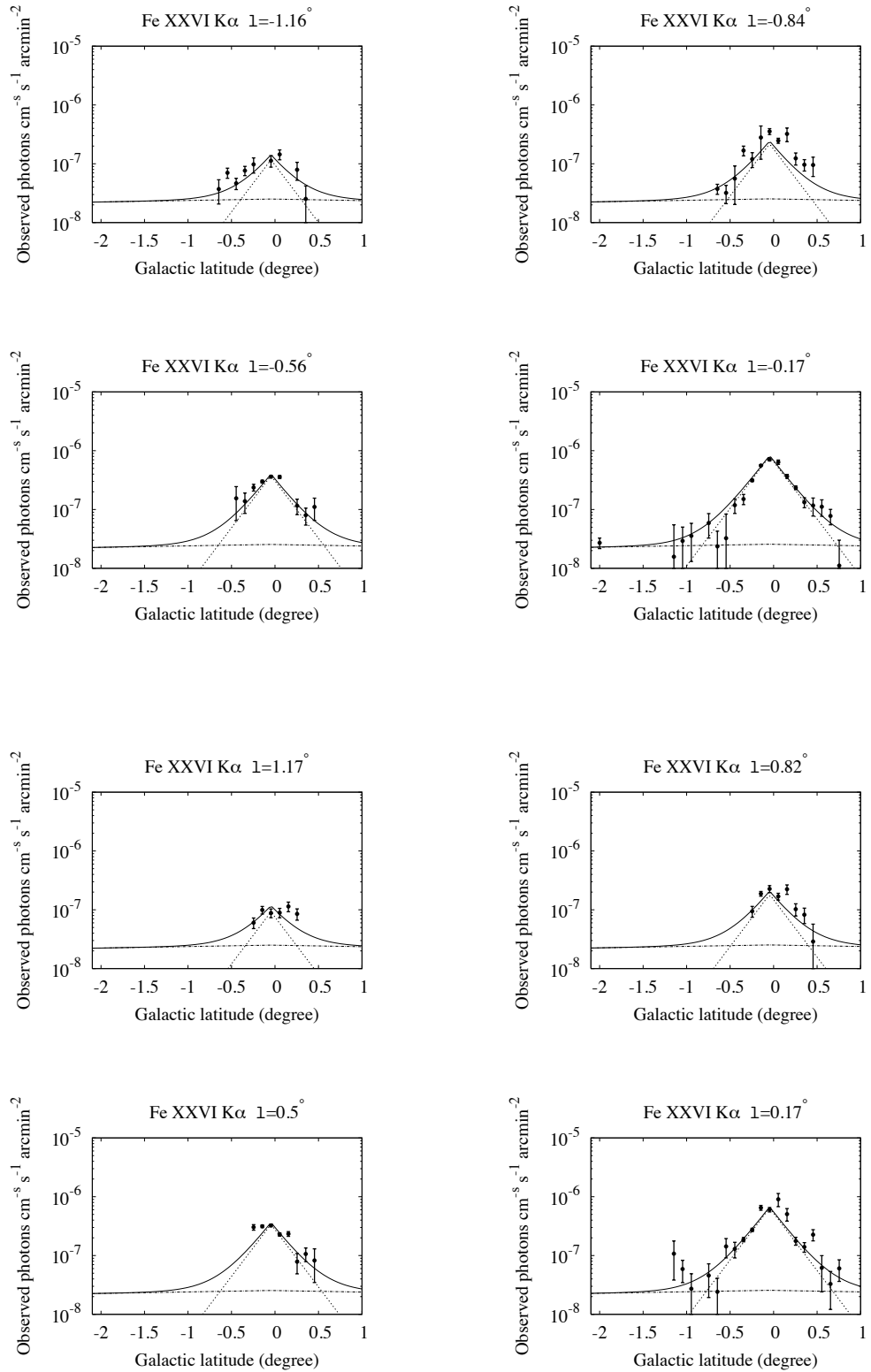


Figure 4.20: Same as figure 4.13 but with the best-fit two-dimensional model shown in equation 4.2. The error bars show the  $1\sigma$  errors. The solid lines show the best-fit two-component models. The dashed and alternate-long-and-short-dash lines show the components with  $A_1$  and  $A_2$  respectively.

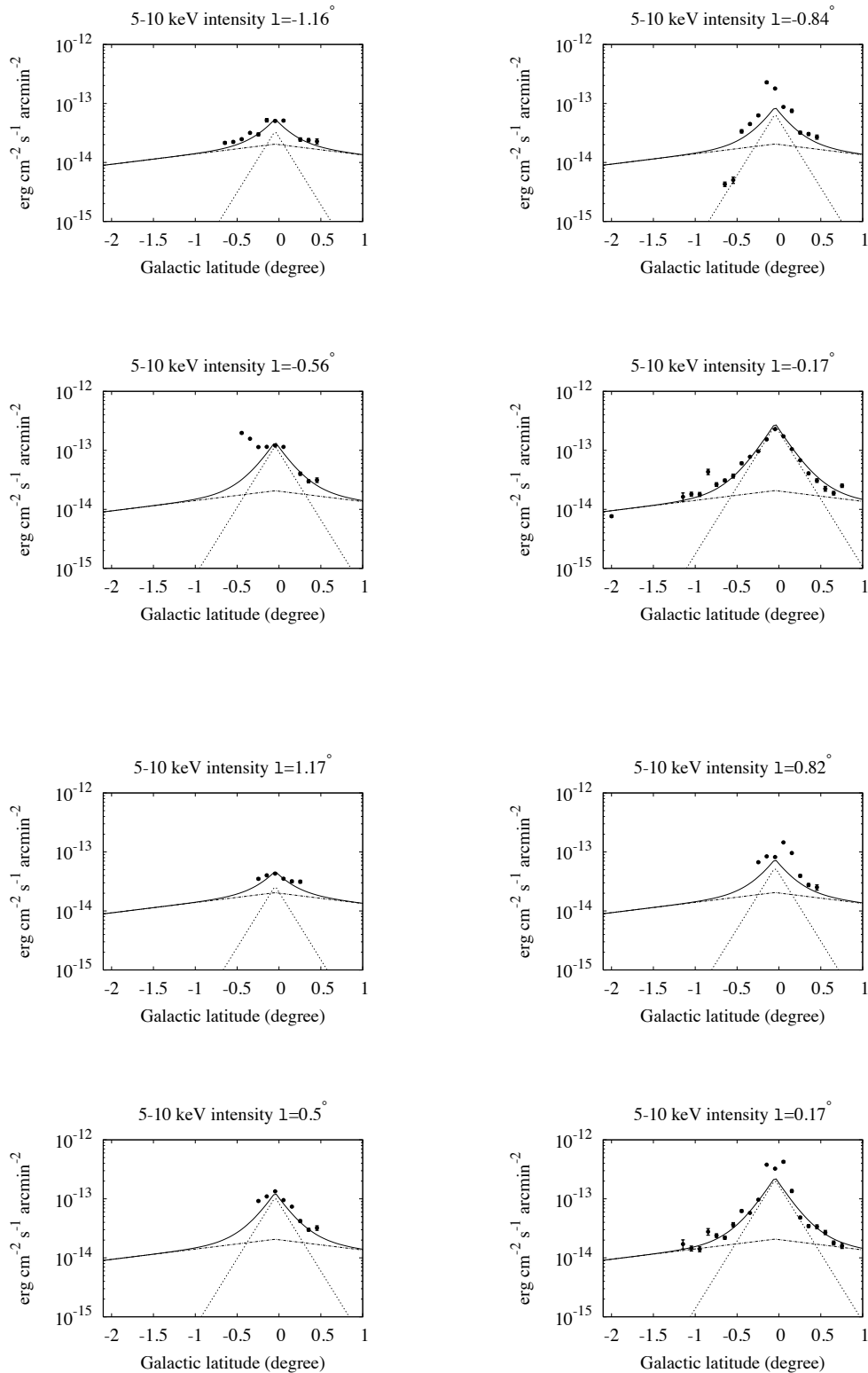


Figure 4.21: Same as figure 4.16 but with the best-fit two-dimensional model shown in equation 4.2. The error bars show the  $1\sigma$  errors. The solid lines show the best-fit two-component models. The dashed and alternate-long-and-short-dash lines show the components with  $A_1$  and  $A_2$  respectively.

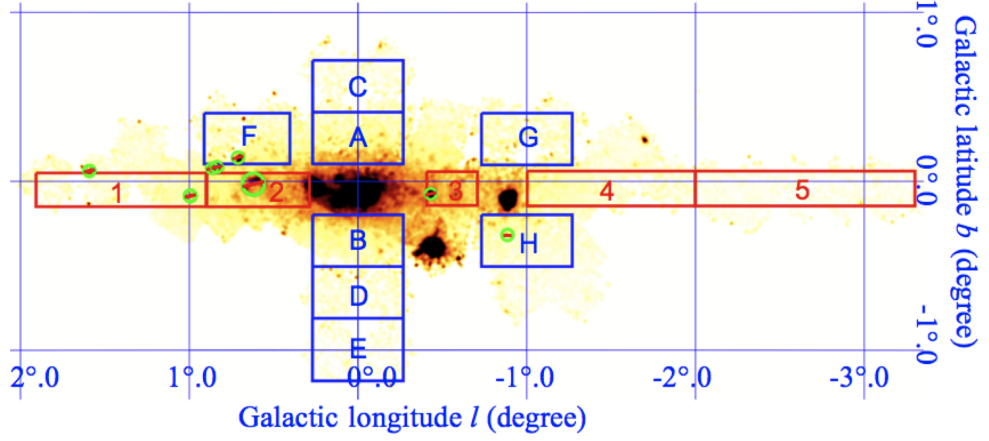


Figure 4.22: Regions where spectra were merged. They are overlaid on the X-ray image in the 6.55-6.8 keV band.

Table 4.12: Emission lines included in the phenomenological model (equation 4.3).

Line	Line center		Width $\sigma$ (eV)	Intensity
	Theoretical value* (eV)	Constraint		
Fe I $K\alpha$	6400	free	free	free
Fe XXV $K\alpha$	6680	free	free	free
Fe XXVI $K\alpha$	6966	free	free	free
Fe I $K\beta$	7059	$[\text{Fe I } K\alpha] \times 1.103$	0 (fixed)	$[\text{Fe I } K\alpha] \times 0.125^\dagger$
Ni I $K\alpha$	7475	$[\text{Fe I } K\alpha] \times 1.168$	0 (fixed)	free
Ni XXVII $K\alpha$	7821	free	0 (fixed)	free
Fe XXV $K\beta$	7881	$[\text{Ni XXVII } K\alpha] + 60$	0 (fixed)	free
Fe XXVI $K\beta$	8251	free	0 (fixed)	free
Fe XXV $K\gamma$	8295	$[\text{Fe XXVII } K\beta] + 44$	0 (fixed)	free
Fe XXVI $K\gamma$	8700	$[\text{Fe XXVII } K\beta] + 449$	0 (fixed)	free

\* We referred to the APEC model [119] for ionized lines and for neutral lines [40].

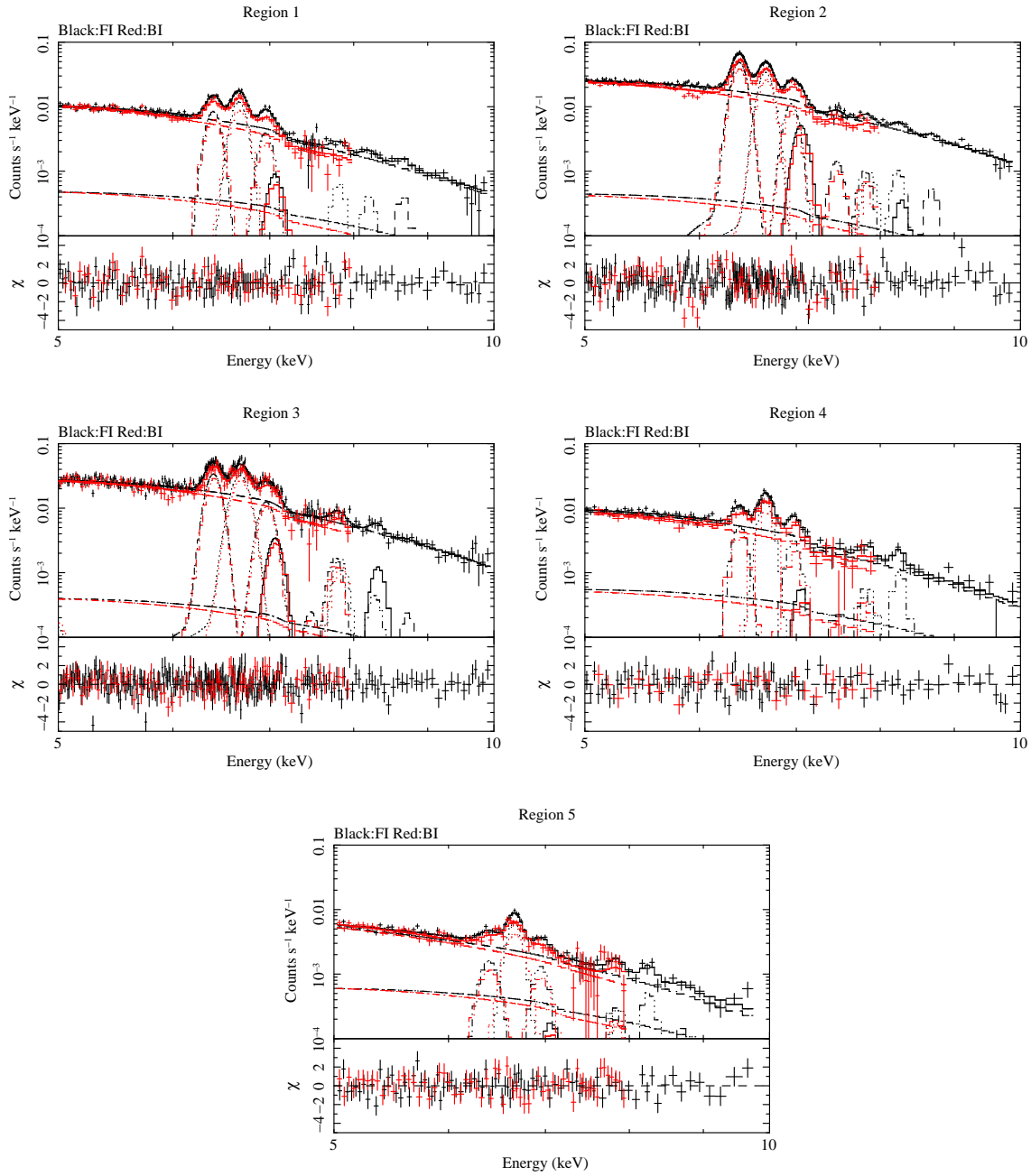


Figure 4.23: On-plane merged spectra. The vertical error bars show the  $1\sigma$  errors. The best-fit results of the phenomenological model are also shown. Black: the FIs spectra. Red: the BI spectra.

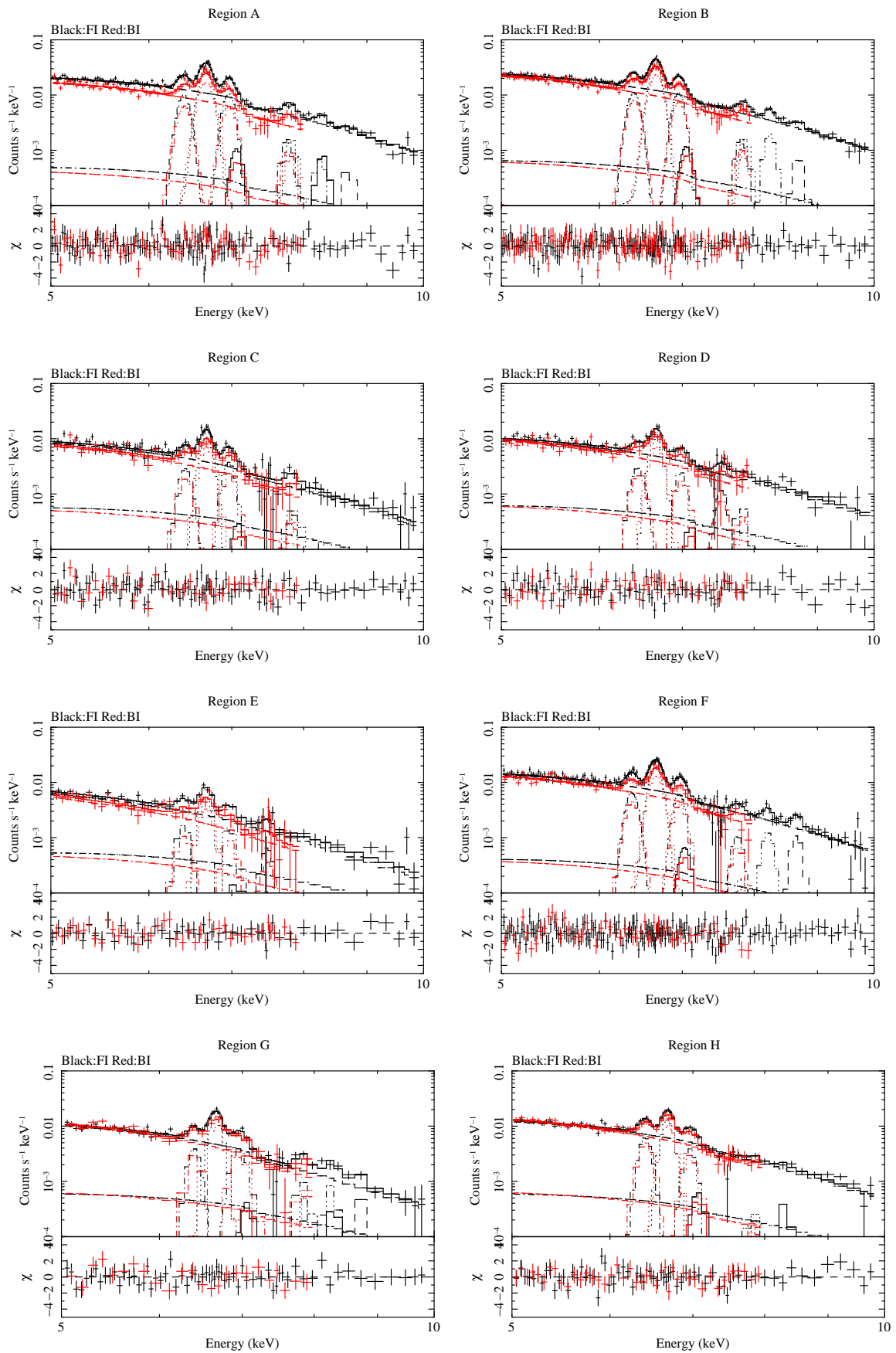


Figure 4.24: Off-plane merged spectra. The vertical error bars show the  $1\sigma$  errors. The best-fit results of the phenomenological model are also shown. Black: the FIs spectra. Red: the BI spectra.

Table 4.13: Best-fit parameters of the phenomenological model to the spectra in 5–10 keV band of the on-plane data.\*

Region	1	2	3	4	5
Fe I K $\alpha$					
Energy (eV)	6404 $^{+5}_{-3}$	6396 $^{+2}_{-1}$	6404 $^{+7}_{-2}$	6400 $^{+10}_{-10}$	6404 $^{+21}_{-20}$
Width (eV)	< 22	< 7	< 21	< 34	< 65
Intensity $^{\dagger}$ ( $10^{-7}$ )	2.78 $^{+0.18}_{-0.12}$	17.9 $^{+0.4}_{-0.3}$	14.1 $^{+1.0}_{-0.6}$	1.58 $^{+0.19}_{-0.20}$	0.39 $^{+0.12}_{-0.05}$
EW (eV)	235 $\pm$ 13	494 $\pm$ 9	341 $\pm$ 19	168 $\pm$ 20	123 $\pm$ 26
Fe XXV K $\alpha$					
Energy (eV)	6668 $^{+4}_{-2}$	6671 $^{+2}_{-2}$	6684 $^{+6}_{-5}$	6670 $^{+5}_{-4}$	6664 $^{+6}_{-4}$
Width (eV)	26 $^{+7}_{-12}$	20 $^{+5}_{-8}$	51 $^{+7}_{-10}$	< 32	< 24
Intensity $^{\dagger}$ ( $10^{-7}$ )	4.39 $^{+0.15}_{-0.20}$	13.8 $^{+0.3}_{-0.4}$	17.8 $^{+0.7}_{-1.3}$	3.93 $^{+0.22}_{-0.27}$	1.44 $^{+0.07}_{-0.10}$
EW (eV)	415 $\pm$ 16	419 $\pm$ 9	474 $\pm$ 23	475 $\pm$ 29	504 $\pm$ 28
Fe XXVI K $\alpha$					
Energy (eV)	6959 $^{+2}_{-11}$	6950 $^{+8}_{-3}$	6966 $^{+17}_{-7}$	6970 $^{+18}_{-10}$	6952 $^{+17}_{-22}$
Width (eV)	< 21	< 12	< 55	< 33	< 44
Intensity $^{\dagger}$ ( $10^{-7}$ )	1.45 $^{+0.15}_{-0.12}$	4.67 $^{+0.27}_{-0.25}$	6.72 $^{+1.74}_{-0.48}$	1.06 $^{+0.18}_{-0.18}$	0.35 $^{+0.07}_{-0.07}$
EW (eV)	154 $\pm$ 14	157 $\pm$ 8	197 $\pm$ 28	147 $\pm$ 25	134 $\pm$ 26
Ni I K $\alpha$					
Intensity $^{\dagger}$ ( $10^{-7}$ )	< 0.13	0.95 $^{+0.51}_{-0.28}$	< 1.27	< 0.54	< 0.10
Ni XXVII K $\alpha$					
Energy (eV)	7756 $^{+45}_{-156}$	7790 $^{+35}_{-190}$	7776 $^{+33}_{-176}$	7803 $^{+39}_{-59}$	7811 $^{+25}_{-211}$
Intensity $^{\dagger}$ ( $10^{-7}$ )	< 0.17	0.77 $^{+0.26}_{-0.25}$	1.50 $^{+0.69}_{-0.62}$	0.36 $^{+0.21}_{-0.25}$	0.13 $^{+0.10}_{-0.06}$
Fe XXV K $\beta$					
Intensity $^{\dagger}$ ( $10^{-7}$ )	0.43 $^{+0.15}_{-0.19}$	0.79 $^{+0.18}_{-0.49}$	1.50 $^{+0.53}_{-1.18}$	0.36 $^{+0.24}_{-0.30}$	0.13 $^{+0.08}_{-0.11}$
Fe XXVI K $\beta$					
Energy (eV)	8203 $^{+199}_{-60}$	8251 $^{+30}_{-31}$	8275 $^{+181}_{-79}$	8251 $^{+25}_{-68}$	8255 $^{+186}_{-55}$
Intensity $^{\dagger}$ ( $10^{-7}$ )	0.34 $^{+0.21}_{-0.19}$	0.95 $^{+0.43}_{-0.32}$	< 1.41	0.77 $^{+0.28}_{-0.41}$	0.28 $^{+0.11}_{-0.14}$
Fe XXV K $\gamma$					
Intensity $^{\dagger}$ ( $10^{-7}$ )	< 0.24	0.34 $^{+0.51}_{-0.26}$	1.42 $^{+0.69}_{-1.17}$	< 0.23	< 0.09
Fe XXVI K $\gamma$					
Intensity $^{\dagger}$ ( $10^{-7}$ )	0.41 $^{+0.15}_{-0.28}$	0.63 $^{+0.37}_{-0.37}$	< 1.51	< 0.27	< 0.22
$\Gamma$	2.66 $^{+0.02}_{-0.03}$	2.33 $^{+0.01}_{-0.01}$	2.31 $^{+0.03}_{-0.02}$	3.10 $^{+0.03}_{-0.05}$	2.46 $^{+0.04}_{-0.04}$
Normalization $^{\S}$ ( $10^{-4}$ )	1.64 $^{+0.02}_{-0.02}$	2.72 $^{+0.02}_{-0.02}$	3.03 $^{+0.05}_{-0.05}$	2.97 $^{+0.08}_{-0.06}$	0.31 $^{+0.01}_{-0.01}$
$N_{\text{H}}$ ( $10^{22}$ cm $^{-2}$ )	18 $^{+1}_{-1}$	19 $^{+1}_{-1}$	18 $^{+1}_{-2}$	22 $^{+2}_{-2}$	4 $^{+2}_{-2}$
Intensity $^{\#}$ ( $10^{-14}$ )	4.3	13.9	16.1	3.1	1.6
$\chi^2/d.o.f.$	219/179	395/248	365/322	139/106	150/132

\* The uncertainties show the 90 % confidence level.  $^{\dagger}$  The unit is photons s $^{-1}$  cm $^{-2}$  arcmin $^{-2}$ . The interstellar absorption is corrected.  $^{\S}$  The unit is photons s $^{-1}$  cm $^{-2}$  arcmin $^{-2}$  keV $^{-1}$  at 1 keV.  $^{\#}$  The unit is ergs s $^{-1}$  cm $^{-2}$  arcmin $^{-2}$  in the 5–10 keV band. The interstellar absorption is not corrected.

Table 4.14: Best-fit parameters of the phenomenological model to the spectra in 5–10 keV band of the off-plane data.\*

Region	A	B	C	D	E	F	G	H
Fe I K $\alpha$								
Energy (eV)	6407 <sup>+11</sup> <sub>-7</sub>	6398 <sup>+7</sup> <sub>-5</sub>	6425 <sup>+22</sup> <sub>-21</sub>	6426 <sup>+32</sup> <sub>-24</sub>	6402 <sup>+44</sup> <sub>-102</sub>	6378 <sup>+9</sup> <sub>-10</sub>	6404 <sup>+19</sup> <sub>-104</sub>	6408 <sup>+192</sup> <sub>-8</sub>
Width (eV)	< 26	< 31	< 66	< 68	< 96	< 28	< 49	< 33
Intensity <sup>†</sup> (10 <sup>-7</sup> )	3.17 <sup>+0.44</sup> <sub>-0.24</sub>	2.45 <sup>+0.20</sup> <sub>-0.17</sub>	0.77 <sup>+0.20</sup> <sub>-0.26</sub>	0.75 <sup>+0.26</sup> <sub>-0.21</sub>	0.40 <sup>+0.26</sup> <sub>-0.15</sub>	2.27 <sup>+0.30</sup> <sub>-0.30</sub>	1.02 <sup>+0.26</sup> <sub>-0.23</sub>	1.57 <sup>+0.21</sup> <sub>-0.20</sub>
EW (eV)	138 ± 14	135 ± 10	112 ± 33	101 ± 31	98 ± 37	130 ± 17	119 ± 28	150 ± 21
Fe XXV K $\alpha$								
Energy(eV)	6673 <sup>+5</sup> <sub>-2</sub>	6665 <sup>+3</sup> <sub>-1</sub>	6679 <sup>+9</sup> <sub>-7</sub>	6670 <sup>+9</sup> <sub>-9</sub>	6675 <sup>+13</sup> <sub>-13</sub>	6668 <sup>+7</sup> <sub>-3</sub>	6667 <sup>+9</sup> <sub>-5</sub>	6680 <sup>+4</sup> <sub>-5</sub>
Width (eV)	33 <sup>+7</sup> <sub>-8</sub>	25 <sup>+6</sup> <sub>-7</sub>	< 33	< 35	< 44	26 <sup>+12</sup> <sub>-11</sub>	37 <sup>+10</sup> <sub>-20</sub>	< 23
Intensity <sup>†</sup> (10 <sup>-7</sup> )	9.90 <sup>+0.39</sup> <sub>-0.44</sub>	8.03 <sup>+0.25</sup> <sub>-0.23</sub>	3.04 <sup>+0.26</sup> <sub>-0.31</sub>	2.49 <sup>+0.31</sup> <sub>-0.23</sub>	1.42 <sup>+0.19</sup> <sub>-0.21</sub>	7.51 <sup>+0.41</sup> <sub>-0.39</sub>	4.21 <sup>+0.38</sup> <sub>-0.34</sub>	3.48 <sup>+0.26</sup> <sub>-0.22</sub>
EW (eV)	477 ± 20	492 ± 15	494 ± 49	370 ± 43	392 ± 77	482 ± 28	560 ± 51	374 ± 31
Fe XXVI K $\alpha$								
Energy (eV)	6966 <sup>+5</sup> <sub>-9</sub>	6957 <sup>+4</sup> <sub>-7</sub>	6966 <sup>+17</sup> <sub>-22</sub>	6985 <sup>+23</sup> <sub>-35</sub>	6967 <sup>+37</sup> <sub>-36</sub>	6967 <sup>+12</sup> <sub>-10</sub>	6964 <sup>+26</sup> <sub>-18</sub>	6962 <sup>+16</sup> <sub>-15</sub>
Width (eV)	< 23	< 15	< 63	< 62	< 80	< 34	58 <sup>+29</sup> <sub>-33</sub>	< 37
Intensity <sup>†</sup> (10 <sup>-7</sup> )	3.80 <sup>+0.35</sup> <sub>-0.30</sub>	2.73 <sup>+0.20</sup> <sub>-0.18</sub>	1.16 <sup>+0.26</sup> <sub>-0.21</sub>	0.69 <sup>+0.22</sup> <sub>-0.19</sub>	0.44 <sup>+0.18</sup> <sub>-0.16</sub>	2.51 <sup>+0.31</sup> <sub>-0.32</sub>	1.52 <sup>+0.39</sup> <sub>-0.32</sub>	1.14 <sup>+0.22</sup> <sub>-0.18</sub>
EW (eV)	204 ± 17	187 ± 13	215 ± 43	116 ± 35	139 ± 56	180 ± 22	234 ± 55	137 ± 24
Ni I K $\alpha$ <sup>#</sup>								
Intensity <sup>†</sup> (10 <sup>-7</sup> )	< 0.51	< 0.26	< 0.12	0.49 <sup>+0.43</sup> <sub>-0.23</sub>	< 0.48	< 0.16	< 0.26	< 0.13
Ni XXVII K $\alpha$								
Energy <sup>‡</sup> (eV)	7768 <sup>+35</sup> <sub>-168</sub>	7810 <sup>+40</sup> <sub>-210</sub>	7821 <sup>+23</sup> <sub>-221</sub>	7821(fixed)	7821(fixed)	7759 <sup>+51</sup> <sub>-159</sub>	7821(fixed)	7821(fixed)
Intensity <sup>†</sup> (10 <sup>-7</sup> )	1.03 <sup>+0.21</sup> <sub>-0.45</sub>	0.70 <sup>+0.14</sup> <sub>-0.24</sub>	0.30 <sup>+0.24</sup> <sub>-0.22</sub>	0.29 <sup>+0.20</sup> <sub>-0.27</sub>	0.29 <sup>+0.34</sup> <sub>-0.20</sub>	0.75 <sup>+0.39</sup> <sub>-0.34</sub>	0.57 <sup>+0.38</sup> <sub>-0.40</sub>	0.13 <sup>+0.21</sup> <sub>-0.13</sub>
Fe XXV K $\beta$								
Intensity <sup>†</sup> (10 <sup>-7</sup> )	1.03 <sup>+0.25</sup> <sub>-0.59</sub>	0.70 <sup>+0.22</sup> <sub>-0.27</sub>	< 0.52	< 0.34	< 0.21	< 0.53	< 0.78	< 0.42
Fe XXVI K $\beta$								
Energy <sup>‡</sup> (eV)	8248 <sup>+25</sup> <sub>-37</sub>	8242 <sup>+28</sup> <sub>-19</sub>	8254 <sup>+746</sup> <sub>-254</sub>	8251(fixed)	8251(fixed)	8209 <sup>+197</sup> <sub>-31</sub>	8251(fixed)	8251(fixed)
Intensity <sup>†</sup> (10 <sup>-7</sup> )	< 0.85	1.04 <sup>+0.24</sup> <sub>-0.30</sub>	< 0.45	< 0.35	< 0.31	1.11 <sup>+0.39</sup> <sub>-0.60</sub>	< 1.16	< 0.30
Fe XXV K $\gamma$								
Intensity <sup>†</sup> (10 <sup>-7</sup> )	0.67 <sup>+0.33</sup> <sub>-0.59</sub>	< 0.28	< 0.27	< 0.39	< 0.31	< 0.31	< 1.05	< 0.53
Fe XXVI K $\gamma$								
Intensity <sup>†</sup> (10 <sup>-7</sup> )	0.49 <sup>+0.50</sup> <sub>-0.42</sub>	0.54 <sup>+0.22</sup> <sub>-0.31</sub>	< 0.40	< 0.40	< 0.36	1.22 <sup>+0.44</sup> <sub>-0.54</sub>	0.49 <sup>+0.37</sup> <sub>-0.38</sub>	< 0.44
$\Gamma$	2.51 <sup>+0.03</sup> <sub>-0.02</sub>	2.59 <sup>+0.02</sup> <sub>-0.02</sub>	3.08 <sup>+0.06</sup> <sub>-0.32</sub>	2.63 <sup>+0.10</sup> <sub>-0.05</sub>	2.84 <sup>+0.38</sup> <sub>-0.33</sub>	2.54 <sup>+0.04</sup> <sub>-0.03</sub>	3.31 <sup>+0.27</sup> <sub>-0.04</sub>	2.67 <sup>+0.05</sup> <sub>-0.13</sub>
Normalization <sup>§</sup> (10 <sup>-4</sup> )	2.45 <sup>+0.03</sup> <sub>-0.04</sub>	2.20 <sup>+0.03</sup> <sub>-0.02</sub>	2.14 <sup>+0.07</sup> <sub>-0.07</sub>	0.99 <sup>+0.04</sup> <sub>-0.05</sub>	0.79 <sup>+0.17</sup> <sub>-0.03</sub>	1.95 <sup>+0.04</sup> <sub>-0.04</sub>	4.03 <sup>+1.27</sup> <sub>-1.24</sub>	1.49 <sup>+0.22</sup> <sub>-0.42</sub>
$N_{\text{H}}$ (10 <sup>22</sup> cm <sup>-2</sup> )	17 <sup>+1</sup> <sub>-1</sub>	14 <sup>+1</sup> <sub>-1</sub>	16 <sup>+3</sup> <sub>-4</sub>	13 <sup>+3</sup> <sub>-3</sub>	5 <sup>+4</sup> <sub>-5</sub>	14 <sup>+1</sup> <sub>-2</sub>	19 <sup>+3</sup> <sub>-3</sub>	15 <sup>+2</sup> <sub>-2</sub>
Intensity <sup>#</sup> (10 <sup>-14</sup> )	8.7	7.2	2.6	2.9	1.8	6.9	3.1	3.8
$\chi^2/d.o.f.$	220/166	245/226	138/111	132/104	66/76	212/188	72/69	86/92

\* The uncertainties show the 90 % confidence level. <sup>†</sup> The unit is photons s<sup>-1</sup> cm<sup>-2</sup> arcmin<sup>-2</sup>. The interstellar absorption is corrected. <sup>#</sup> The center energy of the Ni I K $\alpha$  line was free for the region D because it was relatively strong. The center energy is 7598<sup>+111</sup><sub>-58</sub> eV. <sup>‡</sup> The center energies of the Ni XXVII K $\alpha$  and Fe XXVI K $\beta$  lines were fixed for the region D, E, G and H because the statistics is poor. <sup>§</sup> The unit is photons s<sup>-1</sup> cm<sup>-2</sup> arcmin<sup>-2</sup> keV<sup>-1</sup> at 1 keV. <sup>#</sup> The unit is ergs s<sup>-1</sup> cm<sup>-2</sup> arcmin<sup>-2</sup> in the 5–10 keV band. The interstellar absorption is not corrected.

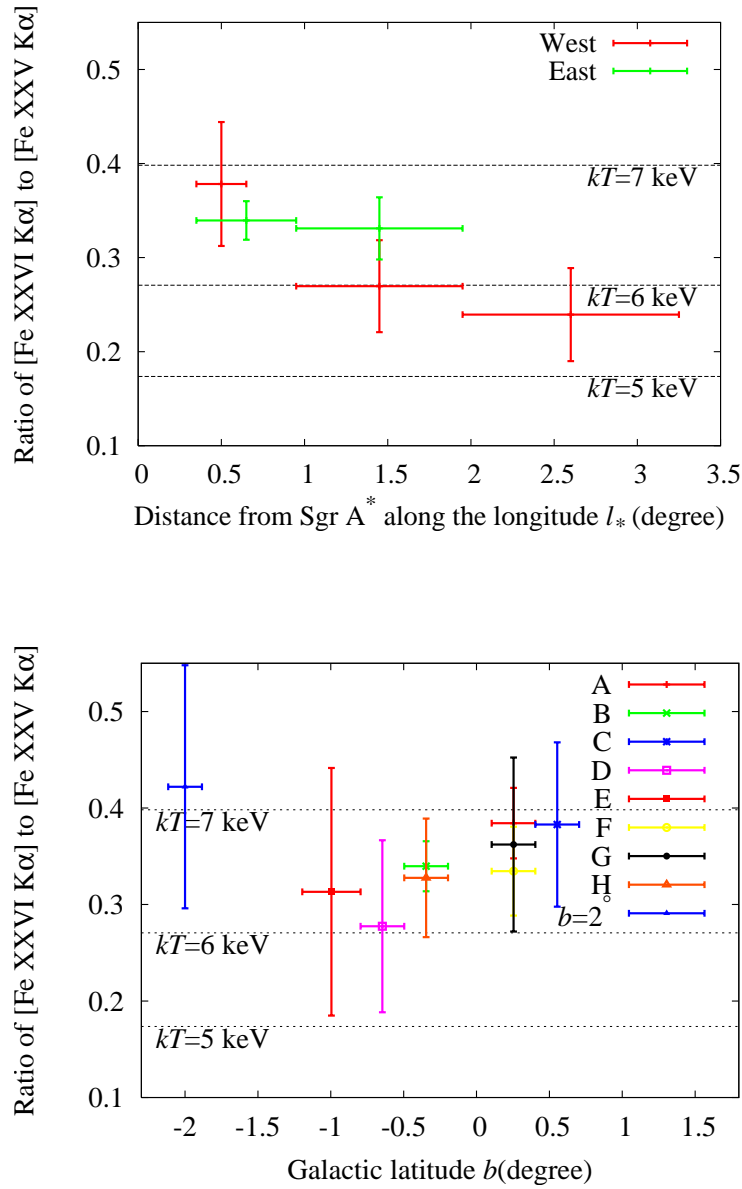


Figure 4.25: Profile of the line intensity ratio of Fe XXVI  $K\alpha$  to Fe XXV  $K\alpha$ . The error bars show the 90 % confidence level. Top: On-plane. Bottom: Off-plane.

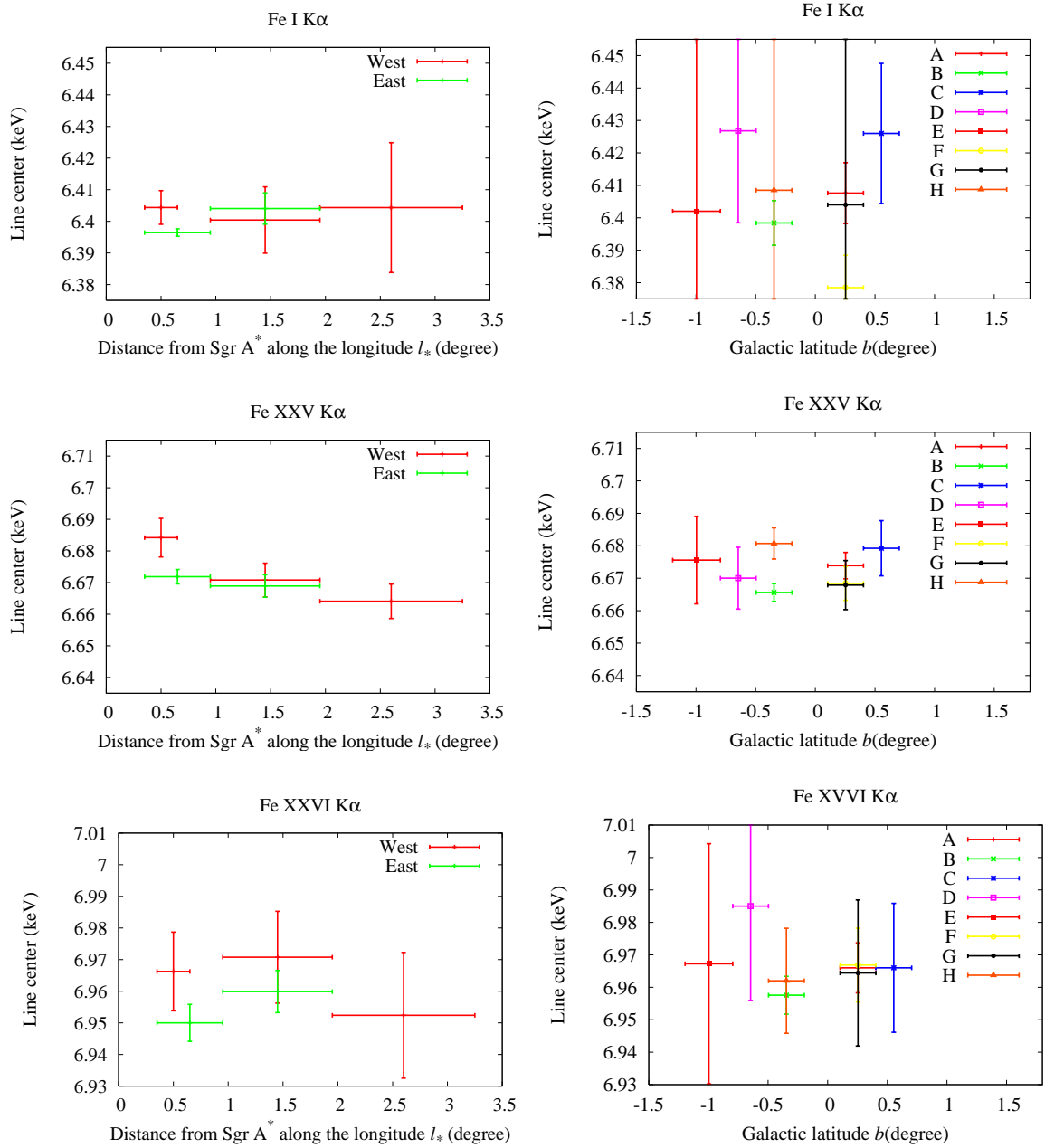


Figure 4.26: Profile of the center energies of the Fe K $\alpha$  lines. The error bars show the 90 % confidence level. Top: Fe I K $\alpha$ . Middle: Fe XXV K $\alpha$ . Bottom: Fe XXVI K $\alpha$ . Left: On-plane. Right: Off-plane.

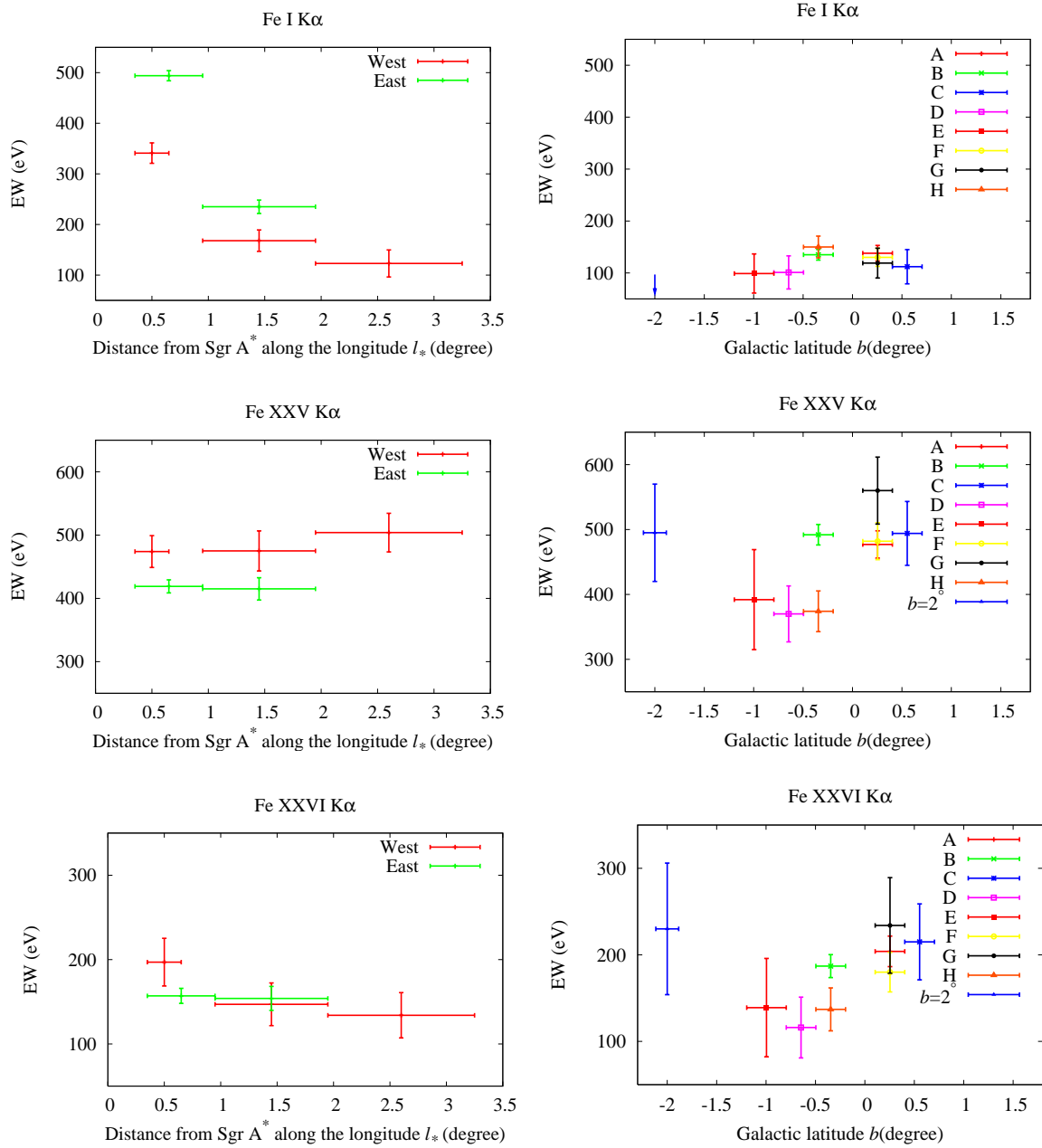


Figure 4.27: Profile of the equivalent widths of the Fe K $\alpha$  lines. The error bars show the 90 % confidence level. Top: Fe I K $\alpha$ . Middle: Fe XXV K $\alpha$ . Bottom: Fe XXVI K $\alpha$ . Left: On-plane. Right: Off-plane.

# Chapter 5

## Sgr A East

In this chapter, we show the result of the Suzaku observation of Sgr A East. As reviewed in section 2.6, previous observations [92, 112] suggest that this SNR have a peculiar hot component comparable to the GDXE. We took advantage of the high energy resolution of the Suzaku to decide the accurate temperature of Sgr A East without the uncertainty of the possible contamination of the non-thermal component. In section 5.1, we describe about the observations and the data reduction. In section 5.2, we show the result of the spectral analysis. In section 5.3, we make the short discussion on Sgr A East.

### 5.1 Observation & Data Reduction

Sgr A East was in the XIS field of view in four pointing observations on 2005 September 23–24 and 29–30 at the aim-points of  $(\alpha, \delta)_{2000} = (266^{\circ}.51, -28^{\circ}.93)$  and  $(266^{\circ}.30, -29^{\circ}.17)$ . The effective exposure time after removing the epoch of low Earth elevation angles less than 5 degrees, day Earth elevation angles less than 20 degrees, and the South Atlantic Anomaly was about 90–95 ksec.

The data were taken with the normal clocking full window mode. The SCI technique was not used because Sgr A East was observed almost just after the launch and the CTI was very small. A composite image that adds all of the XIS data is shown in figure 5.1. The bright spot near the corner of the XIS field of view is Sgr A East. We extracted data from a circle of  $1'.6$  radius, added all of the data from three FI CCDs and made a composite X-ray spectrum. The spectrum of the BI CCD was separately made. Baganoff et al. [3] reports a significant diffuse emission not only from the central region of the Sgr A East shell but also from the Sgr A West region located at the west in the shell. The diffuse emission from Sgr A West is not clear if it is a part of the Sgr A East SNR or the central black hole Sgr A\* or other origins. Due to the limited angular resolution of the Suzaku XRT (half power diameter  $\sim 2'$ ), we can not spatially resolve Sgr A West from Sgr A East. Therefore, the Sgr A East spectrum we refer to in this paper includes all of the diffuse emission inside the shell of the Sgr A East.

The non-X-ray background (NXB) is made from the night Earth data in the same detector area with the same data-selection criteria as those of Sgr A East. The largest background of Sgr A East is the GDXE, which emit the strong  $K\alpha$  lines from FeI, FeXXV and FeXXVI. Koyama et al. [50] reports that the flux ratio of the latter two lines along the Galactic plane (the constant  $b = -0^{\circ}.046$  line) across Sgr A East is almost constant in the  $l = 0^{\circ}.1$  to  $l = -0^{\circ}.4$  area. This means that the spectral shape of the GDXE is essentially the same near Sgr A East. The

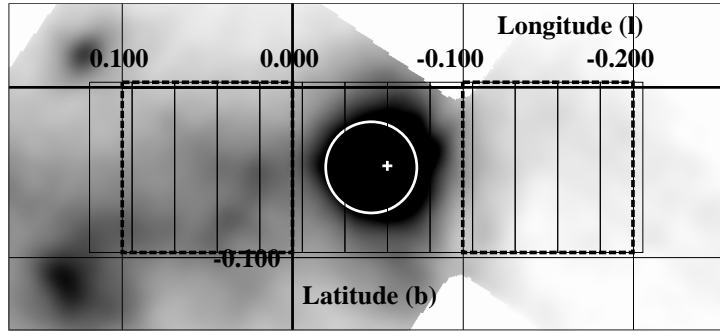


Figure 5.1: The XIS image near the Sgr A East region in the 2–8 keV band. The white circle of  $1'.6$  radius is the source region. The cross inside is the position of Sgr A\* (the Galactic center). The rectangles are the unit area extracting the fluxes of the GDXE and of point sources. The dotted squares indicate the GDXE background regions used for Sgr A East.

2–8 keV fluxes of the GDXE (small triangles in figure 5.2) are smooth near Sgr A East. We also note that Park et al.[91] shows the spatial distributions of Fe XXV  $K\alpha$  and Fe I  $K\alpha$  line emissions with arc-second resolution. The high resolution Chandra image supports that the GDXE emission is smoothly distributed across Sgr A East. We made the GDXE background taken from the regions shown by the dotted squares in figure 5.1, or by the solid bars in figure 5.2. This GCDX background was subtracted from the Sgr A East spectrum (in the  $1'.6$  radius region), where the vignetting was corrected.

The second-largest background is an ensemble of point sources. We simulated the point-source flux in the 2.0–8.0 keV band observed with XIS, putting the positions and fluxes (2.0–8.0 keV band) of the Chandra cataloged sources [78] in and around the 13 rectangles of figure 5.1. After convolving with the response of the XRT+XIS, we extracted the integrated point-source fluxes from each rectangle. The results are plotted along the Galactic plane (the constant  $b = -0^\circ.046$  line), as is shown in figure 5.2. The mean flux of the integrated point sources in this background regions (the regions shown by the solid bars in figure 5.2) is  $0.5 \times 10^{-5}$  photons  $\text{cm}^{-2} \text{ arcmin}^{-2} \text{ s}^{-1}$  (2–8 keV). This flux was already subtracted in the process of the GDXE subtraction. However the integrated point source flux in the source (Sgr A East) region (the  $1'.6$  radius region in figure 5.1) is  $3 \times 10^{-5}$  photons  $\text{cm}^{-2} \text{ arcmin}^{-2} \text{ s}^{-1}$  (2–8 keV) (see figure 2). Therefore, we further subtracted the excess flux of  $2.5 \times 10^{-5}$  photons  $\text{cm}^{-2} \text{ arcmin}^{-2} \text{ s}^{-1}$  (2–8 keV) from the source spectrum. In this subtraction, we assumed that the integrated point source spectrum is that obtained by Munro et al. [80].

## 5.2 Spectral Analysis

### 5.2.1 Emission Lines

The background (GDXE and point sources) subtracted spectra are shown in figures 5.3–5.5. We can see many emission lines. To study these lines, we fit the spectra with a phenomenological model: a thermal bremsstrahlung plus Gaussian lines with absorption edges of the main atoms. Fits for the low energy part (2–5 keV) and the high energy part (5–9 keV) were made separately. The best-fit models and parameters are given in figures 5.3 and 5.4, and in tables 5.1 and 5.2.

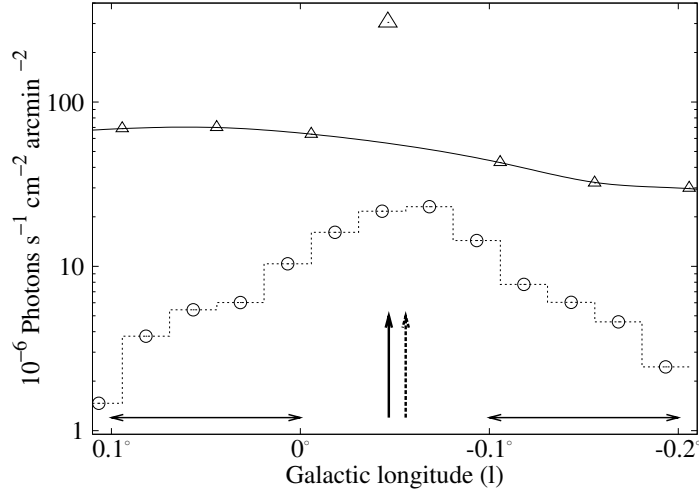


Figure 5.2: Surface brightness distributions of point sources in the 2–8 keV band (circles). The surface brightness in the 2–8 keV band of the GDX along the galactic plane ( $b = -0^\circ.046$ ) are given by small triangles, while that in the Sgr A East region ( $1'.6$  radius) is shown with the large triangle. The solid and dotted arrows show the positions of Sgr A East and Sgr A\* (the Galactic center), respectively. The solid bars indicate the regions of the GDXE backgrounds for Sgr A East.

The  $K\alpha$  lines from S XV, Ar XVII, Ca XIX and Fe XXV (helium-like atoms) have been reported by Sakano et al.[112] and Maeda et al.[63], and the presence of  $K\alpha$  lines from S XVI, Ar XVIII and Fe XXVI (hydrogenic atoms) have been suggested by Sakano et al.[112]. We clearly found these emission lines and newly detected a  $K\alpha$  line from Ni XXVII (helium-like nickel), as well as  $K\beta$  lines from SXV, Ar XVII and Fe XXV, and a  $K\gamma$  line from Fe XXV.

### 5.2.2 Sulfur Line Diagnostics

The  $K\alpha$  flux ratio of SXVI/SXV is  $0.20^{+0.03}_{-0.06}$  (in this chapter, all errors are 90% confidence intervals for one interesting parameter, unless otherwise described). This ratio indicates that the ionization temperature is  $1.1^{+0.1}_{-0.1}$  keV. The flux ratio of  $K\beta/K\alpha$  from SXV is  $0.08^{+0.02}_{-0.03}$ , which constrains the electron temperature to be  $1.4^{+0.7}_{-0.8}$  keV. Since the center energy of the  $K\alpha$  line from SXV decreases as decreasing plasma temperature by increasing contribution of the satellite lines, we can check the plasma temperature using the center energy. The plasma temperature determined from the line centroid is in the range of 0.2–0.6 keV. It seems a little lower than the temperature determined from the line ratio. However if we take into account the systematic error of the XIS gain ( $\sim \pm 5$  eV in this observation data), the allowable range becomes 0.2–2.0 keV, which is consistent with that determined from the line ratio. Therefore, from the emission line alone, we deduce that Sgr A East has at least a  $\sim 1$ -keV plasma in collisional ionization equilibrium (CIE).

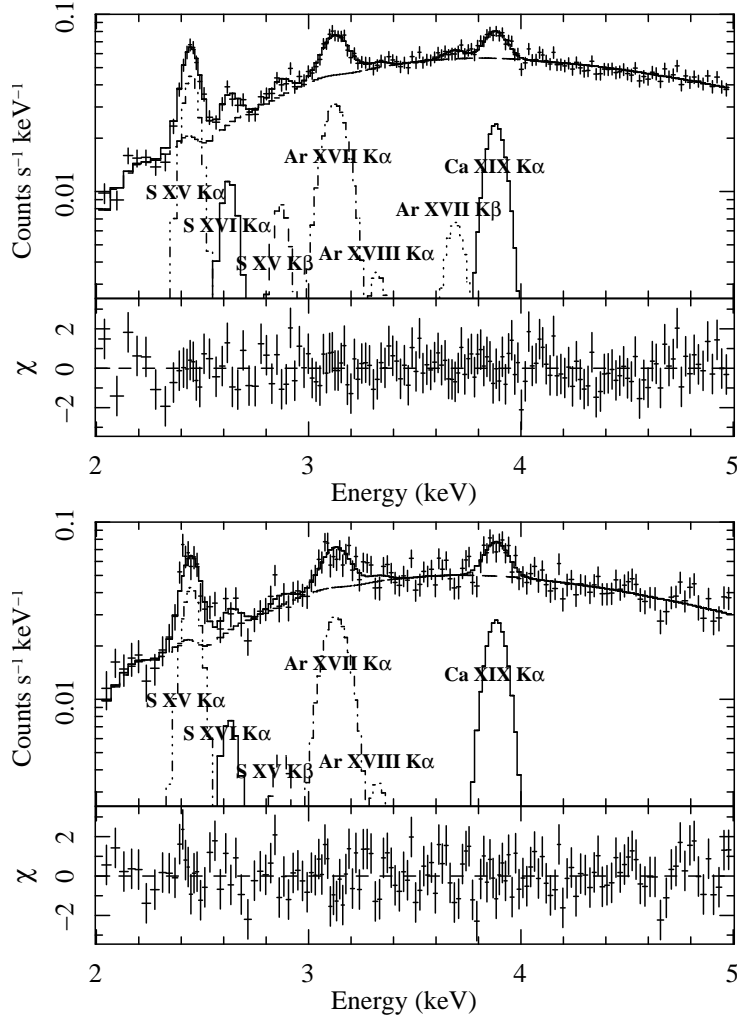


Figure 5.3: Top: X-ray spectrum of the sum of 3 FI CCDs with the best-fit phenomenological model in the 2.0–5.0 keV band. Bottom: same as the top, but of the BI CCD.

### 5.2.3 Iron and Nickel Line Diagnostics

The  $K\alpha$  flux ratio of Fe XXVI / Fe XXV is  $0.05^{+0.01}_{-0.02}$ . This indicates that the ionization temperature is  $3.1^{+0.3}_{-0.4}$  keV. The ratio  $K\beta / K\alpha$  of Fe XXV can not be determined accurately, because the  $K\beta$  line of Fe XXV is contaminated by the nearby Ni XXVII  $K\alpha$  line. We therefore examined the flux ratio of Fe XXV  $K\alpha$  vs Ni XXVII  $K\alpha$  plus Fe XXV  $K\beta$ . The observed ratio is  $0.10^{+0.02}_{-0.03}$ . If the abundance ratios of Fe and Ni are solar, we can then constrain the electron temperature to be  $2.5^{+1.0}_{-0.8}$  keV.

The center energy of Fe XXV  $K\alpha$  is 6650 (6648–6653) eV, which is significantly lower than that from an  $\sim 3$  keV temperature plasma (e.g. MEKAL [39, 61] and APEC [119] models give 6673eV and 6681 eV, respectively). In fact this line-center energy gives a plasma temperature of  $1.4^{+0.1}_{-0.1}$  keV, consistent with those determined from the line -flux ratio of sulfur. Furthermore, the line width of 44 eV is significantly larger than that observed from the GDXE [51]. These facts indicate that the Fe XXV  $K\alpha$  may include lines from lower ionization iron associated with a lower temperature plasma.

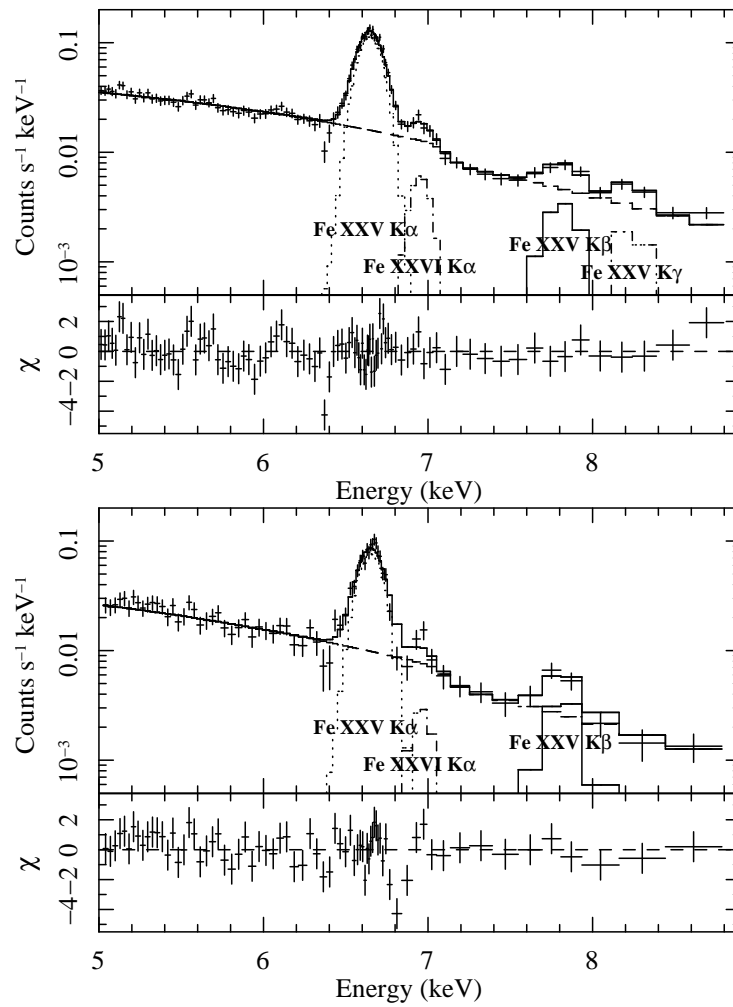


Figure 5.4: Same as figure 3, but in the 5–9 keV band.

Table 5.1: Best fit parameters of the phenomenological model in the 2.0–5.0 keV band

Line Identification	Energy (eV)	Width (eV)	Intensity $f$ (photons s <sup>-1</sup> cm <sup>-2</sup> )
S XV K $\alpha$	2446 (2440–2449)	22 (16–27)	9.53 (8.66–10.1) $\times 10^{-4}$
S XVI K $\alpha$	2625 (2603–2631)	20 (fixed) <sup>a</sup>	1.86 (1.38–2.23) $\times 10^{-4}$
S XV K $\beta$	2869 (2840–2889)	21 (fixed) <sup>a</sup>	7.47 (4.69–9.64) $\times 10^{-5}$
Ar XVII K $\alpha$	3124 (3116–3130)	47 (39–56)	2.27 (2.07–2.51) $\times 10^{-4}$
Ar XVIII K $\alpha$	3324 <sup>b</sup>	23 (fixed) <sup>a</sup>	1.46 (0.08–2.61) $\times 10^{-5}$
Ar XVII K $\beta$	3692 <sup>c</sup>	24 (fixed) <sup>a</sup>	1.86 (0.93–2.68) $\times 10^{-5}$
Ca XIX K $\alpha$	3882 (3873–3890)	24 (10–39)	5.74 (5.03–6.68) $\times 10^{-5}$
Thermal brems	Temperature(keV)		Norm. <sup>d</sup>
	1.89 (1.86–1.93)		4.34 (4.30–4.39) $\times 10^{-2}$
Absorption	$N_H$ ( $\times 10^{22}$ cm <sup>-2</sup> )	$Z_{Si}$ <sup>e</sup>	$Z_S$ <sup>e</sup>
	9.0 (8.9–9.1)	3.2 (3.1–3.3)	2.9 (2.7–3.3)
Flux (1.5–5.0 keV) $f$	photons s <sup>-1</sup> cm <sup>-2</sup>	Luminosity (1.5–5.0 keV) $f$	ergs s <sup>-1</sup>
	$1.1 \times 10^{-3}$		$3.9 \times 10^{35}$
$\chi^2/\text{d.o.f}$	242/266 = 0.91		

The errors in the parentheses are at 90% confidence level.

<sup>a</sup> Fixed to  $30 \times (E/5895)^{0.5}$  eV, where the width of the calibration sources (Mn I K $\alpha$  at 5895 eV) is 30 eV.

<sup>b</sup> Fixed to  $E$  (Ar XVII K $\alpha$ ) + 200 eV

<sup>c</sup> Fixed to  $E$  (Ca XIX K $\alpha$ ) - 190 eV

<sup>d</sup> The units of  $3.02 \times 10^{-15}/(4\pi D^2) \int n_e n_I dV$ , where  $D$ ,  $n_e$  and  $n_I$  are distance to the source (cm), the electron density (cm<sup>-3</sup>), and the ion density (cm<sup>-3</sup>), respectively.

<sup>e</sup> Abundances relative to solar.

<sup>f</sup> Flux is uncorrected for absorption, while intensity and luminosity are corrected.

Table 5.2: The best fit parameters of the phenomenological model in the 5.0–9.0 keV band

Line Identification	Energy (eV)	Width (eV)	Intensity <sup>e</sup> (photons s <sup>-1</sup> cm <sup>-2</sup> )
Fe XXV K $\alpha$	6650 (6648–6653)	44 (41–47)	2.23 (2.16–2.29) $\times 10^{-4}$
Fe XXVI K $\alpha$	6956 (6938–6981)	0 (<34)	1.09 (0.75–1.40) $\times 10^{-5}$
Fe XXV K $\beta$ <sup>a</sup>	7820 (7790–7847)	83 (53–113)	2.12 (1.49–2.53) $\times 10^{-5}$
Fe XXV K $\gamma$	8238 (8199–8286)	35 (fixed) <sup>b</sup>	1.32 (0.66–1.64) $\times 10^{-5}$
Thermal brems	Temperature(keV)		Norm. <sup>c</sup>
	4.5 (4.3–4.6)		9.9 (9.7–10) $\times 10^{-3}$
Absorption	$N_{\text{H}}$ ( $\times 10^{22}$ cm <sup>-2</sup> )		$Z_{\text{Fe}}$ <sup>d</sup>
	9.0 (fixed)		2.8 (2.3–3.2)
Flux (5.0–9.0 keV) <sup>e</sup>	photons s <sup>-1</sup> cm <sup>-2</sup>	Luminosity (5.0–9.0 keV) <sup>e</sup>	ergs s <sup>-1</sup>
	$7.1 \times 10^{-4}$		$7.4 \times 10^{34}$
$\chi^2/\text{d.o.f}$	194/155 = 1.25		

The errors in the parentheses are at 90% confidence level.

<sup>a</sup> This line is a mixture of Ni XXVII K $\alpha$  ( $\sim 7.82$  keV) and Fe XXV K $\beta$  ( $\sim 7.88$  keV).

<sup>b</sup> Fixed to  $30 \times (E/5895)^{0.5}$  eV, where the width of the calibration sources (Mn I K $\alpha$  at 5895 eV) is 30 eV.

<sup>c</sup> The units of  $3.02 \times 10^{-15} / (4\pi D^2) \int n_e n_I dV$ , where  $D$ ,  $n_e$  and  $n_I$  are distance to the source (cm), the electron density (cm<sup>-3</sup>), and the ion density (cm<sup>-3</sup>), respectively.

<sup>d</sup> Abundance relative to solar.

<sup>e</sup> Flux is uncorrected for absorption, while intensity and luminosity are corrected.

## 5.2.4 Thin Thermal Plasmas and Power-Law Component

From the emission line information (sections 5.2.2 and 5.2.3), Sgr A East requires at least a two-temperature plasma. The lower temperature plasma is CIE, while no constraint on the high temperature plasma is obtained from the line information. We therefore fit the full energy range of the spectrum with a model of a  $\sim 1$ -keV CIE plasma plus a higher temperature plasma. Since the spectrum has a systematic line broadening due to the incomplete response function [50], we artificially add a  $1400 \text{ km s}^{-1}$  random motion in the plasma code (APEC) to compensate for the systematic error. The reduced  $\chi^2$  has 2 local minima:  $\sim 43$ – $58 \text{ keV}$  with  $nt > 10^{13} \text{ s cm}^{-3}$  (CIE plasma), and  $\sim 37$ – $54 \text{ keV}$  with  $nt = 10^{11} \text{ s cm}^{-3}$  (non-ionization equilibrium: NEI plasma), where  $nt$  is the ionization parameter. Because these temperatures are outside the XIS band-pass, the parameter ranges for the fit are unreliable. The reduced  $\chi^2$  values are 1.1 with 460–470 degree of freedoms (d.o.f.) at both the local minima. The two-CIE model can not reproduce the Fe XXV  $K\beta$  line flux at  $\sim 7.88 \text{ keV}$ , while the CIE+NEI model fails to fit the Ni XXVII  $K\alpha$  line flux at  $\sim 7.82 \text{ keV}$ . In both cases, significant residuals are found above the Fe XXV  $K\alpha$  energy (7–9 keV). For the CIE case, absorption edge of Fe is 0.5 solar, while for the NEI case, it is as large as 3.4 of solar. These unrealistic parameters and/or significant residuals above the Fe XXV  $K\alpha$  energy surely come from the artificial plasma fitting for the hard X-ray band. We therefore added a power-law component to a two-CIE model in order to naturally explain the high energy band. Although no essential change is found below 7 keV, a significant improvement is noted in the 7–9 keV band, with the reduced  $\chi^2$  of 1.07 (for 453 d.o.f.). The best fit results are given in figure 5.5 and table 5.2.4.

## 5.3 Short Discussion for Sgr A East

### 5.3.1 Thermal Plasma

The X-ray luminosity of the thermal plasma is  $4.2 \times 10^{35} \text{ erg s}^{-1}$  at a distance of 8 kpc. Assuming a uniform density plasma in a sphere of radius ( $1'.6$ ), we estimate the plasma density to be  $4.7 \text{ H cm}^{-3}$  for the 1-keV component and  $0.6 \text{ H cm}^{-3}$  for the 6-keV component. The dynamical age estimated from the SNR size divided by the sound velocity in the high energy plasma is about 4000 years. These arguments are consistent with the previous studies [63, 92, 112].

### 5.3.2 Hard Tail

The Sgr A East spectrum requires a hard tail component with a power-law index of 0.87 (0.84–0.91), although Park et al. [92] and Sakano et al. [112] detected no power-law component in the Chandra or XMM spectra. Since the non-X-ray background of XIS is far lower than those of Chandra and XMM, particularly, in the high energy band ( $\sim \geq 6 \text{ keV}$ , see [50]), where the hard tail is manifested, we believe that our result is more reliable.

Since the response function of the XIS at a high energy of around 10 keV is not well established yet, the absolute value of the photon index may have a larger error than the statistical one. Nevertheless the presence of a hard tail is not in doubt. The hard tail flux in the 7–9 keV band is 1.2 times that of the thin thermal components. Thus, an important question is the origin of the large hard tail. One possibility of the hard tail origin is integrated emission of point sources fainter than the limiting flux ( $3 \times 10^{-15} \text{ erg cm}^{-2} \text{ s}^{-1}$ ) of the Chandra deep

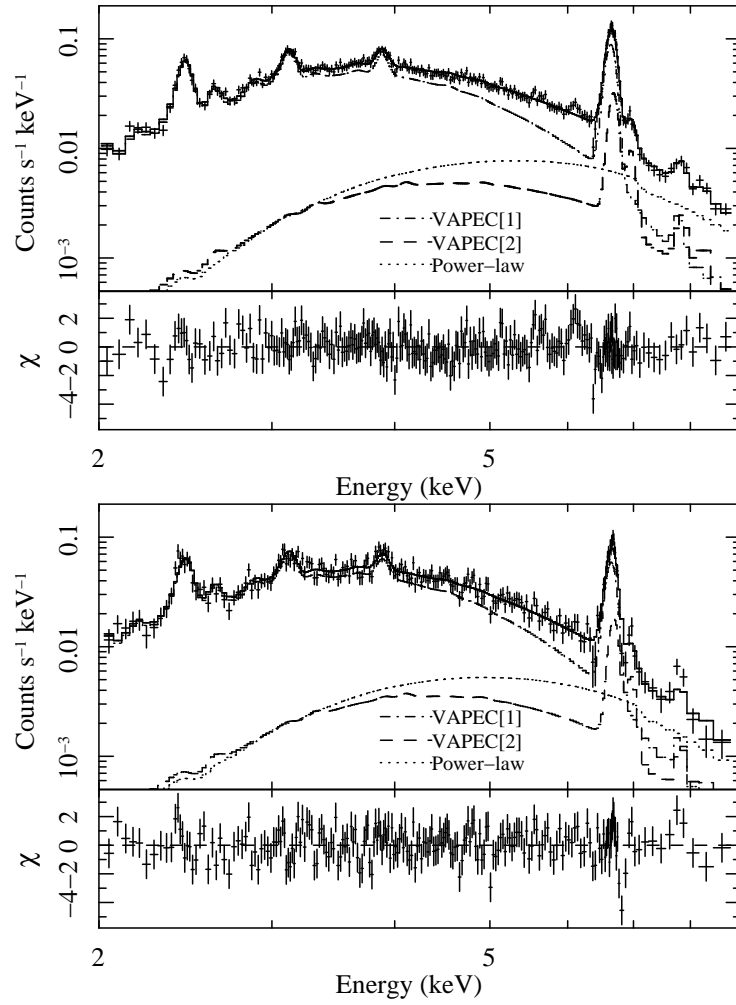


Figure 5.5: Top: the X-ray spectrum of the sum of 3 FI CCDs with the best-fit two-temperature plasma plus power-law model. Bottom: same as the top, but of the BI CCD.

Table 5.3: Best fit parameters of the two-temperature plasma plus power-law model in the 2.0–9.0 keV band

Power-law	index	Norm. <sup>a</sup>	
	0.87 (0.84–0.91)	3.5 (3.3–3.7) × 10 <sup>-4</sup>	
Thin thermal plasma <sup>b</sup>	APEC[1]	APEC[2]	
Temperature (keV)	1.21 (1.18–1.30)	6.0 (5.5–6.4)	
Norm. <sup>c</sup>	0.165 (0.161–0.169)	2.7 (2.5–2.9) × 10 <sup>-3</sup>	
Z <sub>S</sub> <sup>d</sup>	1.17 (1.07–1.24)		
Z <sub>Ar</sub> <sup>d</sup>	1.20 (1.07–1.33)		
Z <sub>Ca</sub> <sup>d</sup>	1.18 (1.03–1.33)		
Z <sub>Fe</sub> <sup>d</sup>	2.63 (2.54–2.70)		
Z <sub>Ni</sub> <sup>d</sup>	2.63 <sup>e</sup>		
Absorption	N <sub>H</sub> (× 10 <sup>22</sup> cm <sup>-2</sup> )	Z <sub>Si</sub> <sup>d</sup>	Z <sub>S</sub> <sup>d</sup> Z <sub>Fe</sub> <sup>d</sup>
	9.66 (9.58–9.74)	3.2 (3.1–3.3)	2.9 (2.7–3.0) 1.33 (1.26–1.40)
Flux (2.0–9.0 keV) <sup>f</sup>	photons s <sup>-1</sup> cm <sup>-2</sup>	Luminosity (2.0–9.0 keV) <sup>f</sup>	ergs s <sup>-1</sup>
	1.8 × 10 <sup>-3</sup>		4.5 × 10 <sup>35</sup>
Plasma mass <sup>g</sup>	total (M <sub>⊙</sub> )	iron (M <sub>⊙</sub> )	
	27 <sup>f</sup> 0.5	0.15 <sup>f</sup> 0.5	
χ <sup>2</sup> /d.o.f	483/453 = 1.07		

The errors in the parentheses are at 90% confidence level.

<sup>a</sup> The unit is photons keV<sup>-1</sup> cm<sup>-2</sup> s<sup>-1</sup> at 1 keV.

<sup>b</sup> Random motion of 1400 km s<sup>-1</sup> velocity is added to the APEC models to compensate the systematic line broadening obtained with the calibration line (Nml Kα).

<sup>c</sup> The units of 10<sup>-14</sup> / (4πD<sup>2</sup>) ∫ n<sub>e</sub>n<sub>H</sub>dV, where D, n<sub>e</sub> and n<sub>H</sub> are distance to the source (cm), the electron density (cm<sup>-3</sup>), and the hydrogen density (cm<sup>-3</sup>), respectively.

<sup>d</sup> Abundances relative to solar.

<sup>e</sup> Fixed to the abundance of Fe.

<sup>f</sup> Flux is not corrected for absorption, while luminosity is corrected.

<sup>g</sup> Filling factor (0 < f < 1). Distance of 8 kpc is assumed (Reid et al. 1993).

exposure (Muno et al. [78]). The fact that the power-law index of the hard tail spectrum of  $\Gamma \sim 0.8-0.9$  is similar to that from the point sources of  $\Gamma \sim 0.8-0.9$  [80] may favor this possibility. The integrated flux of point sources above the limiting luminosity in the Sgr A East region (a  $1'.6$  radius) is  $2.2 \times 10^{-12}$  erg cm $^{-2}$  s $^{-1}$ . The flux of the hard tail is calculated to be  $2.1 \times 10^{-12}$  erg cm $^{-2}$  s $^{-1}$  (2–8keV), nearly the same as that of the integrated point sources. Muno et al. [78] reports that power-index of the log $N$ -log $S$  slope below the flux ( $S$ ) of  $8 \times 10^{-7}$  photons cm $^{-2}$  s $^{-1}$  ( $6.4 \times 10^{-15}$  erg cm $^{-2}$  s $^{-1}$ ) is 1.7 for point sources near the GC. If this luminosity distribution is the same for point sources in the Sgr A East region, and extends by a factor of 5 lower flux than the current Chandra detection limit, then point sources would account for most of the hard tail flux.

The other possibility is clumps and filaments found by Chandra in Sgr A East, because significant fractions of these filaments have non-thermal X-ray spectra [49, 71]. In this case, the hard tail must be closely related to a high energy cosmic ray origin. Sgr A East locates very near the GC, which would be a site of extreme physical conditions. Therefore, more extensive study of the hard X-ray tail using HXD [121] on board Suzaku, for example, is highly required.

### 5.3.3 Chemical Compositions

The chemical compositions averaged over the SNR are nearly solar for S, Ar and Ca, while Fe is overabundant, which is consistent with the Chandra and XMM results [63, 112, 92]. The abundance of Fe averaged over the whole SNR is 2–3 of solar. We estimated the total mass of iron and hot gas to be  $0.15 f^{0.5} M_{\odot}$  and  $27 f^{0.5} M_{\odot}$ , where  $f$  is filling factor. This is consistent with the result of Park et al. [92], who found that the mass of Fe was  $< 0.27 M_{\odot}$  within  $1'$  radius.

As for the interstellar absorption, on the other hand, the Si and S abundances in the ISM are 3 of solar, while iron is moderately overabundant. Similar over abundance are found from other X-ray objects near the GC [51, 130], and hence would be common phenomena.



# Chapter 6

## Suzaku J1740.5–3014

We found a new X-ray source, Suzaku J1740.5–3014, in the data set of the GC observation. In this chapter, we report the results of the analysis of Suzaku J1740.5–3014. If it is located in the intermediate region between the GC and the ridge, it is a precious sample because the property of the point sources around this region has not been studied well. In section 6.1, we describe about the observations and the data reduction. In section 6.2, we show the result of the analysis. In section 6.3, we discuss the properties and distance of Suzaku J1740.5–3014.

### 6.1 Observation & Data Reduction

With the Suzaku XIS, regions near a radio pulsar PSR B1737–30 [21] were observed twice. The observation logs are listed in table 6.1.

Table 6.1: Observation data list.

Target	Obs. ID	Start Time	Stop Time	Exp. (ks)*
GC LARGEPROJECT15	503021010	2008-10-04 03:44:03	2008-10-05 10:57:24	50.1
HESSJ1741-B	503077010	2009-02-26 01:00:60	2009-02-27 11:35:19	46.2

\* Effective exposure after the data screening described in the text.

The XIS observations were made in the normal clocking full window mode. We used cleaned event data distributed from DARTS <sup>1</sup>. The data processing versions are 2.2.11.22 and 2.2.11.24 for the first and second observations, respectively. The data during the epoch of low Earth elevation angles less than 5 degrees, day Earth elevation angles less than 20 degrees, and the South Atlantic Anomaly was removed. The effective exposure times are listed in table 6.1. The SCI technique was used in these observations. We confirmed that the spectral resolutions at 5.9 keV were  $\sim 150$  and  $\sim 200$  eV (FWHM) for the FI and BI CCDs in these observations using the onboard calibration sources.

Due to a star tracker (STT) problem, the Suzaku attitude during the second observation was not locked at the programmed position, and hence drifted by  $\sim 2'$  in the direction of the right ascension between the start and stop time of the second observation.

<sup>1</sup><http://www.darts.isas.jaxa.jp/astro/suzaku.>>

## 6.2 Analysis

We analyzed the data using the software package HEASoft 6.5.1. In this chapter, uncertainties are quoted at the 90 % confidence range unless otherwise stated.

### 6.2.1 Imaging

To make X-ray images, we used only the data of October 2008 when the STT operated correctly. The data of XIS 0, 1 and 3 were merged. We obtained COR-sorted NXB images using `xisnxbgen` [125]. After subtracting the NXB image, we divided the X-ray image by an image of the flat field to correct vignetting. The image of the flat field was made with `xissim` [34].

Since Suzaku has some position error [135], we fine-tuned the nominal Suzaku coordinate using the positions of catalogued visible and near-infrared stars. Since the X-ray from normal stars is generally soft, we made 0.5–2.0 keV band image. In the X-ray image, there are three point sources which corresponds to catalogued visible and near-infrared stars. Using the three stars, we shifted the Suzaku coordinate as is shown in figure 6.1. Before this correction, averaged difference between the coordinates of cataloged stars and X-ray point sources was  $40'' \pm 11''$ , where the error shows the statical uncertainty of the peak positions of the X-ray point sources. After this correction, the averaged difference became  $9''$ .

No significant X-ray is found from the radio pulsar PSR B1737–30, but a bright new source is discovered at about  $90''$  east of PSR B1737–30. From the fine tuned position, we designate this source as Suzaku J1740.5–3014. The position of Suzaku J1740.5–3014 is  $(\alpha, \delta)_{2000} = (17 : 40 : 35.6, -30 : 14 : 16)$  with the uncertainty of  $14''$ . In the Galactic coordinate, the position is  $(l, b) = (-1^\circ.682, 0^\circ.245)$ .

Using the fine-tuned position, we constructed the 1–9 keV band image in figure 6.2. The peak positions of Suzaku J1740.5–3014 are same in the 0.5–2 and 1–9 keV band images.

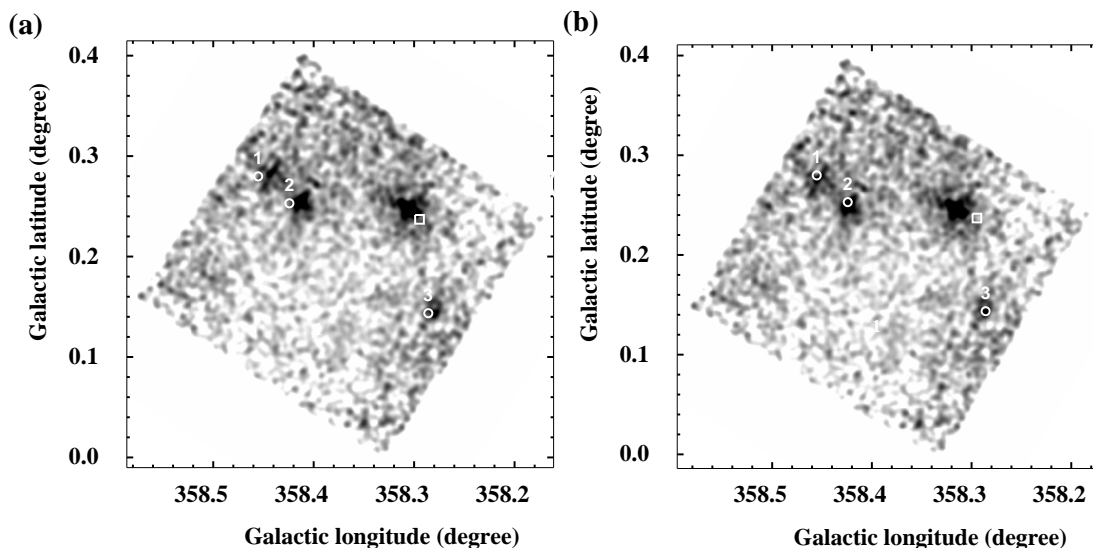


Figure 6.1: X-ray image in the 0.5–2 keV band before (a) and after the coordinate correction (b). The numbered circles represent catalogued stars used as references of the position. (1) DENIS-P J174047.6–300613 (2) HD 316162 (3) DENIS-P J174054.9–301915 [16, 28]. The rectangle mark shows the position of PSR B1737–30 [21].

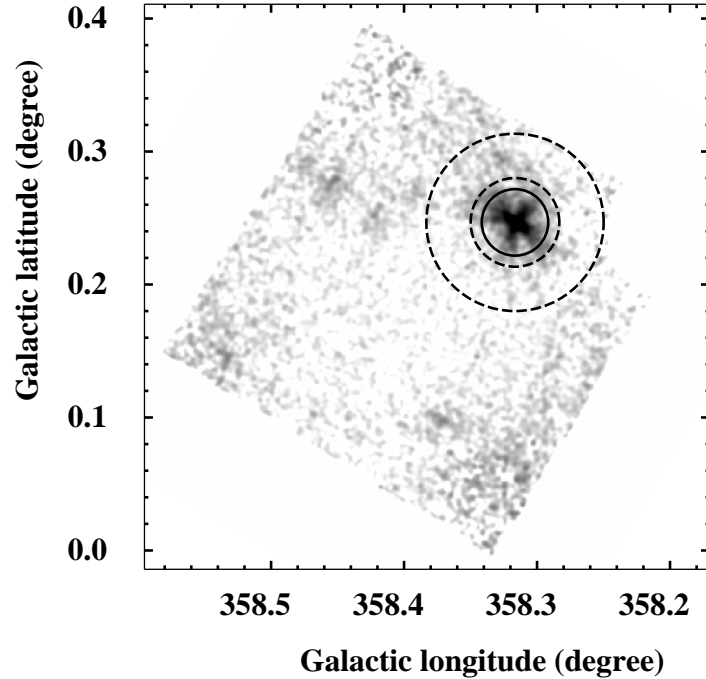


Figure 6.2: X-ray image in the 1–9 keV band after the coordinate correction. The source and background regions are shown by the solid circle and dash annuals, respectively.

### 6.2.2 Spectrum

We made spectra of the two observation separately. For the first observation, the spectrum of Suzaku J1740.5–3014 for each sensor was extracted from the solid circle region in figure 6.2 with a radius of  $1'.5$ . Background spectra were evaluated from the dashed annulus region in figure 6.2 having inner and outer radii of  $2'$  and  $4'$ . The background spectra were subtracted from the spectra of Suzaku J1740.5–3014.

In the second observation, however, the STT was troubled, and the attitude had a large ambiguity. To correct it, we divided the second observation into six epochs. We made an X-ray image of each epoch, and confirmed that the attitude drift caused by the STT problem was less than  $20''$  in each epoch. This value is as small as the nominal positional uncertainty of the XIS [135]. Then we corrected the coordinates of each epoch according to the image of the first observation (figure 6.1). After the correction, we obtained the spectra for the second observation from the regions shown in figure 6.2.

The spectra of the two FIs are co-added because the response functions are almost same between the FIs. We made RMF files using `xisrmfgen`, and ARF files using `xissimarfgen` [34] for each observation.

To check the difference of the spectra between the two observations, we divided the spectra by the corresponding ARF files to correct the difference of the effective area and took the ratio of the spectra of the two observations. The ratio is consistent with unity by  $\chi^2$ -test in the 90% confidence level ( $\chi^2/\text{d.of.}=89/98$ ) and thus we judged that the spectra of the two observations are not different. We combined the spectra of XIS of the both observations to increase the statistics. The RMF files and ARF files were also combined. The X-ray spectrum is shown in

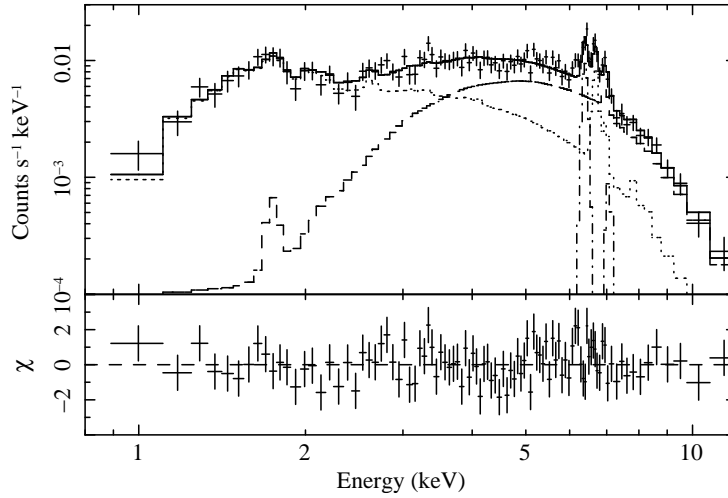


Figure 6.3: Background-subtracted spectrum of Suzaku J1740.5–3014 for the FI CCD. The source spectrum was made from the solid circle in figures 6.2, while the local background spectrum was taken from the dash annals. The vertical error bars of each data point are the  $1\sigma$  error. The solid line is the best-fit result of two-component CIE model (table 6.2(b)). The dash and dot lines represent high and low temperature CIE components. The dash-dot lines are Fe I K  $\alpha$  and  $\beta$ .

figure 6.3. We show only the spectrum of the FI CCD to be easy-to-see.

The X-ray spectra exhibit three lines at 6.4, 6.7, and 7.0 keV. In order to identify these lines, we fitted the spectra in the 5–10 keV band with a phenomenological model of an absorbed power-law model plus three narrow Gaussian lines. The cross section of the photoelectric absorption was obtained from [76]. The best-fit line energies with the equivalent widths ( $EW$ ) of the lines are  $6.40^{+0.04}_{-0.02}$  keV with  $210^{+30}_{-50}$  eV,  $6.67 \pm 0.02$  keV with  $190^{+60}_{-40}$  eV, and  $6.95^{+0.04}_{-0.05}$  keV with  $130^{+40}_{-50}$  eV, respectively. From the line energies, these lines are identified as the  $K\alpha$  lines from Fe I, XXV and XXVI.

We therefore fitted the X-ray spectra of the FI and BI sensors simultaneously with a collisional ionization equilibrium (CIE) plasma model (APEC: [119]) for highly ionized iron lines plus two Gaussian lines for Fe I  $K\alpha$  and  $K\beta$  lines. The center energy ratio of the two Gaussian lines was fixed to be 1:1.103 and the flux ratio to be 1:0.125 [40]. The abundance of the CIE plasma model was free, while the relative ratios among various elements were fixed to be the solar value. The solar abundance of each element was obtained from [1]. The model did not fit well with  $\chi^2/\text{d.o.f.} = 363.3/166$ . We also tried two two-component CIE plasma model where an absorption column density and an abundance are common to the two components. However, this model did not describe the spectra with  $\chi^2/\text{d.o.f.} = 275.7/164$ .

Since large residuals were found in the low energy band, we applied a one-component CIE plasma model with partial absorption. This model gave a marginal  $\chi^2/\text{d.o.f.}$  of 204.9/164. The best-fit parameters are listed in table (a).

We finally tried a two-component CIE plasma model with the independent absorptions and a common abundance, and obtained a reasonable fit with  $\chi^2/\text{d.o.f.} = 190.6/163$ . The best-fit parameters are given in table (b), and the best-fit model together with the spectrum is shown in figure 6.3.

Table 6.2: Best-fit parameters of the model fittings for the background-subtracted spectra\*.

(a) one-component CIE plasma model with partial absorption.		
Model: $\text{Abs1} \times \{(1-\alpha) + \alpha \times \text{Abs2}\} \times (\text{APEC} + \text{Neutral Iron Lines})$		
Iron Lines	Fe I K $\alpha$	Fe I K $\beta$
Energy (keV)	$6.40^{+0.03}_{-0.02}$	$7.06^\dagger$
Flux ( $10^{-6}$ ph s $^{-1}$ cm $^{-2}$ )	$8.8^{+1.7}_{-1.3}$	$1.1^\dagger$
Parameter	APEC	
$kT$ (keV)	$9.5^{+1.2}_{-0.9}$	
Abundance (solar)	$0.49^{+0.11}_{-0.10}$	
Normalization $^\ddagger$	$2.8^{+0.1}_{-0.2}$	
Parameter	Abs1	Abs2
$N_{\text{H}}$ ( $10^{22}$ cm $^{-2}$ )	$1.7^{+0.1}_{-0.2}$	$16 \pm 3$
Covering factor $\alpha$	–	$0.71^{+0.02}_{-0.03}$
Flux ( $10^{-12}$ erg s $^{-1}$ cm $^{-2}$ ) $^\S$	2.0 (2.2)	
$\chi^2/\text{d.o.f.} = 204.9/164$		
(b) two-component CIE plasma model		
Model: $\text{Abs1} \times (\text{APEC1} + \text{Neutral iron lines}) + \text{Abs2} \times \text{APEC2}$		
Iron Lines	Fe I K $\alpha$	Fe I K $\beta$
Energy (keV)	$6.40^{+0.03}_{-0.02}$	$7.06^\dagger$
Flux ( $10^{-6}$ ph s $^{-1}$ cm $^{-2}$ )	$8.4^{+1.7}_{-1.4}$	$1.0^\dagger$
Parameter	APEC1	APEC2
$kT$ (keV)	$64 (\geq 44)$	$6.0 \pm 1.1$
Abundance (solar) $^\parallel$	$1.3^{+0.2}_{-0.3}$	
Normalization $^\ddagger$	$1.6^{+0.2}_{-0.1}$	$0.62^{+0.04}_{-0.03}$
Parameter	Abs1	Abs2
$N_{\text{H}}$ ( $10^{22}$ cm $^{-2}$ )	$11^{+2}_{-1}$	$1.6 \pm 0.1$
Flux ( $10^{-12}$ erg s $^{-1}$ cm $^{-2}$ ) $^\S$	2.1 (2.3)	
$\chi^2/\text{d.o.f.} = 190.6/163$		

\* Errors show the 90% confidence level.

$^\dagger$  The energy and flux of Fe I K $\beta$  line are fixed to be 1.103 and 0.125 times those of Fe I K $\alpha$  line, respectively.

$^\ddagger$  The units of  $10^{-17}/(4\pi D^2) \int n_e n_H dV$ , where  $D$ ,  $n_e$  and  $n_H$  are the distance to the source (cm), the electron density (cm $^{-3}$ ), and the hydrogen density (cm $^{-3}$ ), respectively.

$^\S$  Observed flux in the 2–10 keV band. Values in the parentheses are absorption-corrected fluxes, where we use  $N_{\text{H}} = 1.7 \times 10^{22}$  cm $^{-2}$  for the case (a) and  $N_{\text{H}} = 1.6 \times 10^{22}$  cm $^{-2}$  for the case (b) as an interstellar absorption.

$^\parallel$  The abundance is common to the two APEC components.

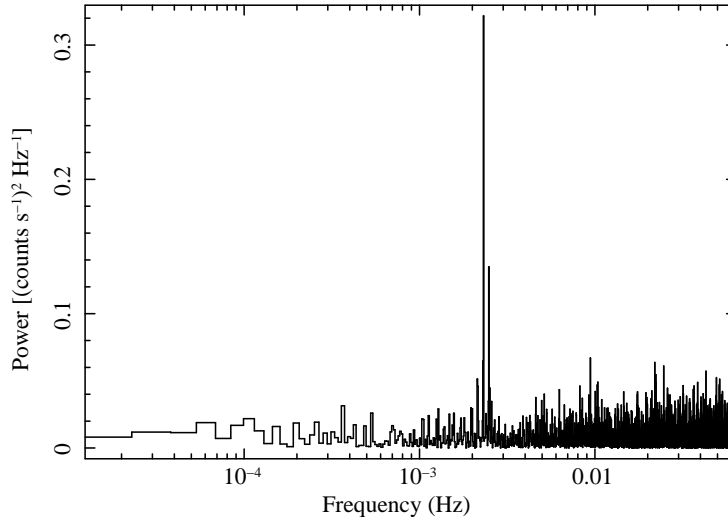


Figure 6.4: Power spectrum in the 1–9 keV band obtained by the FFT analysis. This is the result of the combined data of the two observations.

### 6.2.3 Timing

We extracted light curves of Suzaku J1740.5–3014 from the circular region in figure 6.2. We made the light curves of the two observations separately. The light curves of the two FI sensors were also combined. However, we did not use the BI data, because the NXB dominates the data above 7 keV, and the NXB is time valuable. We searched for pulsations in the 1–9 keV band from the FI data. The fast Fourier transform (FFT) analysis revealed clear peaks at  $\sim 2.31 \times 10^{-3}$  Hz from the light curves of the both observations. We then searched for an accurate pulse period with the folding technique, and found pulse periods of  $432.1 \pm 0.2$  s and  $431.9 \pm 0.3$  s from the data of October 2008 and February 2009. The pulse periods are consistent with the errors and thus we combined the light curves of the two observations to increase the statistics. We made a coherent FFT analysis and a folding search for the combined light curves. The obtained power spectrum is shown in figure 6.4. The pulse period is  $432.1 \pm 0.1$  s. The error of the pulse period was estimated in reference to [59], considering the highest harmonic.

Since we found the two-component CIE plasma in the spectral analysis, we made folded pulse profiles in the 1–3 keV and 4–8 keV bands; they represent the low- and high-temperature components, respectively. These folded pulse profiles are shown in figure 6.5. We calculated the ratio of the low-energy profile to the high-energy profile, and the ratio is fitted with a constant value with  $\chi^2/\text{d.o.f.} = 38.7/25$ . Thus we reject a hypothesis that the low-energy profile is a constant fraction of the high-energy profile with the 96% confidence level. The pulse profile of the high-temperature plasma is quasi-sinusoidal with small humps on both sides of the main peak, while that of the low-temperature plasma is more complicated with nearly equal three peaks.

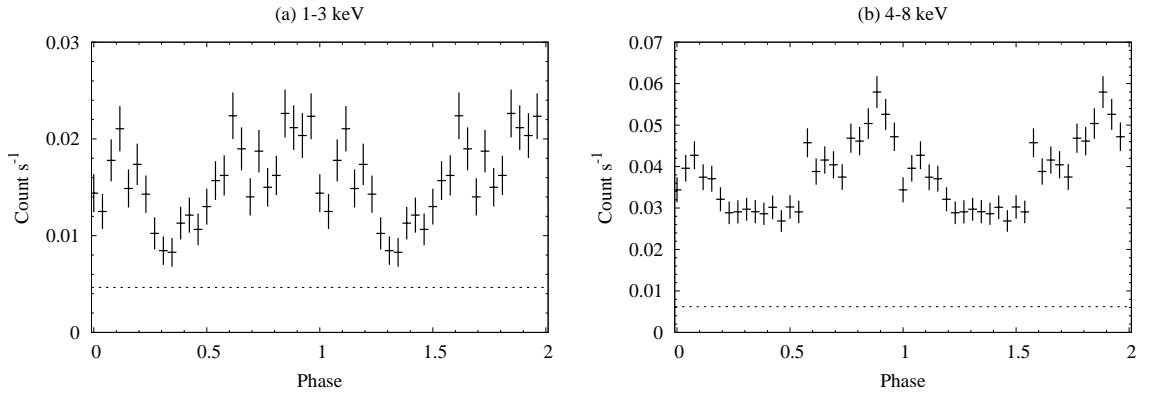


Figure 6.5: Pulse profiles in the 1–3 keV band (a) and in the 4–8 keV band (b). Folded period is 432.1 s. The vertical error bars of each data point are the  $1\sigma$  error. The dotted lines show the background levels.

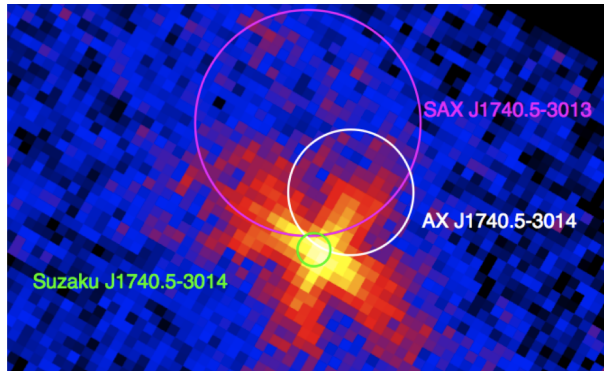


Figure 6.6: Positions of Suzaku J1740.5–3014, AX J1740.5–3014 and SAX J1740.5–3013[110, 30]. The circles show the 90% error uncertainties of the positions. They are overlaid on the Suzaku image of 1–9 keV.

## 6.3 Short Discussion for Suzaku J1740.5-3014

### 6.3.1 Identify of Suzaku J1740.5-3014 by Comparison with Previous X-ray Observations

We searched catalogs of X-ray sources to identify Suzaku J1740.5-3014. Two sources, AX J1740.5–3014[110] and SAX J1740.5–3013[30, 31] were found near Suzaku J1740.5–3014. The positions of them are shown in figure 6.6 where the circles show the 90% uncertainties of the positions. The spectral properties of the each observation are summarized in table 6.3. The positions and spectral properties almost match in the uncertainties so Suzaku J1740.5-3014, AX J1740.5–3014 and SAX J1740.5–3013 are probably a same object. The detection of Fe  $K\alpha$  lines and the pulsation had not been reported in the previous observations. Due to the high energy resolution and high statistics of the Suzaku data, we can find them for the first time.

Table 6.3: Comparison of Suzaku J1740.5–3014, AX J1740.5–3014 and SAX J1740.5–3013.

Object	Flux*	$\Gamma$	$N_{\text{H}}(10^{22} \text{ cm}^{-2})$	Obs. date	Ref.
AX J1740.5–3014	2.5	$3.4_{-3.7}^{+7}$	10 (< 40)	Sep. 95	[110]
SAX J1740.5–3013	2.4	$2.4_{-2.1}^{+1.5}$	$1.5_{-0.7}^{+0.5}$	Apr. 98	[31]
Suzaku J1740.5–3014	2.1	$0.8_{-0.1}^{+0.1}$	$1.5_{-0.2}^{+0.3}$	Oct. 08 + Feb. 09	This work

\*The unit is  $\text{ergs s}^{-1} \text{ cm}^{-2}$ . The interstellar absorption is not corrected.

### 6.3.2 Suzaku J1740.5–3014 as a New Intermediate Polar Candidate

The X-ray spectra of Suzaku J1740.5–3014 exhibit three lines at 6.4, 6.7, and 7.0 keV. The best-fit  $EW$  values of the lines are  $\sim 210$ ,  $\sim 190$ , and  $\sim 130$  eV, respectively. Ezuka and Ishida [20] reported that mCVs have three iron  $K\alpha$  lines at 6.4, 6.7, and 7.0 keV with mean  $EW$  values of  $\sim 100$ ,  $\sim 200$ , and  $\sim 100$  eV, which are nearly the same as those of Suzaku J1740.5–3014.

We found the coherent and clear pulsation of 432.1 s from Suzaku J1740.5–3014. This pulse period is typical for mCVs [106]. Although we found no other periodicity due to orbital modulation, this 432.1 s period would be due to spin, because possible orbital modulation is larger than this value. Furthermore, the pulse profile is energy dependent, which may not be appeared if the pulse is due to orbital modulation.

The overall spectrum was well fitted with the two-component CIE plasma model with temperatures of  $kT = 6.0$  and 64 keV. The spectrum can be fitted with the one-component CIE plasma model with partial absorption marginally. Both models require the  $K\alpha$  and  $K\beta$  lines from neutral iron. Ezuka and Ishida [20] also reported that the spectra of mCVs can be described by a thin thermal plasma model with a mean temperature of  $\sim 20$  keV plus the 6.4 keV line. The one-component CIE plasma model with partial absorption gave a temperature of  $kT = 10$  keV, which resembles to the general feature of mCVs. We, however, favor the two-component CIE plasma model, because the  $\chi^2/\text{d.o.f.}$  value is better and the energy dependent pulse profile is difficult to be explained with the one-component CIE plasma model.

In the two-component CIE model, the absorption for the low-temperature plasma is  $N_{\text{H}} = (1.6 \pm 0.1) \times 10^{22} \text{ cm}^{-2}$ , which may be due to the interstellar absorption. Assuming the uniform density toward the GC, we can estimate the source distance to be  $\sim 2$  kpc. Here the absorption and distance to the GC are thought to be  $N_{\text{H}} = 6 \times 10^{22} \text{ cm}^{-2}$  [96, 110] and 8 kpc (e.g. [66]). Then the absorption-corrected flux of  $2.1 \times 10^{-12} \text{ erg cm}^{-2} \text{ s}^{-1}$  in the 2–10 keV band is converted to the source luminosity of  $1 \times 10^{33} \text{ erg s}^{-1}$  in the 2–10 keV band. This luminosity is typical for an intermediate polar (IP) of  $\sim 10^{31} - 10^{33} \text{ erg s}^{-1}$  [20].

All these facts favor an idea that Suzaku J1740.5–3014 is a mCV, especially an IP, not a polar, because the 432.1 s period is too short as a synchronized orbital-spin period ( $\geq 4000$  s for all catalogued polars by Ritter & Kolb [106]). In figure 6.4, a sub peak appear to be present at the higher-frequency side of the main peak. The frequency of the sub peak is  $\sim 2.48 \times 10^{-3} \text{ Hz}$ . It might be a beat of the spin and orbital periods observed in some IPs (e.g. [88]). The frequency of the beat is  $\Omega \pm \omega$ ;  $\Omega$  and  $\omega$  are the frequency of the orbital and spin motions. If the sub peak is a beat  $\Omega + \omega$ ,  $\omega$  is  $2.31 \times 10^{-3} \text{ Hz}$  and thus  $\Omega$  is  $\sim 1.7 \times 10^{-4} \text{ Hz}$  or the period is  $5.9 \times 10^3 \text{ s}$  ( $\sim 1.6$  hours). The orbital periods of the IPs catalogued by [106] are  $5.1 \times 10^3 \sim 5.6 \times 10^4 \text{ s}$  and thus the period of  $5.9 \times 10^3 \text{ s}$  can be the orbital period. The period is, however, also very close

to the orbital period of the Suzaku satellite so there is a possibility that it is an artificial one.

From the absorption of the low-temperature component, Suzaku J1740.5–3014 would be a foreground source, not a member of the GC sources.

We suggest that a large absorption for the 64 keV plasma is due to the circum-stellar gas, which could be up to several times  $10^{23} \text{ cm}^{-2}$  [20]. This large amount of circum-stellar gas can naturally explain the origin of the strong 6.4 keV line from neutral iron (see e.g. [20]).

The spectrum of the standard model with a cylindrical emission region is given by multi-temperature plasma components with a power-law emission measure distribution of index  $\sim -0.5$  [32]. The multi-component plasma can be approximated by two representative temperatures. The ratio of the volume emission measures of the 6.0 keV plasma to the 64 keV plasma is 1:2.6. This ratio does not follow the power-law relation of  $\sim -0.5$ . It is also strange that the 6.0 keV plasma emission does not suffer the large absorption, if that is attributable to the circum-stellar gas. We thus suspect a standard emission model and geometry should be modified for this new IP. Detailed modeling, however, is beyond the scope of this thesis.



# Chapter 7

## Discussion

In this chapter, we make discussions based on the results in the previous chapters. In section 7.1 and 7.2, the spatial distribution and the spectra of the GDXE are discussed. In section 7.3, the intensity of the GDXE is compared with that of point sources detected with Chandra. In section 7.4 and section 7.5, Sgr A East and Suzaku J1740.5-3014 are compared with other SNRs and CVs, and their contribution to the GDXE is discussed.

### 7.1 Spatial Distributions of the Fe $K\alpha$ Line Emissions of the GDXE

#### 7.1.1 Uncertainty of the Intensity Measurement

Here we evaluate the uncertainties of the intensity measurement. The effect of the interstellar absorption is small in the band of the Fe  $K\alpha$  lines because the photoelectric absorption decreases with the incident energy to  $-2.7$  power, and the energies of the Fe  $K\alpha$  lines are just below the Fe K edge. Only 9% of the incident photons with the energy of 6.5 keV are absorbed by interstellar medium of  $N_{\text{H}} = 6 \times 10^{22} \text{ cm}^{-2}$ . The uncertainty of the interstellar absorption on the Fe  $K\alpha$  line profiles is this level and does not affect the following discussion. In addition, the Fe  $K\alpha$  line emissions are little contaminated by bright point sources and thus a good tracer for the GDXE. Sgr A East is, however, bright in the Fe XXV  $K\alpha$  line. The region of Sgr A East was excluded but the spectra of the GDXE near it are contaminated. We estimated the contamination using the XIS Monte Carlo simulator `xissim` [34]. We inputted the flux of the Fe XXV  $K\alpha$  line emission obtained in chapter 5 and calculated the leak from Sgr A East to the neighbor region. As a result, less than 15% of the Fe XXV  $K\alpha$  line emission in  $l_* < 0^\circ.15$  comes from Sgr A East. In the outer region ( $l_* > 0^\circ.15$ ), the contamination from Sgr A East is less than 1%. The contamination from Sgr A East is ignorable in the following discussion.

#### 7.1.2 Comparisons with Stellar Mass Distribution Observed in the Infrared

We compared the intensity profile of the GDXE with the stellar mass distribution model of the Milky Way galaxy, originally made by Muno et al. [81], based on infrared observations of IRAS ,COBE [60] and IRT of Spacelab 2 [42]. The major emission sources at near infrared (NIR) wavelength ( $1 - 7\mu \text{ m}$ ) are stars and thus NIR is a good tracer of the stellar mass. The stellar mass model consists of the components of the nuclear bulge (NB), Galactic bulge (GB) and

Galactic disk (GD). The NB is composed of the nuclear stellar cluster and the nuclear stellar disk. The further detail of the stellar mass model is shown in Munro et al. [81]. This model has the uncertainty of about 25% in the  $1\sigma$  confidence level. The profiles of the stellar mass model are shown in figure 7.1. We show only the projections along  $l = -0^\circ.056$  and  $b = -0^\circ.046$  but this model is actually a two-dimensional model.

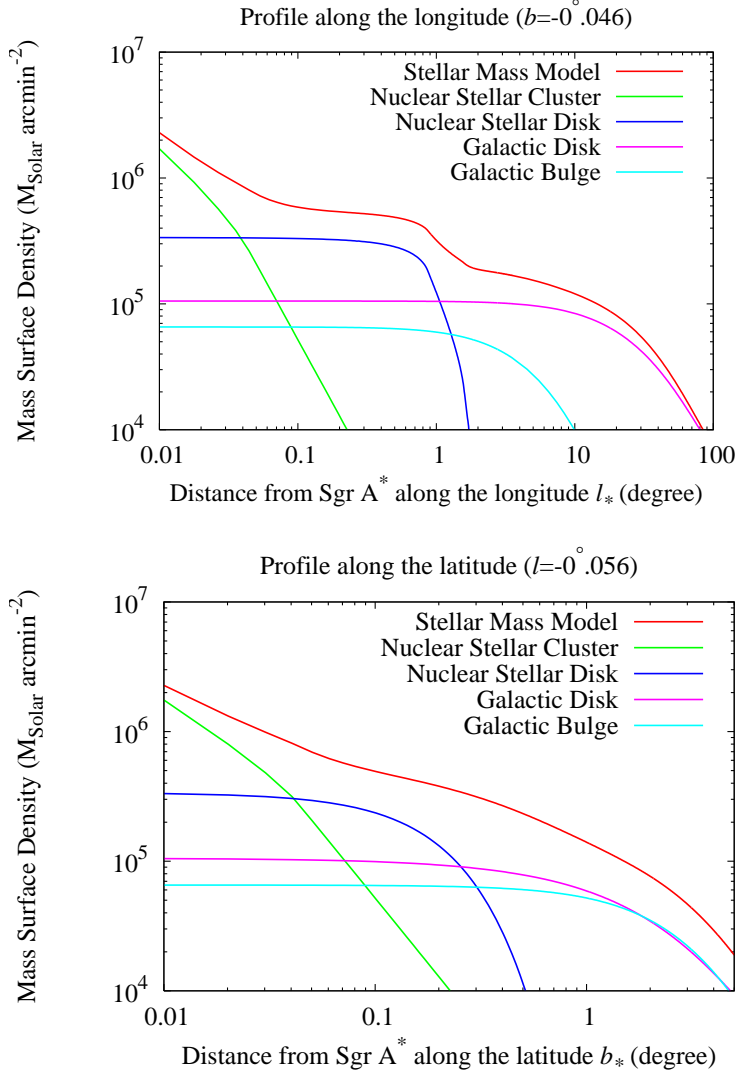


Figure 7.1: Stellar mass model along the galactic longitude (top,  $b = -0^\circ.046$ ) and latitude (bottom,  $l = -0^\circ.056$ ). This model is based on the infrared observations [60, 42]. The detail of this model is described in Munro et al. [81].

We fitted the stellar mass model to the intensity profiles of the Fe  $K\alpha$  lines. The normalization of the model was a free parameter. The intensity profiles along the galactic longitude and latitude were used for the fittings simultaneously. The best-fit result of the Fe XXV  $K\alpha$  line is shown in figure 7.2 and 7.3. Both of the profiles of the GDXE and the stellar mass similarly decrease at  $l = 1^\circ - 2^\circ$  which corresponds to the border of the NB and GD. The profiles of the GDXE and the stellar mass are, however, clearly different. The data points exceed the best-fit model in the inner region ( $l_* < 1^\circ$ ) but fall below in the outer region ( $l_* > 2^\circ$ ) and the  $b = -2^\circ$

region.

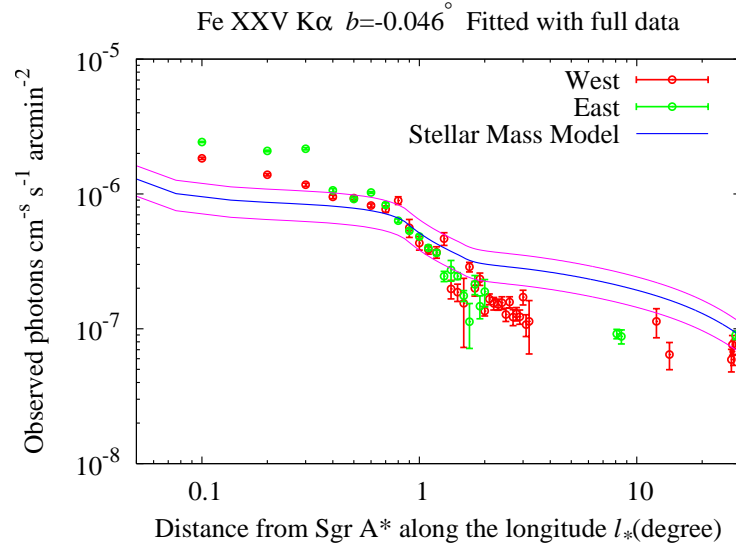


Figure 7.2: The result of the fitting the stellar mass model to the profile of the Fe XXV  $K\alpha$  line emission along the galactic longitude. The magenta lines show the  $1\sigma$  uncertainty.

Revnivtsev et al. [102] reported that the Fe  $K\alpha$  line intensity profile agree with the NIR profile well in  $l_* = 1^\circ$ – $100^\circ$  with the RXTE data. We also excluded the data points in the inner  $2^\circ \times 1^\circ$  region and fitted the stellar mass model to the Fe  $K\alpha$  line intensity profiles. The results are shown in figure 7.4–7.7. The outer region ( $l_* > 1^\circ$  or  $b_* > 0^\circ.5$ ) is fitted well. On the other hand, the Fe  $K\alpha$  line intensities excess the stellar mass model in the inner region.

Revnivtsev et al. [102] reported that, in  $l_* = 1^\circ$ – $100^\circ$ , the ratio of the Fe  $K\alpha$  line intensity to the  $4.9 \mu\text{m}$  NIR intensity is  $I_{\text{Fe}K\alpha} [\text{photon s}^{-1} \text{cm}^{-2} \text{deg}^{-2}] = 4.7 \times 10^{-5} I_{4.9\mu\text{m}} [\text{MJy str}^{-1}]$ . Note that Revnivtsev et al. [102] did not resolve the three Fe  $K\alpha$  lines because they used a proportional counter (PCA) on the RXTE, whose energy resolution is  $\sim 18\%$  at 6 keV. To compare the result of Revnivtsev et al. with ours, we summed the intensities of the three Fe  $K\alpha$  lines and convert our fitting results in the outer region to  $I_{\text{Fe}K\alpha} [\text{photon s}^{-1} \text{cm}^{-2} \text{deg}^{-2}] = (3.6 \pm 0.9) \times 10^{-5} I_{4.9\mu\text{m}} [\text{MJy str}^{-1}]$ . The error shows the uncertainty of the stellar mass model. The ratio of the Fe  $K\alpha$  line intensity to the NIR intensity we obtained is almost consistent with the result of [102] in the uncertainty.

For the inner region ( $l_* < 1^\circ$ ), Revnivtsev et al. [102] did not obtain reliable results because of the low angular resolution (FWHM  $\sim 1^\circ$ ) of the RXTE satellite. We revealed that the inner region, the intensity profiles of the  $K\alpha$  lines do not match the NIR profile and excess it about 40% in  $l_* = 0^\circ.1$ – $1^\circ$ .

We should note that this discussion depends on the uncertainty of the stellar mass model. The stellar mass model is based on the result of COBE whose angular resolution is low (FWHM  $\sim 0.7^\circ$ ) and thus has large uncertainty<sup>1</sup>. If we consider the 90% uncertainty of the stellar mass model, the data points and the model in figure 7.2 and 7.3 roughly match and thus the excess of the GDXE in  $l_* < 1^\circ$  is not clear. A more accelerate stellar mass model is required to compare

<sup>1</sup>The ground-observation data with the high resolution of less than  $1''$  is used to build the stellar mass model of the inner 30 pc ( $R < 0^\circ.2$ ). See Launhardt et al. [60] in detail.

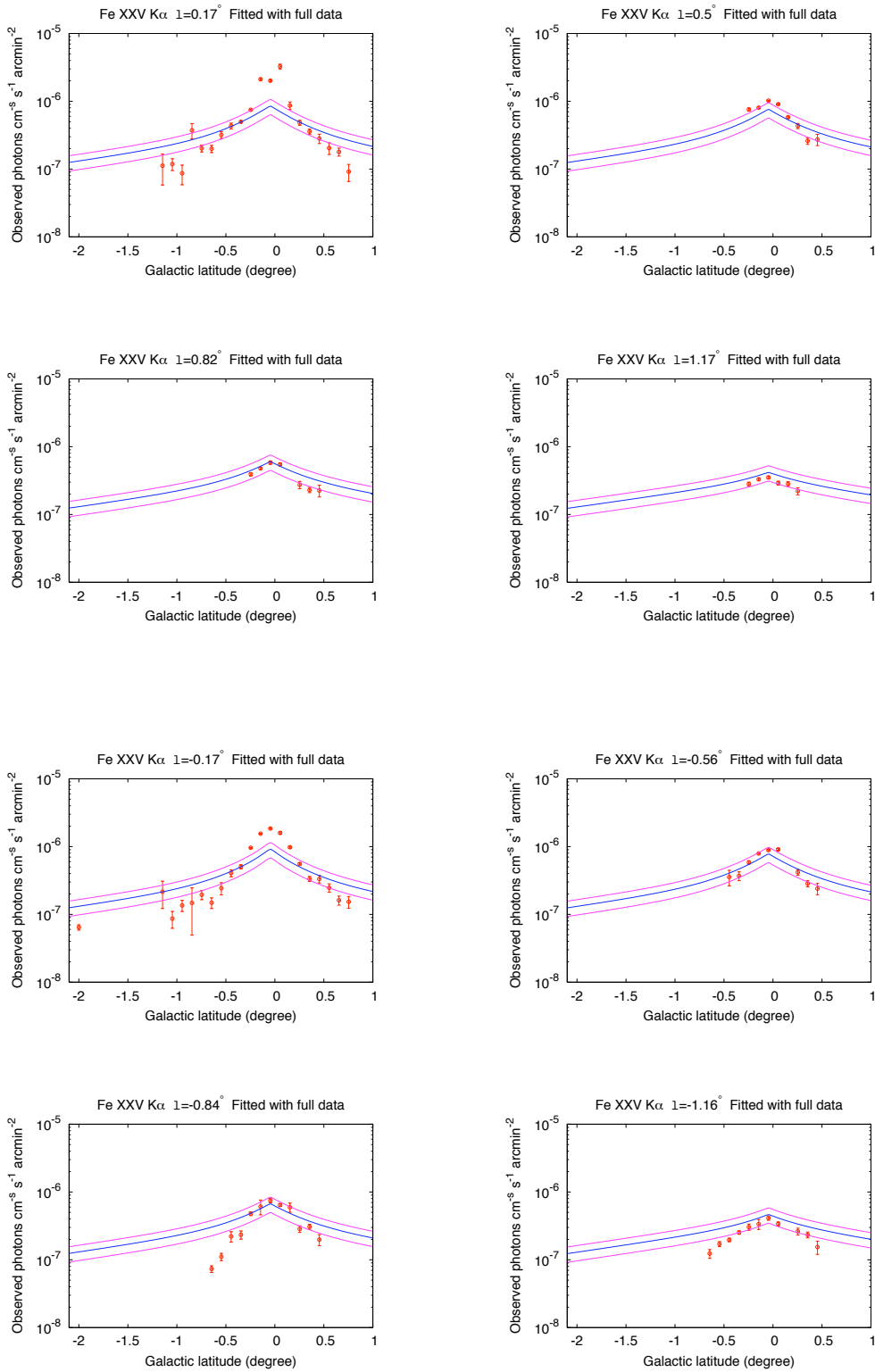


Figure 7.3: The result of the fitting the stellar mass model to the profile of the Fe XXV  $K\alpha$  line emission along the latitudes. The magenta lines show the  $1\sigma$  uncertainty.

with our results.

### 7.1.3 Comparisons with Distribution of X-ray Point Sources Observed with Chandra

We compare the intensity profile of the Fe XXV  $K\alpha$  line with that of X-ray point sources obtained with Chandra. Munro et al. made point source catalog with the Chandra 2 Ms data of the  $2^\circ \times 0^\circ.8$  GC region. It contains 9017 point sources with the photometry data (e.g. hardness ratio, photon flux in the 0.5–2 and 2–8 keV bands etc.) [82]. Using the Chandra catalog, we constructed the number distribution of the point sources in the regions shown in figure 7.8. To preserve completeness limit, we selected the point sources brighter than  $2 \times 10^{-6}$  photons  $\text{cm}^{-2} \text{s}^{-1}$  (0.5–8 keV). The number distributions of the point sources are shown in figure 7.9. The intensity profile of the Fe XXV  $K\alpha$  line in the arbitrary unit are plotted in figure 7.9 for comparison. Koyama et al. reported that the intensity profile of the Fe XXV  $K\alpha$  line at the Sgr A region ( $l_* < 0^\circ.3, b_* < 0^\circ.05$ ) has a gradual increase toward Sgr A\* compared with the sharp profile of point sources [50]. In the region of  $l_* < 0^\circ.8, b_* < 0^\circ.4$ , however, we do not found clear difference between the profiles of the Fe XXV  $K\alpha$  line intensity and point sources.

## 7.2 Spectra of the GDXE

Here we discuss the variation of the GDXE spectra in  $-3^\circ < l < 2^\circ$ . We concentrate on the line intensity ratio of Fe XXVI  $K\alpha$  to Fe XXV  $K\alpha$  and equivalent widths. They are little affected by the uncertainty of the interstellar absorption and the systematic errors of the detector because they are relative relations of the photon intensities in the close energy bands.

### 7.2.1 Line Intensity Ratios of Fe XXVI $K\alpha$ to Fe XXV $K\alpha$

Koyama et al. [51] and Yamauchi et al. [143] reported that the typical line intensity ratios of Fe XXVI  $K\alpha$  to Fe XXV  $K\alpha$  in the Sgr A region ( $l_* < 0.3^\circ$ ) and the ridge ( $l_* > 8^\circ$ ) are  $0.33 \pm 0.02$  and  $0.22 \pm 0.06$ , respectively. We revealed the line intensity ratio in the transition region. The profile of the line intensity ratio along the galactic longitude is shown in the top panel of figure 4.25. The line intensity ratio decrease along with  $l_*$  significantly. The hypothesis of the constant ratio is rejected with the 99.5 % confidence  $\chi^2$ -test.

The ratio at  $l_* = 3^\circ$  is almost same as that in the ridge. The transition of the ratio happens in  $l_* = 1^\circ$ – $2^\circ$  which corresponds to the border between the NB and the GD as shown in the left panel of figure 7.1. Figure 4.18 shows that the e-falling scale of the intensity profile of the Fe XXV  $K\alpha$  line also changes around  $l_* = 1^\circ$ – $2^\circ$ . These facts suggest that the GDXE contains two components which accompany the NB and the GD, respectively. The simplest interpretation of the variation of the line intensity ratio is that the temperature of the plasma emitting the GDXE decreases from  $kT = 7$  keV to 6 keV along  $l_*$ . If there are the two components of the GDXE, the NB component is hotter than the GD component. If the GDXE is truly diffuse plasma, the result show the spatial difference of the plasma temperature. If the origin of the GDXE is the integration of the point sources, the natures of the faint X-ray point sources might be different be the GC (or the NB) and the ridge (or the GD).

The scale heights of the line intensity profiles at  $l = \pm 0^\circ.17$  (figure 4.19) of Fe XXV  $K\alpha$  changes around  $b_* = 0^\circ.5$ – $1^\circ$  which corresponds to the border between the NB, and the GD and

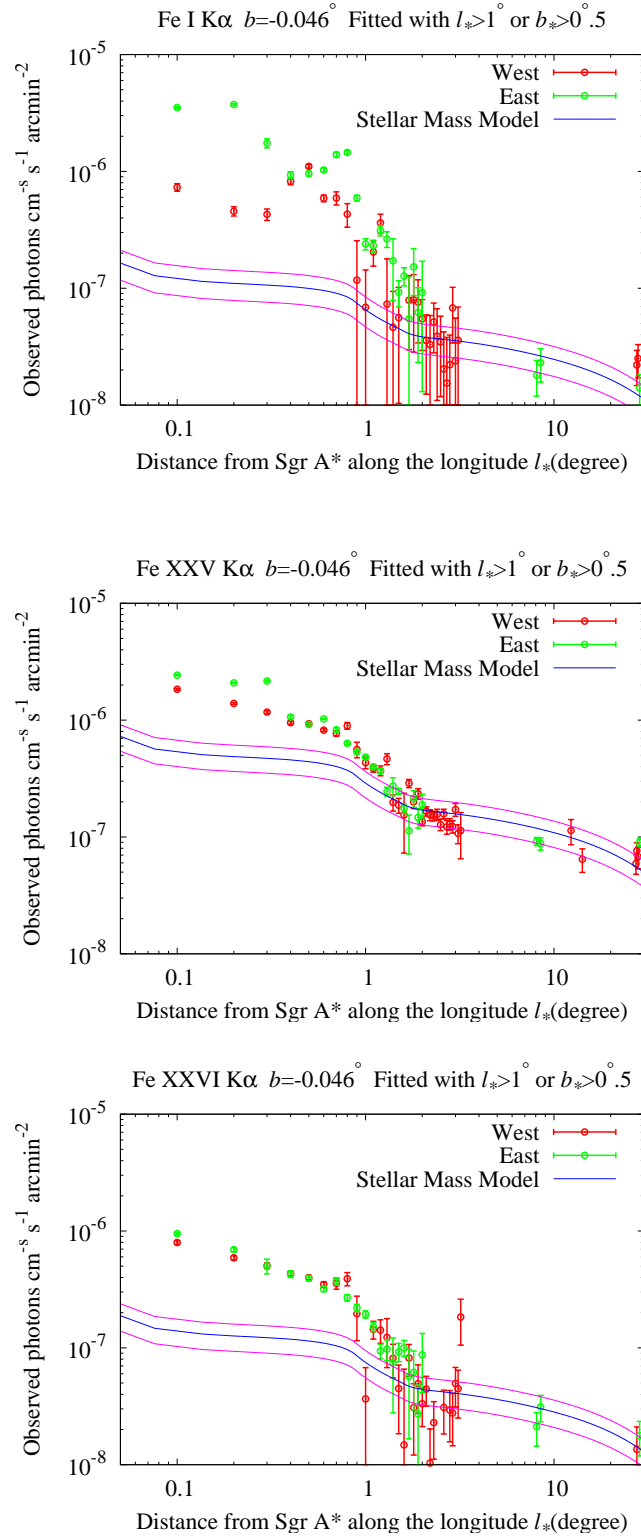


Figure 7.4: The results of the fitting the stellar mass model to the intensity profiles of the Fe K $\alpha$  lines along the galactic longitude. The data points in the inner  $2^\circ \times 1^\circ$  region were not used for the fittings. The magenta lines show the  $1\sigma$  uncertainty. Top: the Fe I K $\alpha$  line. Middle: the Fe XXV K $\alpha$  line. Bottom: the Fe XXVI K $\alpha$  line.

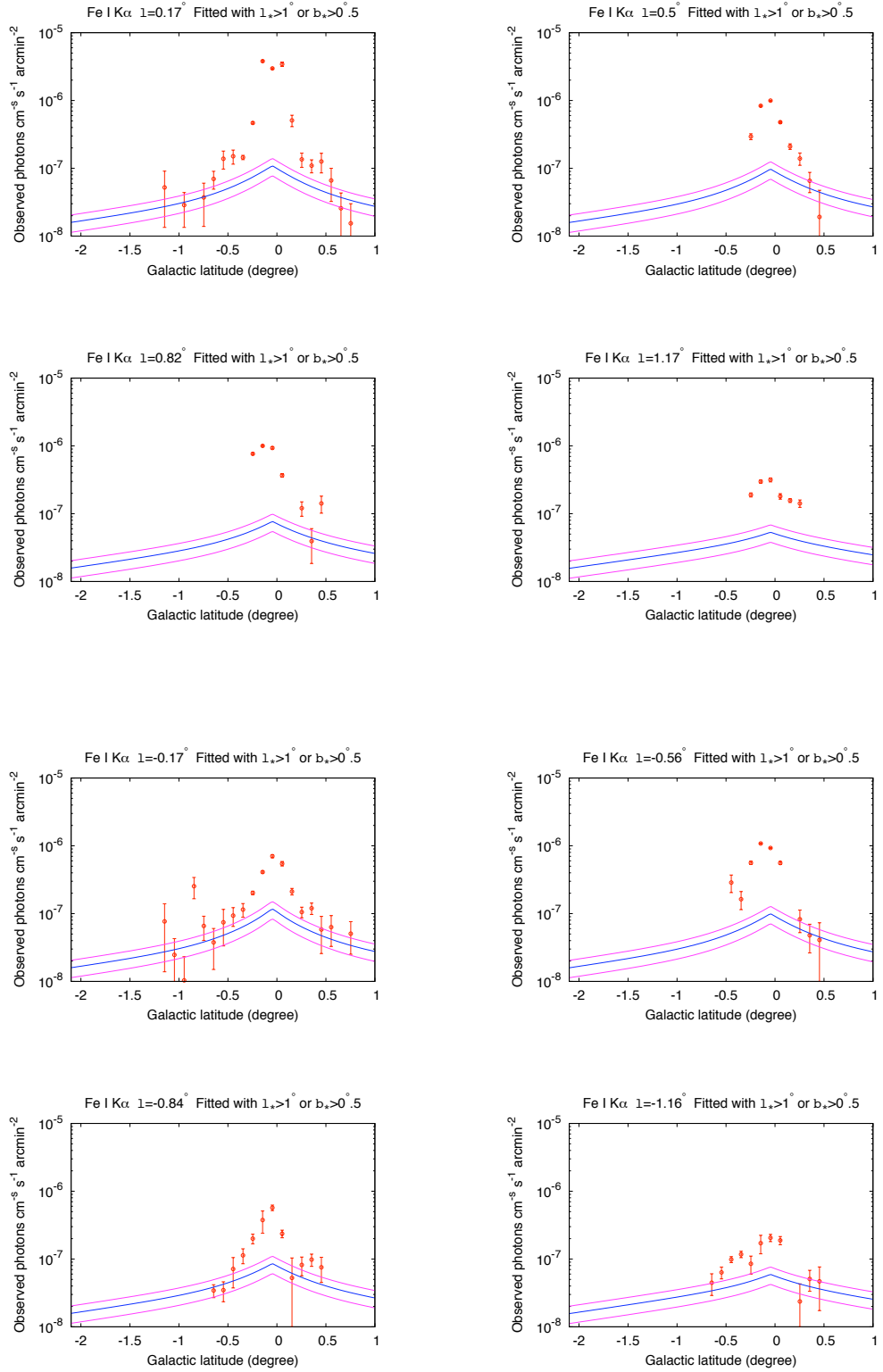


Figure 7.5: The result of the fitting the stellar mass model to the profile of the Fe I K $\alpha$  line emission along the galactic latitude. The data points in the inner  $2^\circ \times 1^\circ$  region were not used for the fitting. The magenta lines show the  $1\sigma$  uncertainty.

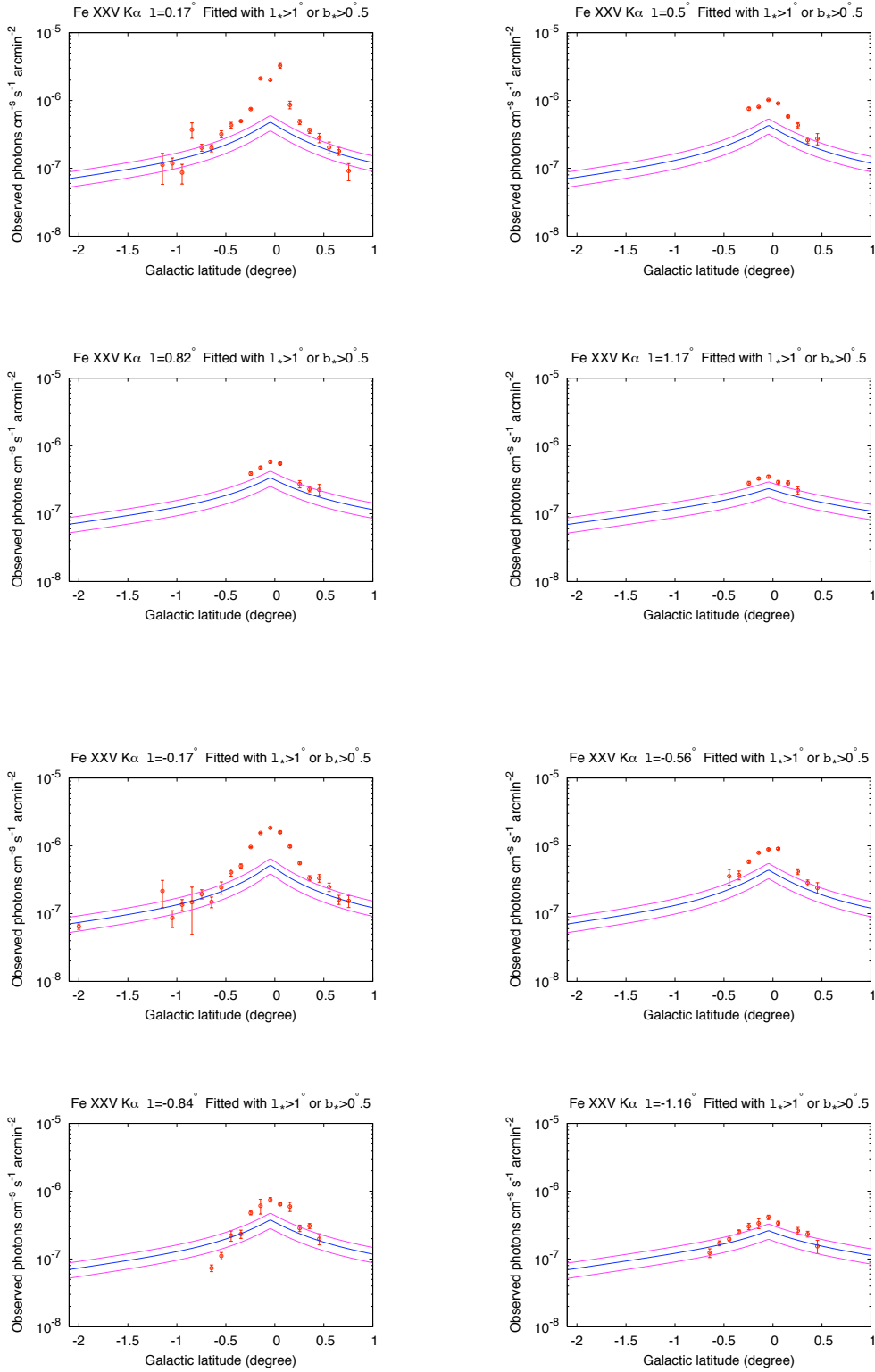


Figure 7.6: The result of the fitting the stellar mass model to the profile of the Fe XXV  $K\alpha$  line emission along the galactic latitude. The data points in the inner  $2^\circ \times 1^\circ$  region were not used for the fitting. The magenta lines show the  $1\sigma$  uncertainty.

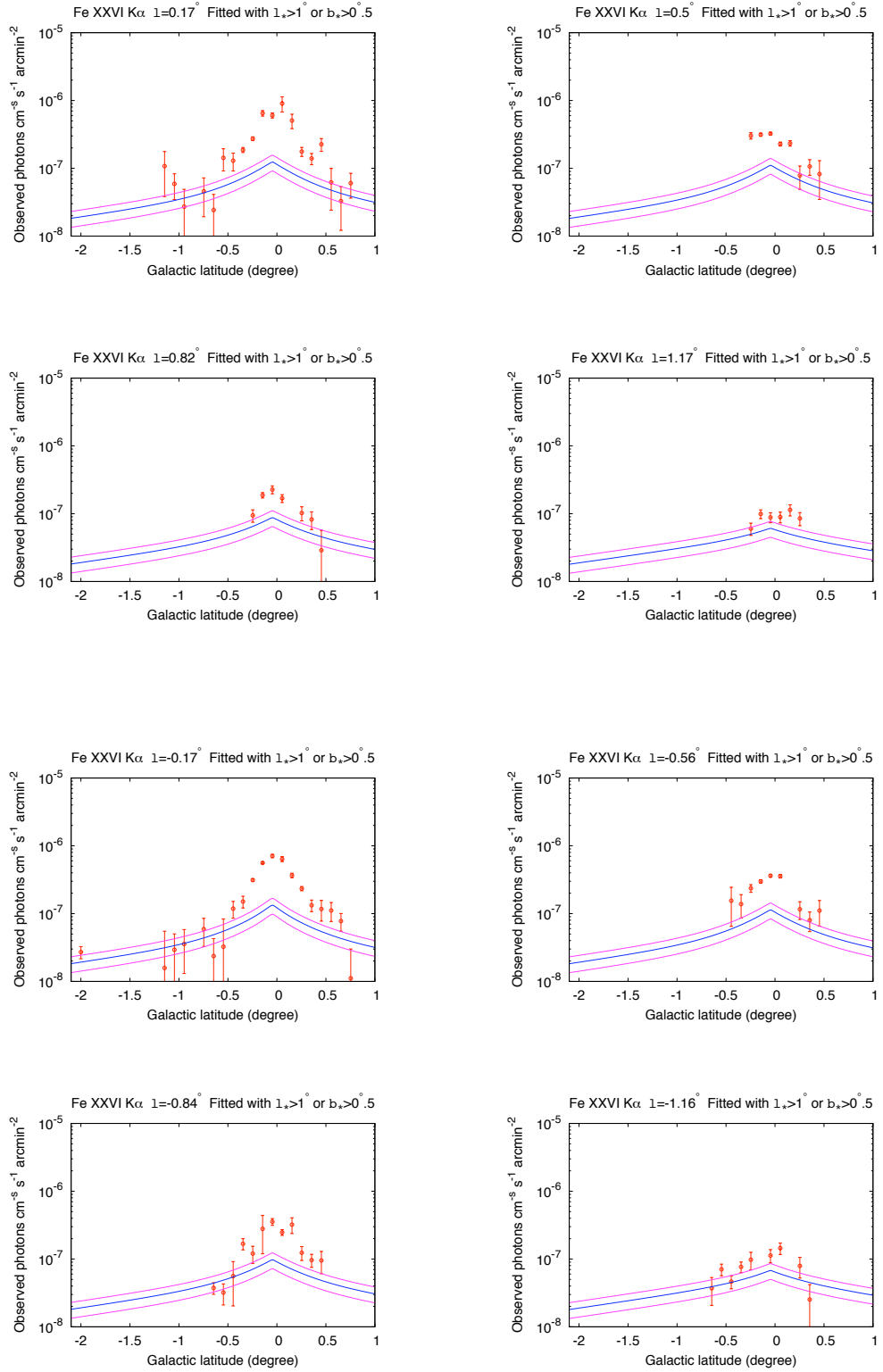


Figure 7.7: The result of the fitting the stellar mass model to the profile of the Fe XXVI  $K\alpha$  line emission along the galactic latitude. The data points in the inner  $2^\circ \times 1^\circ$  region were not used for the fitting. The magenta lines show the  $1\sigma$  uncertainty.

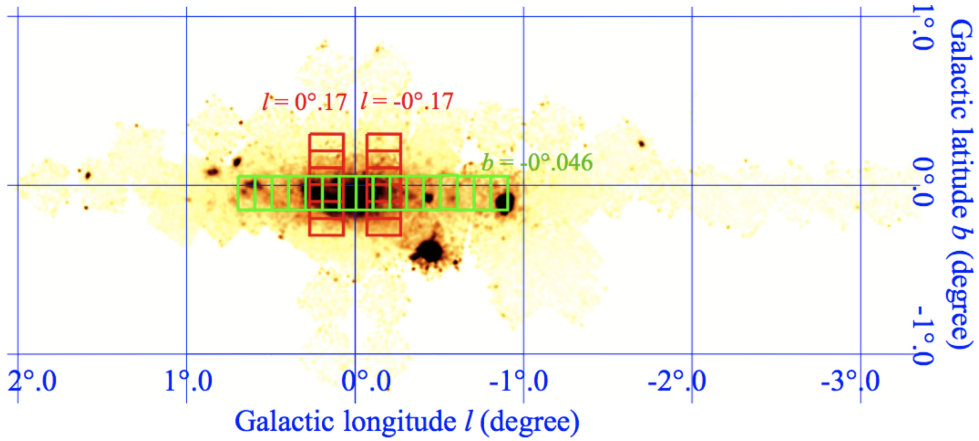


Figure 7.8: The regions where we constructed the number distribution of the X-ray point sources using the Chandra data. They are overlaid on the X-ray image in the 6.55–6.8 keV band obtained with the Suzaku XIS.

GB (the bottom panel of figure 7.1). It indicates that the GDXE might have a component which accompany the GB. On the other hand, the profile of the line intensity ratio of Fe XXVI  $K\alpha$  to Fe XXV  $K\alpha$  along the latitude (the top panel of figure 4.25) does not change over  $b_* = 0^\circ - 2^\circ$  significantly. The line intensity ratios of the GB and GC components might be similar but the current off-plane data are insufficient to clarify the difference between the line intensity ratios between the GC and GB. More observations for the large  $b^*$  regions with the long exposures will reveal it. It is a future work.

## 7.2.2 Relation between the Equivalent Widths of the Fe I $K\alpha$ and Fe XXV $K\alpha$ Line Emissions

Koyama et al. [55] analyzed the GDXE spectra in the Sgr A region ( $l_* < 0^\circ.3$ ) and found the anti-correlation between the equivalent widths of the Fe I  $K\alpha$  and Fe XXV  $K\alpha$  lines. Using this relation, the GDXE in the Sgr A region was decomposed phenomenologically into two components; the Fe I  $K\alpha$  line emission with its associated continuum (6.4-component) and Fe XXV  $K\alpha$  line emission with its associated continuum (6.7-component). The Suzaku data of the Sgr C region were analyzed with the same method by Nakajima et al. [84].

We used the same method to decompose the GDXE into the 6.4- and 6.7-components. The relation between the equivalent widths of the Fe I  $K\alpha$  ( $EW_{6.4}$ ) and Fe XXV  $K\alpha$  ( $EW_{6.7}$ ) lines are shown in figure 7.10. We found two groups in the on-plane data (the left panel of figure 7.10). One group consists of region 2 and 3, which correspond to the giant molecular regions (Sgr B and Sgr C, respectively). This group has large equivalent widths of the Fe I  $K\alpha$  line. The other group consists of region 1, 4 and 5, which are the regions outside the NB ( $l_* > 1^\circ$ ). It has an clear anti-correlation between  $EW_{6.4}$  and  $EW_{6.7}$ . The best-fit linear function is  $EW_{6.7} + 0.83(\pm 0.07) \times EW_{6.4} = 0.61(\pm 0.06)$  (keV). We also plot the average of the data in  $|l| > 8^\circ$  obtained by Yamauchi et al. [143] in figure 7.10. The data point in  $|l| > 8^\circ$  is located on the relation of region 1, 4 and 5. The equivalent width of the Fe I  $K\alpha$  line to its associated continuum ( $EW'_{6.4}$ ), which is obtained as the  $EW_{6.4}$  in the limit of  $EW_{6.7} \rightarrow 0$ , is  $0.74 \pm 0.04$  keV. The  $EW'_{6.4}$  is rid of the effect of the continuum associated with the Fe XXV  $K\alpha$  line and

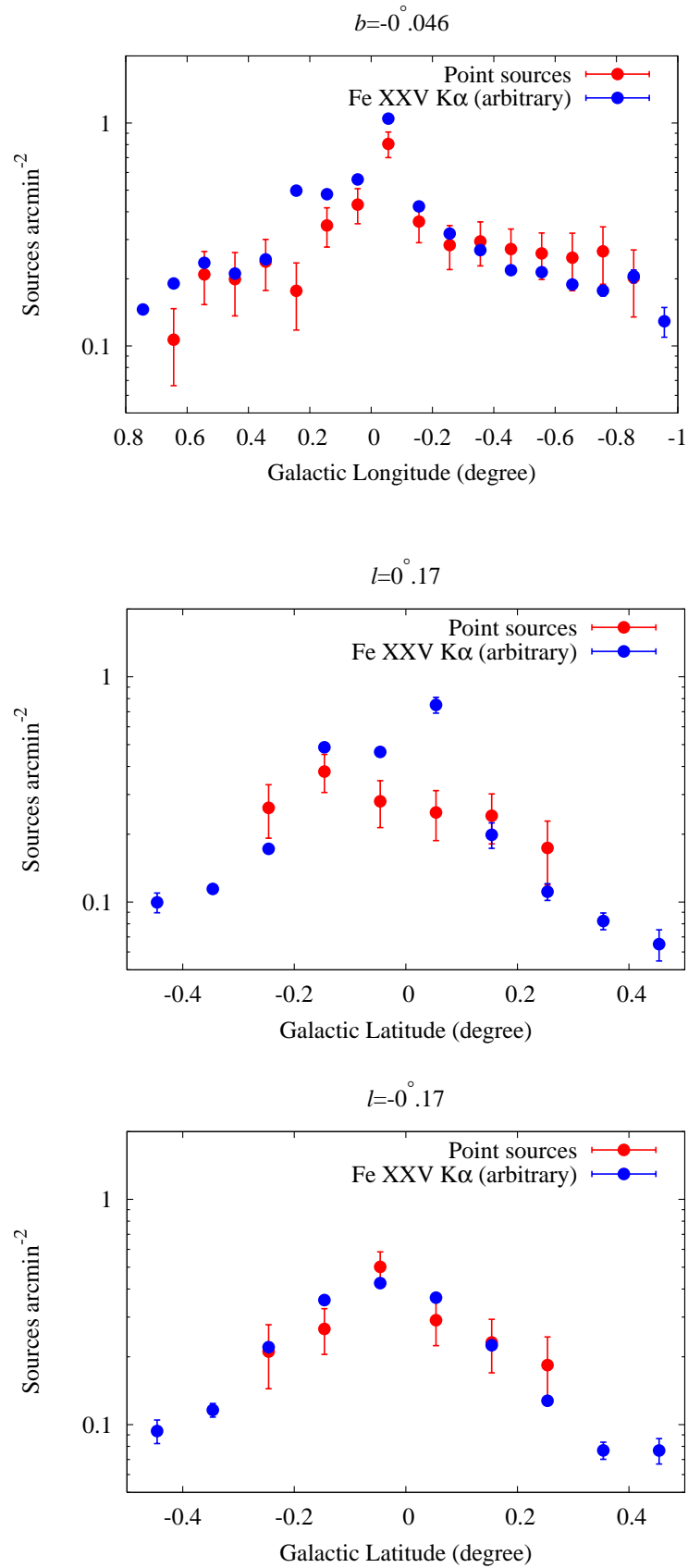


Figure 7.9: The number distributions of the X-ray point sources detected by Chandara. The profiles were measured in the regions shown in figure 7.8. The profiles of the Fe XXV K $\alpha$  line emission in the arbitrary unit are also plotted for comparison.

thus directly reflects the emission process of the Fe I  $K\alpha$  line. The  $EW'_{6.7}$ , which is defined as the  $EW_{6.7}$  in the limit of  $EW_{6.7} \rightarrow 0$ , is  $0.60 \pm 0.06$  keV. The results of the Sgr A, C regions and  $l_* = 1^\circ\text{--}3^\circ$  (region 1, 4 and 5) are summarized in table 7.1. The  $EW'_{6.7}$  is similarly  $\sim 0.6$  keV in the Sgr A, C regions and  $l_* = 1^\circ\text{--}3^\circ$ . On the other hand, the  $EW'_{6.4}$  is  $0.74 \pm 0.04$  keV in  $l_* = 1^\circ\text{--}3^\circ$ , significantly smaller than those in the Sgr A and C regions (1.2 and 2 keV). This result indicates that the origins of the Fe I  $K\alpha$  are different between the inner and outside regions of the NB or the CMZ.

The relation between  $EW_{6.4}$  and  $EW_{6.7}$  of the off-plane data is shown in the right panel of figure 7.10. There is no clear relation. The near center and north east regions (region A, B, C and F) seem to match the relation of the on-plane data (dotted line). The south west region (region D, E, H and  $b = -2^\circ$ ), however, does not follow the relation. The equivalent widths of region D, E and H are close to those of the point sources in the Sgr A region ( $EW_{6.4} \sim 140$  eV,  $EW_{6.7} \sim 400$  eV) [80]. The GDXE of these regions might be the integration of point sources. The spectra of the point sources in these regions have not been studied well and might be different from those in the Sgr A region.

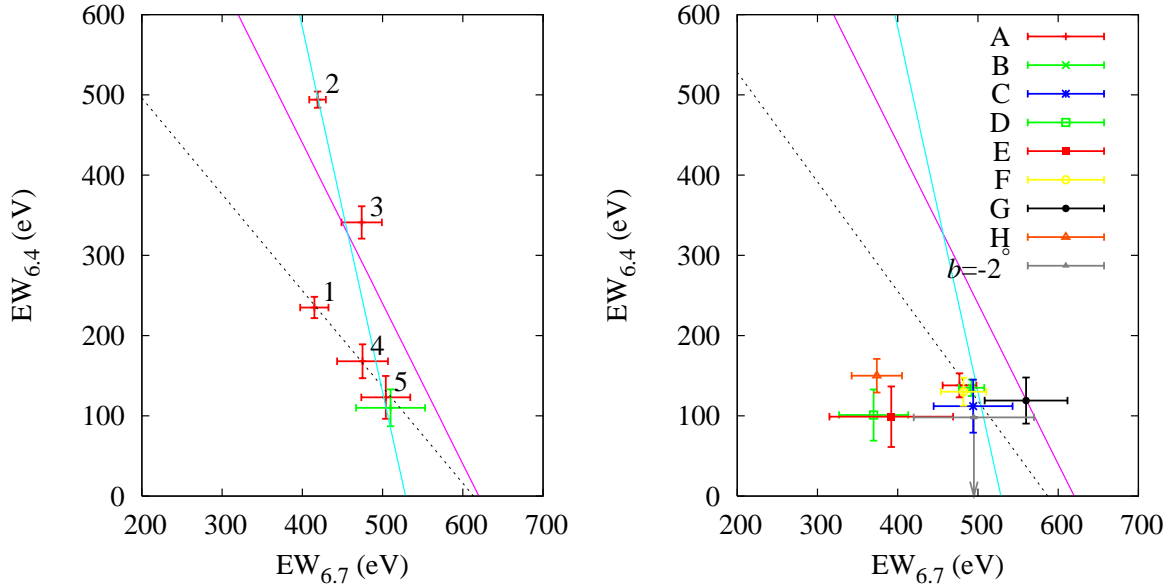


Figure 7.10: The relation between the equivalent widths of the Fe XXV  $K\alpha$  ( $EW_{6.7}$ ) and Fe I  $K\alpha$  ( $EW_{6.4}$ ) lines. The error bars show the 90 % confidence level. The dotted line shows the linear relation determined by region 1, 4 and 5. The magenta and cyan lines show the relations in the Sgr A and C regions [55, 84]. Left: the on-plane data. The green data point shows the averaged result in  $|l| > 8^\circ$  [143]. Right: same but for the off-plane data.

### 7.2.3 Center Energy of the Fe XXV $K\alpha$ Line Emission

We comment on the profiles of the center energies shown in figure 4.26. The center energy of Fe XXV  $K\alpha$  becomes lower at large  $l_*$ . The center energy of Fe XXV  $K\alpha$  in region 5 is  $6664^{+6}_{-4}$  eV which is closer to that of the charge exchange origin than that of the CIE plasma origin [51]. The systematic errors are, however, large and thus the shift of the line center is not reliable. As described in section 3.3.4, the energy scale calibration has large uncertainty due to the CTI. The

Table 7.1: The equivalent widths of the Fe XXV  $K\alpha$  and I  $K\alpha$  lines to their associated continua.\*

Region	$EW'_{6.7}$ [ $EW_{6.4} \rightarrow 0$ ] (eV)	$EW'_{6.4}$ [ $EW_{6.7} \rightarrow 0$ ] (eV)	Ref.
Sgr A	$620 \pm 70$	$1200 \pm 200$	[55]
Sgr C	$530 \pm 60$	$2400^{+2300}_{-700}$	[84]
$l_* = 1^\circ\text{--}3^\circ$	$600 \pm 60$	$740 \pm 40$	This work

\* The uncertainties show the 90 % confidence level.

distinction of the Fe XXV  $K\alpha$  line centers between the charge exchange and the CIE plasma comes from the difference of the line flux ratio of the resonance, intercombination and forbidden lines. The Soft X-ray Spectrometer (SXS) onboard the ASTRO-H satellite will resolve these lines with the energy resolution of  $\leq 7$  eV and reveal whether this shift of the line center energy we observed is true or not.

### 7.3 Comparison between the Intensities of the GDXE and X-ray Point Sources Detected with Chandra

We compare the intensities of the GDXE with that of integrated point sources detected with Chandra [82]. Munro et al. [78] and Revnivtsev et al. [105] made similar comparisons for the Sgr A region. We further analyzed region 2, 3, and A, which the catalog [82] covers. In the Chandra catalog [82], photon flux in the 2–8 keV band and hardness ratio of each point source are listed. Assuming that power-law spectrum for the point sources, we converted the photon flux and the hardness ratio given in [82] into energy flux in the 5–10 keV band. The results are summarized in figure 7.11 and table 7.2. Comparisons with the integrated intensity of the point sources  $I_{\text{point sources}}$  and the observed GRXE intensity  $I_{\text{GDXE}}$  show that 4–15% of the GDXE is resolved into point sources.

The log N-log S distributions in the Sgr A region was studied by Munro et al [82]. The number density per solid angle of point sources brighter than the flux  $F$  is proportional to  $F^{-\alpha}$  which is  $\sim 1.6$  for the Sgr A region. Assuming this relation, we extrapolated from the sensitivity limit of the current observation  $F_{\text{limit}}$  and estimated the necessary limit flux ( $F_{100\% \text{GDXE}}$ ) to resolve all of the GDXE into point sources (figure 7.11). The results are shown in table 7.2.

The necessary limit fluxes are  $5 \times 10^{-18} - 2 \times 10^{-16}$  erg s $^{-1}$  cm $^{-2}$ , 2–3 order smaller than the current limits. The region 2 and 3 corresponds to the Sgr B and C regions which contain the X-ray reflection nebula and the strong 6.4-component emission. This might be the reason why the  $F_{100\% \text{GDXE}}$  of region 2 and 3 is much smaller than that of region A.

### 7.4 Properties of Sgr A East and Other GC SNR and Their Contribution to the GDXE

In this thesis, we successfully determined the temperature of Sgr A East is free from the non-thermal component. Sgr A East has a peculiarly hot component ( $kT \sim 6$  keV) as a SNR, but its line intensity ratio of Fe XXV  $K\alpha$  to Fe XXVI  $K\alpha$  is 0.05, and smaller than that (0.2–0.4) of the GDXE.

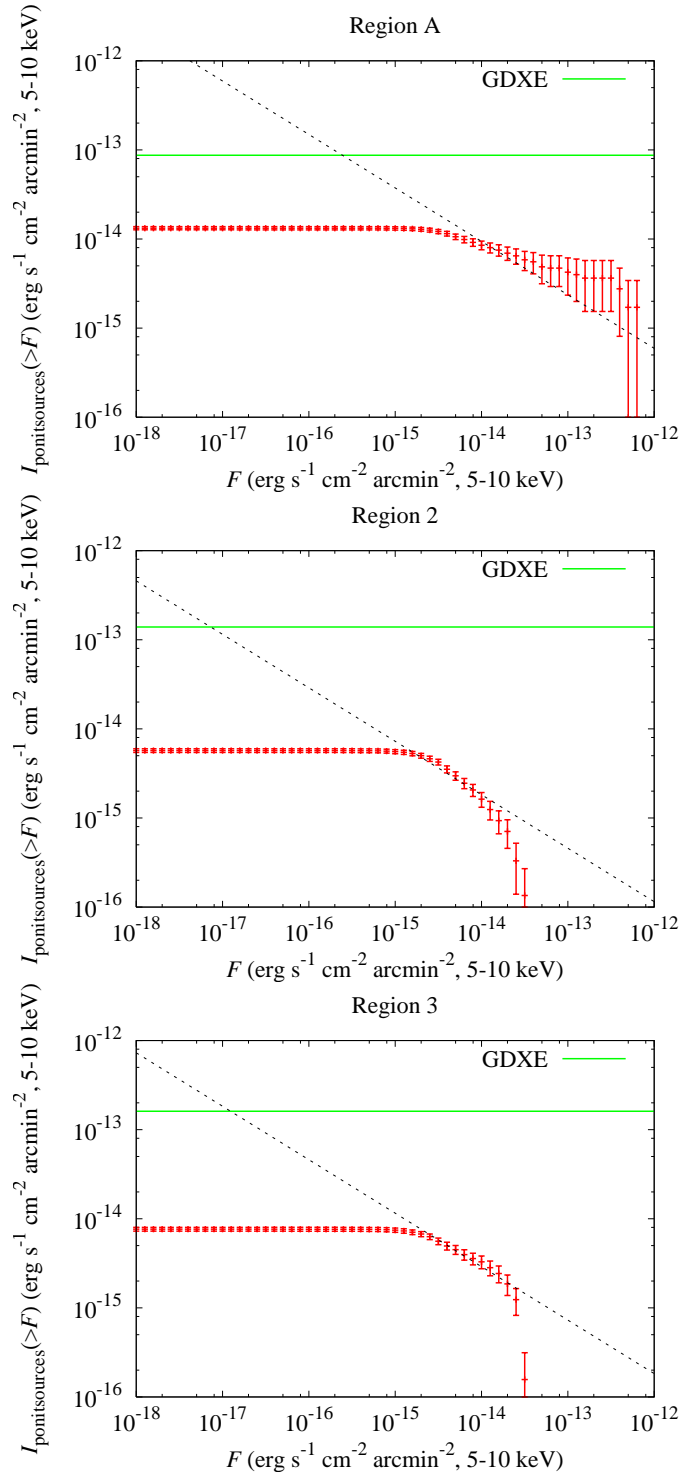


Figure 7.11: Comparison between the intensities of the GDXE and integrated point sources detected with Chandra. The horizontal and vertical axes show the flux of point sources  $F$  and the integrated intensity of the point sources brighter than  $F$ . The green line shows the intensity of the GDXE. The dotted line shows the  $\alpha = 1.6$  relation extrapolated from  $(F_{\text{limit}}, I_{\text{pointsources}(> F_{\text{limit}})})$ .

Table 7.2: Comparison between the Intensities of the GDXE and integrated point sources detected with Chandra.

Region	$I_{\text{GDXE}}^*$ ( $10^{-14}$ )	$I_{\text{pointsources}}^*$ ( $10^{-14}$ )	$F_{\text{limit}}^\dagger$	$F_{100\% \text{GDXE}}^\dagger$
A	8.7	1.3	$1.6 \times 10^{-14}$	$2.4 \times 10^{-16}$
2	13.9	0.56	$6.5 \times 10^{-15}$	$4.5 \times 10^{-18}$
3	16.1	0.75	$1.2 \times 10^{-14}$	$1.3 \times 10^{-17}$

\* The unit is observed  $\text{erg s}^{-1} \text{cm}^{-2} \text{arcmin}^{-2}$  (5–10 keV).  $^\dagger$  The unit is observed  $\text{erg s}^{-1} \text{cm}^{-2}$  (5–10 keV).

Table 7.3: Properties of supernova remnants in the GC region.

	$kT$ (keV)	$L_X$ ( $\text{erg s}^{-1}$ )	Thermal energy (erg)	Ref.
Sgr A East	$1.21 \pm 0.01, 6.0_{-0.6}^{+0.5}$	$4.2 \times 10^{35}$	$2.8 \times 10^{50}$	This work
G359.79-0.26	$1.02_{-0.04}^{+0.03}$	$3.6 \times 10^{35}$	$1.7 \times 10^{50}$	[74]
G359.77-0.09	$0.66_{-0.09}^{+0.08}$	$1.1 \times 10^{35}$	$1.9 \times 10^{50}$	[75]
G359.41-0.21	$0.90_{-0.3}^{+0.2}$	$2.2 \times 10^{34}$	$3.9 \times 10^{49}$	[133]
G0.61+0.01	$3.2_{-0.9}^{+2.3}$	$1.5 \times 10^{34}$	$2.4 \times 10^{49}$	[53]
G1.2-0.0	$0.9 \pm 0.2$	$1.4 \times 10^{35}$	$< 10^{51}$	[113]
G1.02-0.18	$1.9_{-0.3}^{+0.5}$	$4.2 \times 10^{33}$	$3.8 \times 10^{49}$	[86]

The properties of other SNRs in the GC region are summarized in table 7.3. Their temperatures ( $kT \sim 1\text{--}3$  keV) are also too low to explain the line intensity ratio of Fe XXV  $K\alpha$  to Fe XXVI  $K\alpha$  of the GDXE. It is impossible to explain the spectra of the GDXE only by the GC SNRs.

## 7.5 Properties of Suzaku J1740.5-3014 and Other Point Sources and Their Contribution to the GDXE

We studied Suzaku J1740.5-3014 as a candidate source in the intermediate region between the GC and the ridge but it is likely to be in the foreground region (distance  $\sim 2$  kpc). The properties of Suzaku J1740.5-3014, known CVs in the vicinity of the Sun, and the point sources in the Sgr A region are summarized in table 7.4.

The integrated spectrum of the point sources in the Sgr A region (hereafter “the Sgr A point sources”) has about 2–3 times larger equivalent widths of the Fe  $K\alpha$  lines than those of known CVs. On the other hand, It indicates that the metal abundance of the Sgr A point sources might be systematically large. The mean metal abundance of known CVs is 0.3 solar [20] and thus, if the most of the Sgr A point sources are CVs as shown by Munro et al. [80], the metal abundance should be  $\sim 1$  solar. Such a high-abundance CVs might belong to the NB, and ordinary low-abundance CVs might belong to the Galactic bulge and ridge. Systematic observation of X-ray point sources in the intermediate region between the GC and the ridge will reveal that because this region is the transition point. It is one of the future works.

Table 7.4: Properties of Suzaku J1740.5-3014, known CVs in the vicinity of the Sun, and the GC point sources\*.

	$EW_{6.4}$ (eV)	$EW_{6.7}$ (eV)	$I_{6.97}/I_{6.7}$	$L_X$ (erg s $^{-1}$ )	Ref.
Suzaku J1740.5-3014	$210^{+30}_{-50}$	$190^{+60}_{-40}$	$0.68 \pm 0.30$	$1 \times 10^{33}$	This work
Average of non-mCVs	$\sim 50$	$\sim 130$	$\sim 0.48$	$10^{29.5-10^{32.5}}$	[99, 80]
Average of polar CVs	$\sim 120$	$\sim 160$	$\sim 0.67$	$10^{30-10^{33}}$	[20]
Average of IP CVs	$\sim 130$	$\sim 120$	$\sim 0.58$	$10^{31-10^{33}}$	[20, 80]
Sgr A point sources $^\dagger$	$137 \pm 21$	$404 \pm 59$	$0.56 \pm 0.13$	–	[80]

\*The error shows 90% confidence level.  $^\dagger$  The values of faint sources ( $C < 500$ ) in table 4 of [80].

The line intensity ratio of Fe XXVI  $K\alpha$  to Fe XXV  $K\alpha$  is not different among the Sgr A point sources and known CVs (non-magnetic CVs, IPs, polars) in the vicinity of the Sun. The line intensity ratio of Sgr A point sources and known CVs is too high ( $\sim 0.6$ ) for that of the GDXE ( $\sim 0.2-0.4$ ). The characteristics of the Sgr A point sources and known CVs are the strong Fe XXVI  $K\alpha$  line emission. On the other hand, the known Galactic diffuse objects do not emit the strong Fe XXVI  $K\alpha$  line emission. Most of the Fe XXVI  $K\alpha$  line emission of the GDXE might come from point point sources.

# Chapter 8

## Conclusion

With the Suzaku satellite, we performed a study of the GDXE in the region from the GC to the ridge and the bulge ( $-3^\circ < l < 2^\circ$ ,  $-2^\circ < b < 1^\circ$ ). We also studied Sgr A East, the SNR located in the GC, and a newly found X-ray point source, Suzaku J1740.5–3014, in the data set.

The intensity profiles of the highly ionized Fe K $\alpha$  lines and the continuum in the GDXE including the data points in the ridge ( $l_* > 8^\circ$ ) are described with phenomenological two-exponential-component models.

The e-folding scale of the intensity profile along the longitude changes from  $\sim 0^\circ.5$  to  $\sim 30^\circ$  around  $l_* = 1^\circ$ – $2^\circ$ . The line intensity ratio of Fe XXVI K $\alpha$  to Fe XXV K $\alpha$  decrease from  $\sim 0.4$  to  $\sim 0.2$  with the distance from the GC along the longitude. The line intensity ratio at  $l_* = 3^\circ$  is almost same as that in the ridge. The transition of the ratio also happens around  $l_* = 1^\circ$ – $2^\circ$ . The region around  $l_* = 1^\circ$ – $2^\circ$  corresponds to the border between the NB and the GD. These facts suggest that the GDXE contains two components which accompany the NB and the GD respectively. The scale height of the intensity profile along the latitude changes from  $\sim 0^\circ.2$  to  $\sim 3^\circ$  around  $b_* = 0^\circ.5$ – $1^\circ$ . On the other hand, the line intensity ratio of Fe XXVI K $\alpha$  to Fe XXV K $\alpha$  is not different in  $b_* = 0^\circ$ – $2^\circ$ , significantly.

The equivalent widths of the Fe I K $\alpha$  and Fe XXV K $\alpha$  lines are anti-correlated in the GD regions ( $l_* = 1^\circ$ – $3^\circ$ ,  $b_* < 0^\circ.1$ ). From this relation, the equivalent widths of the Fe I K $\alpha$  and Fe XXV K $\alpha$  lines to their associated continua,  $EW'_{6.4}$  and  $EW'_{6.7}$  are obtained. The  $EW'_{6.4}$  is significantly smaller than those of the previously reported results in the inner NB regions (Sgr A and C) though the  $EW'_{6.7}$  is almost same among all the regions. It suggests that the origin of the Fe I K $\alpha$  line emission might be different between the NB and GD.

The non-thermal component of Sgr A East was detected for the first time. Sgr A East has two-temperature plasma of  $kT \sim 6$  keV and  $\sim 1.2$  keV. The temperature of  $kT \sim 6$  keV is peculiarly hot as a SNR and close to that of the GDXE. However, the total line intensity ratio of Fe XXVI K $\alpha$  to Fe XXV K $\alpha$  is 0.05, and too low to explain that (0.2–0.4) of the GDXE.

From Suzaku J1740.5–3014, the three Fe K $\alpha$  lines and the coherent and clear pulsation of 432.1 s are detected. These features are typical for an IP. The interstellar absorption indicates that Suzaku J1740.5–3014 is located not in the GC region but in the distance of  $\sim 2$  kpc from the Sun. The luminosity of  $\sim 10^{33}$  erg s $^{-1}$  is also typical for an IP.

We compared the GDXE spectra with those of Sgr A East, Suzaku J1740.5–3014, other CVs, other SNRs and point sources in the GC region. The spectra of these sources are different from that of the GDXE.

The results of this thesis are summarized in table 8.1 with bold type.

Table 8.1: Same as table 2.3 but the results of this thesis are shown in bold type. The results written in red (blue) support whether diffuse (point sources) origin.

	<b>Sgr A region</b> $ l  < 0.3$	<b>Between GC &amp; Ridge</b> $ l  = 0.3 - 3^\circ$	<b>Ridge</b> $ l  > 8^\circ$	<b>Bulge</b> $ b  > 1^\circ$
<b>Comparison between the profiles of the GDXE and point sources</b>	<ul style="list-style-type: none"> <li>• The profile of Fe XXV <math>K\alpha</math> is different from that of X-ray point sources detected with Chandra.</li> </ul>	<ul style="list-style-type: none"> <li>• <b>The profile of Fe XXV <math>K\alpha</math> in <math> l  &lt; 1^\circ</math> is different from that of the NIR but not distinguished with that of X-ray point sources.</b></li> </ul>	<ul style="list-style-type: none"> <li>• The profile of the GDXE in <math> l  &gt; 1^\circ</math> matches that of the NIR.</li> </ul>	
<b>Equivalent widths (EWs) of Fe <math>K\alpha</math></b>	<ul style="list-style-type: none"> <li>• The EWs of the GDXE are too large as known CVs.</li> <li>• The EWs of the point sources in the GC are as large as those of the GDXE.</li> </ul>	<ul style="list-style-type: none"> <li>• <b>The EWs of the GDXE are too large as known CVs.</b></li> <li>• <b>Suzaku J1740.5 -3014 was studied but it is a foreground source. Its EWs are similar to that of known CVs.</b></li> </ul>	<ul style="list-style-type: none"> <li>• The EWs of the GDXE are too large as known CVs.</li> <li>• The EWs of known CVs near the Sun are too small as the GDXE.</li> </ul>	
<b>EW of Fe XXV <math>K\alpha</math> v.s. EW of Fe I <math>K\alpha</math></b>	<ul style="list-style-type: none"> <li>• They are anti-correlated.</li> </ul>	<ul style="list-style-type: none"> <li>• <b>They are anti-correlated in <math> l  = 1^\circ - 3^\circ</math>, <math> b  &lt; 0.1</math> but the relation is different from those in <math> l  &lt; 1^\circ</math>.</b></li> </ul>	<ul style="list-style-type: none"> <li>• Not studied.</li> </ul>	
<b>Intensity ratio of Fe XXVI <math>K\alpha</math> to Fe XXV <math>K\alpha</math></b>	<ul style="list-style-type: none"> <li>• 0.33</li> <li>• <b>The ratio of Sgr A East is 0.05.</b></li> </ul>	<ul style="list-style-type: none"> <li>• <b>It changes from <math>\sim 0.3</math> to <math>\sim 0.2</math> in the border between the NB and the GD.</b></li> </ul>	<ul style="list-style-type: none"> <li>• 0.22</li> </ul>	<ul style="list-style-type: none"> <li>• <b>0.42</b></li> </ul>
<b>Fraction of the GDXE resolved into point sources.</b>	<ul style="list-style-type: none"> <li>• <b>40%</b></li> </ul>	<ul style="list-style-type: none"> <li>• <b>4-15%.</b></li> </ul>	<ul style="list-style-type: none"> <li>• 19%</li> </ul>	<ul style="list-style-type: none"> <li>• <b>85%</b></li> </ul>

## Appendix A

# X-ray Emission from Thin-Thermal Plasma

The spectrum of X-ray emission from thin thermal plasma composed of continuum and line emission components. The continuum component is bremsstrahlung emission by thermal electrons. The power of the bremsstrahlung per unit time, volume and frequency for typical thermal plasma emitting X-ray is written as

$$\frac{dW}{dt dV d\nu} = \frac{32\pi e^6}{3hm_e^{3/2}c^3} \left( \sum_z z^2 a_z \right) n_e n_H (h\nu)^{-1/2} \exp(-h\nu/kT_e). \quad (\text{A.1})$$

Here,  $kT_e$ ,  $m_e$  and  $n_e$  are the temperature, mass and density of electron.  $n_H$  is the hydrogen density.  $z$  and  $a_z$  are the atomic number and the abundance relative to hydrogen of the element  $Z$  [107]. The spectrum has a cutoff at  $h\nu \sim kT_e$  so we can determine the plasma temperature from the shape of the observed continuum. Combined with the temperature, we can calculate  $n_e n_H$  from the luminosity. If a non-thermal component exists, the temperature determination from the continuum has the ambiguity because the non-thermal component is often difficult to be distinguished with high-temperature bremsstrahlung.

The line emissions also indicate the plasma temperature. We review the line emission process here. For low-density ( $n_e < 10^{14} \text{ cm}^{-3}$ ) plasma, the coronal approximation can be applied. In this approximation, ions are essentially in their ground states. After collisional excitation, the ion emits photons and becomes in the ground state before the next collision. Considering only the dominant process of the collisional excitation, the volume line emissivity of a particular line transition of  $a \rightarrow b$  is written as

$$P_{Z^{+i}}^{ab} = n_e n_H a_z \eta_Z^i S_{Z^{+i}}^{ga} B_{Z^{+i}}^{ab}. \quad (\text{A.2})$$

Here  $\eta_Z^i$  is the ionic fraction of  $Z^{+i}$  ( $\sum_{i=0}^z \eta_Z^i = 1$ ) and a function of the plasma temperature.  $\eta_{\text{Fe}}^i$  is shown in figure A.1 for example. We can inversely define the ionization temperature from the ionic fractions of given plasma. In CIE plasma, the ionization temperature equals to the electron temperature. Plasma in which the ionization temperature is lower than the electron temperature is often found in young supernova remnants (e.g. SN 1006 [141]), and called non-equilibrium ionization (NEI) plasma.  $S_{Z^{+i}}^{ga}$  is the rate coefficient for electron impact excitation of ions  $Z^{+i}$  from its ground state to its excited state  $a$ .  $S_{Z^{+i}}^{ga}$  is calculated by averaging the corresponding cross sections over the Maxwellian electron velocity distribution and thus a

function of the electron temperature.  $B_{Z^{+i}}^{ab}$  is the radiative branching ratio of the transition  $a \rightarrow b$  among all possible transitions from level  $a$ .

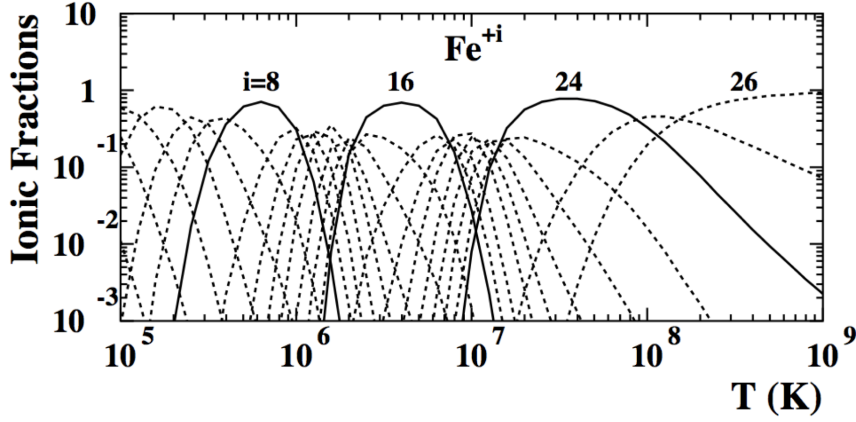


Figure A.1: Iron ionic fractions at ionization equilibrium as a function of plasma temperature [2, 124].

The intensity ratio between the emission lines from the ions of the same element (e.g. Fe XXVI  $K\alpha$ /Fe XXV  $K\alpha$ , Fe XXV  $K\beta$ /Fe XXV  $K\alpha$ , etc.) is written as a combination of  $\eta_Z^i$ ,  $S_{Z^{+i}}^{ga}$  and  $B_{Z^{+i}}^{ab}$  because  $n_e$ ,  $n_H$  and  $a_z$  are canceled.  $\eta_Z^i$  and  $S_{Z^{+i}}^{ga}$  are functions of the temperature and  $B_{Z^{+i}}^{ab}$  is constant. Thus, we can obtain the plasma temperature from the observed line intensity ratio. We calculated the some examples of the relations between the line ratio and the temperature shown in figure A.2 with CIE plasma model code APEC [119].

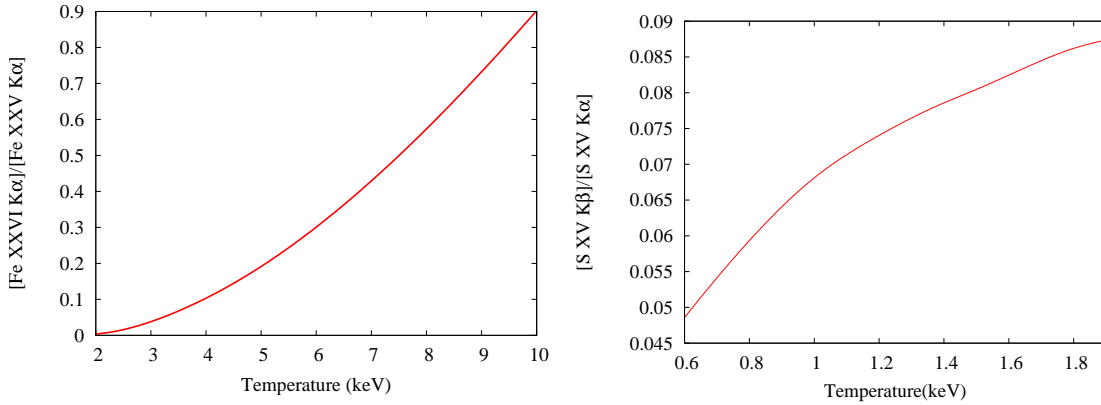


Figure A.2: Relations between the temperature and the line intensity ratio. Left:  $[\text{Fe XXVI } K\alpha]/[\text{Fe XXV } K\alpha]$ . Right:  $[\text{S XV } K\beta]/[\text{S XV } K\alpha]$ .

The equivalent width is the ratio of the line flux to the flux per unit energy of the underlying continuum at the line energy. Equations A.1 and A.2 show that the equivalent width is a function of  $a_z$  and the temperature. If we obtained the plasma temperature from the line intensity ratio or the continuum, we can determine the metal abundance  $a_z$  from the equivalent width. We show an example of the relation between the line equivalent width and the temperature in figure A.3 assuming the solar abundance with the APEC code.

A He-like  $K\alpha$  emission line (e.g. Fe XXV  $K\alpha$ ) has fine structure of the resonance ( $w:1s^2$

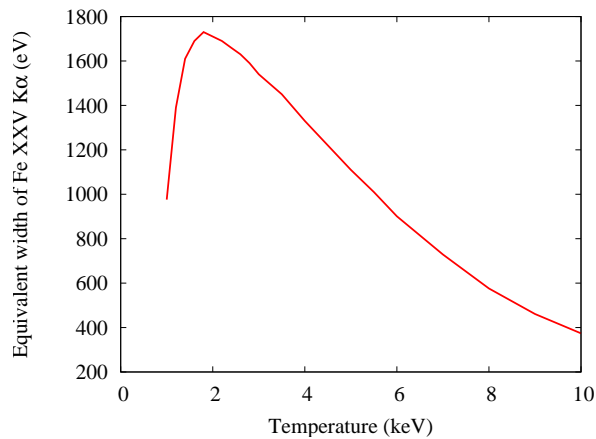


Figure A.3: Relations between the temperature and the equivalent width of the Fe XXV  $K\alpha$  line.

$^1S_0-1s2p\ ^1P_1$ ), the intercombination ( $x+y:1s^2\ ^1S_0-1s2p\ ^3P_{2,1}$ ), the forbidden ( $z:1s^2\ ^1S_0-1s2s\ ^3S_1$ ) lines (figure A.4) and the satellite lines ( $s$ :Li-like  $1s^22p-1s2p^2$  etc.). The center energies are higher in the order of the resonance, intercombination and forbidden lines. The center energies of the satellite lines are lower than that of the resonance line. With the higher temperature, the relative intensity ratio of the resonance line to the sum of the intercombination and forbidden lines become higher and the intensity of the satellite lines get lower. The blend of the resonance, intercombination, forbidden and satellite lines is observed as a single He-like  $K\alpha$  line with a CCD camera, because its energy resolution (FWHM  $\sim 150$  eV) is not enough to resolve the fine structure. Thus, the center energy of an observed He-like  $K\alpha$  line indicates the plasma temperature. The relation between the temperature and the center energy of the Fe XXV  $K\alpha$  line calculated with the APEC code is shown in figure A.5.

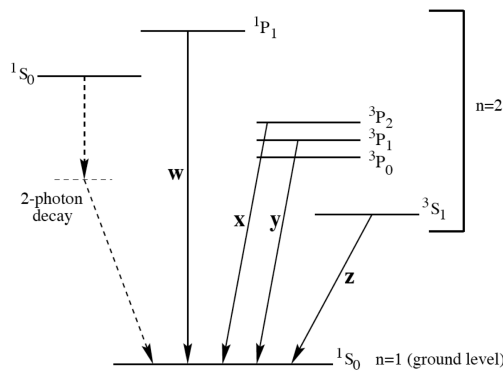


Figure A.4: Scheme of the first energy levels of He-like ions [124].

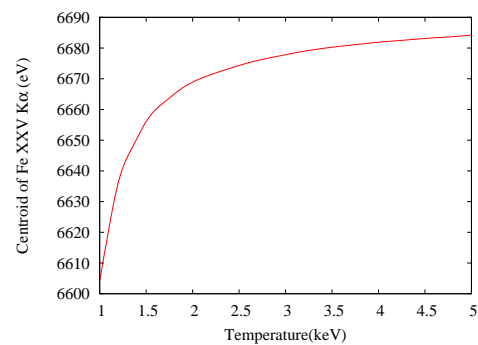


Figure A.5: Relation between the temperature and the center energy of the Fe XXV  $K\alpha$  line.



## Appendix B

# CTI Correction and In-Orbit Calibration for SCI

The CTI correction method and in-orbit calibration of the SCI technique are described in this chapter. The SCI technique was in practical use for the first time in the Suzaku XIS. It is the key technique to decrease the systematic error of the long-period observation data used in this thesis. These results are also reported in Uchiyama et al.[134].

### B.1 Property of the CTI in the SCI Mode and the “Sawtooth” CTI model

In the SCI mode of the Suzaku XIS, a charge is injected into every 54th row. The amounts of the injected charge into each pixel are equivalent to the X-ray energy of  $\sim 6$  keV and of  $\sim 2$  keV, for the front-illuminated (FI) and back-illuminated CCD (BI), respectively.

We, especially Nakajima et al. [83] and Ozawa et al. [89], have revealed the properties of the CTI in the SCI-off mode as below. A charge packet in the XIS loses its charge during (a) the fast transfer ( $24 \mu\text{s pixel}^{-1}$ ) in the imaging area, (b) the fast transfer in the frame-store region, (c) the slow transfer ( $6.7 \text{ ms pixel}^{-1}$ ) in the frame-store region, (d) the slow transfer to the read-out node. The CTI depends on many parameters such as the transfer speed, the number density of the charge traps [26], pixel size, and the structure of transfer channel. The imaging area and the frame-store region may have different trap densities since the pixel size are different among these areas. Also the frame-store region is covered by the shield and is not exposed to the radiation directly. The transfer (d) is examined by using the calibration source data taken in 2007 April, and no significant decrease of the pulse height along the ActX axis is found. It shows that the charge loss in the transfer (d) is ignorable. We define that  $i$  is the transfer number in the imaging area ( $i = \text{ActY} + 1$ ; here,  $\text{ActY}$  is a coordinate value where an incident X-ray generates a charge packet). Then the relation between  $PH'(i)$  and  $PH_o$  is expressed as

$$\begin{aligned} PH'(i) &= PH_o(1 - c_a)^i(1 - c_b)^{1024-i}(1 - c_c)^i, \\ &\sim PH_o \{1 - i(c_a - c_b + c_c) - 1024c_b\}, \end{aligned} \tag{B.1}$$

where  $c_a$ ,  $c_b$  and  $c_c$  are the CTI values in the transfers (a), (b), and (c), respectively. Here the fact

Table B.1: The list of notation.

Notation	Meaning
$i$	Transfer number.
$PH_0$	Original pulse height.
$PH'(0)$	Readout pulse height of a pixel at $i = 0$ .
$PH'(i)$	Readout pulse height of a pixel at $i$ .
$j$	Row number between a pixel and its preceding CI row. $j = i \bmod 54$ .
$c_1(i)$	CTI1 of equation B.2 for a pixel at $i$ .
$c_{1t}, c_{1b}$	The $c_1$ values at the peak and valley of the sawtooth (see figure 1a).
$c_2$	CTI2 of equation B.2 for a pixel at $i$ .
$-s(j)$	Slope for a pixel with $j$ . It is equal to $c_1(i) \cdot PH_0$ .
$-s_t$	Slope for the tops of the sawtooth. It is equal to $c_{1t} \cdot PH_0$ .
$-s_b$	Slope for the bottoms of the sawtooth. It is equal to $c_{1b} \cdot PH_0$ .
$\beta$	CTI depends on the pulse height as $c_{1,2} \propto PH_0^{-\beta}$ . See equation B.3.

that the CTI values are much smaller than 1 is used. Thus we can separate the charge loss into  $i$ -dependent component (the second term in the right-hand side of equation B.1) and constant component (the third term). We therefore substitute CTI to CTI1 (the former component) and CTI2 (the latter component), which have the CTI values of  $c_1 = c_a - c_b + c_c$  and  $c_2 = c_b$ , respectively. Then equation B.1 can be written as

$$PH'(i) \sim PH_0(1 - ic_1 - 1024c_2). \quad (\text{B.2})$$

Since the CTI values ( $c_1, c_2$ ) depend on the amount of transfer charge, we assume the CTI dependence on the PH (proportional to the charge) as

$$c_1 = k_1(PH)^{-\beta} \quad \text{and,} \quad c_2 = k_2(PH)^{-\beta}, \quad (\text{B.3})$$

where  $k_1$  and  $k_2$  are scale factors for the CTI1 and CTI2, and the index  $\beta$  is common to CTI1 and CTI2.

To make clear for further descriptions of the SCI, relevant terminologies and notations are summarized in table B.1.

The CTI in the SCI mode is assumed to consist of two components as CTI1 and CTI2 following the result in SCI-off mode. The relation among readout pulse height ( $PH'$ ), original pulse height generated by an X-ray of energy  $E$  ( $PH_0$  at  $E$ ), CTI1 ( $c_1$ ), CTI2 ( $c_2$ ), and transfer number  $i$  are formalized in equation B.2, where the detector coordinates are defined as  $ActX$  and  $ActY$ . The CCD consists of four segments (A, B, C, and D); each segment consists of 256 columns along  $ActX$  and has a dedicated read-out node.

In the SCI mode, a radiation-induced trap is filled with a probability  $p$  when a sacrificial charge passes through the trap. The filled trap does not capture a signal charge produced by an X-ray. However, the electron once filling the trap will be re-emitted with the time scale  $\tau$ . Thus the probability of the trap holding the electron is proportional to  $p \cdot \exp(-t/\tau)$ , where  $t$  is the time elapsed since the sacrificial charge passes the trap. Thus it is reasonable to assume that a pixel which is  $j$  rows away from its preceding charge injected row has the  $c_1$  value proportional to  $1 - p \cdot \exp(-\delta t \cdot j/\tau)$ , where  $\delta t$  is time for one vertical transfer;  $\delta t \cdot j$  represents a time lag

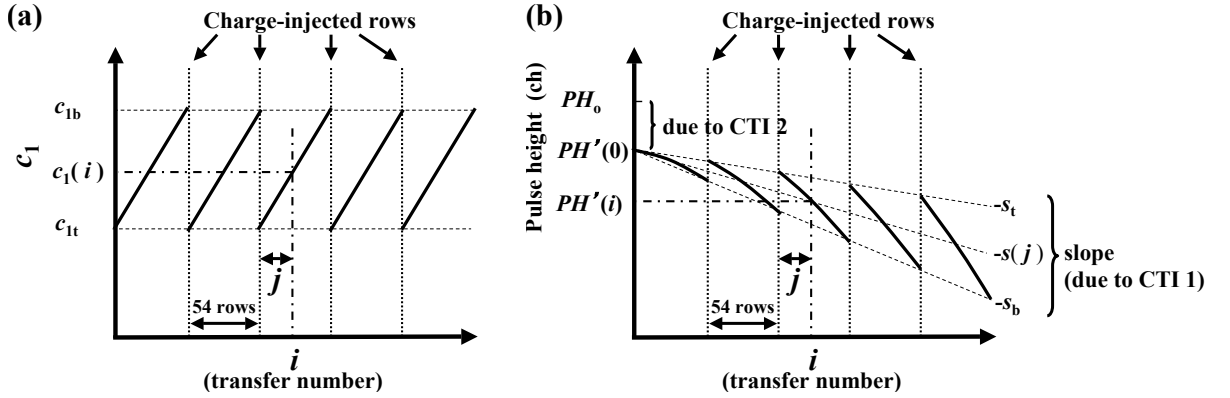


Figure B.1: Our model of the “sawtooth” variation. We assume the  $c_1$ - $i$  relation show in (a), and it generates the  $PH'$ - $i$  relation shown in (b).

between the pixel and the charge injected row. We assume  $\delta t \cdot j/\tau$  is a small value, and hence  $1 - p \cdot \exp(-\delta t \cdot j/\tau)$  is a linear function of  $j$  approximately. The charge is injected into every 54th row, and hence  $j = i \bmod 54$ <sup>1</sup>. We, consequently, can model the  $c_1$ - $i$  relation of the SCI mode as,

$$c_1(i) = c_{1t} + \frac{c_{1b} - c_{1t}}{54} \cdot (i \bmod 54). \quad (\text{B.4})$$

Equation B.4 is a periodic sawtooth function as demonstrated in figure B.1a. This  $c_1$ - $i$  relation generates the  $PH'$ - $i$  relation in figure B.1b, and the shape is nicely reproduced by the ground experiments using the heavily damaged CCD as demonstrated in figure 15 of [128].

The sawtooth distribution is also found in the XIS in-orbit. We measured the  $PH'$ - $i$  relations using the onboard calibration source data in October 2006 with an effective exposure time of 1 Ms, and show the results in figures B.2a and b. Figure B.2 shows that the sawtooth of the BI sensor is shallower than that of the FI sensors. The results based on the data in February 2008 are also shown in figures B.2c and d. Compared with October 2006, the sawtooth became deeper. The pulse height just after the charge injected rows changed more in the case of the BI sensor than the FI sensors. This difference might be resulted in part from the smaller amount of charge injected in the BI sensor.

Our sawtooth CTI model can represent the complicated relation between  $PH'$  and  $i$ , and make it possible to convert  $PH'(i)$  to  $PH_0$  with only three parameters,  $c_{1t}$ ,  $c_{1b}$ , and  $c_2$ . Our goal is to convert  $PH'(i)$  to  $PH_0$  by deciding the three parameters.

## B.2 CTI Measurement in Orbit

### B.2.1 Calibration Data

To study the CTI in the SCI mode, we analyzed the data of the onboard calibration sources  $^{55}\text{Fe}$ , the Perseus cluster of galaxies, and 1E 0102.2–7219, whose properties are summarized below.

<sup>1</sup>The modular arithmetic  $i \bmod 54 = j$  means that when  $i$  is divided by 54, it leaves  $j$  as the remainder, hence  $i - j$  is divisible by 54. For example,  $111 \bmod 54 = 3$ . Strictly speaking, charges are injected in rows of  $i = 54 \cdot n - 1$  ( $n = 0, \dots, 18$ ) and 1023 for full window mode. Thus  $j$  should be  $(i + 1) \bmod 54$ . We nevertheless use this simplified description to avoid unnecessary confusion. We treated  $j$  properly for actual CTI measurement.

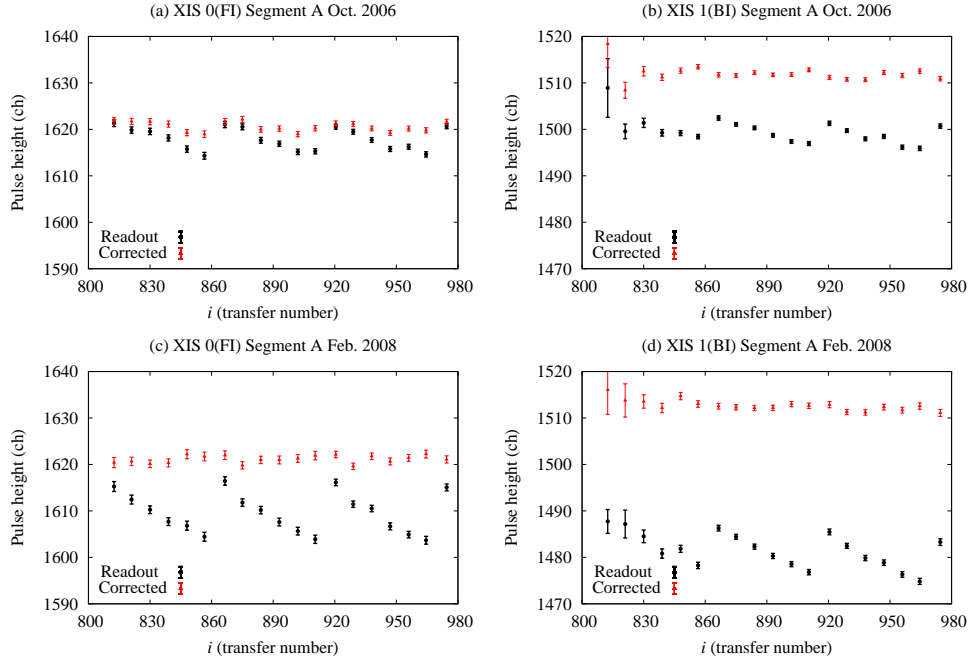


Figure B.2: Pulse height of the MnI  $K\alpha$  line from the onboard calibration source as a function of  $i$ : October 2006 (a and b) and February 2008 (c and d). We show the results of the segment A in XIS 0, 1 as typical examples. X-ray events of grade 02346 were analyzed. Black and red marks are data before and after our new CTI correction, respectively.

### Onboard Calibration Source $^{55}\text{Fe}$

The onboard calibration source  $^{55}\text{Fe}$  produces the Mn I  $K\alpha$  line. The center energy is 5.895 keV and the intrinsic line width is negligible for our purposes. Thus the observed line width directly reflects the energy resolution of the XIS. We used the archival trend data of the calibration source distributed by the Data Archives and Transmission System (DARTS)<sup>2</sup> of ISAS/JAXA. The data were obtained between August 2006 and March 2008, and the total effective exposure is about 23.7 Ms.

### The Perseus Cluster of Galaxies

The Perseus cluster of galaxies is one of the X-ray brightest clusters in the sky at redshift  $z = 0.0176$ . It has the X-ray spectrum of thermal plasma with strong  $K\alpha$  lines of FeXXV. Its radius is about  $15'$  [13]. Since the XIS combined with the X-Ray Telescope (XRT) onboard Suzaku has a field-of-view (FOV) of  $18' \times 18'$  on the sky, the X-ray emission from the cluster fills the entire field of view. The temperature of the plasma changes smoothly from  $kT \sim 4$  keV to  $\sim 7$  keV toward the outer region. The line center energy of the FeXXV  $K\alpha$  triplet is almost constant ( $\sim 6.56$  keV at  $z = 0.0176$ ) within the temperature range, and the line is suitable to measure the CTI. However, we do not use this line to determine the absolute energy scale because of the uncertainty of the absolute energy of the line. We have observed the Perseus cluster with the SCI mode every six months for calibration.

<sup>2</sup><http://darts.isas.jaxa.jp/index.html.en>

Table B.2: Log of Observations for Calibration.

Obs. ID	Observation time (UT)		Exposure time [ks]
	Start	End	
The Perseus cluster			
101012010	2006/08/29 18:55:07	2006/09/02 01:54:19	50.0
101012020	2007/02/05 15:57:48	2007/02/06 14:30:14	43.9
102011010	2007/08/15 12:40:49	2007/08/16 11:27:22	42.3
102012010	2008/02/07 02:09:42	2008/02/08 10:30:19	41.6
1E 0102.2–7219			
101005090	2006/12/13 18:53:16	2006/12/14 03:04:19	28.2
101005110	2007/02/10 22:13:47	2007/02/11 19:30:14	36.2
102001010	2007/04/10 10:35:08	2007/04/10 19:30:19	18.1
102002010	2007/06/13 10:10:12	2007/06/14 03:31:19	27.9
102003010	2007/08/12 05:21:09	2007/08/13 03:45:24	39.5
102004010	2007/10/25 12:24:45	2007/10/26 09:00:14	26.2
102005010	2007/12/01 19:25:40	2007/12/02 09:50:19	24.8
102022010	2008/02/14 16:57:28	2008/02/16 03:10:24	26.5
102006010	2008/03/15 05:43:27	2008/03/15 20:45:24	28.2

### 1E 0102.2–7219

This is one of the brightest supernova remnants (SNR) in the Small Magellanic Cloud. Chandra resolved its ring-like structure of the  $30''$ -diameter [22] though it is regarded as a point source with the spatial resolution of Suzaku. The spectrum of 1E 0102.2–7219 has strong lines from highly-ionized O, Ne and Mg. These lines are resolved to resonance, forbidden and intercombination lines by the XMM-Newton RGS, and thus the accurate energies of the line centroids are known [98]. 1E 0102.2–7219 has been used for calibrations in a soft-energy band by several satellites, and an empirical model for calibrations has been constructed [94]. We have observed 1E 0102.2–7219 with the SCI mode regularly for the calibration of the low energy gain and the contamination.

XIS 2 suddenly showed an anomaly on November 9, 2006, and it has not been operated since then. Thus only the data of XIS 0, 1 and 3 are studied.

All data were acquired with the normal clocking mode and the full window option using the SCI. The editing mode was  $3 \times 3$  or  $5 \times 5$ . [50] provide details of these modes.

As mentioned in [50], a small fraction of the charge in a pixel is left behind (trailed) to the next pixel during the transfer. This charge-trail phenomenon changes the spatial extent of an X-ray event. All data were corrected for the phenomenon based on the in-orbit data<sup>3</sup>, otherwise some X-ray events would be judged as grade 7, and the detection efficiency would decrease.

The observations of the celestial objects are summarized in table B.2.

<sup>3</sup>The details about the charge-trail correction is shown in [http://xmm2.esac.esa.int/external/xmm\\_sw\\_cal/icwg/presentations/Suzaku\\_XIS.pdf](http://xmm2.esac.esa.int/external/xmm_sw_cal/icwg/presentations/Suzaku_XIS.pdf)

### B.2.2 Determination of the CTI Parameters

The procedures for the CTI determination are as follows:

- *Step 1:* deciding  $PH_o$  at 5.895 keV and 6.56 keV.
- *Step 2:* measuring  $c_2$  for  $PH_o$  at 6.56 keV.
- *Step 3:* measuring  $c_{1t}$  and  $c_{1b}$  for  $PH_o$  at 5.895 keV or 6.56 keV.
- *Step 4:* deciding the CTIs for any  $PH'$  values.

In the case of the SCI-off mode, we can measure the CTI of each column by the checker flag CI [83, 89]. Since the checker flag CI is a complicated operation, we have not used this technique in the SCI mode. We, therefore, measured the averaged CTI of each segment.

In the normal analysis of the XIS data, both of single-pixel and multi-pixel events (grade 0 and 2346 events; see [50]) are used. To determine the CTI, however, we analyzed only the grade 0 events; if we use the multi-pixel events, it is difficult to measure the CTI correctly, because the CTI depends on the amount of transferred charge, and the amounts of charge in each pixel comprising the multi-pixel event is different with each other. We will mention how to correct the data of grade 02346 events in step 4.

#### Step 1: $PH_o$ at 5.895 keV and 6.56 keV

We determined the  $PH_o$ s of the FeXXV  $K\alpha$  line from the Perseus cluster (6.56 keV) by using the data of the first SCI observation on 29 August, 2006. Because it is impossible to measure the  $c_2$  value in August 2006, we assumed that value is equal to zero. Even if this assumption would not be reasonable, we can cover it by adjusting the  $PH_o$ - $E$  relation. Then the  $PH'$  at  $i = 0$  ( $PH'(0)$ ) is equal to  $PH_o$ .

Since the statistics are limited, we divided each segment to four regions along the  $ActY$  axis, and obtained the center pulse height of the iron line from each region. An example of  $PH'$  as a function of  $i$  is shown in figure B.3. By fitting the data with a linear function of  $i$ , the  $PH_o$  value was obtained as  $PH'(0)$

For the segments A and D, we obtained the  $PH_o$  value of the Mn I  $K\alpha$  line (5.895 keV) using the data of the calibration sources in August, 2006. We obtained the  $PH'$ - $i$  relation, but in this case, the  $i$  values are limited at around 900 because the calibration sources irradiate only the two far-end corners from the read-out node of the imaging area [50]. We extrapolated the relation to  $i = 0$  by using a linear function, the slope of which was fixed to a value  $s_{Mn}$  calculated as follows. Because the slope represents an averaged  $-c_1 \cdot PH_o$ , the slope should be proportional to  $PH_o^{1-\beta}$ . Then we calculated  $s_{Mn}$  from the slope for the 6.56 keV data ( $s_{Fe}$ ) as  $s_{Mn} = s_{Fe} \cdot (5.895/6.56)^{1-\beta} = s_{Fe} \cdot (0.90)^{1-\beta}$ .

#### Step 2: $c_2$ for $PH_o$ at 6.56 keV

We obtained the  $PH'(0)$  values for all data of the Perseus cluster (table B.2) with the same method of step 1. The  $PH'$ - $i$  relations are shown in figure B.3. As is found in figure B.3,  $PH'(0)$  is decreased with time;  $PH'(0)$  becomes different from  $PH_o$ . We assumed the difference  $PH_o - PH'(0)$  is attributable to  $c_2$ . Assuming that  $c_2$  is a linear function of time, the increasing rate of  $c_2$  for  $PH_o$  (at 6.56 keV) is typically  $\sim 2 \times 10^{-6} \text{ yr}^{-1}$  for the FI sensors and  $\sim 6 \times 10^{-6} \text{ yr}^{-1}$  for the BI sensor.

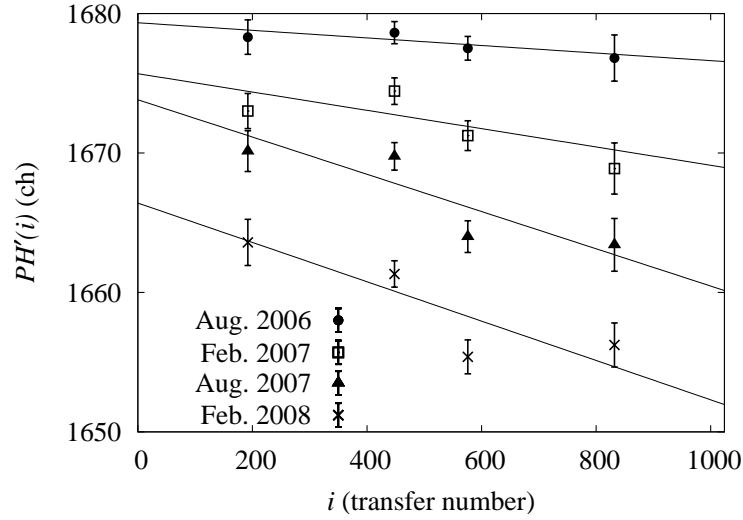


Figure B.3:  $PH'$  as a function of  $i$  obtained using the FeXXV  $K\alpha$  line from the Perseus cluster. The result of the XIS 1 segment C is shown as a typical example.

### Step 3: $c_{1t}$ and $c_{1b}$ for $PH_o$ at 5.895 keV and 6.56 keV

For the segments A and D, we determined  $s_t$  and  $s_b$  for  $PH_o$  at 5.895 keV by using the data of the calibration sources. For the segments B and C, we measured those for  $PH_o$  at 6.56 keV by using the Perseus data. We fitted the  $PH'-i$  relation with the sawtooth function shown in figure B.1b, and determined  $s_t$  and  $s_b$ . In the fitting, we fixed the  $PH_o$  and  $c_2$  to the values obtained in step 1 and step 2. Typical examples of the fitting are shown in figures B.4 and B.5. Using  $s_t$  and  $s_b$ , we calculated  $c_{1t}$  and  $c_{1b}$ .

In the case of the FI sensors, the  $c_{1t}$  and  $c_{1b}$  values for  $PH_o$  at 5.895 keV at August 2006 are typically  $< 10^{-7}$  and  $\sim 3 \times 10^{-6}$ , respectively. The increasing rates are  $\sim 1 \times 10^{-6} \text{ yr}^{-1}$  and  $\sim 5 \times 10^{-6} \text{ yr}^{-1}$ , respectively. In the case of the BI sensor, the parameters  $c_{1t}$  and  $c_{1b}$  at August 2006 are  $\sim 6 \times 10^{-6}$  and  $\sim 1 \times 10^{-5}$ , and the increasing rates are  $\sim 5 \times 10^{-6} \text{ yr}^{-1}$  and  $\sim 8 \times 10^{-6} \text{ yr}^{-1}$ , respectively. Typical examples of the time evolution of the  $c_1$  values for  $PH_o$  at 5.895 keV are shown in figure B.6.

The CTI of the BI sensor is larger, and increases more rapidly than that of the FI sensors. It might be the reason that the amount of the injected charge to the BI sensor is less than that of FIs.

### Step 4: CTI for any $PH'$ values

For an event of  $PH'$ , we calculated the CTI with an equation of  $c_{1,2} \times \{PH'/(PH_o \text{ at } 5.895 \text{ keV or } 6.56 \text{ keV})\}^{-\beta}$ . Here, we assumed the same  $PH_o$ - $c_{1,2}$  relation as that of the SCI-off mode and used the same  $\beta$  (typically  $\sim 0.25$ ; [89]).

Since we obtained the CTI for all pulse-height values, we can now correct the CTI of multi-pixel events (grade 2346 events). By using the Mn I  $K\alpha$  line of the calibration sources or the Fe XXV  $K\alpha$  line from the Perseus cluster, we examined the CTI correction for the grade 02346 events. Figure B.7 shows the line centroid of the grade 0 and grade 02346 events as a function of time. While the line centroid of the grade 0 events is temporally constant, that of the grade 02346

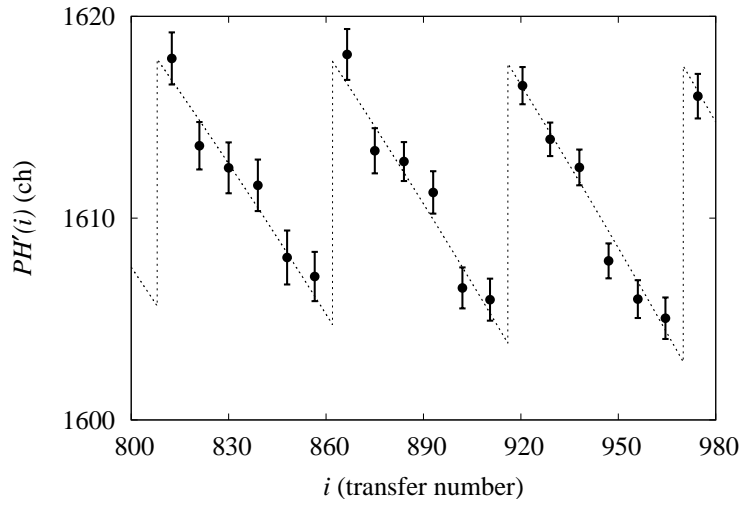


Figure B.4: Best-fitting result of the sawtooth function for the MnI  $K\alpha$  line of the calibration source. The result of the XIS 0 segment A in February 2008 is shown as a typical example. Only grade 0 events were used.

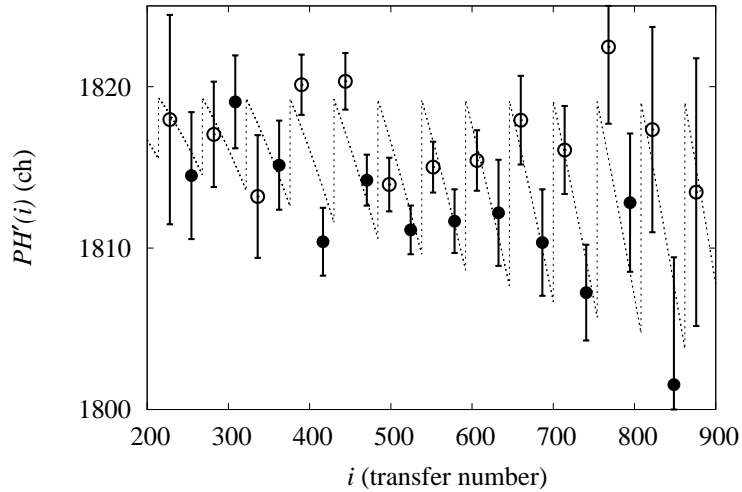


Figure B.5: Best-fitting result of the sawtooth function for the FeXXV  $K\alpha$  line from the Perseus cluster. The result of the XIS 0 segment C in February 2008 is shown as a typical example. The white and black circles show the pulse height of regions with smaller and larger  $j$  values, respectively. Only grade 0 events were used.

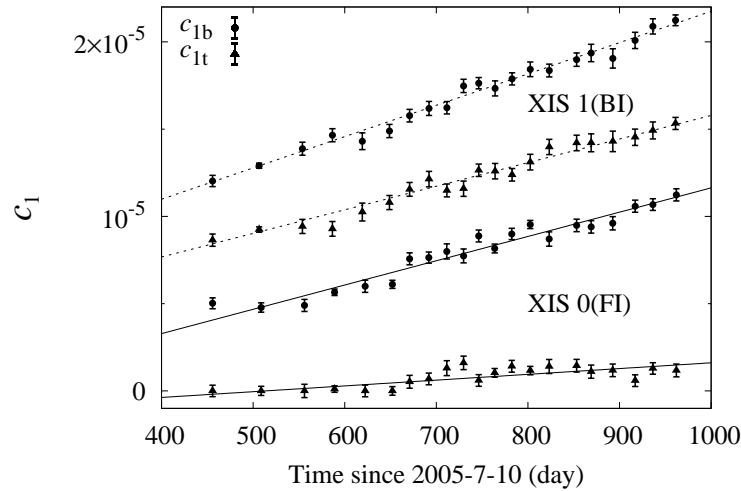


Figure B.6: Time history of  $c_{1t}$  and  $c_{1b}$  for  $PH_o$  at 5.895 keV. The segment A of XIS 0 and 1 are shown as typical examples.

events increases with time. This means that the CTI parameters for the grade 2346 events are smaller than those for the grade 0 events. The CTI of the grade 2346 events can be smaller, because the split charge acts as the sacrificial charge.

We then fine-tuned the parameters  $c_{1t}$ ,  $c_{1b}$ , and  $c_2$  by multiplying a common time-independent factor. We determined the factor of each segment so that the line center of the grade 02346 events becomes temporally constant. The factors are typically 0.9. Figure B.7 also shows that the result of the grade 02346 data corrected with the fine-tuned CTI parameters. The adjusted pulse height becomes constant. However, as a result, the value becomes different from  $PH_o$  measured in step 1. We regarded this adjusted pulse height as  $PH_o$  at 5.895 keV, and determined the  $PH_o$ - $E$  relation.

To check the CTI correction in the low-energy band, we applied the fine-tuned CTI parameters to the grade 02346 data of 1E 0102.2–7219. We fitted the spectrum with the empirical calibration model<sup>4</sup>. Figure B.8 shows the pulse height of the OVIII  $K\alpha$  line after the CTI correction. We can see that the line centroid is constant, which supports the validity of our method.

### B.3 Energy Scale Uniformity and Resolution in the SCI Mode

The pulse height of the MnI  $K\alpha$  line after our new CTI correction is shown in figure B.2. The sawtooth structure disappeared, and hence our new method greatly reduces the variation of the pulse height. Comparing between October 2006 and February 2008 shows that the CTI variation with time is also corrected properly.

The  $PH_o$ - $E$  relation for each segment is assumed to be the same function form with a similar fine-tuning process of the absolute energy as [89]: a model of two slopes crossing at the energy of the Si-K edge (1.839 keV) with the same ratio of the two slopes as that obtained in the ground experiments [50].

<sup>4</sup>See <http://cxc.harvard.edu/acis/E0102/>

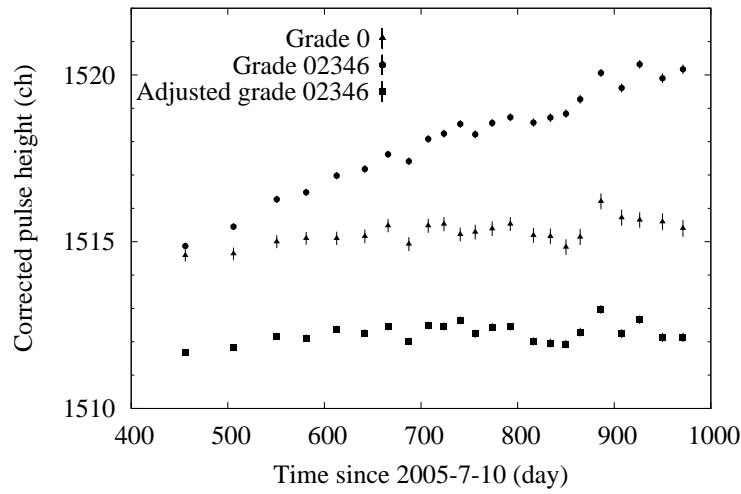


Figure B.7: Time history of the line centroid of MnI  $K\alpha$  line. We show the result of the XIS 1 segment A as a typical example. The triangle and circle marks show the data of grade 0 and 02346 after the CTI correction with the parameters based on only the grade 0 events. The rectangle marks show the data of grade 02346 events after the CTI correction with the fine-tuned parameters as described in the text.

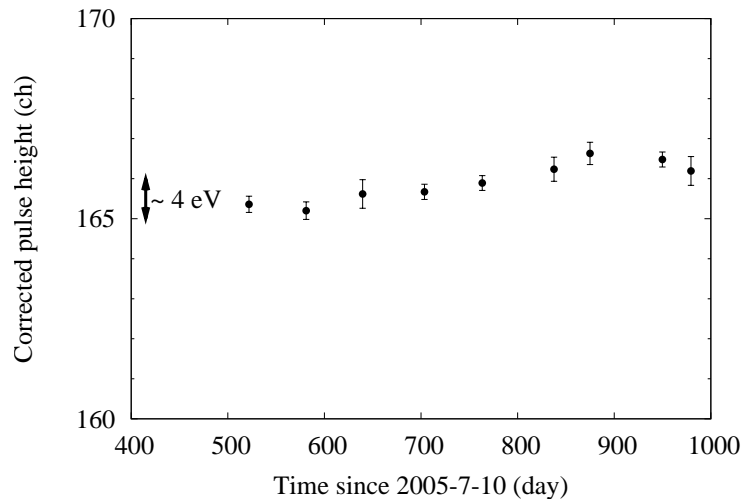


Figure B.8: Time history of the line centroid of OVIII  $K\alpha$  (0.653 keV). We show the result of the XIS 1 segment C as a typical example. The results are based on the grade 02346 events corrected with the fine-tuned CTI parameters as described in the text.

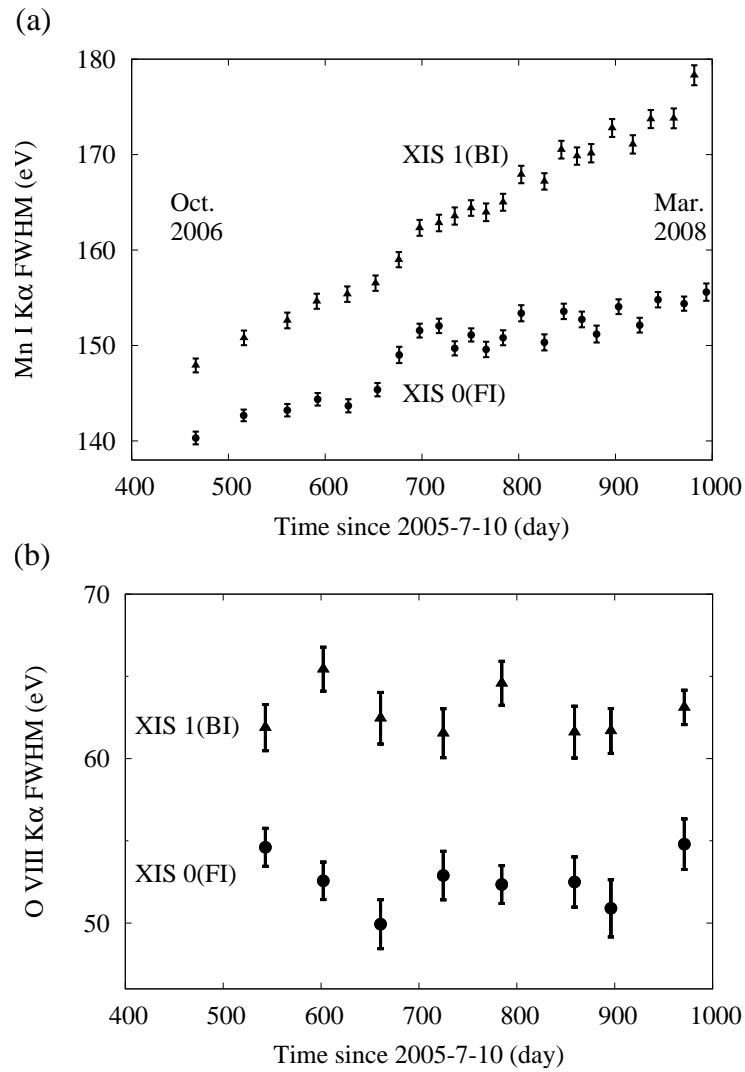


Figure B.9: Time history of the energy resolution (FWHM) at MnI K $\alpha$  (5.895 keV) (a) and at OVIII K $\alpha$  (0.653 keV) (b). The averaged value of the segments A and D are shown for each sensor. The results are based on the grade 02346 events corrected with the fine-tuned CTI parameters as described in the text.

The time histories of the energy resolution of the corrected data are shown in figure B.9. At the high energy (5.895 keV), the energy resolution of XIS 0 at March 2008 is improved from  $\sim 160$  eV to  $\sim 155$  eV by the sawtooth correction. On the other hand, the energy resolution of XIS 1 at March 2008 is not improved in spite of the sawtooth correction, and stays at  $\sim 175$  eV. At the low energy (0.653 keV), no clear effect of the sawtooth correction is seen in both FI and BI. The energy resolutions at March 2008 are  $\sim 53$  eV (XIS 0) and  $\sim 62$  eV (XIS 1) independently of the correction.

As we mentioned in section B.1, the sawtooth of the BI sensor is shallower than that of the FI sensors. We think it causes the difference of the effect of the sawtooth correction between BI and FI. We speculate, at the low energy, the effect of the sawtooth correction was not seen because the original degradation of the energy resolution was small. In fact, the energy resolutions at OVIII  $K\alpha$  are almost same between the SCI and SCI-off mode.

The results of our new method to correct the sawtooth structure has been implemented to the software package released by HEASARC<sup>5</sup> since HEASoft version 6.3. Now, all of the XIS data of the SCI mode after the processing version 2.0 are corrected by the sawtooth method.

---

<sup>5</sup><http://heasarc.gsfc.nasa.gov/>

# Bibliography

- [1] Anders, E., & Grevesse, N. 1989, *Geochim. Cosmochim. Acta*, 53, 197
- [2] Arnaud, M., & Raymond, J. 1992, *ApJ*, 398, 394
- [3] Baganoff, F. K., et al. 2003, *ApJ*, 591, 891
- [4] Balucinska-Church, M., & McCammon, D. 1992, *ApJ*, 400, 699
- [5] Bautz, M. W., Kissel, S. E., Prigozhin, G. Y., LaMarr, B., Burke, B. E., & Gregory, J. A. 2004, *Proc. SPIE*, 5501, 111
- [6] Bautz, M. W., et al. 2007, *Proc. SPIE*, 6686, 66860Q
- [7] Balucinska-Church, M., & McCammon, D. 1994, *VizieR Online Data Catalog*, 6062, 0
- [8] Bearden, J. A. 1967, *Reviews of Modern Physics*, 39, 78
- [9] Becker, R. H., White, N. E., Boldt, E. A., Holt, S. S., & Serlemitsos, P. J. 1980, *ApJL*, 237, L77
- [10] Bradt, H. V., Rothschild, R. E., & Swank, J. H. 1993, *A&AS*, 97, 355
- [11] Breitschwerdt, D., McKenzie, J. F., & Voelk, H. J. 1991, *A&A*, 245, 79
- [12] Burke, B. E., Gregory, J. A., Bautz, M. W., Prigozhin, G. Y., Kissel, S. E., Kosicki, B. B., Loomis, A. H., & Young, D. J. 1997, *IEEE Transactions on Electron Devices*, 44, 1633
- [13] Churazov, E., et al. 2003, *ApJ*, 590, 225
- [14] Cooke, B. A., Griffiths, R. E., & Pounds, K. A. 1970, *Non-Solar X- and Gamma-Ray Astronomy*, 37, 280
- [15] Cropper, M. 1990, *Space Science Reviews*, 54, 195
- [16] Cutri, R. M., et al. 2003, *The IRSA 2MASS All-Sky Point Source Catalog*, NASA/IPAC Infrared Science Archive. <http://irsa.ipac.caltech.edu/applications/Gator/>
- [17] Diehl, R., et al. 2006, *Nature*, 439, 45
- [18] Ebisawa, K., et al. 2005, *ApJ*, 635, 214
- [19] Ebisawa, K., et al. 2008, *PASJ*, 60, 223
- [20] Ezuka, H. & Ishida, M. 1999, *ApJS*, 120, 277

- [21] Fomalont, E. B., Goss, W. M., Manchester, R. N., & Lyne, A. G. 1997, *MNRAS*, 286, 81
- [22] Gaetz, T. J., Butt, Y. M., Edgar, R. J., Eriksen, K. A., Plucinsky, P. P., Schlegel, E. M., & Smith, R. K. 2000, *ApJL*, 534, L47
- [23] Giacconi, R., Gursky, H., Paolini, F. R., & Rossi, B. B. 1962, *Physical Review Letters*, 9, 439
- [24] Giacconi, R., et al. 2002, *ApJS*, 139, 369
- [25] Gillessen, S., Eisenhauer, F., Fritz, T. K., Bartko, H., Dodds-Eden, K., Pfuhl, O., Ott, T., & Genzel, R. 2009, *ApJL*, 707, L114
- [26] Hardy, T., Murowinski, R., & Deen, M. J. 1998, *IEEE Transactions on Nuclear Science*, 45, 154
- [27] Hatsukade, I., Tsunemi, H., Yamashita, K., Koyama, K., Asaoka, Y., & Asaoka, I. 1990, *PASJ*, 42, 279
- [28] Hog, E., Kuzmin, A., Bastian, U., Fabricius, C., Kuimov, K., Lindegren, L., Makarov, V. V., & Roeser, S. 1998, *A&A*, 335, L65
- [29] Hyodo, Y., Tsujimoto, M., Koyama, K., Nishiyama, S., Nagata, T., Sakon, I., Murakami, H., & Matsumoto, H. 2008, *PASJ*, 60, 173
- [30] Huovelin, J., Schultz, J., Vilhu, O., Hannikainen, D., Muhli, P., & Durouchoux, P. 1999, *A&A*, 349, L21
- [31] Huovelin, J., Schultz, J., Vilhu, O., Hannikainen, D., Muhli, P., & Durouchoux, P. 2002, *arXiv:astro-ph/0208179*
- [32] Ishida, M., Makishima, K., Mukai, K., & Masai, K. 1994, *MNRAS*, 266, 367
- [33] Ishida, M., Okada, S., Hayashi, T., Nakamura, R., Terada, Y., Mukai, K., & Hamaguchi, K. 2009, *PASJ*, 61, 77
- [34] Ishisaki, Y., et al. 2007, *PASJ*, 59, 113
- [35] Inui, T., Koyama, K., Matsumoto, H., & Tsuru, T. G. 2009, *PASJ*, 61, 241
- [36] Jansen, F., et al. 2001, 365, L1
- [37] Jansky, K. G. 1933, *Proceedings of the IRE* Volume 21, Issue 10, Oct. 1933 Page(s):1387 - 1398
- [38] Jones, L. R., & Pye, J. P. 1989, *MNRAS*, 238, 567
- [39] Kaastra, J.S., 1992, *An X-Ray Spectral Code for Optically Thin Plasmas* (Internal SRON-Leiden Report, updated version 2.0)
- [40] Kaastra, J. S., & Mewe, R. 1993, *A&AS*, 97, 443
- [41] Kaneda, H., Makishima, K., Yamauchi, S., Koyama, K., Matsuzaki, K., & Yamasaki, N. Y. 1997, *ApJ*, 491, 638

- [42] Kent, S. M., Dame, T. M., & Fazio, G. 1991, *ApJ*, 378, 131
- [43] Kelley, R. L., et al. 2007, *PASJ*, 59, 77
- [44] Koyama, K., Makishima, K., Tanaka, Y., & Tsunemi, H. 1986, *PASJ*, 38, 121
- [45] Koyama, K., Ikeuchi, S., & Tomisaka, K. 1986, *PASJ*, 38, 503
- [46] Koyama, K., Tsunemi, H., Becker, R. H., & Hughes, J. P. 1987, *PASJ*, 39, 437
- [47] Koyama, K., Awaki, H., Kunieda, H., Takano, S., & Tawara, Y. 1989, *Nature*, 339, 603
- [48] Koyama, K., Maeda, Y., Sonobe, T., Takeshima, T., Tanaka, Y., & Yamauchi, S. 1996, *PASJ*, 48, 249
- [49] Koyama, K., Senda, A., Murakami, H., & Maeda, Y. 2003, *Chinese Journal of Astronomy and Astrophysics Supplement*, 3, 297
- [50] Koyama, K., et al. 2007, *PASJ*, 59, 23
- [51] Koyama, K., et al. 2007, *PASJ*, 59, 245
- [52] Koyama, K., Uchiyama, H., Hyodo, Y., Matsumoto, H., Tsuru, T. G., Ozaki, M., Maeda, Y., & Murakami, H. 2007, *PASJ*, 59, 237
- [53] Koyama, K., et al. 2007, *PASJ*, 59, 221
- [54] Koyama, K., Inui, T., Matsumoto, H., & Tsuru, T. G. 2008, *PASJ*, 60, 201
- [55] Koyama, K., Takikawa, Y., Hyodo, Y., Inui, T., Nobukawa, M., Matsumoto, H., & Tsuru, T. G. 2009, *PASJ*, 61, 255
- [56] Krause, M. O., & Oliver, J. H. 1979, *Journal of Physical and Chemical Reference Data*, 8, 329
- [57] Krasnopolsky, V. A., Greenwood, J. B., & Stancil, P. C. 2004, *Space Science Reviews*, 113, 271
- [58] Kushino, A., Ishisaki, Y., Morita, U., Yamasaki, N. Y., Ishida, M., Ohashi, T., & Ueda, Y. 2002, *PASJ*, 54, 327
- [59] Larsson, S. 1996, *A&AS*, 117, 197
- [60] Launhardt, R., Zylka, R., & Mezger, P. G. 2002, *A&A*, 384, 112
- [61] Liedahl, D. A., Osterheld, A. L., & Goldstein, W. H. 1995, *ApJL*, 438, L115
- [62] Lutovinov, A. A., Grebenev, S. A., Pavlinsky, M. N., & Sunyaev, R. A. 2001, *Astronomy Letters*, 27, 501
- [63] Maeda, Y., et al. 2002, *ApJ*, 570, 671
- [64] Matsumoto, H., et al. 2006, *Proc. SPIE*, 6266,

- [65] Matteucci, F., Panagia, N., Pipino, A., Mannucci, F., Recchi, S., & Della Valle, M. 2006, *MNRAS*, 372, 265
- [66] Matsunaga, N., Kawadu, T., Nishiyama, S., Nagayama, T., Hatano, H., Tamura, M., Glass, I. S., & Nagata, T. 2009, *MNRAS*, 399, 1709
- [67] Mewe, R. 1996, *Sol. Phys.*, 169, 335
- [68] Mezger, P. G., Duschl, W. J., & Zylka, R. 1996, *A&A Rev.*, 7, 289
- [69] Mitsuda, K., et al. 2007, *PASJ*, 59, 1
- [70] Moretti, A., Campana, S., Lazzati, D., & Tagliaferri, G. 2003, *ApJ*, 588, 696
- [71] Morris, M., et al. 2003, *Astronomische Nachrichten Supplement*, 324, 167
- [72] Mori, H., et al. 2005, *PASJ*, 57, 245
- [73] Mori, H., et al. 2007, *Proc. SPIE*, 6686,
- [74] Mori, H., Tsuru, T. G., Hyodo, Y., Koyama, K., & Senda, A. 2008, *PASJ*, 60, 183
- [75] Mori, H., Hyodo, Y., Tsuru, T. G., Nobukawa, M., & Koyama, K. 2009, *PASJ*, 61, 687
- [76] Morrison, R. & McCammon, D. 1983, *ApJ*, 270, 119
- [77] Murakami, H., Koyama, K., Tsujimoto, M., Maeda, Y., & Sakano, M. 2001, *ApJ*, 550, 297
- [78] Munro, M. P., et al. 2003, *ApJ*, 589, 225
- [79] Munro, M. P., et al. 2004, *ApJ*, 613, 326
- [80] Munro, M. P., et al. 2004, *ApJ*, 613, 1179
- [81] Munro, M. P., Bauer, F. E., Bandyopadhyay, R. M., & Wang, Q. D. 2006, *ApJS*, 165, 173
- [82] Munro, M. P., et al. 2009, *ApJS*, 181, 110
- [83] Nakajima, H., et al. 2008, *PASJ*, 60, 1
- [84] Nakajima, H., Tsuru, T. G., Nobukawa, M., Matsumoto, H., Koyama, K., Murakami, H., Senda, A., & Yamauchi, S. 2009, *PASJ*, 61, 233
- [85] Nobukawa, M., et al. 2008, *PASJ*, 60, 191
- [86] Nobukawa, M., Sawada, M., Matsumoto, H., Tsuru, T. G., & Koyama, K. 2009, *Advances in Space Research*, 43, 1045 2008, *PASJ*, 60, 1
- [87] Nobukawa, M. et al. 2009 in prep.
- [88] Norton, A. J., Watson, M. G., King, A. R., Lehto, H. J., & McHardy, I. M. 1992, *MNRAS*, 254, 705
- [89] Ozawa, M., et al. 2009, *PASJ*, 61, 1
- [90] Paul, J. M. 1971, *Nuclear Instruments and Methods*, 94, 275

- [91] Park, S., Munro, M. P., Baganoff, F. K., Maeda, Y., Morris, M., Howard, C., Bautz, M. W., & Garmire, G. P. 2004, *ApJ*, 603, 548
- [92] Park, S., et al. 2005, *ApJ*, 631, 964
- [93] Patterson, J. 1994, *PASP*, 106, 209
- [94] Plucinsky, P. P., et al. 2008, *Proc. SPIE*, 7011
- [95] Porquet, D., Decourchelle, A., & Warwick, R. S. 2003, *A&A*, 401, 197
- [96] Predehl, P. 1995, *Advances in Space Research*, 16, 159
- [97] Prigozhin, G., Burke, B., Bautz, M., Kissel, S., & Lamarr, B. 2008, *IEEE Transactions on Electron Devices*, 55, 2111
- [98] Rasmussen, A. P., Behar, E., Kahn, S. M., den Herder, J. W., & van der Heyden, K. 2001, *A&A*, 365, L231
- [99] Rana, V. R., Singh, K. P., Schlegel, E. M., & Barrett, P. E. 2006, *ApJ*, 642, 1042
- [100] Reid, M. J., & Brunthaler, A. 2004, *ApJ*, 616, 872
- [101] Revnivtsev, M., Sazonov, S., Gilfanov, M., Churazov, E., & Sunyaev, R. 2006, *A&A*, 452, 169
- [102] Revnivtsev, M., Molkov, S., & Sazonov, S. 2006, *MNRAS*, 373, L11
- [103] Revnivtsev, M., & Sazonov, S. 2007, *A&A*, 471, 159
- [104] Revnivtsev, M., Vikhlinin, A., & Sazonov, S. 2007, *A&A*, 473, 857
- [105] Revnivtsev, M., Sazonov, S., Churazov, E., Forman, W., Vikhlinin, A., & Sunyaev, R. 2009, *Nature*, 458, 1142
- [106] Ritter, H., & Kolb, U. 2003, *A&A*, 404, 301
- [107] Rybicki, G. B., & Lightman, A. P. 1979, New York, Wiley-Interscience, 1979. 393 p.,
- [108] Ryu, S. G., Koyama, K., Nobukawa, M., Fukuoka, R., & Tsuru, T. G. 2009, *PASJ*, 61, 751
- [109] Sakano, M., Imanishi, K., Tsujimoto, M., Koyama, K., & Maeda, Y. 1999, *ApJ*, 520, 316
- [110] Sakano, M., Koyama, K., Murakami, H., Maeda, Y., & Yamauchi, S. 2002, *ApJS*, 138, 19
- [111] Sakano, M., Warwick, R. S., Decourchelle, A., & Predehl, P. 2003, *MNRAS*, 340, 747
- [112] Sakano, M., Warwick, R. S., Decourchelle, A., & Predehl, P. 2004, *MNRAS*, 350, 129
- [113] Sawada, M., Tsujimoto, M., Koyama, K., Law, C. J., Tsuru, T. G., & Hyodo, Y. 2009, *PASJ*, 61, 209
- [114] Schwope, A. D., Brunner, H., Buckley, D., Greiner, J., Heyden, K. v. d., Neizvestny, S., Potter, S., & Schwarz, R. 2002, *A&A*, 396, 895

- [115] Sazonov, S., Revnivtsev, M., Gilfanov, M., Churazov, E., & Sunyaev, R. 2006, *A&A*, 450, 117
- [116] Sciortino, S. 2008, *Memorie della Societa Astronomica Italiana*, 79, 192
- [117] Serlemitsos, P. J., et al. 2007, *PASJ*, 59, 9
- [118] Sidoli, L., Belloni, T., & Mereghetti, S. 2001, *A&A*, 368, 835
- [119] Smith, R. K., Brickhouse, N. S., Liedahl, D. A., & Raymond, J. C. 2001, *ApJL*, 556, L91
- [120] Strüder, L., et al. 2001, *A&A*, 375, L5
- [121] Takagi, S., Ph.D thesis, Kyoto University, 2006
- [122] Tanaka, Y., Koyama, K., Maeda, Y., & Sonobe, T. 2000, *PASJ*, 52, L25
- [123] Tanaka, Y. 2002, *A&A*, 382, 1052
- [124] Tatischeff, V. 2003, *EAS Publications Series*, 7, 79
- [125] Tawa, N., et al. 2008, *PASJ*, 60, 11
- [126] Takahashi, T., et al. 2007, *PASJ*, 59, 35
- [127] Tibolla, O., Chaves, R. C. G., de Jager, O., Domainko, W., Fiasson, A., Komin, N., & Kosack, K. 2009, [arXiv:0907.0574](https://arxiv.org/abs/0907.0574)
- [128] Tomida, H., et al. 1997, *PASJ*, 49, 405
- [129] Tsuboi, M., Handa, T., & Ukita, N. 1999, *ApJS*, 120, 1
- [130] Tsujimoto, M., Hyodo, Y., & Koyama, K. 2007, *PASJ*, 59, 229
- [131] Tucker, W. H. 1970, *Ap&SS*, 9, 315
- [132] Tsunemi, H., Yamashita, K., Masai, K., Hayakawa, S., & Koyama, K. 1986, *ApJ*, 306, 248
- [133] Tsuru, T. G., Nobukawa, M., Nakajima, H., Matsumoto, H., Koyama, K., & Yamauchi, S. 2009, *PASJ*, 61, 219
- [134] Uchiyama, H., et al. 2009, *PASJ*, 61, 9
- [135] Uchiyama, Y., et al. 2008, *PASJ*, 60, S35
- [136] van Loon, J. T., et al. 2003, *MNRAS*, 338, 857
- [137] Warwick, R. S., Turner, M. J. L., Watson, M. G., & Willingale, R. 1985, *Nature*, 317, 218
- [138] Weisskopf, M. C., Brinkman, B., Canizares, C., Garmire, G., Murray, S., & Van Speybroeck, L. P. 2002, *PASP*, 114, 1
- [139] Watson, M. G., et al. 2009, *A&A*, 493, 339
- [140] Yamaguchi, H., et al. 2006, *Proc. SPIE*, 6266,

- [141] Yamaguchi, H., et al. 2008, PASJ, 60, 141
- [142] Yamauchi, S., & Koyama, K. 1993, ApJ, 404, 620
- [143] Yamauchi, S., Ebisawa, K., Tanaka, Y., Koyama, K., Matsumoto, H., Yamasaki, N. Y., Takahashi, H., & Ezoe, Y. 2009, PASJ, 61, 225
- [144] Yusef-Zadeh, F., Melia, F., & Wardle, M. 2000, Science, 287, 85
- [145] The Suzaku Technical Description Announcement of Opportunity #5,  
[http://www.astro.isas.jaxa.jp/suzaku/proposal/ao5/suzaku\\_td/](http://www.astro.isas.jaxa.jp/suzaku/proposal/ao5/suzaku_td/)



# Acknowledgement

First of all, I am deeply grateful to my supervisor, Prof. K. Koyama, Assoc. Prof. T. Tsuru, and Res. Assoc. H. Matsumoto for their continual guidance, advice and support throughout my graduate career. Their patience and sometimes strict guidance led me to complete this work.

In particular, Tsuru-san checked and revised this thesis until really late night even in the New Year day. I sincerely appreciate and want to say sorry to him and his family.

I thank all the members of the current and past Suzaku team, especially the XIS team. The quality of the GC data used in this thesis is excellent and it is due to a lot of their efforts.

I thank all the members of the current and past CR laboratory during my graduate career. Special thanks to M. Nobukawa and S. Kabuki. Thanks to my "comrade-in-arms", K. Ueno, T. Mizukami, and M. Ozawa.

I really thank my family.

I thank the Suzaku satellite who provides the data used in this thesis and is working alone in orbit at this moment.